Posiva SKB Report 04
July 2018

Mechanical design analysis for the canister

Mikael Jonsson
Göran Emilsson
Lars Emilsson

POSIVA OY

Olkiluoto
FI-27160 Eurajoki, Finland
Phone +358 2 8372 31
posiva.fi

SVENSK KÄRNBRÄNSLEHANTERING AB

SWEDISH NUCLEAR FUEL
AND WASTE MANAGEMENT CO

Box 3091, SE-169 03 Solna
Phone +46 8 459 84 00
skb.se

ISSN 2489-2742
Posiva SKB Report 04
SKB ID 1524476
Posiva ID RDOC-104919
July 2018

Mechanical design analysis for the canister

Mikael Jonsson, Göran Emilsson, Lars Emilsson
Svensk Kärnbränslehantering AB

This report concerns a study which was conducted for Svensk Kärnbränslehantering AB (SKB) and Posiva Oy.

A pdf version of this document can be downloaded from www.skb.se or www.posiva.fi.

Summary

This report summarises the mechanical design analysis of a KBS-3 copper canister for the disposal of spent nuclear fuel. The report presents the reference design of the canister, the derived load cases, and the material properties including the failure criteria and summarises the deterministic performance analyses carried out for the mechanical verification of the canister. Interactions between the canister and other engineered barriers of the KBS-3 system, in particular the bentonite buffer, are included in this study.

The content of this report is linked to the climate conditions in Finland and Sweden from a million-year time perspective and considers the rock shearing conditions, properties of the spent nuclear fuel, buffer and materials in the canister components, and research and engineering towards constitutive models for the canister materials. The report also incorporates the regulations and statements from the Swedish Radiation Safety Authority that specify that the safety factors derived according to the American ASME code that should be applied during canister design. Guides of Radiation and Nuclear Safety Authority in Finland (STUK) do not specify design guides or codes but requires that norms, standards and codes used in designing shall be defined, justified and documented. It is justified to use common approach designing the final disposal canister.

The reference design requirements for the mechanical properties and acceptable idealised defects in the canister components are determined. The report mainly addresses the long-term properties of the canister, but operational safety aspects are also included since they may affect the post-closure safety. In addition, the acceptable handling loads are therefore determined. The requirements are derived from deterministic analyses. The governing cases are the isostatic load case and rock shear case.

The isostatic pressure load case indicates the high robustness of the canister, and this result has been obtained from several deterministic and probabilistic studies.

For the rock shear load case, the stresses and strains in the canister may be high, depending on the shear amplitude, shear angle and intersection point. The governing rock shear case for the insert involves a shear-load impact perpendicular to the canister main axis at approximately 75–80 % of its length, whereas the governing case for the copper shell is a shear-load impact perpendicular to the canister axis at 90 % of the insert height. The ability of the copper shell to withstand plastic deformation is especially high. The insert also experiences plastic deformation in the rock shear load case.

This report supports the SKB preliminary safety analysis report (PSAR) and Posiva final safety analysis report (FSAR) for a spent fuel repository concerning the description of the disposal canister under the expected repository conditions during its post-closure safety.

Sammanfattning

Denna rapport är en sammanställning av de hållfasthetsanalyser som gjorts för KBS-3-metodens kopparkapsel för slutförvaring av använt kärnbränsle. Rapporten redovisar kapselns referensutformning, de härledda lastfallen, materialegenskaper inklusive kriterier för kapselbrott samt sammanställer de deterministiska analyser som utförts för verifiering av kapselns mekaniska integritet. De gränssnitt som finns mellan kapseln och övriga barriärer i KBS-3 systemet har beaktats.

Innehållet i rapporten har kopplingar till klimatförhållandena i Finland och Sverige under ett miljonårsperspektiv, förutsättningar för bergskjuvning, egenskaperna hos det använda kärnbränslet, bufferten och materialen i kapselns ingående delar, konstitutiva modeller för kapselmaterial och buffert som härletts ingenjörsmässigt eller genom forskning. Rapporten berör även föreskrifter och bestämmelser från den svenska Strålsäkerhetsmyndigheten (SSM) som specificerar den amerikanska ASME-koden för härledning av säkerhetsfaktorer vid dimensionering av kapseln. Styrande dokument från Strålsäkerhetscentralen i Finland (STUK) specificerar inte riktlinjer eller föreskrifter för dimensionering men kräver att normer, standarder och koder som används, ska vara definierade, välgrundade och dokumenterade. Det är berättigat att använda beprövade metoder för dimensionering av kapseln.

Referensutformningskrav med avseende på mekaniska egenskaper och acceptabla idealiserade defekter i kapselkomponenterna har härletts. I huvudsak har den långsiktiga säkerheten för kapseln efter förslutning beaktats, men vissa driftsrelaterade aspekter har också inkluderats på grund av att den långsiktiga säkerheten kan påverkas. Därför har acceptabla hanteringslaster utretts. Referensutformningskraven är härledda från deterministiska analyser. De dimensionerande lastfallen är det isostatiska lastfallet och skjuvlastfallet.

Kapseln har i flera deterministiska och probabilistiska analyser visat god robusthet för det isostatiska lastfallet.

Skjuvlastfallet kan ge upphov till höga spänningar och töjningar i kapseln, beroende på skjuvamplituden, skjuvvinkeln och angreppspunkten. Den styrande skjuvlasten för insatsen är ett skjuvplan vinkelrätt mot kapselns huvudaxel som angriper kapseln cirka 75-80 % från änden, medan den styrande skjuvlasten för kopparhöljet är ett skjuvplan vinkelrätt mot kapselns huvudaxel som angriper kapseln cirka 90 % från änden. Kopparhöljets förmåga att utstå plastisk deformation är mycket hög. Insatsen utsätts också för plasticering på grund av skjuvlastfallet.

Rapporten utgör en viktig grund för SKB:s preliminära säkerhetsredovisning (PSAR) och Posivas slutgiltiga säkerhetsredovisning (FSAR) med avseende på beskrivningen av slutförvarskapseln vid de förväntade långtidsförhållandena i slutförvaret efter förslutning.

Tiivistelmä

Tämä raportti kokoaa yhteen käytetyn ydinpolttoaineen KBS-3 loppusijoituskapselin mekaanisen suunnittelun aineiston. Raportti esittää kapselin referenssiratkaisun, kapseliin vaikuttavat kuormitustapaukset, kapselin materiaaliominaisuudet sekä kapselin rakenteen ja materiaalien vauriokriteerit. Raportissa on myös esitetty yhteenveto suunnittelun tueksi ja kuormankantokyvyn varmistamiseksi laadituista deterministisistä toimintakykyanalyyseistä. Vuorovaikutukset kapselin ja muiden KBS-3-systeemin teknisten vapautumisesteiden, erityisesti bentoniittipuskurin, välillä on otettu huomioon tarkasteluissa.

Tämän raportin sisältö huomioi ilmasto-olosuhteet Suomessa ja Ruotsissa miljoonan vuoden aikaskaalalla, peruskallion kalliosiirroksen, käytetyn ydinpolttoaineen ominaisuuksia, bentoniittipuskurin ja kapselikomponenttien materiaaliominaisuudet sekä käsittelee myös kapselin materiaalien konstitutiivista mallintamista. Raportti huomioi myös Ruotsin Säteilyturvaviraston (SSM) säännökset ja lausunnot, joiden perusteella ASME suunnitteluohjeen mukaisia varmuuskertoimia tulee käyttää osana suunnittelua. Suomen Säteilyturvakeskuksen (STUK) ohjeistuksissa ei määritellä suunnitteluohjeita vaan edellytetään, että suunnittelussa käytettävät normistot, standardit ja määräykset on määriteltävä, perusteltava ja dokumentoitava. On perusteltua käyttää myös Posivan tapauksessa yhtenäistä lähestymistapaa loppusijoituskapselin suunnittelussa.

Raportissa määritetään referenssikapselin suunnitteluvaatimukset sekä kapselin materiaaliominaisuuksien että kapselin rakenteelle suurimpien sallittujen vikakokojen osalta. Raportti käsittelee pääasiassa kapselin pitkäaikaisturvallisuuteen liittyviä kysymyksiä, mutta myös käytönaikaiseen turvallisuuteen liittyvät kysymykset on käsitelty, koska osalla niistä voi olla vuorovaikutusta pitkäaikaisturvallisuuteen. Tästä johtuen myös suurimmat sallitut kapselin käsittelykuormat on määritetty. Kapselin suunnitteluvaatimukset on määritetty deterministisien analyysien perusteella. Määräävät kuormitustapaukset kapselille ovat isostaattinen paine sekä kalliosiirros.

Isostaattisen paineen kuormitustapauksen analyysit osoittavat kapselin merkittävän kuormankantokyvyn. Tämä tulos pohjautuu useisiin deterministisiin ja probabilistisiin rakenneanalyyseihin.

Kalliosiirroskuormitustapauksessa kapselin rasitustila, erityisesti jännitykset ja venymät, voivat olla suuria, jos kalliosiirroksen suuruus, leikkaustason kulma ja sijainti kapseliin nähden ovat mahdollisimmat epäsuotuisat. Kapselin sisäosan kannalta kriittisin leikkauskuormitus vaikuttaa tasolla, joka sijaitsee noin 75-80 % korkeudella kapselin pohjaan nähden ja jonka normaali on kapselin pituusakselin suuntainen. Kapselin kuparivaipan kannalta kriittisin leikkaustaso sijaitsee 90 % korkeudella. Kuparivaipan plastinen muodonmuutoskyky on merkittävä. Myös kapselin sisäosa kokee plastista muodonmuutosta kalliosiirroskuormitustapauksessa.

Tämä raportti tukee SKB:n alustavaa turvallisuusselostetta (PSAR) ja Posivan lopullista turvallisuusselostetta (FSAR) käytetyn polttoaineen loppusijoituslaitokselle, erityisesti koskien loppusijoituskapselin käyttäytymistä odotetuissa loppusijoitusolosuhteissa loppusijoituslaitoksen sulkemisen jälkeisellä ajalla.

Contents

1 Introduction 9
1.1 Purpose and scope 10
1.1.1 Technical design requirements of the canister 11
1.1.2 Relation between the design premises, verification and requirements 13
1.2 Overview of this report 13

2 Loads 17
2.1 Operational handling loads 17
2.2 Loads in the repository 17
2.2.1 Types of loads 17
2.2.2 The pressure evolution as a function of time 18
2.2.3 Summary of the load cases 20
2.2.4 Case 1 – asymmetric loads on the canister due to uneven water saturation of the buffer 22
2.2.5 Case 2 – asymmetric loads on the canister after buffer saturation 26
2.2.6 Case 3 – isostatic pressure load 31
2.2.7 Case 4 – glacial isostatic pressure load 31
2.2.8 Case 5 – rock shear load 32

3 Mechanical failure criteria for the canister 33
3.1 Load cases and associated mechanical processes 33
3.2 Mechanical failure processes 34
3.2.1 Copper shell 34
3.2.2 Insert 35
3.3 Failure criteria 35
3.3.1 Copper shell including the welds 36
3.3.2 Insert 36
3.3.3 Summary of the relevant failure criteria 39

4 Material properties, models and constitutive equations 41
4.1 The relation between the mechanical tests and numerical simulations of the canister 42
4.2 The influence of the stress state on the ductility of metallic materials 42
4.2.1 Common theory 42
4.2.2 Nodular cast iron 43
4.2.3 Copper 44
4.3 Properties of nodular cast iron – BWR 45
4.3.1 Compressive properties 45
4.3.2 Tensile properties 45
4.3.3 Fracture toughness properties 46
4.4 Properties of nodular cast iron – PWR 48
4.4.1 Tensile properties 49
4.4.2 Fracture toughness properties 49
4.4.3 Fracture toughness in predeformed compressed cast iron 49
4.5 Summary – ductility of nodular cast iron 49
4.6 Properties of steel 51
4.7 Properties of copper 52
4.7.1 Background of the test data 52
4.7.2 Model for considering elastic-plastic deformation at 125 °C 55
4.7.3 Models for considering elastic-plastic deformation at room temperature 55
4.7.4 Creep deformation 58
4.8 Summary – ductility of copper 64
4.9 Properties of bentonite 64
4.9.1 Theory for von Mises stress for different swelling pressures 67
4.9.2 Theory for the rate-dependent deviatoric stresses 67
4.9.3 Theory for converting densities into swelling pressure values 68
4.9.4 Rate-dependent elastic-plastic stress-strain relations 69

5 Canister shape and dimensions 71
5.1 BWR and PWR inserts 71
5.1.1 Dimensions of the copper shells 78

6 Analysis results 79
6.1 Operational loads 79
6.1.1 Lifting the canister by the lid flange 79
6.1.2 Static and dynamic load as a result of handling contact pressure on the copper shell 80
6.1.3 Accidental surface deformation in the copper shell 80
6.1.4 Lifting the insert in the M45 screw holes 82
6.2 Loads in the repository 82
6.2.1 Loads on the nodular cast iron insert 82
6.2.2 Loads on steel lid 99
6.2.3 Loads on the steel cassette 99
6.2.4 Loads on the copper shell 100

7 Assessment of the effects of input data and conceptual uncertainties 113
7.1 Uncertainty analysis and handling loads 113
7.1.1 Insert 113
7.1.2 Copper shell 113
7.2 Uncertainty analysis, uneven swelling loads, insert 114
7.2.1 Uncertainties in input 114
7.2.2 Uncertainties in the analysis methodology 114
7.2.3 Estimation of uncertainties in the results 115
7.3 Uncertainty analysis, uneven swelling loads, copper shell 115
7.3.1 Uncertainties in the inputs 115
7.3.2 Uncertainties in the analysis methodology 116
7.3.3 Estimation of uncertainties in the results 116
7.4 Uncertainty analysis, glacial load, insert 116
7.4.1 Overview of the uncertainties in the analysis methodology and results 117
7.4.2 Residual stresses in inserts 123
7.4.3 Summary of the analysis of the canister and insert under the glacial load 124
7.5 Uncertainty analysis, glacial load, copper shell 124
7.5.1 Uncertainties in the input data 125
7.5.2 Uncertainties in the calculations 126
7.5.3 Uncertainties in the results 126
7.5.4 Residual stresses in the copper shell 126
7.5.5 Summary of the analysis of the canister under glacial load for the copper shell 126
7.6 Uncertainty analysis, rock shear load, insert 127
7.6.1 Uncertainties in the inputs 127
7.6.2 Uncertainties in the analysis methodology 128
7.6.3 Estimation of the uncertainties in the results 129
7.7 Uncertainty analysis, rock shear load, copper shell 133
7.7.1 Uncertainties in the input parameters 133
7.7.2 Uncertainties in the analysis methodology 134

8 Assessment of analysis results against the failure criteria 135
8.1 Plastic collapse criteria 135
8.2 Strain criteria – copper shell 135
8.3 Strain criteria – insert 136
8.4 Fracture resistance criteria and acceptable defect sizes 137
8.5 Essential design parameters 137

9 Summary 139

References 141

Appendix A Compilation of defect acceptance criteria for idealised postulated defects of the inserts 149

1 Introduction

Copper canisters are planned to be used for disposal of spent nuclear fuel in both Sweden and Finland using the KBS-3 method. The canister is a gas and water leak tight container that consists of two main components: a load bearing insert with channels for the spent fuel and an outer corrosion-resistant shell of copper with a 5 cm wall thickness.

The canister comprises the following components: A cast iron insert with a steel tube cassette, steel lid, copper tube with a welded or integrated base and welded copper lid; see Figure 1-1.

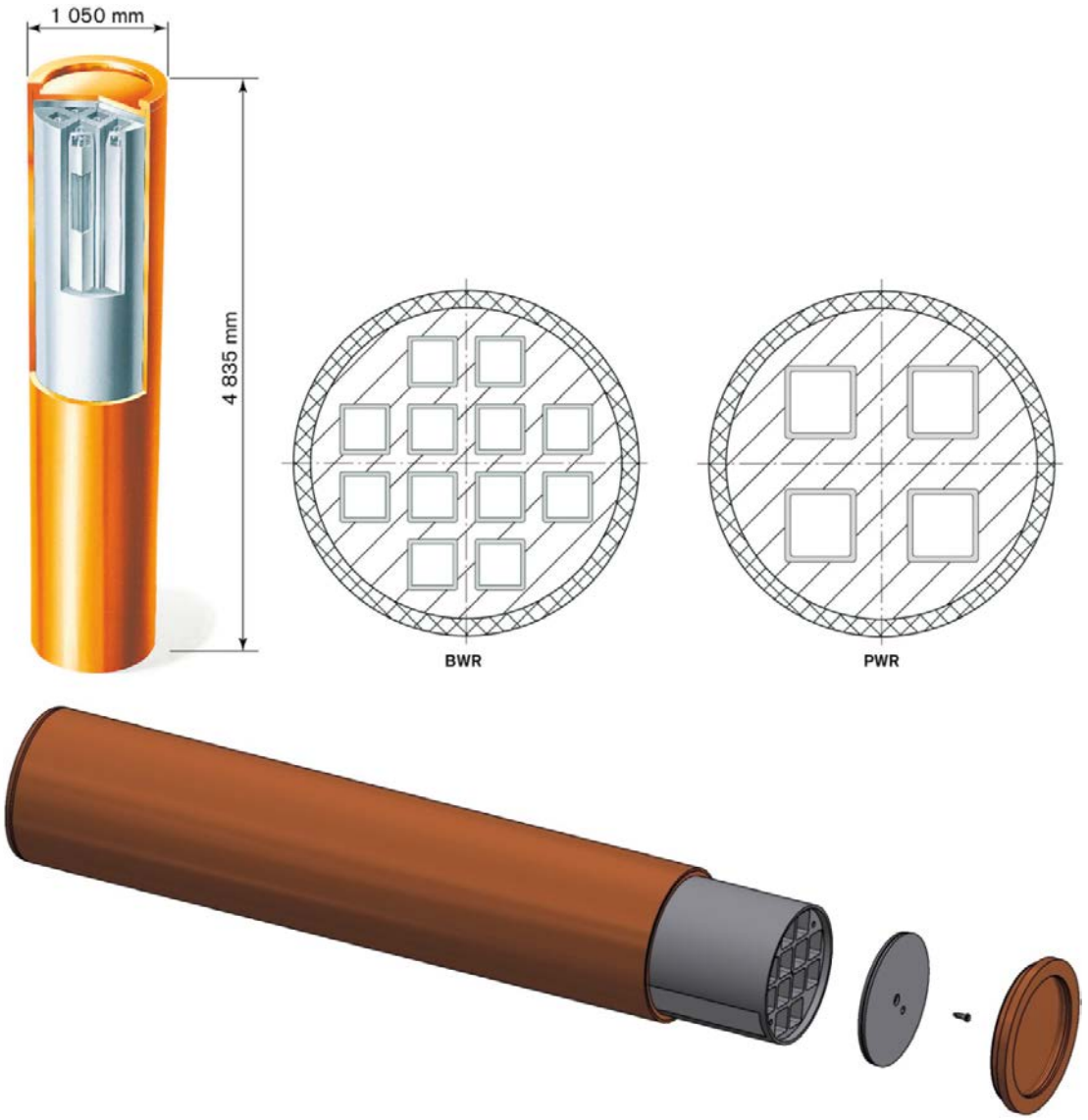

Figure 1-1. *Upper left: Schematic of the general design of the KBS-3 canister showing the insert and copper shell. Upper right: cross section of the BWR insert and the PWR insert. Lower: Schematic exploded view of the canister and its components (from the left: copper tube with a base, insert, steel lid for the insert, screw for the steel lid and copper lid).*

The materials were chosen based on the component functions. The copper shell material selected for the corrosion barrier is Cu-OFP (oxygen-free copper alloyed with 30–100 ppm phosphorus), which has adequate corrosion-resistant properties under repository conditions and a high ductility that will maintain its integrity under the loads that are expected in the repository. The materials in the insert are nodular cast iron and steel channel tubes. The fuel is placed in the canisters as whole fuel assemblies. A steel lid is bolted to the top of the insert after the fuel elements are put into place. To seal the canister, the copper tube and lid are welded together using friction stir welding (FSW). To facilitate handling the canister, the copper lid is provided with a flange to allow handling equipment to grip the canister.

Within the Swedish nuclear programme, two main types of fuel elements exist: Boiling Water Reactor (BWR) and Pressurised Water Reactor (PWR) elements. These elements are geometrically different, which results in the need for two different insert designs, as shown in Figure 1-1. The capacity of the canister is 12 assemblies of BWR and 4 assemblies of PWR fuel.

The Finnish programme for spent nuclear fuel is similar to the Swedish programme; however, a few differences exist. The canister has three versions: one for each reactor type in Finland. The capacity of the canister is 12 assemblies of BWR or VVER 440 (Vodo-Vodyanoi Energetichesky Reactor) fuel and 4 assemblies of EPR (European Pressurised Reactor) fuel. See Figure 1-2 for an illustration.

1.1 Purpose and scope

The design analysis report consists of relevant mechanical analyses of the canister for spent nuclear fuel performed until 2016. The previous report from Raiko et al. (2010) was completed during 2010, and the present report shall be considered as substitution to that report; however, the report by Raiko et al. (2010) was an important reference for this new report. The scope of this report is to verify the reference design of canisters with BWR or PWR spent fuel in terms of the mechanical loads. The report is intended to provide a part of the SKB preliminary safety assessment report, PSAR, and the Posiva final safety analysis report, FSAR.

Figure 1-2. *An artist rendition of the copper/iron canisters: (left) VVER 440 type, (middle) BWR type, and (right) EPR type (Raiko 2013).*

The analyses presented in this report cover the mechanical strength aspects of the canister; the main effort was focused on analysing the repository conditions, while analyses regarding handling the canisters, including lifting the canisters, are included. The scope of the handling analyses is to determine the magnitude of the handling loads that the canister can withstand without affecting the post-closure safety of the canister, that is, determining if the canister can still be deposited. The results from the handling analyses can in turn provide input for detailed specifications of the handling operations in the corresponding facilities or during transportation to the final repository.

The chemical integrity, criticality and possible degradation mechanisms of the canister materials, such as radiation embrittlement, are not analysed in this report. Requirements relating to these issues are given in the following references: Posiva SKB (2017) and SKB (2010b).

1.1.1 Technical design requirements of the canister

The main safety functions of a KBS-3 repository are to, either directly or indirectly by protecting other barriers in the barrier system, isolate the waste from the surface environment, contain the radionuclides and retain and retard their dispersion in the environment. Successful containment depends first and foremost on the mechanical strength of the canister inserts and the corrosion resistance and endurance of the copper shell surrounding it.

The relevant mechanical loading types are defined in the design premises report (Posiva SKB 2017). The canister shall contribute to the safety of a KBS-3 repository according the following criteria:

- *The copper shell shall remain leak tight and the canister shall maintain its ability to resist loads for an isostatic pressure of 50 MPa.*
- *The copper shell shall remain tight and the canister maintain its ability to resist loads for 5 cm rock displacements at all angles and at a rate of 1 m/s and exerted on the canister by a buffer with an unconfined compressive strength at failure of 4 MPa at a deformation rate of 0.8 %/min.*
- *The copper shell shall remain tight and the canister shall maintain its ability to resist loads for the bending of the canister resulting from asymmetric loads according to Figure 1-3.*
- *The copper shell shall remain tight and the canister shall maintain its ability to resist loads for the shearing of the canister resulting from asymmetric loads according to Figure 1-4.*
- *The copper shell shall be designed to bear the load from canister handling and transport. Indentations and scratches on the copper surface shall be minimised during canister handling and transport (SKB 2010c).*

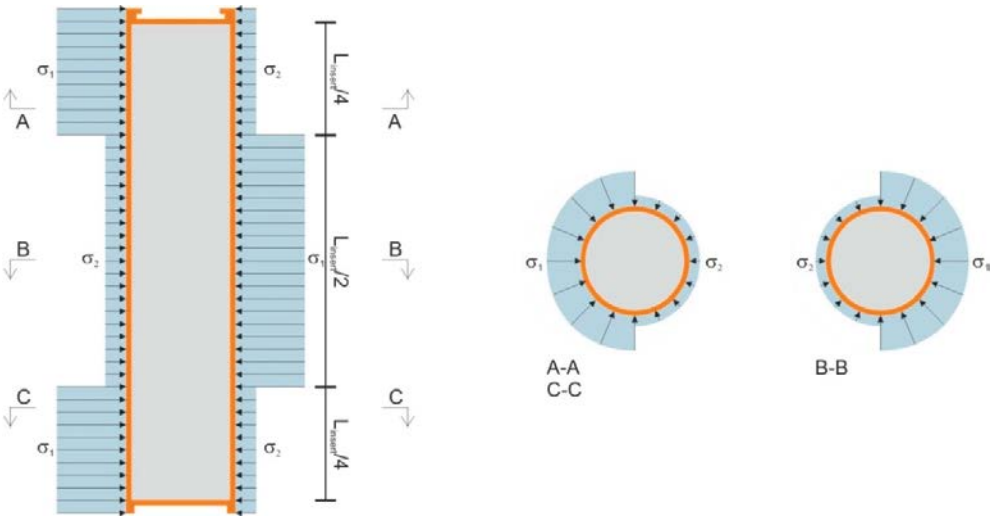

Figure 1-3. *Bending of the canister: σ_1 is the maximum swelling pressure, and σ_2 is the minimum swelling pressure of the buffer, that is 10 and 3 MPa, respectively. To σ_1 and σ_2, a hydrostatic pressure of 5 MPa at the repository depth shall be added. The right schematics refer to section A-A, B-B and C-C (Posiva SKB 2017).*

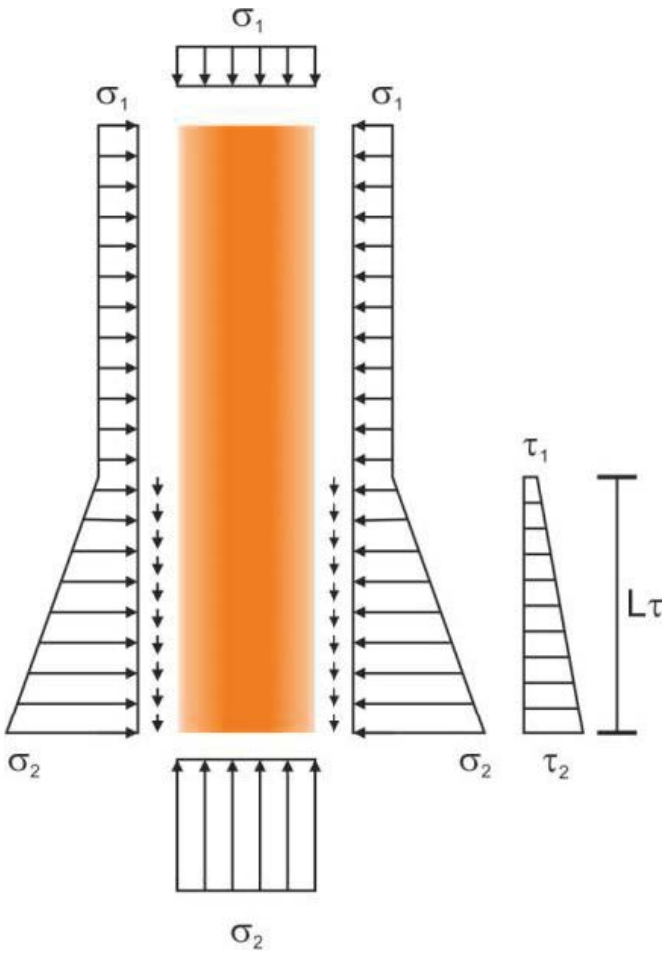

Figure 1-4. *Shearing of the copper canister, σ_1 is the maximum swelling pressure and σ_2 the minimum swelling pressure of the buffer, i.e. 10 and 3 MPa respectively. The hydrostatic pressure of 5 MPa at repository depth shall be added to σ_1 and σ_2. τ_1 and τ_2 are the resulting shear stresses that act along the length $L\tau$ of the surface of the canister (Posiva SKB 2017).*

These design requirements shall be verified for the canister as a whole, which includes the insert with the steel cassette, lid and copper shell. The verification shall comprise design and damage tolerance analyses indicating that the strength and pressure-bearing ability of the canister are sufficient to withstand the mechanical loads. This process includes verifying that the canister will not be affected or deformed in such a way that the integrity of the copper shell is breached or the ability of the canister to withstand future isostatic loads is lost.

The most important properties of the cast iron insert with its steel cassette for withstanding the isostatic load, asymmetric loads and shear load are the yield strength, elongation at failure and fracture toughness of the nodular cast iron. The copper shell is not primarily load bearing. It shall, however, have a sufficiently high ductility to withstand inelastic deformation such that it remains tight under isostatic, asymmetric and shear loads.

In addition, the design and damage tolerance analyses will determine the acceptable values of the design parameters such as the yield limit and rupture strength, elongation, area reductions and fracture toughness. Moreover, as inputs for the non-destructive testing (NDT) inspection requirements of authentic manufacturing defects, the acceptable sizes of idealised defects will be determined.

1.1.2 Relation between the design premises, verification and requirements

The expected environmental conditions used for the design verification of the canister are presented in Section 2.2, in which all possible processes are discussed, and the relevant load processes are identified. Accordingly, the mechanical loads are then processed in a series of loading, strength and fracture tolerance analyses and finally summarised in this report.

Figures 1-5a and 1-5b show schematically how results from the long-term safety assessment are used to update the design basis for the canister in terms of the updated design requirements and updated load cases that are fed into a renewed design analysis. In addition, some basic handling load cases are considered from operational point of view with a focus on long-term safety. Figure 1-6 shows the structure of the canister design analysis.

The blue areas in Figure 1-5a and Figure 1-6 are SKB related activities and reports. For the purple areas, applicable regulations from SSM (SSMFS 2008:1) should be considered. The applicability of SSMFS 2008:13 for the KBS-3 canister is not considered in Figures 1-5a and 1-6. The purpose is to show the regulations related to and derived from SSMFS 2008:13 at this point in the design analysis.

Most of the relevant information regarding design specifications (Swedish: konstruktionsspecifikationer) according to SSMFS 2008:13 can be derived from SKB (2010a, c) and this report. According to SSMFS 2008:13 Chapter 4 Clause 4, the design basis, which is a part of the design specification, must be reported to the Swedish Radiation Safety Authority (SSM). In order to fulfil the requirements of SSMFS 2008:13 regarding the design, information is required from different parts of the report structure and is visualised in both Figures 1-5a and 1-6. Note that the initial state of the canister is considered to be in the repository, and the initial state also provides an input for the verification processes.

Posiva has a slightly different approach than SKB, as shown in Figure 1-5b. A significant aspect is the guidelines from STUK that are taken into account because the present report is considered to be a part of the Posiva construction plans. The same approach as the SKB is applied regarding the structure of the canister design analysis report in terms of the initial data, modelling, results and assessment, as shown in Figure 1-6.

Normally for nuclear facilities, a design basis should cover the loads and load combinations that the safety analysis determines to be important. Additional information that should be specified includes the frequency of occurrence for each load and load combination. Two more sets of criteria that should be specified are the design and failure criteria that are evaluated against the design.

The technical design requirements in Posiva SKB (2017) and the specified loads in Sections 2.1 and 2.2 form the design basis specified in SSMFS 2008:13. For post-closure safety, Table 2-1 is especially relevant. In addition, the specified failure criteria in Chapter 3 are relevant for fulfilling the requirements of the design basis.

1.2 Overview of this report

In the following sections, the loads that the canister may be subjected to throughout its lifetime are given in Chapter 2, the failure criteria against which the outcome of the load analyses will be evaluated are presented in Chapter 3, the material properties, models and constitutive equations used during the analyses are given in Chapter 4, and the designs of the BWR and PWR canisters are given in Chapter 5. The results of the analyses of the load cases are given in Chapters 6 and 7, in which the main results are presented in Chapter 6, and some key uncertainties of the inputs are evaluated in Chapter 7. The results in Chapters 6 and 7 are compared to the relevant failure criteria in Chapter 8, and Chapter 9 provides a summary of the findings and conclusions.

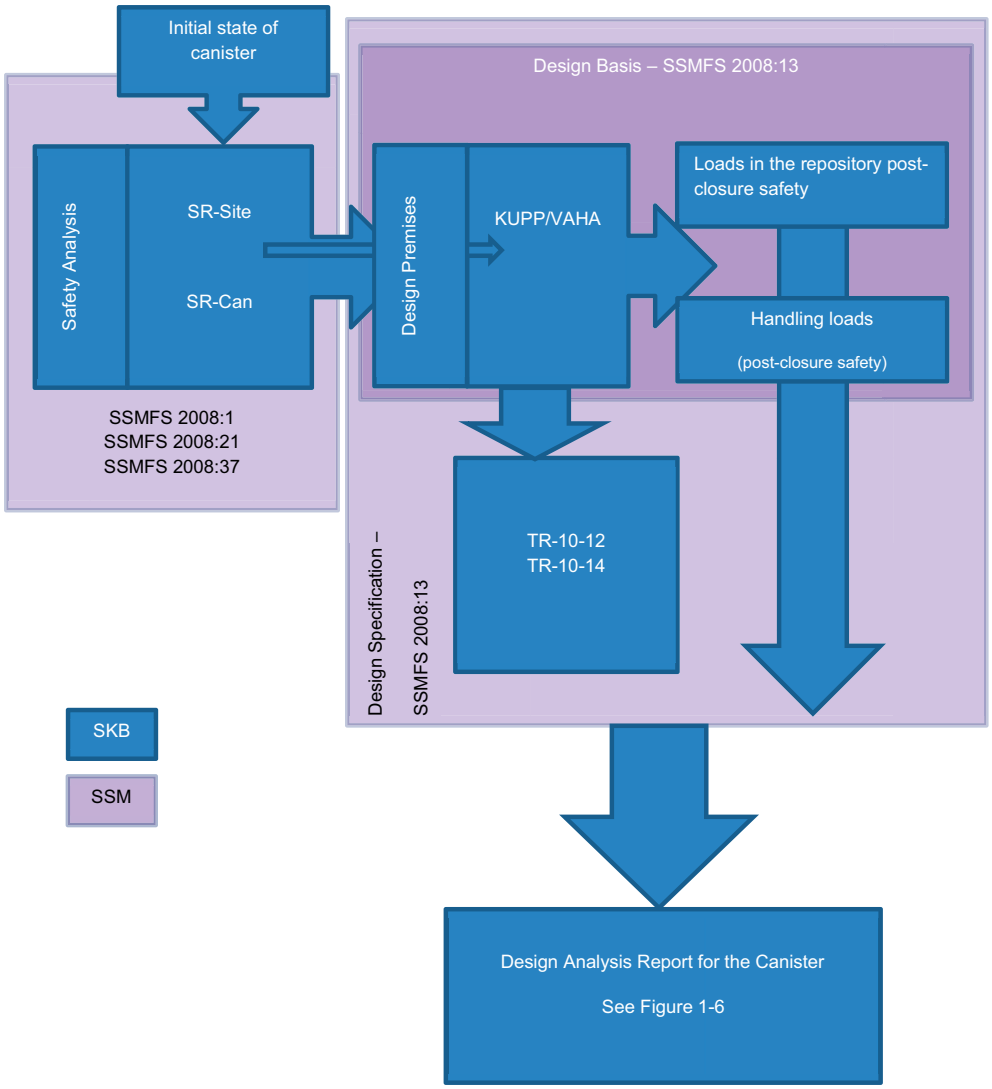

Figure 1-5a. *The relations among the design premises, initial data, models, results and assessment during the verification of the mechanical design of the canister for the case of SKB. The same procedure is valid for all mechanical loads. KUPP/VAHA is an abbreviation for Posiva SKB (2017) in the figure.*

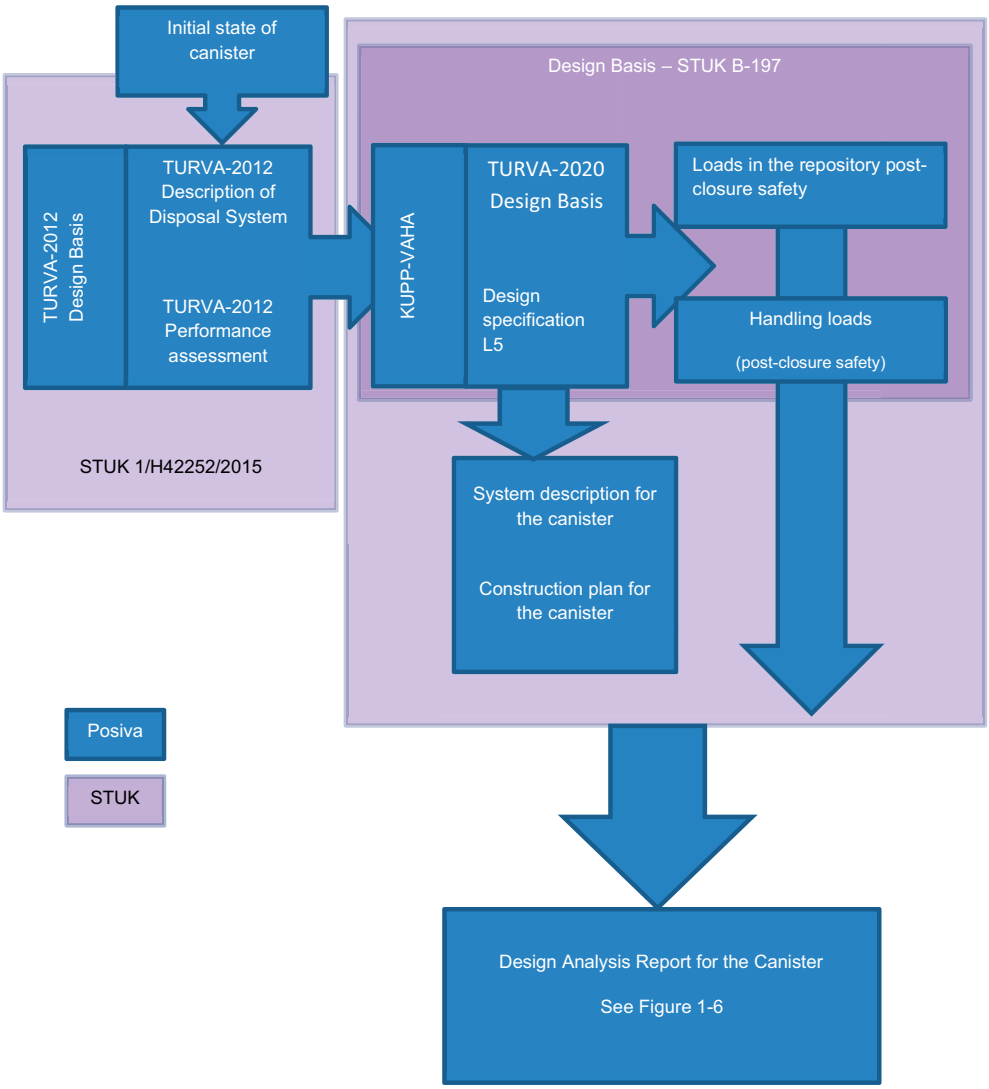

Figure 1-5b. *The relations among the design premises, initial data, models, results and assessment during the verification of the mechanical design of the canister for the case of Posiva. The same procedure is valid for all mechanical loads. KUPP/VAHA is an abbreviation for Posiva SKB (2017) in the figure.*

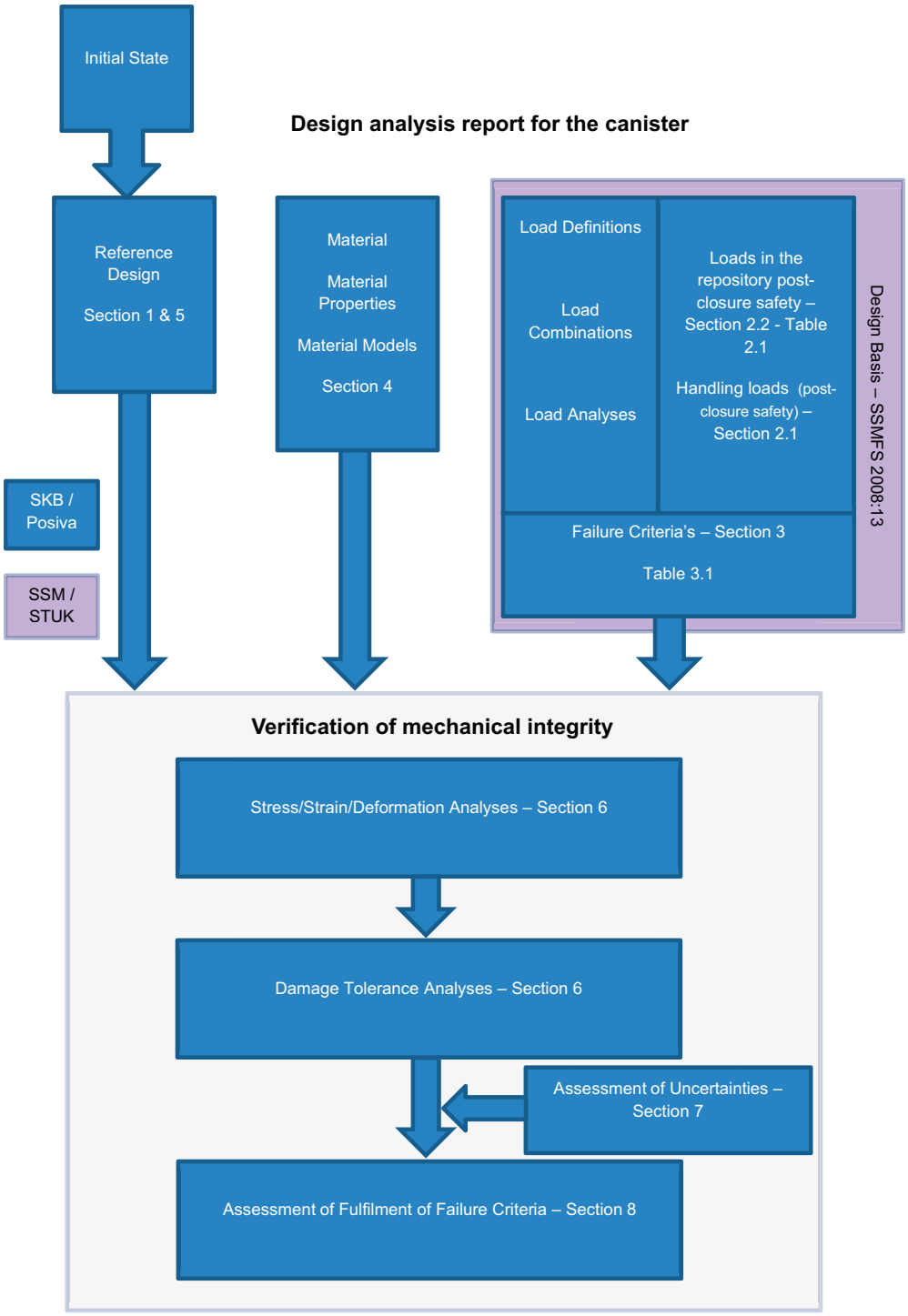

Figure 1-6. *Verification method, and overview of the canister design analysis report regarding the initial data, models, results and assessment. The figure shows the general flow of the input specification data and the strategy for verification of mechanical integrity. The same procedure is valid and applicable to both Posiva and SKB.*

2 Loads

Before the canister reaches its final position in the repository it will be handled at the encapsulation plant and during transportation and deposition. The canister should be lifted by the upper flange, and also during any unplanned stoppages while lowering the canister, without any risk of damage to the copper shell. The canister can also experience mechanical contact loads on the copper shell during handling. The operational handling loads are presented in Section 2.1.

The majority of the loads associated with the canister arise from anticipated conditions in the repository. These loads, which will affect the canister during 1 000 000 years, are presented in Section 1.1.1 and further in Section 2.2. Both the copper shell and insert contribute to the ability of the canister to withstand mechanical loads. The main load-bearing component of the canister is the insert; the primary purpose of the copper shell is to provide protection against corrosion. When the load from the groundwater pressure and bentonite swelling develops, the copper shell will deform until it contacts the cast iron insert (Posiva SKB 2017).

2.1 Operational handling loads

The canister shall be designed and handled such that the barrier function of the canister will not be compromised. The canister will be lifted by its lid during handling in nuclear facilities. The gripping is made with a special device that creates a distributed surface load. The payload of the gripper includes the total weight of the canister and its contents. For lifting operations, an additional dynamic factor is added according to the lifting device design verification practices. Transportation and handling will also subject the copper shell to mechanical contact pressure due to alignment during assembly, such as from welding machine clamps or support equipment onboard a vehicle or vessel. There is also a risk of accidental surface deformation that creates plastic deformation in the copper shell. The operational handling or transfer load processes of the canister will occur when the copper shell has temperatures ranging from 0 °C to +100 °C. The upper limit +100 °C is considered during the analyses of the handling loads because this temperature is significant when the copper shell is the primary load-bearing part of the canister. Further, in the repository after disposal, 100 °C is set as the highest acceptable temperature in the copper shell according to Posiva SKB (2017).

The current report will determine the acceptable handling loads of the canister. The governing load cases for the lifting operation are as follows:

1. Dynamic load as a result of lifting in the lid flange.
2. Static and dynamic load as a result of the handling contact pressure on the copper shell.
3. Accidental surface deformation in the copper shell due to indentation from handling.

2.2 Loads in the repository

2.2.1 Types of loads

Mechanical external loads in the repository come from the natural environment and the bentonite buffer. A repository depth between 400–500 m has been demonstrated to be suitable for a KBS-3 repository during assessments of the post-closure safety, considering the thermal, mechanical, chemical and hydrogeological conditions at the Olkiluoto and Forsmark sites (Posiva SKB 2017).

An isostatic load of 50 MPa, corresponding to a groundwater pressure of 40 MPa plus 10 MPa of swelling pressure from the bentonite itself, is set as the design load of the canister. The total pressure on the canister is the sum of the external hydrostatic pressure and the swelling pressure from the bentonite. The total pressure is somewhat lower than the arithmetic sum of these two terms. According to Posiva SKB (2017), a performance target for the canister is the ability to shall withstand an isostatic load of 50 MPa, which sets the upper limit for the groundwater pressure.

The bentonite buffer is not water saturated during installation. In the final repository, the buffer will absorb groundwater until it is fully water saturated, which may take between tens to hundreds of years at a dry site such as Forsmark. At the end of this wetting phase, the buffer will develop a swelling pressure as it is prevented from further swelling due to the confinements of the canister and rock wall.

The bentonite swelling pressure component can be unevenly distributed as long as it maintains the requirement of remaining in the range of 3–10 MPa (see Section 1.1.1). An uneven distribution in swelling pressure is expected during the wetting phase and also at saturated conditions if the dimensions of the deposition hole and density of the bentonite vary. The maximum load from the bentonite is 10 MPa (Posiva SKB 2017). To achieve the elastic-plastic stress-strain relations for the buffer, the buffer density is considered. The swelling pressure expected from sodium bentonite MX-80 at a maximum density and saturation of 2 022 kg/m^3 is 10 MPa, using the models presented in Börgesson et al. (2018).

During the early years after disposal, the maximum temperatures of the canister insert and copper shell will be 125 °C and 100 °C, respectively, as stated in Posiva SKB (2017). After water saturation of the bentonite buffer, the canister temperature will decrease from the calculated maximum temperature due to the higher thermal conductivity between the canister surface and buffer and between the buffer and rock. A load description for the uneven swelling of the buffer material that influences the canister is given in Sections 2.2.4 and 2.2.5.

The maximum swelling pressure of the bentonite depends on its chemical content and saturation level. Originally, after installation, the bentonite is in the form of sodium bentonite with a maximum swelling pressure of approximately 10 MPa. Then, after the sodium ions have been exchanged and replaced with calcium ions, which may occur in calcium-rich groundwater, the maximum pressure on the outer surface of the canister may be as high as the sum of the hydrostatic pressure (5 MPa) and the highest swelling pressure from the bentonite, (10 MPa): thus, 5 + 10 = 15 MPa. This ion change is possible, but it takes several thousands of years. Thus, the maximum possible swelling pressure varies over time. This condition, with a total of 15 MPa of external pressure, is named the “normal operation condition” of the canister for the period preceding the first glaciation. This period is expected to last for tens of thousands of years. A load description for a uniform pressure of 15 MPa that influences the canister is given in Section 2.2.6.

A load case that will occur and affect all canisters in the repository is the glacial pressure load. This load is associated with periods of time when a thick layer of ice covers the area where the repository is located. An isostatic load of 50 MPa may occur for canister temperatures between 0 °C and +20 °C. A description of these isostatic load cases is given in Section 2.2.7.

In very rare cases, the canister can be exposed to loads due to shear-type rock movements, if the shear plane intersects the deposition hole and the shear magnitude is sufficiently large. The canister insert temperature would typically be between 0 °C and +20 °C; however, it cannot be excluded that a rock shear could occur during an earlier phase when the canister temperature is higher. A description of these rock shear load cases is given in Section 2.2.8.

2.2.2 The pressure evolution as a function of time

The pressure loads were chosen with a margin to provide the limit-setting load cases in Hernelind (2015a). A glacial load of 60 MPa was assumed in the analyses of the canister. The definition of the simulation cases for both wet and dry holes is provided below, and Figure 2-1 shows the schematic evolution of the pressure as it was used in Hernelind (2015a).

For **wet** holes, the water saturation process is assumed to start immediately, and the maximum swelling and water pressure are reached after 10 years (Pressure 1 in Figure 2-1). The case is chosen to examine the normal evolution in a wet area. A hypothetic glacial load is applied after 20 000 years (Pressure 1).

For **dry** holes, the water saturation process is assumed to start after 10 years, and the full pressure is postulated to be reached after 100 years (Pressure 3 in Figure 2-1). The load component in the axial direction (Pressure 2 in Figure 2-1) is assumed to develop quickly at the top of the canister and will gradually be *replaced* by Pressure 3, which is assumed to gradually develop in less than 100 years, and a hypothetic glacial load is applied after 20 000 years.

Some processes taking place inside the canister may cause **internal loads** in the canister structure. This may result from, gas production from corrosion processes or radioactive decay of the fuel. These were handled in a study by Lilja (2012) and were shown to be negligible, since the internal pressure is more than ten times lower than the pressure on the outer surface of the copper shell. Additionally, thermal stresses due to the behaviour of the bimetallic canister structure generate potential internal loads, as do the possible residual stresses in the material that originated during manufacturing. The effect of residual stresses is discussed further in Section 7.4.2 for cast iron and in Section 7.5.4 for the copper shell. The exact definitions of the gap and gap tolerances between the insert and copper shell are further investigated in Section 6.2.

The expected pressure evolution due to gas production and thermal expansion of the gas in a BWR or PWR canister is presented in Lilja (2012) (see Figure 2-2).

It was assumed in Hernelind (2015a) that the pressure acting on the inside of the copper shell will gradually build up during the first ten years. The pressure change with time used in the analyses is shown in Figure 2-3.

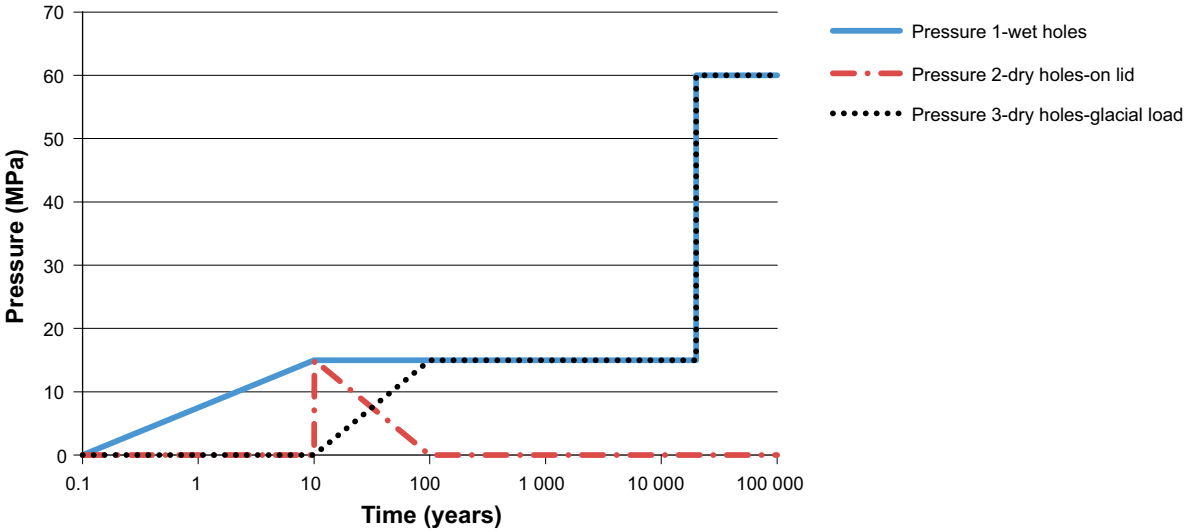

Figure 2-1. *Different pressures on the outer surface of the copper shell as a function of time after disposal time = 0. The figure represents a pessimistic assumption of the pressure as function of time used in Hernelind (2015a).*

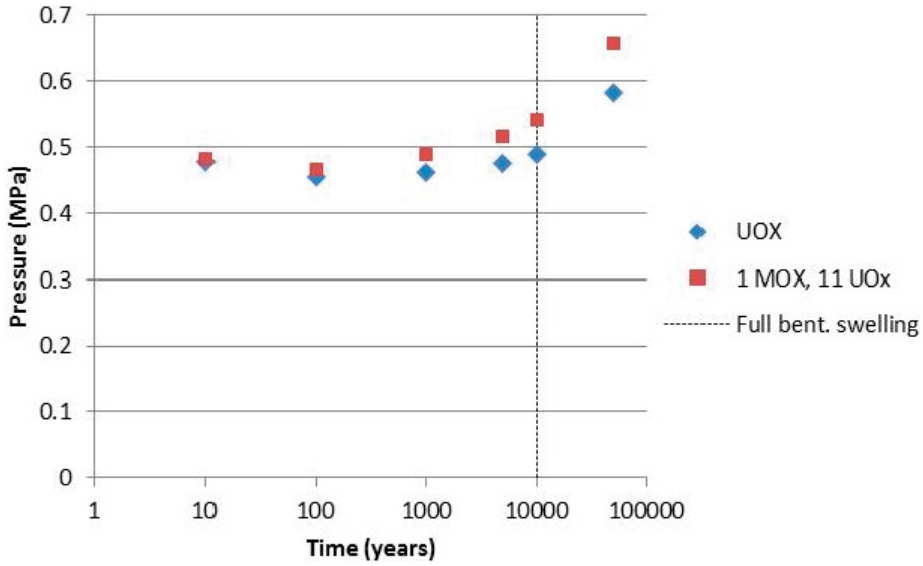

Figure 2-2. *Evolution of the internal pressure in the canister. Argon, water/hydrogen and helium from the prepressure treatment of the fuel rods are included (see Lilja 2012). Full bentonite swelling is assumed at 10 000 years as an assumption and highlighted with the dotted line. UOX is uranium dioxide fuel, and MOX is mixed oxide fuel that constitutes a part of the Swedish spent nuclear fuel.*

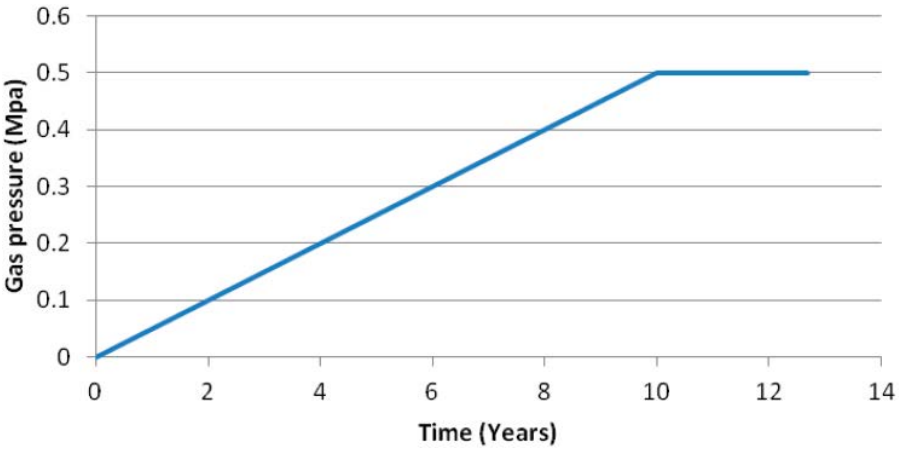

Figure 2-3. *Internal gas pressure variation used in Hernelind (2015a). This initial phase is not included in Figure 2-2.*

2.2.3 Summary of the load cases

Table 2-1 describes the postulated evolution of the canister in the repository with regards to time, temperature, saturation, bentonite swelling, hydrostatic pressure and earthquake-induced rock shear load cases. The isostatic load is much less than 50 MPa during the first 100 000 years and only reaches 50 MPa after 100 000 years. In that sense, Table 2-1 should be considered as a pessimistic approach. Loads affecting the copper shell or cast iron insert are considered separately.

Table 2-1. The canister loads extracted from the postulated repository evolution. Loads that may act simultaneously are combined. Coloured boxes correspond to the possible periods for the load case (1…5) in question.

Repository evolution phase		**Water saturation**	**Temperate**	**Glacial**	**Subsequent permafrost and glacial periods**
Years after closure of the repository		**0 years → 10 000 years**	**10 000 year → 50 000 years.**	**50 000 years→ 60 000 years**	**60 000 years → 1 000 000 years.**
Canister temperature T (°C)		**T < 125/100 (Fe/Cu)**	**20 < T < 125/100**	**0 < T < 20**	**0 < T < 20**
Load case #)	**Deformation rate**				
1) Asymmetric loads due to uneven water saturation and imperfections in the deposition hole geometry. No simultaneous hydrostatic pressure. Uneven water saturation effects will decay later and be replaced by permanent loads 2) and 3) acting under saturated conditions.	**Insert** Static	Water saturation effects are assumed to reach their maximum. Load 1) can create bending loads			
	Copper shell Creep or static	Load 1) can create compressive loads			
2) Permanent asymmetric loads due to an uneven bentonite density and imperfections in the deposition hole geometry. 3) Groundwater hydrostatic pressure + isostatic swelling pressure of the bentonite.	**Insert** Static		Bending loads from load 2) and isostatic loads from load 3)	Loads 2) and 3) are expected to act throughout the analysis period	
	Copper shell Creep or static		Uneven pressure loads from load 2) and isostatic loads from load 3)	Loads 2) and 3) are expected to act throughout the analysis period	
4) Glacial isostatic pressure (additional isostatic pressure only occurs during the glacial period).	**Insert** Static				Load 4) will cause additional isostatic pressure on the insert
	Copper shell Creep or static				Load 4) will cause additional isostatic pressure on the shell
5) Shear load due to rock displacement.	**Insert and copper shell** Short-time displacement controlled			Load 5) is primarily expected in post-glacial periods	

2.2.4 Case 1 – asymmetric loads on the canister due to uneven water saturation of the buffer

During the first period, the development in the near zone of the canister is of interest. Owing to groundwater inflow in the deposition hole, the bentonite will slowly saturate. The swelling is caused by water inflow from the surrounding rock and causes a radial swelling pressure, which acts on the outer surface of the copper shell. Depending on where the water will intrude in the deposition hole, local swelling can occur and cause temporary stresses in the canister. These swelling effects are analysed in combination with the geometric imperfections of the deposition hole. The duration of this period will differ depending mainly on the geohydrology of the rock. Hence, 65 % of the deposition holes can be saturated during the first ~2 000 years, and most of the other holes can be saturated within 300–2 000 years according to SKB (2013). Therefore, it is justified to consider 10 000 years after closure of the repository to be a pessimistic upper limit, as identified for load case 1 in Table 2-1. This load case exists only before water saturation of the bentonite buffer and can be combined with the rock shear case.

The thermal evolution (time history of the typical temperature in the near zones of the canisters) will proceed in parallel with the swelling effects and reach its maximum after approximately 10 years before slowly decaying. For the insert, the maximum temperature is less than 125 °C, and for the bentonite, it is less than 100 °C (Ikonen 2017). It should be emphasised that in the study by Ikonen (2017), dry hole conditions were considered.

Case 1a – swelling pressure in combination with a banana-shaped hole

In Börgesson et al. (2009), a simple approach was used, in which an upper-bound estimate for the swelling distribution was defined and analysed to solve the complex problem of water inflow versus swelling. The load case is the result of simplified and pessimistic assumptions during the complicated wetting phase, and the pressure derived from bentonite swelling is stated to be in the range of 3–10 MPa (Posiva SKB 2017), see Figure 1-3.

The worst case that may occur, if the requirements of the buffer and deposition hole are fulfilled, is the formation of a banana-shaped hole. The resulting swelling pressure on the canister may, in the worst case, be a triangular load distribution in combination with a banana-shaped hole. A schematic of the case is shown in Figure 2-4. The banana shape of the hole results in a deviation distance of $\delta_1 = 8$ mm according to Börgesson et al. (2009). This case was investigated using the finite element method presented in Börgesson and Hernelind (2013). The case with $\delta_1 = 85$ mm was also analytically investigated in studies by Hernelind and Börgesson (2018).

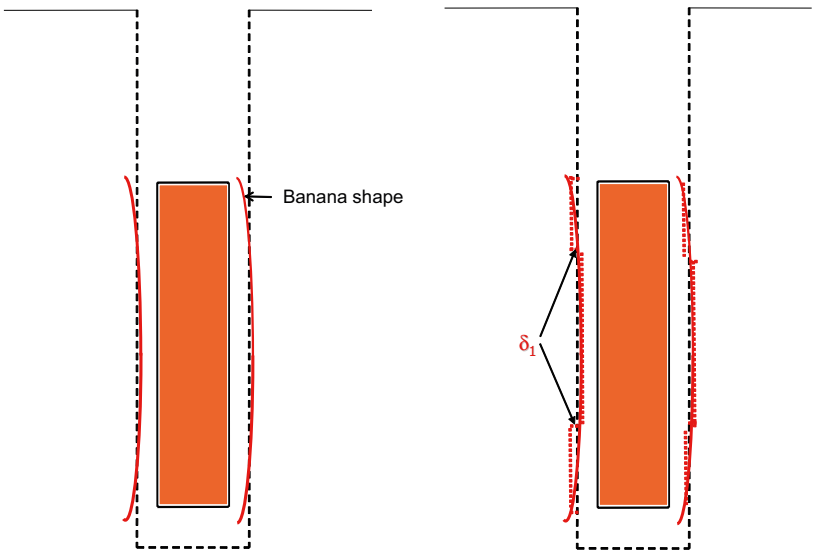

Figure 2-4. *Schematic of the studied load case in Börgesson et al. (2009). Left: The red lines illustrate the banana-shaped hole. Right: δ_1 corresponds to the average deviation from the nominal distance between the rock and canister surface caused by the banana-shaped hole.*

Cases 1b and 1c – radial swelling pressure at the outer surface of the copper lid flange and buffer swelling along the canister

In Hernelind (2014f), the load case was further investigated. Two extreme and pessimistic assumptions were studied (see also Figure 2-5 for a schematic overview):

- Case 1b: An assumed horizontal fracture in the rock near the copper lid flange causes radial swelling pressure at the outer surface of the flange. At the same time, it is pessimistically assumed that no radial counter swelling pressure will be built up during the water saturation phase because the recess in the copper lid cannot be fully filled with bentonite along the periphery. Furthermore, it cannot be excluded that an axial swelling pressure will also develop that acts on the lid and interacts with the radial pressure.
- Case 1c: Several evenly distributed horizontal cracks cause radial swelling pressure at the outer surface of the copper shell that generates axial expansion of the bentonite, which implies axial shear stresses at the outer surface of the copper shell; the same assumptions regarding the counter pressure and vertical pressure on the lid hold, as in the previous case.

External pressure from the buffer swelling caused by the water saturation phase

The maximum load from the bentonite is 10 MPa (Posiva SKB 2017).

- The swelling pressure is applied to the copper shell.
- The buffer swelling along the canister also causes shear forces on the outer surface of the copper shell. However, the shear stress is limited to 1.75 MPa (Börgesson et al. 2010), which corresponds to the shearing capacity of the buffer. The distribution of the axial shear stresses must be in equilibrium (if the gravity load is neglected, half of the length of the copper shell surface has shear stresses pointing upwards, and the other half has shear stresses pointing downwards). The most pessimistic assumption is that the shear stress reaches its maximum value and has a constant magnitude along the surface of the canister of 1.75 MPa.

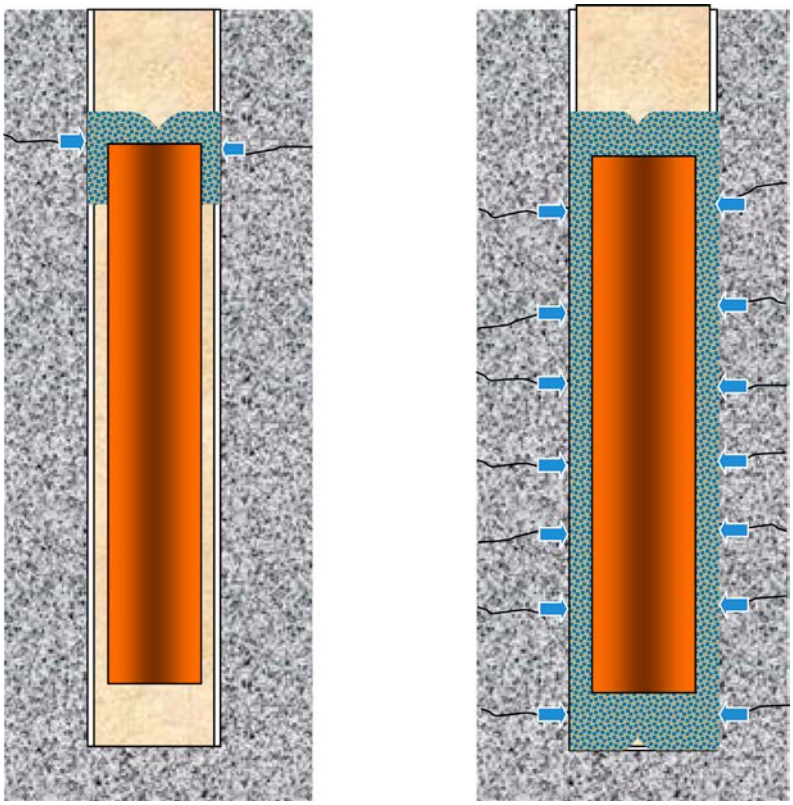

Figure 2-5. *Schematic of the studied load case in Hernelind (2014f). Left plot case 1b: swelling from water flow in a horizontal fracture through the deposition hole at the top of the canister. Right plot case 1c: swelling from water flow in several horizontal cracks cutting through the deposition hole.*

The main focus was on the copper shell, and the insert stiffness could be approximated by an axi-symmetric geometry. Figure 2-6 shows all loads (except the gravity load) and boundary conditions for the two cases studied. Figures 2-7 and 2-8 show the details of the loads and boundary conditions. In the numerical solution, the symmetric conditions were specified for the symmetry plane (displacements in the normal direction to the symmetry plane were prescribed to zero), and the copper shell was prescribed zero displacements in the vertical direction at the base (see Figure 2-8). In Figure 2-9, the buffer swelled in the vertical direction from the bottom of the rock, but the analyses were simplified by replacing the buffer with the corresponding pressures and shear stresses on the copper shell. The upper part of the canister had shear stresses that were directed upwards, and the lower part of the canister had shear stresses that were directed downwards.

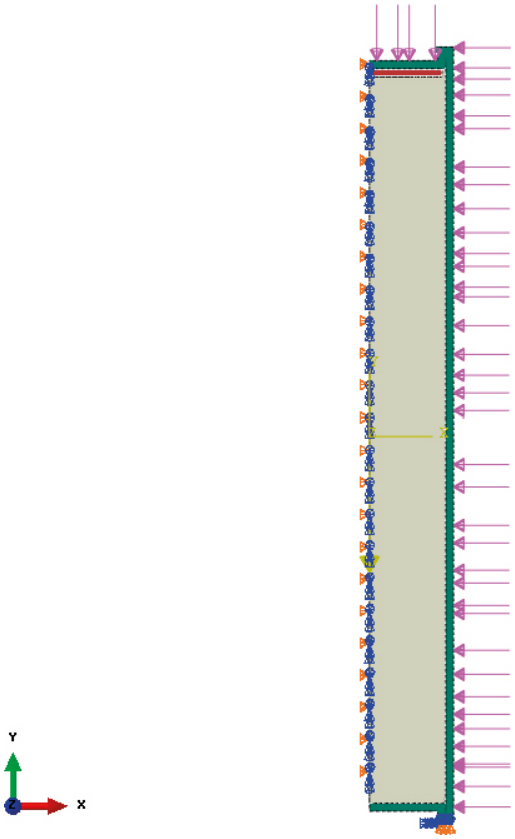

Figure 2-6. *Overall plot showing the prescribed boundary conditions (blue and orange symbols) and applied loads (arrows). The left plot shows case 1b with radial and axial swelling pressure on the copper lid and outer top of the copper shell. The right plot shows case 1c with gravity and swelling pressure on the copper lid and outer surface of the copper shell.*

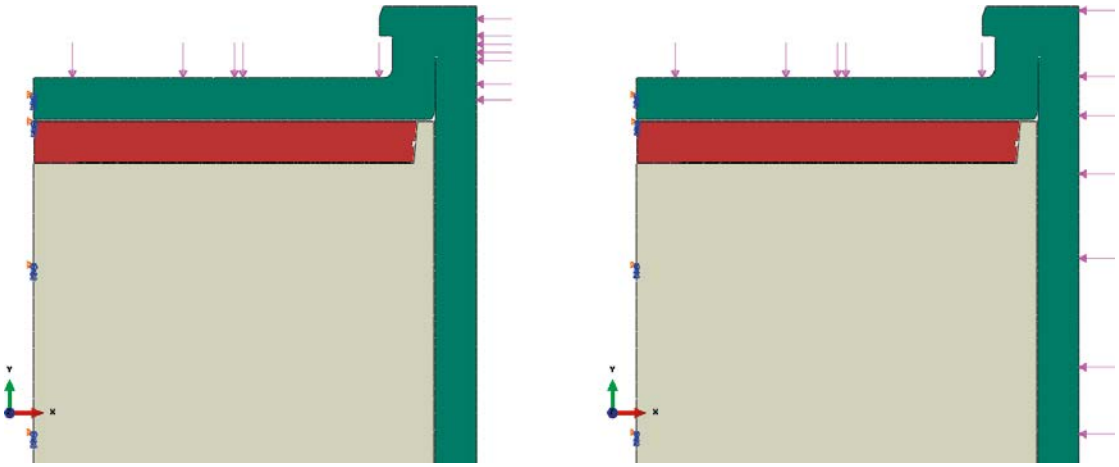

Figure 2-7. *Plot showing prescribed the boundary conditions (blue and orange symbols using symmetric conditions) and applied loads (arrows). The left plot shows case 1c with swelling pressure on the copper lid and outer top of the copper shell. The right plot shows case 1d with gravity and swelling pressure on the copper lid and outer surface of the copper shell.*

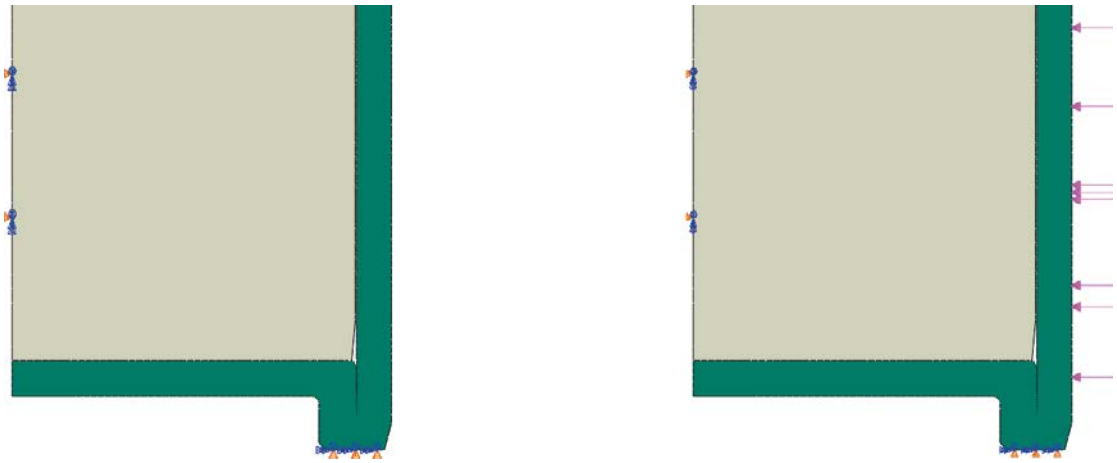

Figure 2-8. *Plot showing the prescribed boundary conditions (blue and orange symbols) and applied loads (arrows). The left plot shows case 1b with swelling pressure on the welded copper base and outer top of the copper shell. The right plot shows case 1c with gravity and swelling pressure on the welded copper lid and outer surface of the copper shell. The symmetry is defined by prescribed displacements in the normal direction (left), and the copper shell is also fixed at the base (right).*

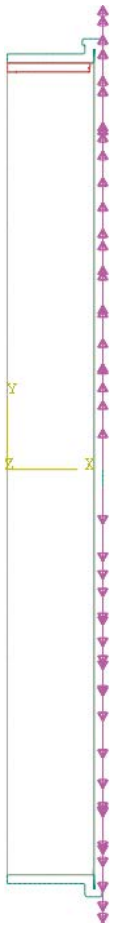

Figure 2-9. *Plot showing the applied shear load caused by swelling of the buffer in case 1c. Note the different directions – upward for the top half and downward for the base half – for the case with gravity and swelling pressure on the copper lid and outer surface of the copper shell.*

2.2.5 Case 2 – asymmetric loads on the canister after buffer saturation

In this case, the uneven swelling pressure caused by uneven wetting is successively equalised, and ultimately, the entire repository is water saturated. Finally, the pressure will be the sum of the bentonite swelling pressure and water pressure. While the water pressure will be isostatic, the bentonite density variations in combination with imperfections in the deposition hole can lead to asymmetric pressure, which is considered to be permanent. As in the water saturation case, the worst situation for the canister in terms of the swelling distribution is defined and analysed. Because the start of the period in relation to the end of the water saturation period is not well defined, it is assumed that the insert temperature can reach 125 °C and that this temperature coincides with the maximum swelling effects. These assumptions refer to load case 2 in Table 2-1. It was not trivial to estimate an upper time limit for this load case, so it is considered to last in the range from 100 to 100 000 years or more after closure of the repository. The results are reported in Section 6.2. There are several factors that may affect the rock contour after drilling the bore hole. The most important factors are listed as follows:

- The inclination of the hole may not be vertical.
- The deposition hole can be curved (banana-shaped).
- There may be rock fallout caused by, for example, spalling.
- There may be a change in the diameter due to a change in the bore head or other reasons.

Because the load case is sensitive only to factors that cause a difference in the buffer density for the same horizontal section, neither a change in the borehole diameter, such as the case described earlier, nor an inclined deposition hole will cause bending loads because they will only cause the canister to tilt. Overall, the forces must equilibrate in the horizontal direction, which means that a rock fallout on one side of the deposition hole will not be severe because the canister will be displaced or tilted, unless the rock fallout is localised at the central part of the canister. This load case can be combined with the rock shear case.

Case 2a – swelling pressure in combination with a banana-shaped hole and rock fallout

Two scenarios may yield a stress distribution that results in more severe bending of the canister:

- Curved deposition hole (banana-shaped).
- Rock fallout at critical locations.

Thus, these two scenarios combined include a curved deposition hole with rock fallout at places that accentuate the shape, as illustrated in Figure 2-10 (Börgesson et al. 2009).

The technical design requirements for the buffer and deposition hole affect the stresses in the canister. In Börgesson et al. (2009), the effects of having a combined load case of a banana-shaped deposition hole and rock fallout were analytically investigated (see the illustration in Figure 2-10 using a banana shape with 8 mm). This case may yield a stress distribution corresponding to the one shown in Figure 1-3.

The case of a banana-shaped deposition hole and possible rock fallout that yields the maximum allowable deviation from the centre line was also studied by Hernelind and Börgesson (2018). The maximum allowed deviation from the centre line was taken from SKB (2010d), which yielded at most 0.085 m (0.925 m minus 0.84 m) as the deviation from the centre line of the banana shape for an extremely pessimistic case, while the saturated bentonite buffer density was still below 2 022 kg/m^3.

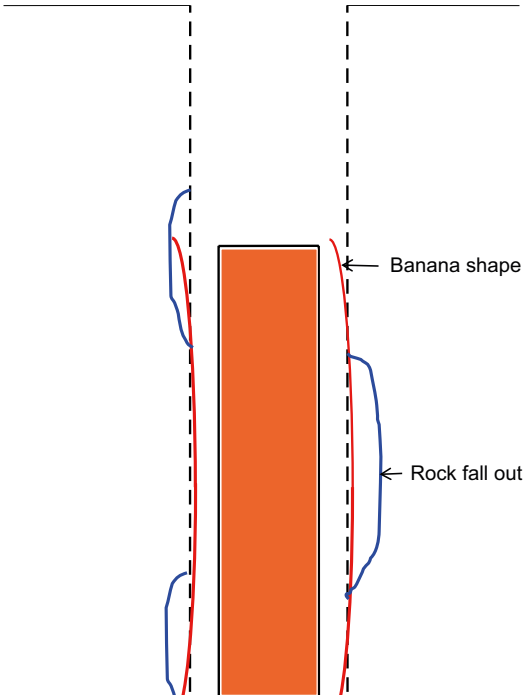

Figure 2-10. *Schematic of the curved deposition hole and rock fallout at critical locations for case 2a. The red lines illustrate the banana-shaped hole, and the blue lines illustrate the rock fallouts that accentuate the banana shape.*

The combination of the banana-shaped hole and rock fallout illustrated in Figure 2-10 may, in the worst case, cause a rectangular load on the canister due to the resulting swelling pressure. These density intervals are valid only for the bentonite MX-80. For another bentonite material, the actual densities may be different, whereas the technical design requirements regarding the buffer are set in such a way that the resulting swelling pressures will be the same, as was assessed in this case.

In Figure 2-11, the numerical approach to these cases is schematically illustrated, and the densities at saturation correspond to the combined load case in Börgesson and Hernelind (2013),

which yield the following swelling pressures:

σ_1 = 7.8 MPa

σ_2 = 3.7 MPa

This case was also studied by Hernelind and Börgesson (2018), which yielded the following swelling pressures:

σ_1 = 16.6 MPa

σ_2 = 4.3 MPa

In addition to these swelling pressures, a water pressure of 5 MPa was added.

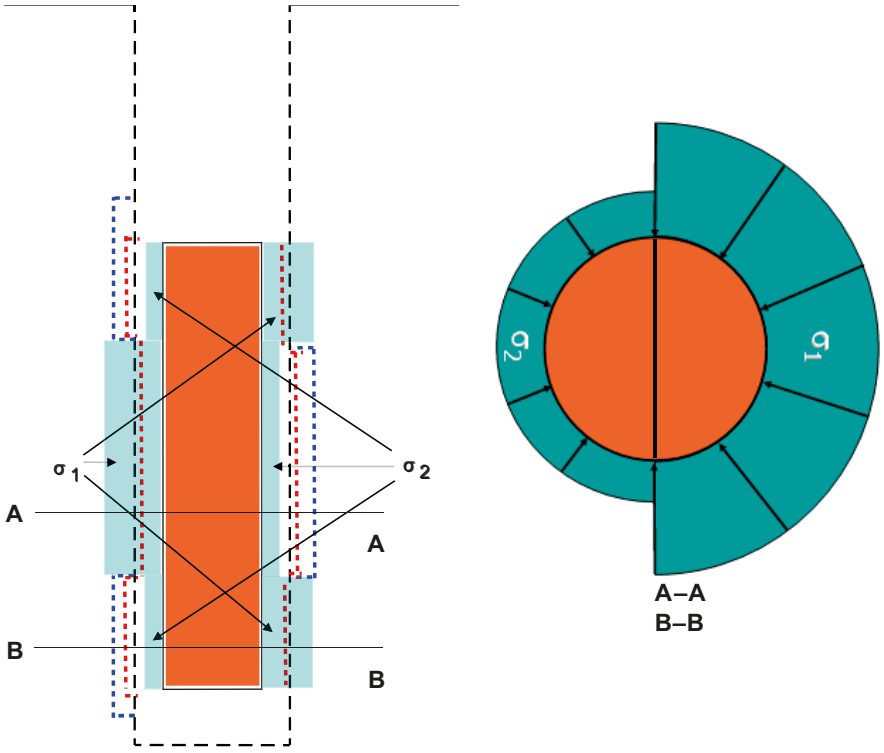

Figure 2-11. *The combined load case of the banana-shaped deposition hole and rock fallout used in the calculation of the curved deposition hole for case 2a. The right figure refers to section B–B and is mirrored for section A–A.*

Cases 2b and 2c – stresses caused by homogenisation of the buffer and density gradients in the buffer

Two cases of a permanent inhomogeneous buffer after full water saturation have been investigated.

Initially, after installing the buffer and canister in the deposition hole, gaps will exist between the copper shell and buffer and between the insert lid and copper lid. These gaps become mostly closed when the buffer swells during homogenisation.

A homogenisation analysis and the case of a permanent inhomogeneous buffer after full water saturation were investigated by Hernelind and Börgesson (2018).

Vertical shear stresses along the barrel surface of the copper shell, as shown in Figure 1-4, can be caused by vertical uneven swelling of the buffer, which is attributed to the deposition hole geometry, consequent differences in the density and swelling pressure of the buffer. The justification and investigation of this behaviour was performed in Hernelind and Börgesson (2018).

It should be noted that these analyses are valid only for the case of using bentonite MX-80. For another bentonite material, the actual densities may be different, whereas the technical design requirements regarding the buffer are set such that the resulting swelling pressures will be the same, as is assessed in this case. These cases are illustrated in Figure 2-12.

- Stresses and strains for the copper shell after homogenisation are considered in case 2b, especially close to the geometrical discontinuities, such as the welded regions in the lid and base of the copper shell,. The load consists of prescribed pore pressure at the rock wall. No other external loads are defined, that is, the gravity load is neglected.
- Vertical inhomogeneity caused by the maximum allowed difference in density between the upper and lower halves of the deposition hole is considered in case 2c.

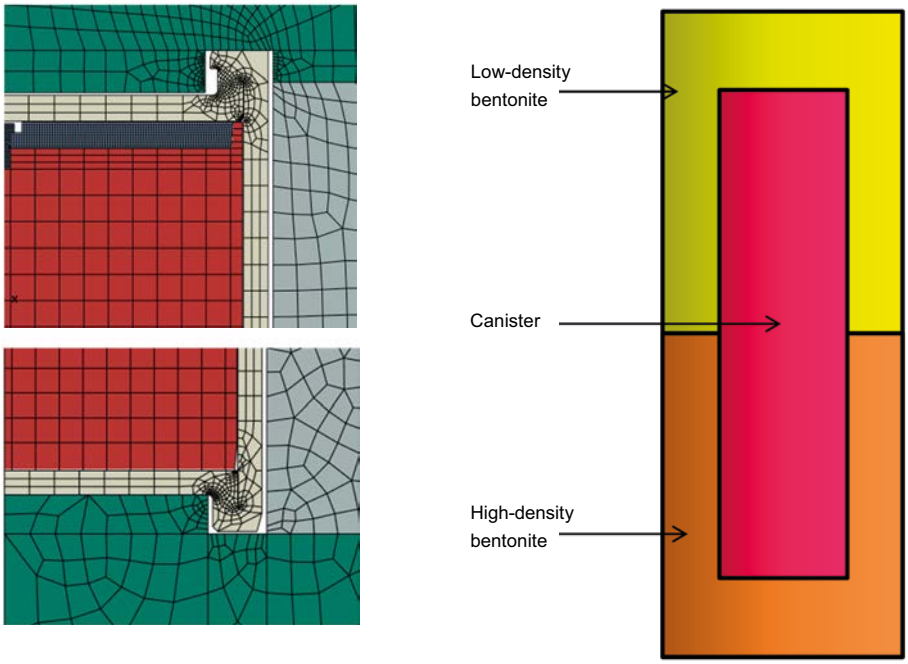

Figure 2-12. *Two load cases investigated by Hernelind and Börgesson (2018). Left: (Case 2b) gaps exist between the copper shell and buffer blocks and between the insert lid and copper lid. Right: (Case 2c) vertical inhomogeneity caused by the maximum allowed difference in density between the upper and lower halves of the deposition hole.*

The properties of the deposition hole are taken from SKB (2010d) and are shown as a schematic in Figure 2-13. The buffer properties are shown in Table 2-2. The investigation was performed in Hernelind and Börgesson (2018) using the finite element method.

Further, it was assumed that the buffer was initially installed with bentonite blocks and rings with standard dimensions that were not adapted to the size of the deposition hole.

Table 2-2. Buffer properties (Hernelind and Börgesson 2018).

Region	Saturated density ρ (kg/m^3)	Water content (%)	Dry density ρ_d (kg/m^3)
Block	2000	17	1709
Rings	2070	17	1769
Pellets	1035	17	885

The idealised FE-geometry in Figure 2-14 represents an extreme case where the diameter of the hole is assumed to be a constant equal to the smallest allowable diameter, and then, in one step, it increases to the largest allowable diameter. The two extreme diameters yield the lowest and highest density and swelling pressure, respectively, thus causing the largest differences in the swelling pressure and largest vertical shear stresses on the canister surface.

In Figure 2-15, the stress acting on the canister in case 2c is shown. Since the friction angle between the canister and bentonite is limited to a maximum of 5 degrees, the shear stress (τ) acting on the copper shell surface will be $\tau = 8.8 \cdot \tan 5°$, that is, $\tau = 0.77$ MPa.

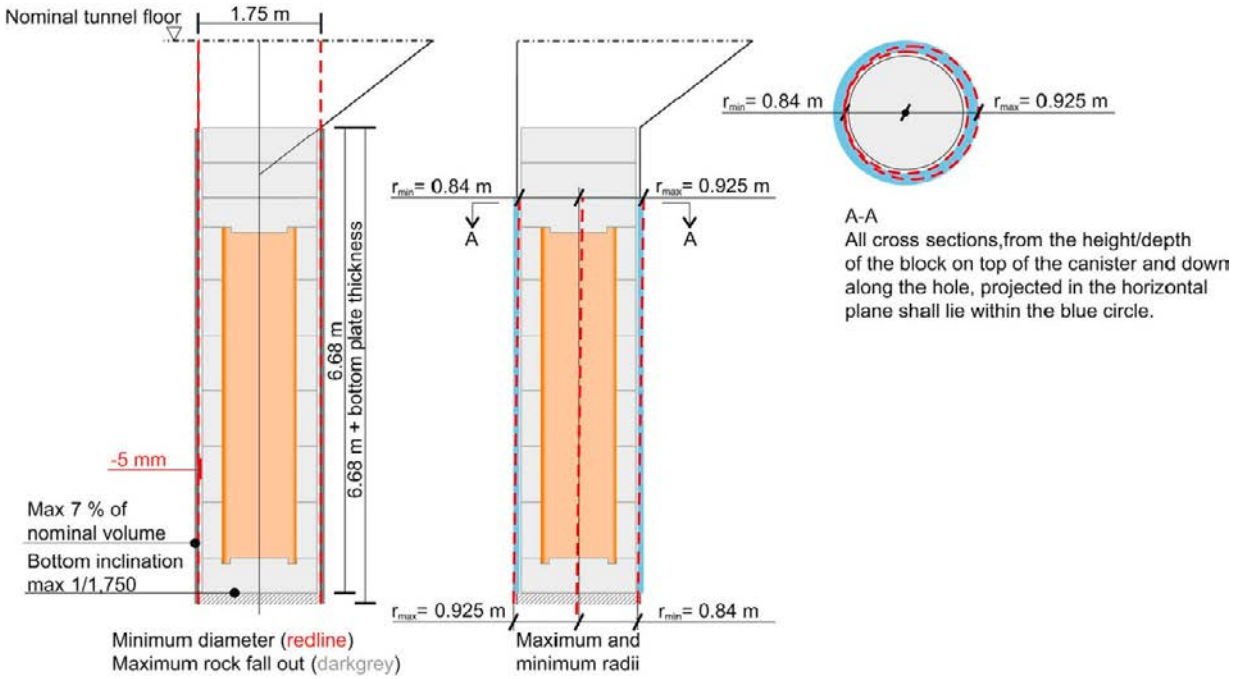

Figure 2-13. *Nominal deposition hole geometry (black thin line) and acceptable deviations in the geometry (red dotted line). The scale of the deviations in section A-A is enlarged by a factor of two. The acceptable deviations concern the part of the deposition hole where the buffer is going to be installed. The top of the deposition hole is designed with respect to the operational requirement (SKB 2010d).*

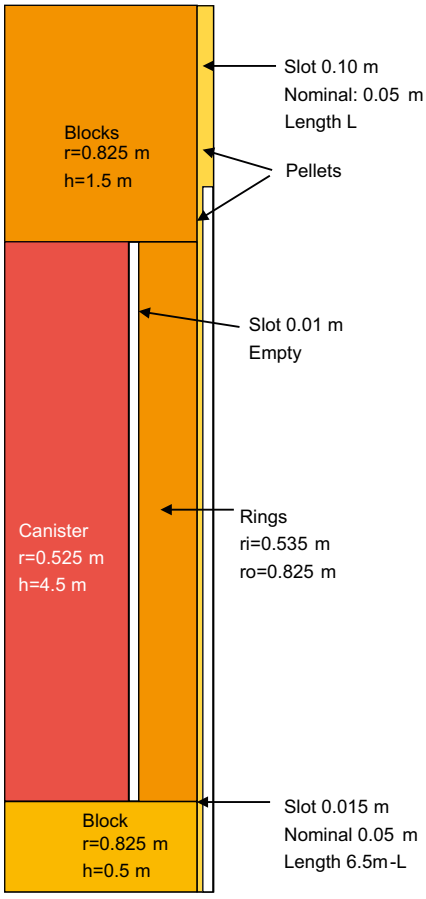

Figure 2-14. *FE-geometry of the deposition hole (Hernelind and Börgesson 2018).*

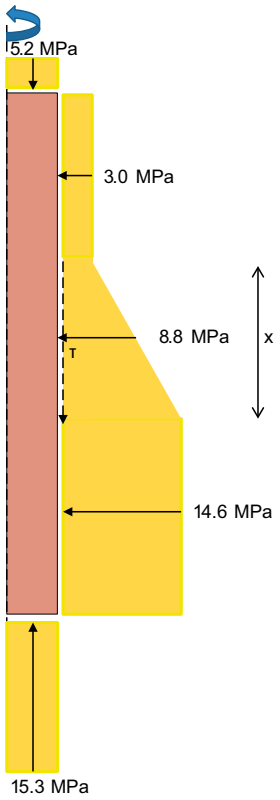

Figure 2-15. *Stresses acting on the canister in case 2c with an axial symmetry (Hernelind and Börgesson 2018).*

2.2.6 Case 3 – isostatic pressure load

For this case, the maximum load from the bentonite is 10 MPa (Posiva SKB 2017), and the superposition of the hydrostatic pressure (5 MPa) and swelling pressure (10 MPa) is 15 MPa, which is referred to as "the normal operation condition". These conditions refer to load case 3 in Table 2-1. Similar to load case 2, load case 3 is expected to last during the temperate and permafrost evolution phases of the repository, and load case 3 is considered to last in the range of 100 to 100 000 years after closure of the repository. This load case can only be combined with the rock shear case.

2.2.7 Case 4 – glacial isostatic pressure load

During the glacial period, the pressure will increase further. The loads contributing to the overall isostatic load consist of the swelling pressure of the buffer (10 MPa at maximum), the groundwater pressure at the repository depth (4–5 MPa), and the increase in the groundwater pressure due to the presence of an ice sheet at the site. Accordingly, an increase of at least 35 MPa in the groundwater pressure due to the ice load is considered in Posiva SKB (2017). Therefore, the isostatic pressure load (50 MPa), which is the total sum of all the pressure components (10 + 5 + 35 = 50 MPa), was used in the analysis of the mechanical integrity of the canister. These conditions refer to load case 4 in Table 2-1. Such a maximum thickness could possibly occur only after the first 120 000 year glacial cycle, according to Posiva SKB (2017). According to Table 2-1, it is expected that this load case will begin after 60 000 years; however, in the analyses, it was assumed that the case begins after 20 000 years and continues to occur until 100 000 years as a result of uncertainties in the ice age scenario. The temperature at the repository level will decrease but remain higher than 0 °C (Hökmark et al. 2010).

2.2.8 Case 5 – rock shear load

Rock shear movements may occur when stresses in the bedrock are released. The integrity of the canister can also be threatened due to shear-type rock movements if the shear plane intersects the deposition hole and the shear movement and rate are sufficiently large (load case 5 in Table 2-1). The detailed background is given in Posiva SKB (2017).

In the case of SKB, the justification for the classification of rock shear load failure as a low-probability case is based on results from the safety assessment of the SR-Site. The calculated probability of any of the 6000 canisters failing due to shear load, after being exposed to shear movement exceeding 5 cm during a one-million-year assessment period, is less than 0.1 (Section 10.4.5, Figure 10-124 and Table 10-20 in SKB 2011). In the case of Posiva, the justification is based on results from the safety case TURVA-2012 (Posiva 2012b). According to the discussion in the performance assessment report (and references therein), the number of canisters potentially failing due to shear load is between 35 and 78 out of 4500 canisters, depending on the criteria used to select the canister positions potentially exposed to the same shear loads considered for the SR-site (Section 7.2.4 in Posiva 2012a). Posiva will reassess the number of potentially failing canisters in the next safety assessment (TURVA-2020). Total number of canisters to be disposed has been diminished to 3 200–3 300.

The copper shell shall remain tight, and the canister will maintain its ability to resist loads for 5 cm rock displacements at all angles at a rate of 1 m/s exerted on the canister by a buffer with an unconfined compressive strength at failure of 4 MPa and a deformation rate of 0.8 %/min. The premises for the rock shear load case were further investigated regarding the specified properties for the buffer, shear plane position, shear angle and deformation rate.

The upper limit of the specified buffer swelling pressure has a direct impact on the rock shear load case because the stiffness of the buffer is affected.

The rock shear movement was considered to have an average velocity of 1 m/s, and the total movement was 5 cm. The maximum velocity of the movement has been explained by Rydén (2012). The mathematical description of the displacement velocity was found to be well approximated using a sine half period. Therefore, a maximum displacement velocity of 1.6 m/s occurred after a half displacement of 2.5 cm. These analyses are accounted for in Section 7.6.3.

Case 5a – symmetric loads in combination with the rock shear load case

The effects of the hydrostatic pressure and isostatic pressure are combined with the rock shear load case. The rock shear load is also analysed in combination with the glacial pressure load for two scenarios, in which a glacial load develops and thus occurs simultaneously with the rock shear, and the rock shear precedes the glacial load. Both scenarios are analysed in Section 6.2. Lower temperatures (0 °C) during rock shear are assumed to be the least favourable because the fracture toughness of the cast iron insert decreases with the decreasing temperature. These conditions are considered for load case 5a.

Case 5b – asymmetric loads in combination with the rock shear load case

This rock shear case is not combined with the asymmetric loads because both these loads are extreme values that are considered to have a low probability of occurrence, as discussed above. The combination would then be the combination of two events with low probability. However, the combination was investigated and is presented as a sensitive analysis in Section 7.6.3. In addition, the case of permanent stresses in the insert after full water saturation of the buffer for a combination of a banana-shaped deposition hole and rock fallout was analysed for four different subcases and compared with the rock shear case using a homogeneous buffer density at saturation: $\rho_m = 2\,050$ kg/m^3 (Börgesson and Hernelind 2013).

3 Mechanical failure criteria for the canister

The overall safety function of the canister is to provide containment and isolation of spent nuclear fuel. This is interpreted to be fulfilled as long as the copper barrier is not breached. The ultimate aim of the analysis of the canister response to any mechanical load is, therefore, to determine whether the load leads to penetration of the copper shell, in which case the canister is considered to have *failed*.

While evaluating the mechanical load cases, the copper shell will be considered as disrupted if the mechanical conditions in the shell itself exceed certain failure criteria directly associated with its rupture. The direct rupture criteria are specified in this section. The mechanical or structural conditions in the insert that exceed the failure criteria associated with its structural collapse or severe weakening are also specified. In the latter case, the damaged insert is also assumed to lead to loss of integrity in the copper shell. This is a pessimistic assumption because Section 1.1.1 states that the copper shell shall remain leak tight for any mechanical load case. Hence, a damaged insert in the rock shear case may still maintain its pressure-bearing properties against isostatic loads, and the integrity of the copper shell is still fulfilled.

The nature of the mechanical conditions induced in both the copper shell and insert will depend on the nature of the mechanical load for the load case under consideration. Static loads may be associated with either direct mechanical effects, such as gross plastic collapse and/or excessive crack growth, or excessive post-closure creep deformation.

Due to their different functions and material properties, different failure criteria are required for the shell and insert under various load conditions.

It is thus necessary to develop a complete set of failure criteria that cover the mechanical alterations associated with all conceivable load cases for both the copper shell and the insert. In principle, the consequences of any load case should be tested against all failure criteria. However, in practice, the specific load conditions and ambient conditions will be much more sensitive to some of the failure criteria than to others.

The loads are not variable or cyclic in nature but are stable and unique in character; therefore, there is no need to consider fatigue as a failure criterion.

3.1 Load cases and associated mechanical processes

The following mechanical load phenomena have been assessed to be relevant to the integrity of the canister under the repository conditions:

- Failure due excessive plastic deformation that is attributable to incorrect handling.
- Effects on the canister due to bentonite swelling pressure during wetting, saturation and thereafter.
- Isostatic loads associated with the hydrostatic pressures under temperate climate conditions and increased pressures under glacial conditions.
- Shear loads associated with rock displacements in fractures intersecting the deposition holes.

The possible loads and load combinations are considered in more detail in Table 2-1 in Chapter 2, which provides an overview of the relevant mechanical load cases and ambient conditions under which they are expected to occur. This report also assesses the effects of the postulated handling loads of the canister in the encapsulation plant and possible scratches or dents during transport (see Sections 2.1 and 6.1). The effects of the residual stresses from the manufacturing process shall be limited so that the ductility requirements are fulfilled at the initial state.

3.2 Mechanical failure processes

3.2.1 Copper shell

The following processes may lead to mechanical failure of the copper and must be considered under the conditions given in Chapter 2:

- Loosening of the lifting equipment due to excessive plastic deformation.
- Failure due to excessive plastic deformation attributable to incorrect handling.
- Failure due to excessive plastic deformation after deposition.
- Failure due to creep deformation after deposition.

The following potential failure processes are excluded:

- Plastic instability due to buckling will not occur with the identified load cases. As long as the insert is supporting the copper shell, the shell cannot collapse inwards.
- *Brittle failure*
  Cu-OFP is so ductile that unstable crack growth is irrelevant at the repository temperatures. The fracture mechanics tests of Cu-OFP show that the cracks in the test specimen were blunted but not growing (see Wells 2008). Unstable crack growth is not necessary when considering the design of the KBS-3 canister (see Björkblad and Faleskog 2016). Any inelastic deformation in the copper is ductile under the repository conditions. In practice, failure occurs after the criteria for plastic and /or creep deformation are exceeded, and brittle failure is excluded as a failure process.
- *Creep crack growth*
  Failure due to creep crack growth relates to cracks that initiate and grow due to creep deformation, and it should not be mistaken for failure due to creep deformation as mentioned above, which, in contrast, is a ductile phenomenon. Creep crack growth has been investigated in different reports: Wu and Sandström (2015) and Björkblad and Faleskog (2016). Creep crack growth was generally associated with a relatively small creep deformation zone around the crack tip. Below the creep temperatures, the crack growth was also associated with a small zone of plastic deformation around the crack tip. However, in the case of Cu-OFP, global deformation occurred before any crack growth (and crack tip blunting) could be seen.

  In Wu and Sandström (2015), compact tension (CT) specimen tests were performed at 75, 100, 125 and 175 °C. Four specimens were tested without side grooves, one at each temperature. For comparison, one specimen at 125 °C had side grooves. All tests were interrupted before rupture. Only the specimen with side grooves showed crack propagation. However, the deformation was ductile. In Danielsson (2016), an evaluation of the inelastic deformation and stress states was performed for different creep-test geometries, such as CT, notched and shear specimens. The results showed that the creep behaviour of Cu-OFP was not notch sensitive (see also Section 4.2.3).

  Creep tests on compact tension (CT) and notched specimens from 75 to 175 °C showed that initially, the sharp notches were blunted due to the high ductility of Cu-OFP (see Björkblad and Faleskog 2016). Signs of crack growth initiation were observed in tests carried out at 175 °C. The ensuing crack growth was typical of ductile fracture initiation characterised by void nucleation, growth and coalescence, where the initial increments of growth often follow predictions from conventional slip line theory. In such a CT test, it is typical for the crack to no longer be characterised as a sharp crack but rather as blunted notch defined by its opening. Most importantly, no evidence of intergranular creep fracture with diffusion-driven nucleation of the cavities at the grain boundaries was observed. For tests in the temperature range from 75 to 125 °C, cracks formed that immediately started to blunt, thus creating a new subnotch. In addition, creep crack growth did not occur. In this lower temperature range, preliminary stages of both void-coalescence and shear localisation initiation could be observed. In these cases, no evident crack initiation could be observed from a fracture mechanics point of view and neither ductile nor brittle crack growth was observed. These observations justify excluding creep crack growth as a failure process for the canister.

3.2.2 Insert

The following processes may lead to mechanical failure of the cast iron insert under the conditions given in Table 2-1:

- Plastic collapse (instability).

  The compressive stress condition may involve the loss of stability. Effects that may contribute to the buckling tendency include low yield stress, geometric inaccuracy, and volumetric defects.

- Crack initiation or stable crack growth.
- Exceeding the acceptable plastic strain.

The following potential failure processes are excluded:

- *Brittle fracture*
  Fracture mechanics tests of the nodular cast iron at 0 °C and room temperature showed that the test specimens exhibited stable behaviour under the testing conditions. The fracture toughness testing focused on finding evidence of 2 mm stable crack growth in the test specimens. The result showed that stable crack growth in the range of 30–40 mm, or even more, was achieved in the large fracture toughness test specimens (Jonsson 2017). These results provide the justification for using the fracture toughness achieved for 2 mm stable crack growth in the damage tolerance analyses of the rock shear case. In addition, a series of high loading rate tests were conducted. The results showed that the static fracture resistance curves were representative, even for dynamic loads, and the higher loading rate did not lower the fracture resistance of the insert material at these temperatures (see Öberg 2009 and Rydén 2012). The presence of brittle fractures was investigated, and it was found that the brittle area fraction was less than 1 % (see Section 4.5).
- *Failure due to creep*
  Nodular cast iron has been investigated under long-term loading conditions up to +125 °C, and the tests evidenced creep behaviour that was only logarithmic in nature that is, the creep rate decreased with time (Martinsson et al. 2010). The tests showed that the creep strain after extended periods of time, even at stress levels near the yield of the material, was likely to be small or negligible at all tested temperatures. Hence, creep phenomena in the cast iron under the repository conditions is excluded from the mechanical analyses (see Martinsson et al. 2010).
- *Failure attributable to corrosion or radiation mechanisms*
  Nitric acid that is formed due to the radiolysis of water and air remaining in the canister when it is sealed may cause corrosion of the cast iron insert and copper shell. Also, any remaining water itself can corrode the insert. A technical design requirement is stated in Posiva SKB (2017) in which "*the atmosphere in the insert shall consist of > 90 % argon*" and further "*the maximum content of water in a sealed canister is 600 g*." Therefore, it is judged that the corrosion inside the canister is negligible and can be excluded as a mechanical failure process.

  In the repository, the canister is exposed to radiation from the spent nuclear fuel. Consequently, because neutron and gamma radiation from the fuel could give rise to minor material changes in the nodular cast iron, this must be considered in the technical design requirements. Precipitation of copper particles due to radiation is a well-known problem in reactor vessel steels. Calculations of the radiation doses in the repository resulted in an upper limit for the copper content (<0.05 %) in the insert cast iron to avoid precipitation embrittlement (Brissonneau et al. 2004). A technical design requirement is therefore stated in Posiva SKB (2017) in which "*to limit gamma radiation caused hardness and brittleness in cast iron the Cu-content shall be < 0.05 %.*" Hence, radiation from the spent fuel is excluded as a failure mechanism for the canister.

3.3 Failure criteria

The failure criteria were derived with respect to the canister in the final repository, and based on the failure criteria, a number of essential design parameters for the canister components were derived (see Chapter 8). The design parameters that have an influence on the canister integrity have an effect on either the static strength or the damage tolerance of the canister.

3.3.1 Copper shell including the welds

Relevant criteria for potential failure mechanisms in the copper shell:

- Failure due to excessive plastic deformation caused by lifting the canister. This failure mode can be derived from handling the copper canister. In the encapsulation plant, the canister must be lifted, lowered and handled during working operations. In the component analysis used in the Finnish and Swedish nuclear industries, the acceptance criteria are usually adopted from the American ASME code. For the purpose of lifting the canister, the criterion for the limit load described in NB-3228.3 is used (ASME 2008a). The purpose of the method described in NB-3228.3 is to show that the applied normal load does not exceed 2/3 of the calculated collapse load. For emergency and faulty conditions, the applied load may not exceed 4/5 of the collapse load (Alverlind 2016c).
- Failure due to excessive plastic deformation attributable to incorrect handling.

  This failure mode can be derived from handling the copper canister. After encapsulation, the transfer process to the deposition hole will subject the canister to acceleration-related (dynamic) loads, possibly causing indentations in the copper shell. The depth of the indentations should not exceed the maximum acceptable depth (5 mm) because this depth has been proven to not significantly decrease the mechanical integrity of the canister (see Mannesson and Andersson-Östling (2014) and Section 6.1.3).
- Rupture due to excessive plastic deformation creep deformation. Very large deformations, on the order of a reduction in area, are needed to initiate this type of failure. The principal difference between the elastic-plastic deformation and creep deformation is the strain rate, from a macroscopic point of view. Because the strain in the copper shell can have components of both elastic-plastic deformation and creep, the same design criterion for any inelastic deformation in the copper shell should be used. This failure mode can also be represented by the reduction in area of uniaxial cross-section tensile test specimens, which is 80–90 % for Cu-OFP and FSW materials (Burman 2005, Brosius 2008, Jonsson and Ronneteg 2014). The true failure ductility of a tensile test specimen is the true plastic strain at failure (ε_f), which is defined as

  $$\varepsilon_f = \ln\frac{A_0}{A_1} \quad (3\text{-}1)$$

  where A0 is the initial cross-section area and A1 is the area at failure. The expression in Equation (3-1) is valid under the assumptions of negligible elastic strain (in relation to the total strain at failure) and incompressible plasticity theory. Equation (3-1) is chosen because it is also valid when the tensile test specimen exhibits necking, which is the case for Cu-OFP. A safety factor of 2 is applied in terms of the ductility of the copper; the required ductility (ε_f) is twice as high as the acceptable inelastic true strain (ε) in the copper shell in the final repository

  $$\varepsilon_f = 2\varepsilon \quad (3\text{-}2)$$

  In Section 6.2.4, a detailed derivation of ε_f and ε will follow.

3.3.2 Insert

The failure criteria for the insert are classified as follows:

- Plastic collapse (instability).

  This criterion is used for **force-controlled cases**, in other words, for external pressure load cases of the insert (load cases 3 and 4 in Table 2-1). Plastic collapse is the first and most common failure mode for an externally pressure-loaded thick-wall shell that is supported on the inside by bulkheads. This phenomenon can be considered during the analysis by using large deformation theory in the numerical models when external pressure load cases are analysed.

  During analyses to determine the collapse loads of components used in the Swedish nuclear industry, acceptance criteria are usually adopted from the ASME code (ASME 2008a). Judgements from an engineering standpoint are used to determine when the ASME III code is considered applicable. In the design analysis report, the criteria for plastic analysis described in ASME III, Div 1, NB-3228.3, (ASME 2008a) are used. The calculated collapse load is defined in ASME Section III, Mandatory Appendix II, Article II-1430, Figure II-1430-1, shown as Figure 3-1

in the present report. The purpose of the method described in NB-3228.3 is to show that the applied load does not exceed 2/3 of the calculated plastic analysis collapse load. In other words, a safety factor of 1.5 is used for the (global) collapse load analyses for design pressure loads. If this criterion cannot be met, then the limits of General Membrane Stress Intensity (NB-3221.1), Local Membrane Stress Intensity (NB-3221.2), and Primary Membrane Plus Primary Bending Stress Intensity (NB-3221.3) need not be satisfied at specific locations (ASME 2008a). In ASME III, Div 1, NB-3213.25, (ASME 2008a), the definition of a plastic analysis collapse load can be found. The following criterion for determining the collapse load shall be used. A load-deflection or load-strain curve is plotted using the load as the ordinate and deflection or strain as the abscissa. The angle made by the linear part of the load-deflection or load-strain curve with the ordinate is called θ. A second straight line, hereafter called the collapse limit line, is drawn through the origin such that it makes an angle $\varphi = \arctan(2 \tan \theta)$ with the ordinate. The collapse load is the load at the intersection of the load–deflection or load–strain curve and the collapse limit line. This is also shown in more detail in ASME III Div 2. Article NB-3228.3 in (ASME 2008a), which shows how to determine this collapse load.

- Crack initiation or stable crack growth.

  This criterion is used for all load cases with respect to the insert.

  In the isostatic load case, when the load controls the stresses and causes primary stresses, the damage tolerance analysis is conducted using K_{Ic} data that are based on crack initiation, and not limited stable crack growth such as J_2 (mm). This means that crack initiation is not allowed during the load-controlled isostatic load case.

  When performing a damage tolerance analysis of components with cracks, different approaches may be used with regards to the method of analysis and safety factor decisions during assessment. In Sweden, the Swedish Radiation Safety Authority (SSM) has published a handbook (Dillström et al. 2008). In this handbook, a procedure is described that can be used for both detected cracks or crack-like defect assessments and defect tolerance analyses.

  – The method utilised in this procedure is based on the R6 method. This is also the method chosen for the damage tolerance analysis of the insert in the case of an external pressure load (R6, option 1 failure assessment curve). In the case of a displacement-controlled load, which is a rock shear load, the damage tolerance analysis is based on a *J*-integral analysis.

  – Within the SSM procedure, a deterministic safety evaluation system is defined (which is not present in the original version of the R6 method). When choosing safety factors for nuclear applications, the objective has been to retain the safety margins expressed in ASME-Sect. III in ASME (2008a) and Section XI in ASME (2008b). The safety margins used are for assessing the nuclear pressure vessels under normal operation. These safety recommendations give a margin of $S_{FK} = 3.16$ against fracture and 2.7 against plastic collapse (normal/upset load event), and $S_{FK} = 1.41$ (emergency/faulted load event), as defined in the SSM handbook (when using a *J*-integral analysis, S_{FJ} should be used, where $S_{FJ} = (S_{FK})^2$). These safety factors are taken from ASME XI, Div 1, IWB-3612 (acceptance criteria are based on the applied stress intensity factor). ASME XI, Div 1, IWB-3611 (acceptance criteria based on the crack size) cannot be used, according to the Swedish Radiation Safety Authority.

  – A damage tolerance analysis using these safety factors does not require that one must fulfil other code requirements within the ASME code (regarding inspection, fabrication, etc.). The only purpose is to use established safety factors for nuclear applications (within Sweden and Finland) when performing damage tolerance analyses.

  – The aspect ratio chosen for the postulated (initial) defects is mainly related to the assumed damage mechanism. For defects in the nodular cast iron with crack-like characteristics from a fracture mechanical point of view, an aspect ratio (length/depth) of 2.5 may be used for surface defects based on the evaluation of defects in the manufactured inserts (see Dillström and Alverlind 2014). In the damage tolerance analysis for the insert, different assumptions regarding the aspect ratio have been used (both for the surface and internal defects). The purpose has been to show that it is possible to introduce reasonably sized defects and demonstrate the impact of the aspect ratio on the requirements for inspection using non-destructive testing (NDT).

The initiation of crack growth can be allowed in the displacement-controlled load cases, but a reasonable safety margin shall be applied for stable crack growth. The dimensioning value will be $J_{2\text{mm}}$, which corresponds to a stable crack growth of 2 mm in the fracture test specimens. Reasonably small crack growth can be allowed because limited local crack growth does not lead to global rupture. This is justified from the fracture toughness testing as discussed in Section 4.2.2.

In the case of a **displacement-controlled load**, such as uneven swelling or rock shear (load cases 1, 2 and 5 in Table 2-1), the influenced stresses are secondary in nature. The stable crack growth criterion is then taken as

$$J(a) < J_{2mm} / 2 \tag{3-3}$$

where $J(a)$ is the calculated J-integral parameter value of the postulated crack, J_{2mm} is the J-integral value corresponding to 2 mm stable crack growth in the fracture toughness test specimen, and 2 is the safety factor. A safety factor of 2 for a low-probability load case (under a postulated emergency or faulted condition) is taken according to the ASME Boiler and Pressure Vessel Code, ASME XI, Division 1, Article IWB-3600, (ASME 2008b). The discrepancy in the safety factors comes from the relation between J and K_I, which is valid for the plane-strain state:

$$(K_I)^2 = J \cdot E / (1-\nu^2) \tag{3-4}$$

where E is Young's modulus and ν is Poisson ratio. This means that $J \sim K_I^2$. The justification for the classification of the shear load failure as a low-probability case is based on results from the safety assessment of the SR-Site. The calculated probability of any of the 6 000 canisters failing due to shear load after being exposed to a shear movement exceeding 5 cm during the one-million-year assessment period is less than 0.1 (see Section 2.2.8). This also means that the calculated likelihood that none of the 6 000 canisters will fail due to shear load is greater than 90 %. This approach is applied in the Posiva case as well.

The acceptable amount of crack growth is assessed from the fracture resistance curves (R-curves), which are measured during fracture mechanical tests at various temperatures. These curves provide the relation between stable crack growth and the respective J-integral. The phenomenon involves limited stable crack growth in a ductile material. According to Brickstad (2009), a toughness value of 2 mm of stable growth can be used in this case since the insert is subjected to short-term displacement-controlled loading; thus, the load is considered secondary.

- The plastic strain is exceeded.

  This criterion is used for the displacement-controlled load cases. The rock shear case is an exceptional load case that possibly only hits a few canisters during a very long period of time, and therefore, this type of effective stress criterion is used. The rock shear load is displacement-controlled, which means that the consequent stresses are secondary in nature (Dillström 2017). A safety factor of 3 is considered to be adequate in Dillström (2017). The required true plastic strain (ε_{req}) of the nodular cast iron and steel materials is

  $$\varepsilon_{req} = 3\varepsilon_{sim} \tag{3-5}$$

  where ε_{sim} is the true plastic strain achieved from the analyses of the rock shear case. In Section 6.2.1, a detailed determination of ε_{sim} and ε_{req} is presented.

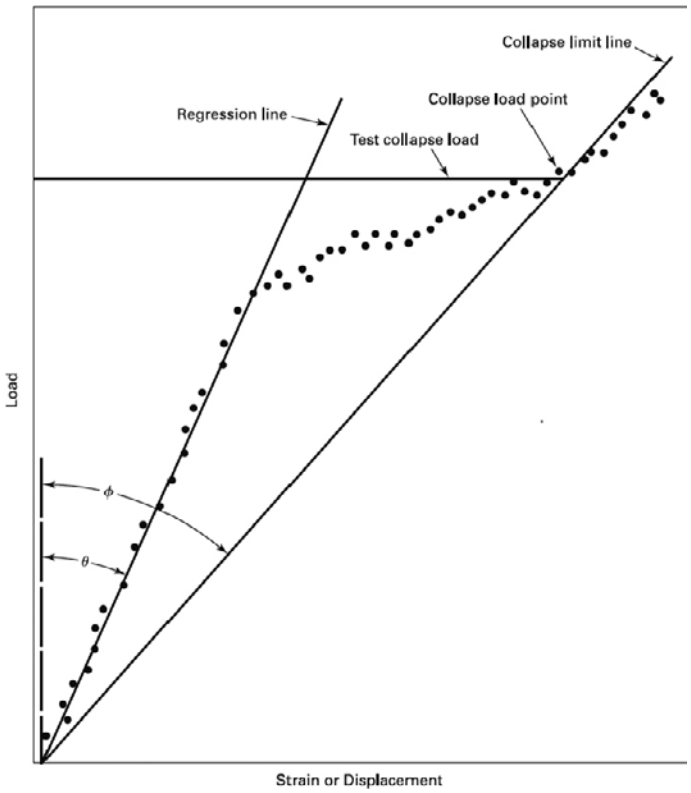

Figure 3-1. *Definition of the collapse load according to ASME Section III, Mandatory Appendix II, Article II-1430, Figure II-1430-1.*

3.3.3 Summary of the relevant failure criteria

The relevant failure criteria for the cast iron and copper are summarised in Table 3-1. Brittle fracturing at actual operating temperatures does not occur due to the adequate fracture resistance properties of both materials. Nodular cast iron and copper are very dissimilar metals, so different types of failure criteria are needed. The differences in the material behaviours and component geometries may allow for excluding some failure criteria.

Table 3-1. Summary of failure criteria relevance.

Failure criteria	Insert	Copper shell
Plastic collapse (instability)	Yes (for primary stresses)	—
Crack initiation or stable crack growth	Yes (for all load cases)	—
Fracture due to excessive plastic deformation	Yes (for secondary stresses)	Yes (isostatic load and asymmetric pressure load cases, rock shear case)
Creep	—	Yes (isostatic load and asymmetric pressure load cases)
Brittle fracture	—	—

4 Material properties, models and constitutive equations

To perform the design analysis, adequate data and models representing the canister materials are needed. This section describes the material data, sampling methods for the data analysis and models for plastic deformation and creep in copper.

The mechanical properties of the canister structural materials to be used in the design analyses are based on a large amount of test data from demonstration-manufacture tests, reflecting the actual material properties of the inserts, copper tubes, lids and welds. To address the scatter in the data, basic statistical methods have been used. The average values taken from mechanical test data are used for the stress-strain relationships of the nodular cast iron and copper shell. The strategy is to use relevant methods for evaluating the results in combination with the safety factors derived in Section 3.3.

To perform the assessments, the yield strength, ultimate tensile strength, critical stress intensity factor and J_r -curves of the material must be determined. If possible, data obtained from testing the actual material of the component should be used. This is not always possible, and therefore, minimum values from codes, standards or material specifications may be used. These data should be determined at the actual temperature (Dillström et al. 2008).

These values were used in the analyses for load cases 1, 2 and 3 regarding even and uneven swelling and case 5 for the rock shear load in Table 2-1. The most significant load case is, however, load case 4 in which isostatic pressure is applied during the glacial period, as in shown in Table 2-1. For this load case, the cast iron stress-strain curve is scaled to represent the minimum design requirements defined by the minimum yield stress.

It should be noted that values used in the calculations may differ from those stated in the SKB and Posiva specifications for manufacturing the canister components. While this report specifies the reference parameters for the canister components, the manufacturing specifications contain parameters applied to material testing standards and other conventional methods. One example regards the concepts of true stress and engineering stress. The reference parameter is expressed in terms of true stress derived from finite element simulations of the canister, and the manufacturing parameter is expressed in terms of engineering stress because it is a common practice in mechanical tensile testing.

The material models for the canister materials are based on elastic-plastic behaviour with isotropic linear elasticity and von Mises plasticity. This is a very common way to model structural metallic materials. The elastic part is described using any two of the four material parameters: Young's modulus, Poisson ratio, bulk modulus and shear modulus. The plastic part is defined using the yield surface, flow rule and deformation hardening function (true stress versus plastic strain). The latter can be defined either as a continuous analytical function or as a piecewise linear function using commercial finite element software. The justification to use von Mises plasticity for copper is given in Unosson (2017). For nodular cast iron, the justification is given in Smedstad (2016) and in Martin et al. (2009). The steel materials are modelled in the same way. For nodular cast iron, three separate models for the stress-strain relationship are used, depending on the character of the stress state, static tension, static compression or strain-rate-dependent deformation (in the dynamic rock shear load case). The von Mises model is symmetric for both tension and compression. The flow rule is based only on the deviatoric stress state (pressure stresses are excluded but triaxiality is considered such that perfect triaxiality does not cause plasticity). Due to this behaviour, the parameters should be calibrated for tension- and compression-dominated cases separately. The numerical values for the nodular cast iron and steel models are given in Tables 4-1 to 4-7. There are basically two main types of constitutive models for copper; the main difference is whether creep is considered or not.

4.1 The relation between the mechanical tests and numerical simulations of the canister

During the verification procedure of the mechanical integrity, the stress/strain/deformation analyses of the full-scale canister must be compared and evaluated with the material properties determined from the mechanical tests of the canister materials. The goal of the mechanical tests is to report the "engineering" magnitudes of stress and strain. However, this simplification must be considered in the evaluation; the correct way to express stresses and strains is to use and express the "true" magnitudes.

In the 3D-stress state, the effective stress σ_e is defined as the effective von Mises stress according to Equation (4-3) below and has been used during the evaluation of the test specimens and full-scale canister.

In the 3D-strain state, an effective plastic strain $\bar{\varepsilon}^{pl}$ has been used in conjunction with the effective von Mises stress. This quantity is defined as

$$\bar{\varepsilon}^{pl} = \int_0^t \sqrt{\frac{2}{3}\dot{\varepsilon}_{ij}^{pl}\dot{\varepsilon}_{ij}^{pl}}\,dt \tag{4-1}$$

where the inelastic strain rate is given by $\dot{\varepsilon}_{ij}^{pl}$, and the summation over i and j is assumed. In ABAQUS (2014) terms, $\bar{\varepsilon}^{pl}$ is designated *PEEQ* for the elastic-plastic analyses or *CEEQ* if the user-defined subroutine CREEP in Section 4.7.3 is used.

The constitutive models in this section have been compared with the models of different test specimens and validated accordingly. Thus, $\bar{\varepsilon}^{pl}$ and ε_f can be used for comparing results from simulations and physical tests. Ductility is considered to be the effective plastic strain at failure. A straightforward approach for evaluating the ductility of uniaxial cross-section tensile test specimens is to use Equation (3-1).

4.2 The influence of the stress state on the ductility of metallic materials

4.2.1 Common theory

The canisters are required to withstand several load cases, such as high hydrostatic pressure from a future glaciation event and rapid rock shear loads. These load cases represent loading the material with very different stress states. Below an outline of a von Mises model for the material behaviour under different stress states is presented.

The ductility of a metallic material depends on the stress triaxiality (T), which is defined as

$$T = \frac{\sigma_I + \sigma_{II} + \sigma_{III}}{3\sigma_e} \tag{4-2}$$

where $\sigma_I \geq \sigma_{II} \geq \sigma_{III}$ are the principal stresses and the effective von Mises stress σ_{Mises} is defined as

$$\sigma_{Mises} = \sqrt{\frac{1}{2}((\sigma_I - \sigma_{II})^2 + (\sigma_{II} - \sigma_{III})^2 + (\sigma_{III} - \sigma_I)^2)} \tag{4-3}$$

It has been demonstrated that the stress triaxiality alone is insufficient to determine the ductility at low triaxialities (see Barsoum and Faleskog 2007). In addition to the stress triaxiality, a second parameter is required that provides information about the deviatoric stress state itself. Such a parameter is the so-called Lode parameter (L), which characterises the deviatoric stress state and is defined as

$$L = \frac{2\sigma_{II} - (\sigma_I + \sigma_{III})}{\sigma_I - \sigma_{III}} \tag{4-4}$$

The Lode parameter (L) is in the range of $-1 \leq L \leq 1$. The ductility is inversely related to the value of T (the ductility increases with decreasing T). The mechanical tests of the nodular cast iron and copper have been evaluated in terms of the strains and triaxiality stress states because the ductility (strain at failure) depends on the triaxiality.

4.2.2 Nodular cast iron

In Dahlberg et al. (2014) and further in Dahlberg et al. (2017), the plastic properties of the nodular cast iron material were found to exhibit a nontrivial dependence on the hydrostatic stress. The effect was found to be due to not only the microstructure, where a relatively high volume fraction of graphite nodules acted as porosities, but also the matrix material showing a so-called strength differential effect.

The triaxiality was $T = 0$ for the pure shear and $T \geq 0.33$ for the uniaxial cross-section tensile test (Shipsha 2014). An overview is given in Figure 4-1 below. The uniaxial cross-section tensile test specimens are axisymmetric in nature, so $L = -1$ ($\sigma_I > 0$, $\sigma_{II} = \sigma_{III} = 0$). As concluded in Faleskog (2012a), the magnitude of the failure strain does not significantly diverge from the magnitude of the local strain in a tensile test specimen at the initiation of necking. Therefore, in the case of nodular cast iron, it is justified to neglect the influence of necking, and the evaluation of the failure strain (ε_f) in the material can be performed using $T = 0.33$ for the uniaxial cross-section tensile specimens.

The presented results also suggest that the nodular cast iron ductility depends only on the triaxiality T and is independent of the deviatoric stress state. Therefore, the simple model presented in Figure 4-1 is judged to be sufficient to predict the effective plastic strains at failure as a function of the triaxiality. In practice, the effect of triaxiality is of minor importance for most load cases experienced by the nodular cast iron inserts.

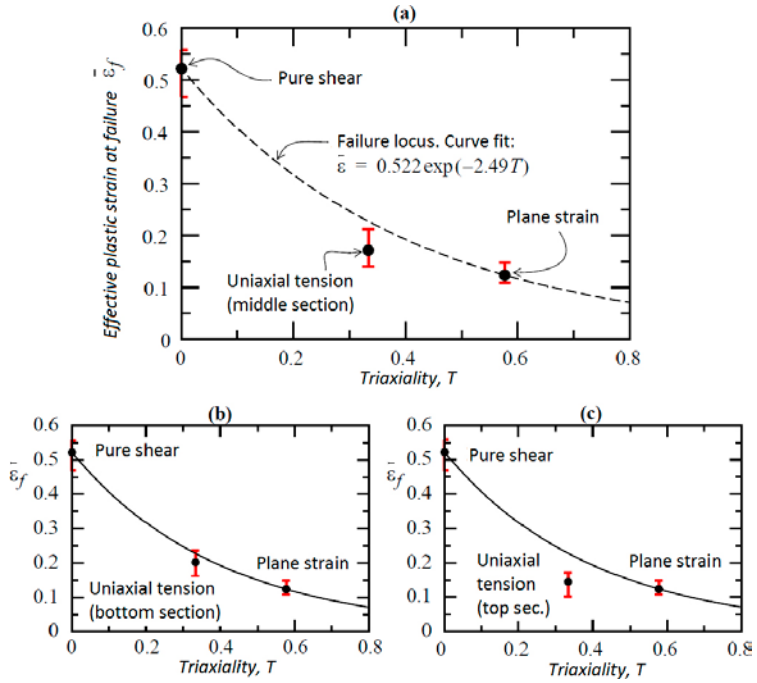

Figure 4-1. *The effective plastic strains at failure in the nodular cast iron as a function of the triaxiality (T) (Shipsha 2014). The plots have been derived from test specimens from the middle (a), bottom (b) and top sections (c) of BWR inserts I53 and I57.*

4.2.3 Copper

Mechanical testing has also been conducted in terms of strain and triaxiality stress for copper. In principle, two main types of testing exist for copper: elastic-plastic testing and creep testing. However, the approaches for evaluating uniaxial cross-section test specimens are identical. Copper is a ductile material, and test specimens that undergo large deformation in the range of hundreds of percent must be considered during testing.

During tensile testing, after the initiation of necking, the specimen no longer has a primarily uniaxial cross-section stress state at the necking section. The specimen radius at the neck decreases sharply, meaning that the radial and tangential stresses increase such that a more pronounced three-dimensional stress state arises.

In the case of copper, the triaxiality factor $T = 0.33$ was used for evaluating the failure strain. The justification was derived from the fact that the triaxiality increased after the initiation of necking, and the deformation in the neck was evaluated pessimistically. Therefore, the triaxiality (T) at failure for the test specimens was greater than 0.33 (see Figure 4-2).

Over the years, a comprehensive mechanical testing programme for creep ductility has been conducted. The main purpose has been to establish a well-substantiated knowledge basis to allow quantitative determination of the creep ductility in copper with respect to different stress states and the influence of notches from a post-closure perspective. The ductility is a *material* property, and this characteristic can be tested and estimated in different ways, such as by using different test specimen geometries. The most common specimen is the round uniaxial cross-section tensile test specimen. The ductility can be evaluated in terms of elongation at failure or in terms of area reduction in the neck after failure. The elongation at failure measurement is easy to use, but it reflects the properties of the test specimen and is not useful for more accurately determining the ductility in a ductile metal, such as copper. Because of the large displacement and necking that occur in tensile specimens, a more accurate way is to use the area reduction in the neck after failure. Other specimens that have been used include square cross-section tensile specimens, compact tension (CT) specimens, notched specimens and so-called shear specimens. These specimens are not trivial to evaluate in terms of ductility, so numerical methods must be used. In Danielsson (2016), the ductility and triaxiality were investigated.

Danielsson concluded that the ductile failure depends on the stress triaxiality and possibly also on the character of the deviatoric stress state. Therefore, it seems necessary to test *and* model, for example, notched specimens to accurately obtain the stress triaxiality.

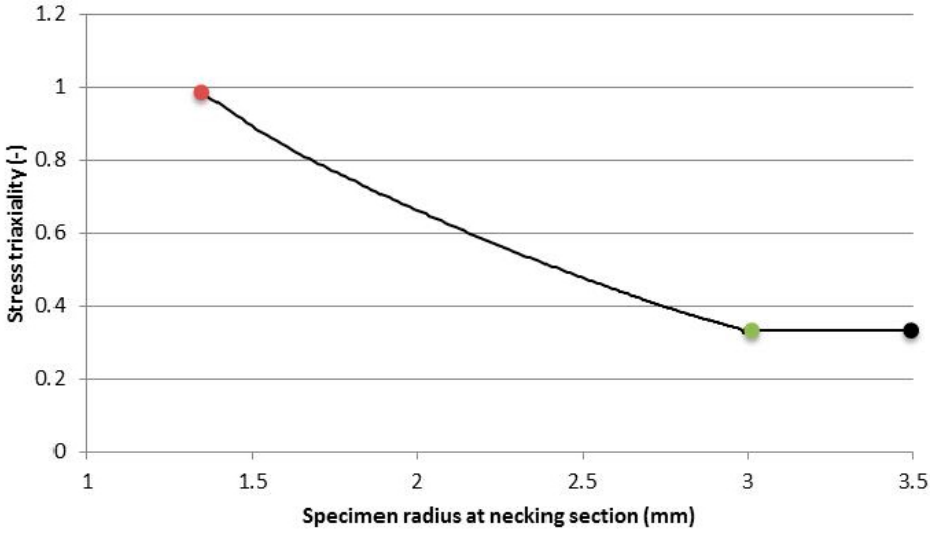

Figure 4-2. *Stress triaxiality as a function of the tensile test specimen radius at the necking section. The black marker denotes the initiation of the plastic state (the yield point), the green marker denotes the initiation of necking, and the red marker denotes material/specimen failure (Unosson 2017).*

4.3 Properties of nodular cast iron – BWR

The mechanical properties of the nodular cast iron in the BWR insert are given in Tables 4-1 to 4-3. Standard values for the yield stress and ultimate stress are used to indicate the minimum required material test values based on standard-type uniaxial cross-section tension tests according to SS-EN 10002-1:2001 or SS-EN ISO 6892:2009 using round samples and standard low strain-rate tension tests. Strength values referenced in the tables below are mainly based on either tension or compression tests depending on the load case type. The ultimate stress or the given stress/strain relationship is converted from the uniaxial test result into a true stress/ true strain relation. Jonsson (2017) provided most of the test result details on which the given engineering value is based. The results from tensile testing, compression testing and fracture toughness testing are included in Jonsson (2017). The engineering stresses and strains converted into corresponding true values can be used directly as inputs for the material model. A Young's modulus of E = 166 000 MPa and Poisson ratio of ν = 0.32 are used for the nodular cast iron in all analyses (Raiko et al. 2010).

4.3.1 Compressive properties

The most significant load case is the isostatic pressure under the glacial period, which is defined as load case 4 in Table 2-1. For this load case, the cast iron stress-strain curve is based on compression test results of I24 and I25 (Jonsson 2017) but is scaled to represent the minimum design requirements defined by the minimum yield stress of 240 MPa (true stress) to show the strength of the inserts (see Table 4-1 below and Alverlind 2016a). The reason is to confirm the suitability of the 240 MPa yield stress during compression as a minimum requirement of the nodular cast iron. The justification for using compression data in the isostatic load case is derived such that a compressive state occurs, and the strain is elastic in this load case with nominal geometry without defects.

Table 4-1. True stress-strain curve for the nodular cast iron used in Alverlind (2016a) for the isostatic load case of 50 MPa.

Strain [–]	Stress [MPa]	Comment
0.001446*	240	Stress values from Jonsson (2017) scaled with the decreased yield stress relation 240/270. Poisson ratio v = 0.32.
0.02	296	
0.041	350	
0.062	381	
0.105	428	
0.221	475	
0.649	489	
1.718	489	

* (Yield stress R_p = 240 MPa) / (Young's modulus E = 166 000 MPa).

4.3.2 Tensile properties

Based on the results from tensile tests using material from the top discs of BWR inserts I53–I57, a stress-strain table was created and is shown in Table 4-2 (Jonsson (2017)). This curve has been used for damage tolerance analyses of the rock shear case (Dillström 2017, Bolinder et al. 2017).

Table 4-2. True stress-strain curve in tension based on the top discs of I53–I57 (Jonsson 2017).

Strain (%)	Stress (MPa), strain rate=0
0	0
0.160	267
1.998	330
4.000	366
6.000	392
9.998	427
15.00	456
49.99	480

The tension data are represented by the stress-strain data from a series of stress-strain tests made at both +21 °C and 0 °C using standard and elevated strain rates. The used data are taken from Jonsson (2017). The rock shear analysis used a strain-rate dependent material model, so the material stress-strain curve was presented for the static case and the case with a strain rate of 0.5 s^{-1}. A strain rate factor was determined to consider the strain rate (see Table 4-3). These data are used in the analyses of uneven swelling defined as load cases 1 and 2 in Table 2-1 and in the rock shear analyses of load case 5 in Table 2-1 (see the reports Hernelind (2010, 2014b, d, f, 2015b), Börgesson and Hernelind (2013) and Unosson (2016)).

Table 4-3. True stress–true strain definitions for the nodular cast iron in global analyses of uneven swelling and rock shear load cases.

Plastic strain (%)	Stress (MPa) Strain rate = 0	Stress (MPa) Strain rate = 0.5	Strain rate factor at strain rate = 0.5 (–)
0	293	348	1.19
1	324	367	1.13
2	349	385	1.10
3	370	406	1.10
4	389	423	1.09
5	404	438	1.09
6	418	451	1.08
7	428	464	1.08
8	438	474	1.08
9	447	483	1.08
10	456	490	1.07
11	465	498	1.07
12	472	504	1.07
13	478	510	1.07
14	484	516	1.07
15	488	520	1.07

4.3.3 Fracture toughness properties

The measured fracture toughness mean value tested at 0 °C in liquid for BWR inserts I54, I55 and I57 was found to be in the range of $88.1 \leq J_{2mm} \leq 93.5$ kN/m when expressed as a J- parameter value. See Dillström and Bolinder (2010) for further information about the evaluation of the fracture toughness data measured for cast iron. The value used for the damage tolerance analyses, $J_{2mm} = 88$ kN/m, for the rock shear case is taken from the measured data with 90 % confidence, which is more pessimistic than the average value. This approach is justified in Dillström et al. (2008) because the data was acquired while testing the actual material; the statement was also substantiated by the total large amount of fracture tests using specimens of nodular cast iron from BWR I53–I57, I68, I72 and I76, as described in Jonsson (2017).

The influence of temperature on the fracture toughness behaviour was investigated in Müller et al. (2002) (see Figure 4-3). The upper shelf region of the fracture toughness extended to −40 °C, and therefore, it is justified to use fracture toughness data from testing at 0 °C or room temperature and to consider the fracture toughness as independent of the temperature in the range 0–125 °C that occurs in the insert in the final repository (Posiva SKB 2017). Extensive fracture toughness testing has been performed; the data on the BWR inserts are presented in more detail in Jonsson (2017), and diagrams of the fracture toughness testing results are shown in Figure 4-4 to Figure 4-6.

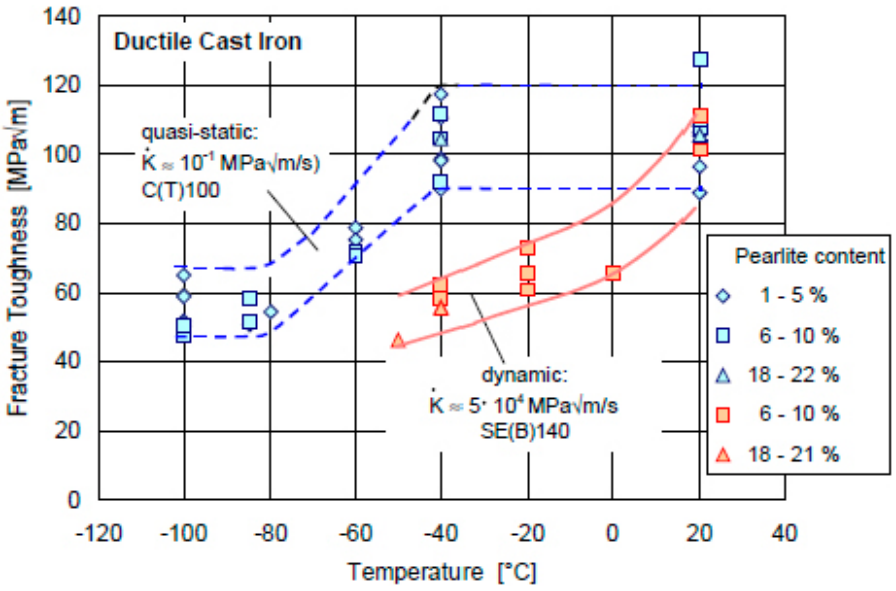

Figure 4-3. *Fracture toughness behaviour of ductile cast iron as a function of the test temperature and loading rate (Müller et al. 2002).*

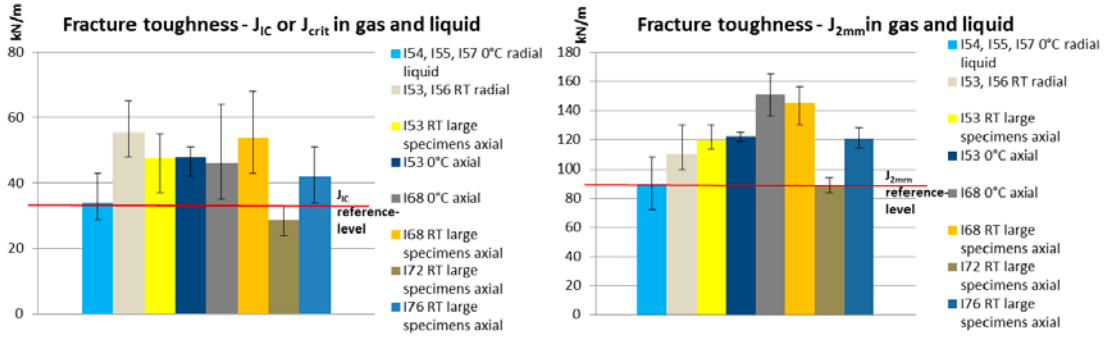

Figure 4-4. *Schematic of the BWR cast iron fracture toughness. At initiation, J_{IC} or J_{crit} (left) and J_{2mm} (right) are shown for the specimens (Jonsson 2017). The testing was performed in air or nitrogen if nothing else is stated. The bars represent the average values from different fracture toughness tests; the minimum-maximum range of the specimens in the populations is also shown. The reference levels of J_{IC} = 33 kN/m and J_{2mm} = 88 kN/m are shown.*

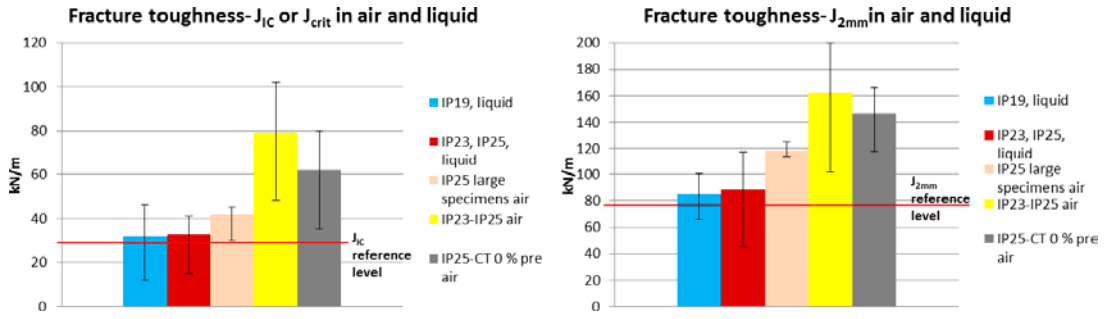

Figure 4-5. *Schematic of the PWR cast iron fracture toughness. At initiation, J_{IC} or J_{crit} (left) and J_{2mm} (right) are shown for the test specimens (Jonsson 2017). The testing was performed in air or nitrogen if nothing else is stated. The bars represent the average values from the different fracture toughness tests. The minimum–maximum range of the specimens in the populations is also shown. The reference levels of J_{IC} = 27 kN/m and J_{2mm} = 78 kN/m are shown. The "IP25-CT 0 % pre air" population comprises specimens without any predeformation, and the same population with that designation is shown in Figure 4-6 below.*

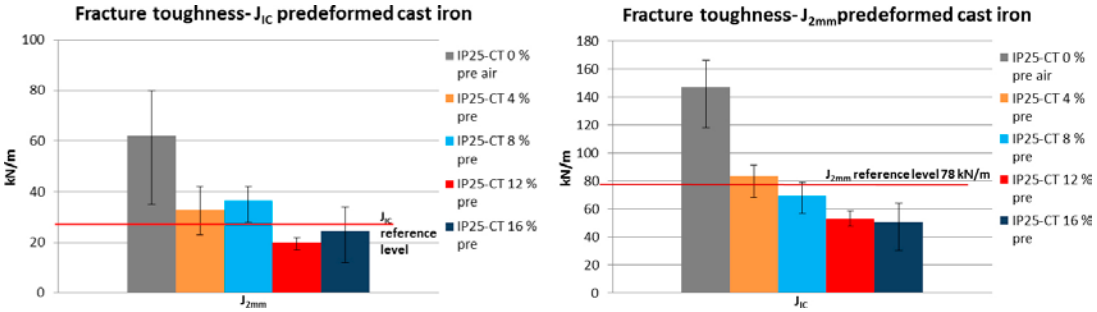

Figure 4-6. *Schematic of the fracture toughness values J_{IC} and J_{2mm} for predeformed PWR IP25 from Jonsson (2017). The bars represent the average values from different fracture toughness tests; the minimum–maximum range of the specimens in the populations is also shown. The reference levels of J_{IC} = 27 kN/m and J_{2mm} = 78 kN/m are also shown.*

It should be noted that the external environment significantly affects the fracture toughness tests. The fracture toughness is higher when the testing is performed in air or nitrogen than in a mixture of water and ethanol. The justification to use fracture toughness data performed in a gas atmosphere is derived from the gas atmosphere inside the canister. However, as seen from Figure 4-4, it does not matter whether the specimens are localised in axial or radial directions in the full-scale insert. During the probabilistic use of the measured material data, some data may be below the reference limit, but this is an approach that has been judged as necessary for a cast iron component of this size, in which local inhomogeneities may have a large influence on a single data point. To use the single lowest value as the reference limit value would be unnecessarily pessimistic because it is unrepresentative of the properties of the entire insert. The lowest value approach is normally used only when a very limited amount of data are available. In this case, there is a comprehensive amount of data from mechanical tests.

In this case, a multitude of data points/values are available from fracture toughness tests, so it is possible to use a statistical approach instead of using the lowest value. This has been accomplished by using a confidence interval, as recommended in the well-known R6 method (R6 uses a 95 % confidence level). The same approach with a confidence interval was used in SSM report 2009:26 (Dillström 2009b), in which a 90 % confidence level is recommended for deterministic analyses. By implementing safety factors during the analysis, as described in Section 3.2.2, local variations in the fracture toughness in the insert are considered to be negligible.

For information and comparison, it was calculated that the lower J_{2mm} would be 87.6 kN/m for a 95 % confidence level compared with 88.1 kN/m for a 90 % confidence. In the case of an external pressure load, when the load controls the stresses and causes primary stresses, the damage tolerance analysis is conducted using K_{IC} data that are based on crack initiation, not limited crack growth as with J_{2mm}. The safety factor used for K_{IC} is $10^{0.5} = 3.16$, which is the ASME Code requirement for normal operational loads. The fracture toughness K_{IC} value measured for the BWR cast iron at 0 °C is 78.0 MPam$^{0.5}$ with a 90 % confidence level, when declared as a stress intensity factor K_{IC} value (see Alverlind 2016a). The parameter K_{IC} = 78 MPam$^{0.5}$ is equivalent to J_{IC} = 33 kN/m.

4.4 Properties of nodular cast iron – PWR

The mechanical properties for the nodular cast iron of the PWR insert are given in Jonsson (2017), but for the analyses of PWR inserts, the BWR data in Tables 4-1 to 4-3 have also been used for PWR inserts. In all analyses, the Young's modulus was E = 166 000 MPa and Poisson ratio was ν = 0.32 for the nodular cast iron.

For the isostatic load case of 50 MPa, the scaled stress-strain relation for the nodular cast iron in Table 4-1 is used in Alverlind (2016a) for the PWR. The justification is derived in Shipsha (2013) as only elastic deformation occurs in the isostatic load case with the nominal geometry without defects, so the difference is considered to be negligible. The difference in the yield stress during compression at 0.2 % strain is ~0.5 %.

4.4.1 Tensile properties

The rock shear analyses used a strain-rate dependent material model, so the material stress-strain curves are presented for the static case and case with a strain rate of 0.5 s^{-1} (see Table 4-2). These data are used in the analyses of load cases 1, 2, 3 and 5 in Table 2-1 and for the PWR inserts. Thus, for these load cases, the same data that were used for the BWR inserts have been applied to the PWR cast iron. The justification for using the BWR tensile data for the analyses of PWR inserts has been evaluated in Shipsha (2013). Regarding the stress-strain curve in tension, this was used when performing a damage tolerance analysis, and in the case of an earthquake-induced rock shear load, there is only a small difference between the BWR and PWR. This difference is judged to not be significant for the mechanical analyses. The true yield stress, true ultimate stress and elongation at failure are compared in Jonsson (2017):

- Yield stress, mean value (BWR I53–I57) = 280 MPa.
- Yield stress, mean value (PWR IP23–IP25) = 270 MPa.
- Ultimate stress, mean value (BWR I53–I57) = 449 MPa.
- Ultimate stress, mean value PWR IP23–IP25) = 462 MPa.
- Elongation at failure, mean value (BWR I53–I57) = 14.8 %.
- Elongation at failure, mean value (PWR IP23–IP25) = 14.8 %.

4.4.2 Fracture toughness properties

The fracture toughness data measured for the PWR cast iron IP19 are $78.0 \leq J_{2mm} \leq 94.0$ kN/m when expressed as a *J*-parameter value. The number used for the damage tolerance analyses, J_{2mm} = 78 kN/m, for the rock shear case is taken from the measured data with a 90 % confidence level for IP19 at 0 °C in liquid. See Dillström and Bolinder (2010) for further information regarding the evaluation of the fracture toughness data of the cast iron. For the PWR, extensive fracture toughness testing has also been performed; the data regarding the PWR inserts are presented in more detail in Jonsson (2017) and in Shipsha (2013), and a schematic of the fracture toughness results is shown in Figure 4-5. In the case of an external pressure load, when the load controls the stresses and causes primary stresses, the damage tolerance analysis is performed using K_{IC} data based on crack initiation, not limited crack growth as with J_{2mm}. The K_{IC} value measured for the PWR cast iron at 0 °C in liquid is 70.6 $MPam^{0.5}$ with a 90 % confidence level (Alverlind 2016a). The parameter K_{IC} = 70.6 $MPam^{0.5}$ is equivalent to J_{IC} = 27 kN/m.

4.4.3 Fracture toughness in predeformed compressed cast iron

Plasticity in the nodular cast iron caused by compressive isostatic loads is not expected to occur. However, the effects of compressive plasticity on nodular cast iron have been studied to investigate how the fracture toughness of the material is influenced. A rock shear case may occur after an isostatic load case. The use of "as-manufactured" fracture toughness requires justification. The compressive predeformation was conducted at different strain levels in Jonsson (2017): "as manufactured" = 0 %, 4 %, 8 %, 12 % and 16 %. The results in Figure 4-6 show that the fracture toughness of the nodular cast iron is affected by the degree of compressive predeformation and the crack growth is stable in terms of compressive predeformation. Stable 2 mm crack growth could still occur.

4.5 Summary – ductility of nodular cast iron

The ductility of nodular cast iron is complex by nature. To further understand and justify the mechanical properties of the nodular cast iron material, a number of investigations have been performed. The most representative test series for the BWR inserts regard data from inserts I53, I54, I55, I56, I57 and I63 (see Jonsson 2017). The factors affecting the elongation at failure have been investigated in Dillström and Alverlind (2014) and in Dahlberg et al. (2014). The elongation at failure of BWR inserts was also investigated in Holst and Sarnet (2017) from a statistical point of view. It was concluded that there are systematic variations in the mechanical properties in the manufactured inserts between inserts and/or sample positions as is shown in Figure 4-7. However the variations were reasonably low which justifies using constitutive modelling-based mechanical testing for test specimens during trial manufacturing.

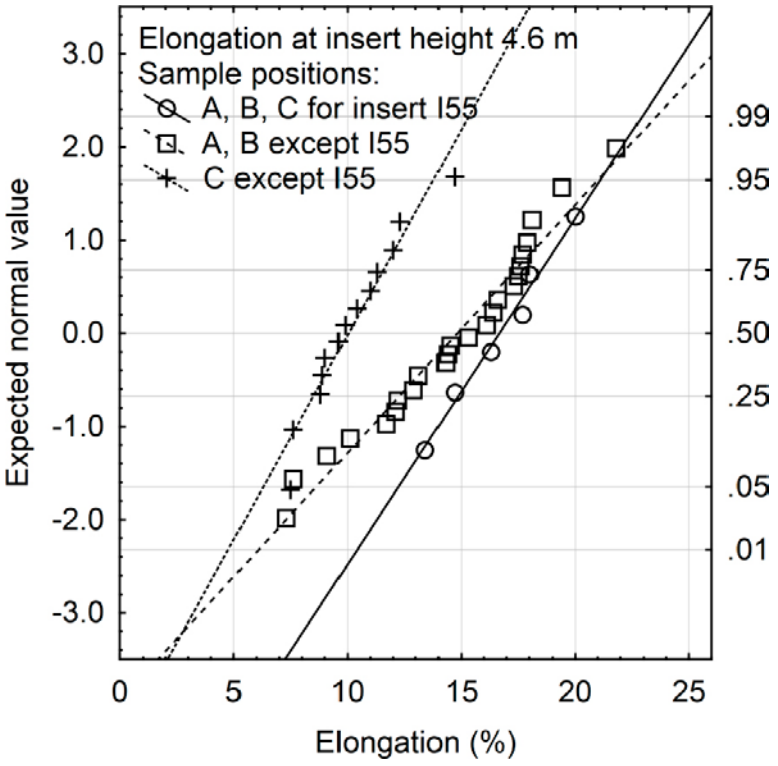

Figure 4-7. *Elongation at failure data and chosen distributions for I53, I54, I55, I56, I57, I63, I72, and I76. The groups are respectively of sizes 6, 28, 14, averages 16.68 %, 14.82 %, 10.43 %, and standard deviations 2.39 %, 3.55 %, 2.26 % (Holst and Sarnet 2017).*

In Dahlberg et al. (2014), the primary cause of the strong influence of the mean stress on the plastic response was due to the presence of graphite nodules in the cast iron material. Further, in Dahlberg et al. (2014), the average volume fraction of the graphite nodules was 12.5 %. These investigations also revealed that the concentrations of the graphite nodules exhibited substantial variations in space and size. The influence of these variations on the plastic response was minimal. However, the relatively large scatter in the strain to failure data was somewhat associated with these variations. The fracture at uniaxial stress states was characterised as a "ductile necking failure mode", in which microvoids in the material grew, leaving zero distance between the ligaments in the voids. This phenomenon was compared with the necking in a uniaxial tensile test specimen; the difference was due to the micro and macroscales. Fractures at shear stress states and low triaxiality $T \approx 0$ were also characteristics of a "shear-off failure mode", which included microvoids in the material, but the voids could collapse and thus created crack-like defects that rotated and linked together when the ligaments were sheared off.

In Dillström and Alverlind (2014), the influences of the defects in the graphite/dross and porosity were investigated. The tensile specimens from BWR inserts I53–I57 and PWR inserts IP23–IP25 were used for metallographic examinations, and it was clear that the porosity surface area was weakly correlated to the elongation at failure. The area of the graphite/dross defects was more strongly correlated with the elongation at failure. This indicates that graphite/dross defects are more significant for the ductility than the porosity.

In total, the fracture mechanism of the nodular cast iron is ductile. The presences of brittle fracturing was investigated in a few test tensile and shear specimens in Fourlakidis (2013). The fracture was ductile in the range of 99–100 %, given that the brittle area fraction was also less than 1 %. Therefore, it can be concluded that the plastic failure is ductile, and it is justified that brittle failure can be excluded as a failure mechanism, as in Section 3.2.2.

4.6 Properties of steel

The material models for the channel tubes, insert lid, support plates, bottom plates and screws in the insert are based on the von Mises material definition with elastic behaviour defined by Young's modulus and Poisson ratio. The plastic behaviour is defined as true stress versus true plastic strain. Furthermore, a Young's modulus of E = 210 GPa and Poisson ratio of v = 0.3 according to Raiko et al. (2010) (Table 4-3) are used.

The steel channel tubes in the inserts were manufactured using cold- or hot-formed steel S355J2H, such as Domex 355 MC B (see Raiko et al. 2010). SKB has previously, in Platdepan (2003) and Persson (2005), supplied test data for the yield point of this material; however, there is no stress-strain data available for the plastic analysis. The stress-strain curve for Domex 355 MC B can be scaled using the yield stress (R_e) and tensile ultimate stress (R_m) measured by SKB: R_e = 412 MPa (yield stress) and R_m = 511 MPa (ultimate stress). With this procedure, a simplified stress-strain curve is obtained and described in Table 4-4. It was assumed during the analyses that the casting process did not affect the stress-strain properties of the steel components.

Table 4-4. Stress-strain definitions for the steel channel tubes used during the analyses of the BWR and PWR inserts.

Strain (%)	Stress (MPa)	Log strain (%)	True stress (MPa)	Plastic effective strain (%)
0	0	0	0	0
0.196	412	0.196	412	0
15	509	14.3	587	14.0
20	511	18.5	613	18.2

However, the mechanical properties of the steel channel tubes after casting the BWR and PWR inserts have been investigated in Kallio (2016, 2017) and further in Dillström and Manngård (2017) as well as in Hernelind and Börgesson (2018). The steel in the channel tubes was found to be affected by the casting process. Two of these steel tensile test specimens from BWR insert I76 were investigated in Brorsson (2017). The steel exhibited transcrystalline facets that indicated brittle cleavage fracture. The rest of the fracture areas on the tensile test specimens had a ductile or mixed ductile/brittle appearance. Nevertheless, the elongation at failure for all tensile test specimens of the pure steel material in Kallio (2016, 2017) reached reach over 10 % or more.

The material in the insert lid is specified as steel S355J2G3. The strain versus stress curve for steel Domex 355 MC B with R_e = 389 MPa (yield stress) and R_m = 484 MPa (ultimate stress) can be found in Raiko et al. (2010). According to SS-EN 10025-2:2004, the material S355 with a nominal thickness of 40–63 mm has a R_e = 335 MPa (yield stress) and R_m = 470–630 MPa (ultimate stress). The scaling stress-strain curves for Domex 355 using the minimum values given in SS-EN 10025-2:2004 provide the simplified material definitions (engineering data) shown in Table 4-5.

Table 4-5. Stress-strain definitions for the insert lid, support plates, base plates and screws: SS-EN 10025-2:2004, material S355, nominal thickness 40–63 mm.

Strain (%)	Stress (MPa)	Log strain (%)	True stress (MPa)	Plastic effective strain (%)
0	0	0	0	0
0.1595	335	0.1593	335	0
15	470	13.98	540	13.7
20	470	18.2	564	17.9

4.7 Properties of copper

4.7.1 Background of the test data

To model the deformation in the copper canisters, accurate data for inelastic deformation is required. In the present section, slow strain rate tensile data will be summarised for oxygen-free copper alloyed with 30–100 ppm phosphorus (Cu-OFP). The representation of the creep data is described in Section 4.7.4. The standardised phosphorus alloyed copper grades that are most similar to those specified by SKB and Posiva are US alloys C10100 from the ASM (1990). These are called oxygen-free extra-low phosphorus copper and oxygen-free low phosphorus copper.

According to the SKB and Posiva specifications, the phosphorus content should be in the interval from 30 to 100 ppm to ensure sufficient ductility. The manufacturing process of the copper components has been investigated in Leskinen and Ronneteg (2013) further in Jonsson and Ronneteg (2014). One of the conclusions from these studies is that the mechanical properties of the copper lids and tubes are affected by the amount of cold work and heat treatment during manufacturing. In particular, the yield stress $R_{p0,2}$ is affected and also the ductility, to some extent; the yield stress $R_{p0,2}$ was found to be in the range of 33–132 MPa at normal strain rates during tensile tests using copper lid TX214 with different heat treatments (Jonsson and Ronneteg 2014). The ductility was also affected. For example, the elongations at failure for the specimens with a nominal length of 70 mm and a nominal diameter of 14 mm were in the range of 33–65 %, and the area reductions at failure were in the range of 66–90 %. For comparison, tensile tests of specimens with a nominal length of 70 mm and a nominal diameter of 14 mm from extruded tubes T53 and T58 were conducted (Brosius 2008, 2009), resulting in elongations at failure in the range of 51–57 % and area reductions at failure in the range of 81–90 %. The results of the hot-forming processes of the copper components exhibited slight variations in the mechanical properties, which is normal for any manufacturing process, slightly affecting the stress-strain curves for the copper. The manufacturing process of the tensile test specimens themselves may have affected the cold work in the specimen and, consequently, the test results. The influence of different machine parameters has been studied in Olsson (2015). The mechanical properties are also affected by the testing temperature; an increased temperature will cause a decreased $R_{p0,2}$. This phenomenon must be considered certain load cases because inelastic deformation in the copper shell can occur during manufacturing and handling of the canister.
In Table 4-6, examples of elastic-plastic testing are shown, and in Table 4-7, examples of creep test results are shown.

As stated in Chapter 2, the copper shell will be subjected to mechanical loads, and inelastic deformation in the copper shell may occur. This means that large deformations must be considered during the evaluation of the mechanical tests and simulations of copper.

Over the years, a number of constitutive models for the inelastic deformation of the copper shell have been developed and used during verification analyses of the KBS-3 canister. The constitutive models have considered mechanical testing of copper specimens to various extents. This report will divide the constitutive models into two main groups: elastic-plastic models and models considering creep.

Table 4-6. Elastic-plastic testing of extruded tubes and a forged lid with or without heat treatment after forging. Data are from Brosius (2008, 2009), Jonsson and Ronneteg (2014) and Olsson (2015). The specimen-id is the same as in the references.

Specimen-id	Nominal diameter (mm)	$Rp_{0.2}$ (MPa)	Elongation at failure (%)	Reduction of area (%)	Comment
T58-1	14	56	56	86	Extruded tube
T58-121	14	54	54	86	Extruded tube
T58-161	14	57	51	86	Extruded tube
T58-308	14	58	56	90	Extruded tube
T58-326	14	54	57	89	Extruded tube
T53-a	14	52	53	87	Extruded tube
T53-b	14	50	55	86	Extruded tube
T53-c	14	52	54	84	Extruded tube
T53-d	14	53	50	81	Extruded tube
T53-e	14	51	51	86	Extruded tube
T53-f	14	52	56	88	Extruded tube
T53-g	14	52	56	86	Extruded tube
T53-h	14	55	54	88	Extruded tube
T53-i	14	52	56	87	Extruded tube
T53-j	14	53	57	89	Extruded tube
TX214-A1	14	128	46	86	Lid ”as forged”
TX214-A2	14	132	46	86	Lid ”as forged”
TX214-A1	14	112	35	66	Lid ”as forged”
TX214-A2	14	113	33	66	Lid ”as forged”
TX214-R1	14	67	64	89	Lid ”as forged”
TX214-R2	14	110	57	89	Lid ”as forged”
20	14	41	56	92	Lid, heat treated after forging
21	14	46	60	92	Lid, heat treated after forging
22	14	52	59	91	Lid, heat treated after forging
13	14	62	49	93	Lid, heat treated after forging
14	14	80	60	91	Lid, heat treated after forging

Table 4-7. Creep test results from the 2007 creep test study on the lid, tube and friction stir welds in Andersson-Östling and Sandström (2009).

Test ID	Copper batch	Structure	Temperature (°C)	Nominal stress (MPa)	Nominal diameter (mm)	Gauge length (mm)	Rupt. time (h)	Plastic strain on loading (%)	Elongation at failure (%)	Reduction in area (%)
LID75_1	TX104	PM lid	75	175	10	80	1 162	9.3	43.6	90.2
LID75_2				170			13 925	10.3	43.4	91.0
LID75_3				180			175	11.2	45.6	92.2
LID75_5				170			9 585	8.3	51.1	90.9
TUB75_2	T18	PM tube	75	170	10	80	7 877	10.1	52.7	91.6
TUB75_1				175			6 974	14.3	47.1	90.6
TUB75_4				180			120	14.4	48.1	92.1
WINR75_1	L21	CW inner	75	175	10	60	32	10.7	47.4	89.1
WINR75_2				170			398	10.8	47.5	86.2
WINR75_3				160			6 271	9.9	46.2	84.7
WMI75_1	L21	WM inner	75	175	10	50	1 868	13.8	63.8	89.6
WMI75_2				170			2 207	10.7	64.9	87.4
WMY75_2	L21	WM outer	75	170	10	50	4 378	14.2	65.3	82.9
WMY75_3				180			28	15.2	65.1	90.1
WYTT75_1	L21	CW outer	75	175	10	60	62	13.5	54.3	92.8
WYTT75_2				170			835	15.7	53.7	88.0
HAZ75_1	L21	HAZ weld	75	175	10	50	25	10.7	67.2	91.1
HAZ75_2				170			360	16.4	66.2	90.8

Parent metal = PM, weld metal = WM, heat affected zone = HAZ, crosswelds = CW.

4.7.2 Model for considering elastic-plastic deformation at 125 °C

This elastic-plastic model is used during analyses of operational handling loads. The maximum temperature of the copper shell is specified as 100 °C in Posiva SKB (2017), and the properties of the copper material at 125 °C are used. The stress-strain curve was derived from test specimen L171N in Nilsson (2014), which was the most pessimistic specimen in the report in terms of yield stress. The data from test specimen L171N are equivalent to the data for soft annealed copper at 125 °C, which is considered to be a pessimistic assumption compared with the copper material used in the canister in terms of both temperature and cold work. A theoretical model was created using a combination of the elastic line and results from test specimen L171N. The elastic region is defined fully by Young's modulus. The multilinear plastic part of the material model of the copper starts at the intersection of the stress-strain curve and the line representing the Young's modulus of E = 120 GPa. Figure 4-8 shows the plastic part of the material model, implemented in the FE software programme ANSYS (2007), presented and used in Alverlind (2016c). Also specified are the Poisson ratio v = 0.308 and yield stress $R_{p0,2}$ = 9.9 MPa.

4.7.3 Models for considering elastic-plastic deformation at room temperature

Over the years, research and development have been undertaken regarding constitutive models of elastic-plastic deformation in copper. These elastic-plastic models have been used during analyses of the inelastic deformation of the copper shell in the final repository and for simulations of the mechanical test specimens. The models have been created from elastic-plastic mechanical testing at strain rates from 1×10^{-8} s^{-1} to 1 s^{-1}. After necking, the material in the neck in a tensile test specimen was computed to be subjected to strain rates in the range of 1–100 s^{-1} (Unosson 2014). However, the testing was performed at quasi-static conditions, and the calculated strain rate in the neck of the specimen was an artefact caused by the tensile test specimen geometry. It was concluded that the strain rate is not significant for elastic-plastic modelling of copper at room temperature because the mechanical testing data and mathematical model in Unosson (2014) correlate well.

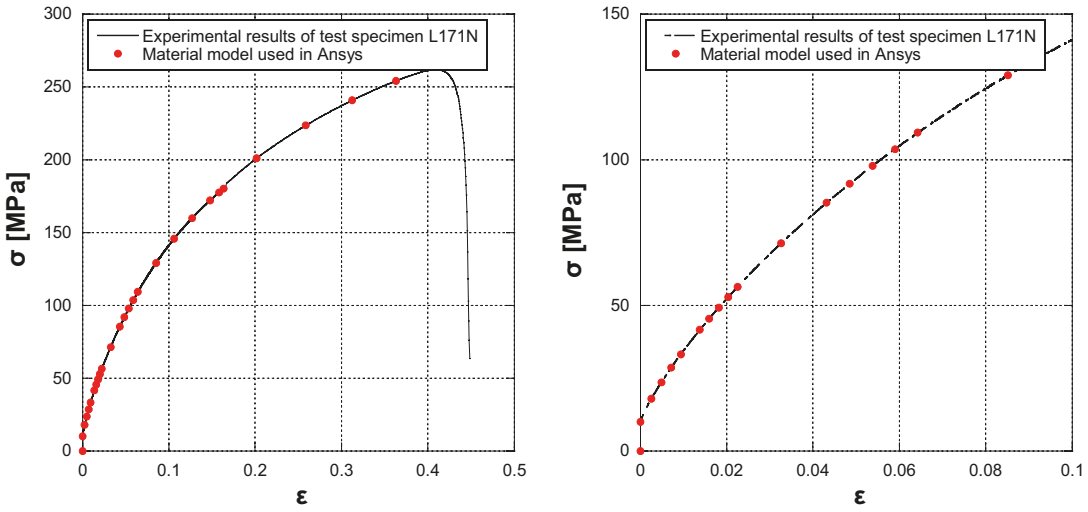

Figure 4-8. *True stress-strain curves for the copper material at 125 °C used in the analyses of the operational handling loads in Alverlind (2016c). Left: strain ε in the range of 0–0.5. Right: strain ε in the range of 0–0.1.*

Copper material model used for the rock shear case and uneven swelling

The material model for the rock shear analysis and uneven swelling is based on a simplified elastic-plastic material model (see Table 4-8) using data from the creep model, assuming a strain rate of 5×10^{-3} s^{-1}. This model has been used in Hernelind (2010, 2014b, d, f, 2015b), Börgesson and Hernelind (2013) and in Hernelind and Börgesson (2018).

The stress-strain properties of the copper in the copper shell were investigated at Swerea KIMAB, and the results are represented from a creep material model developed by Rolf Sandström (see Sandström and Andersson 2008, Jin and Sandström 2008 and Sandström et al. 2009). The flow curve data were calculated from Sandström et al. (2009), wherein Equation (17) was used along with the parameter values defined in Table 4-2 in the same report: m = 3.06, α = 0.19, and ω = 14.66. The copper model data are shown in Figure 4-9. The yield stress $R_{p0,2}$ = 72 MPa. The data are available and valid up to 50 % plastic strain; the failure strain is not included in this model. This simplified elastic-plastic material model can be used for *deformation-controlled load* scenarios for the copper shell, which includes the uneven swelling and rock shear cases.

Table 4-8. True elastic-plastic material data for copper at a strain rate of 0.005 s^{-1}.

Elastic part		Plastic part: von Mises stress s_e (MPa) at the following plastic strains (ε_p)					
E (GPa)	v	0	0.10	0.20	0.30	0.40	0.50
120	0.308	72	178	235	269	288	300

Copper material model used for the isostatic load case 50 MPa

The material model for the copper in Table 4-9 was developed by Dillström et al. (2010) and is used in Alverlind (2016a) for the investigation of isostatic load case 4 in Table 2-1. The model incorporates a multilinear isotropic hardening model that assumes a von Mises yield criterion and associated flow rule. The values of the yield stress, $R_{p0,2}$ = 58 MPa, and engineering tensile strength, R_m = 214 MPa, used were the minimum yield stress and tensile strength, respectively. The values were derived from readings of the stress-strain curves from mechanical tests from the trial manufacturing of extruded copper tubes T25–T27 and T39–T42. A Young's modulus of 114 GPa and Poisson ratio of 0.35 were used. The failure strain is not included in this model.

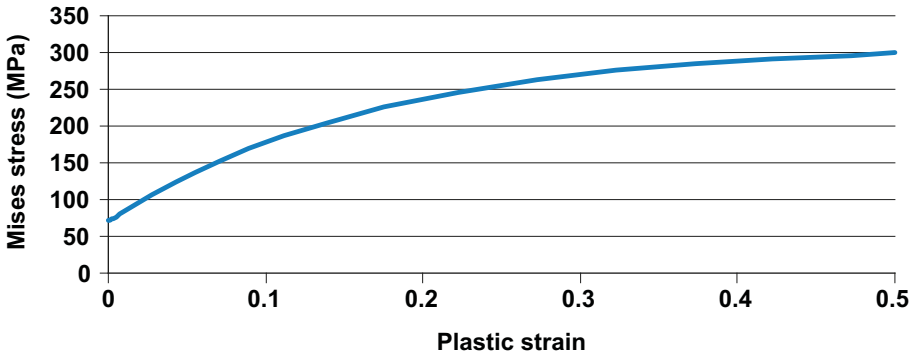

Figure 4-9. *Copper shell stress-strain curve from Table 4-6 showing the von Mises stress as a function of the logarithmic plastic effective strain, from Hernelind (2010).*

Table 4-9. Engineering stress-strain curve in tension for the copper used in Alverlind (2016a) and Hernelind (2015c).

Strain (–)	Stress (MPa)
0	0
0.0005088	58
0.1	150
0.2	200
0.595	214
1	214

Copper texture-dependent material model

A plasticity model for texture-dependent deformation hardening and initiation of ductile failure in copper was developed by Unosson (2014). The model considers changes in the texture and is able to capture the differences in deformation hardening between uniaxial loading and shear loading. The model has been validated against data from tension tests as well as shear/torsion tests, and the parameter values for the copper material were derived in Unosson (2014). In addition, E = 114 GPa and v = 0.35. The von Mises stress versus plastic strain, that is, the deformation hardening function, for uniaxial tension is shown in Figure 4-10. For loading paths that deviated from uniaxial tension, the deformation hardening function in Figure 4-10 was modified using an expression that accounts for texture evolution.

The texture-dependent plasticity model has been used to simulate indentations in the copper shell and creep test specimens in Unosson (2015) and for global analyses of the rock shear case in Hernelind (2015d). Furthermore, the plastic strain and triaxiality in different creep test specimens have been investigated in Danielsson (2016) and in Unosson (2017). In Figure 4-11, a graphic representation of the pressure-dependent, or stress triaxiality-dependent, failure strain function is given for Cu-OFP, along with data from the literature on oxygen-free high conductivity copper (Cu-OFHC) (Johnson et al. 1985) for comparison. Using the average value of the area contraction at failure from the tensile tests in Brosius (2008), the true plastic strain at tensile failure (ε_f) was computed as ε_f = 210 % for T = 0.33.

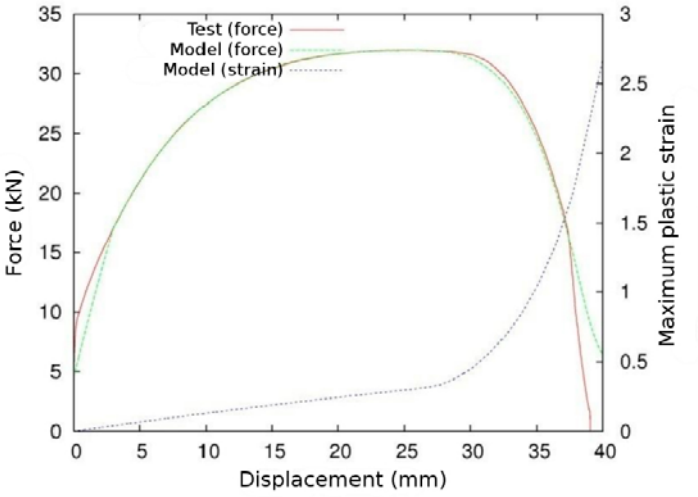

Figure 4-10. *Comparison of results from tensile tests and the texture-dependent material model. The test data is represented by a mean value curve corresponding to five tensile tests (Unosson 2014).*

Copper material model used for elastic-plastic modelling considering welded copper

Using constitutive equations developed from slow strain-rate tensile testing data on weld zones, elastic-plasticity analyses from contact modelling of a friction-stir-welded canister copper shell under isostatic and uneven swelling load cases were conducted at 75 °C. The conditions in Figure 4-12 were 75 °C and 1×10^{-8} s^{-1}, corresponding to a service time of approximately 1 year (see Jin and Sandström 2013). The thermomechanically affected zone (TMAZ) and the heat-affected zone (HAZ) exhibited harder behaviour for the welds than the parent Cu-OFP metal. The weld zones also had higher yield stresses than the parent metal. Although the weld zones initially exhibited lower hardening rates, their flow curves were above those of the parent metal for all strains. Both the TMAZ and HAZ possessed E = 109 GPa and ν = 0.308 at 75 °C, which were the same values as the parent Cu-OFP metal. The differences between the parent metal, HAZ, the centre part of the weld zone and TMAZ were comparatively small.

4.7.4 Creep deformation

Creep simulations in copper have been performed for the copper shell of the KBS-3 canister with spent nuclear fuel in the final repository. Two models for inelastic deformation including creep have been developed. SKB has run creep testing and the development of a copper creep model at Swerea KIMAB and KTH. Posiva has run creep testing and modelling in copper at VTT in Finland. Both models have been used for verification analyses of load case 4 defined in Section 2.2.7 and a closer description will follow below.

All creep mechanisms are related to atomic diffusion and dislocation movement driven by stress, which leads to creep deformation. The strain data acquired from the most common creep tests, constant load (or stress) tests, are classically divided into three characteristics as shown in Figure 4-13.

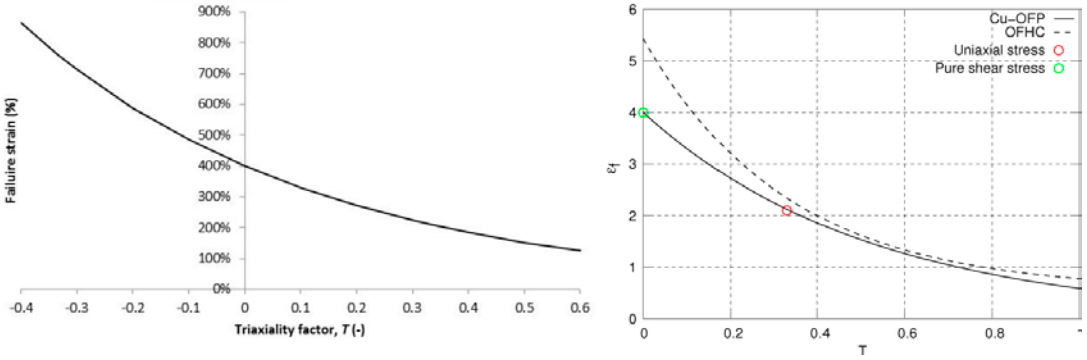

Figure 4-11. *Schematics of the triaxiality-dependent true failure strain (ε_f) function for Cu-OFP. Data for Cu-OFHC at room temperature and the strain rate (1/ s) are shown for comparison (Unosson 2014).*

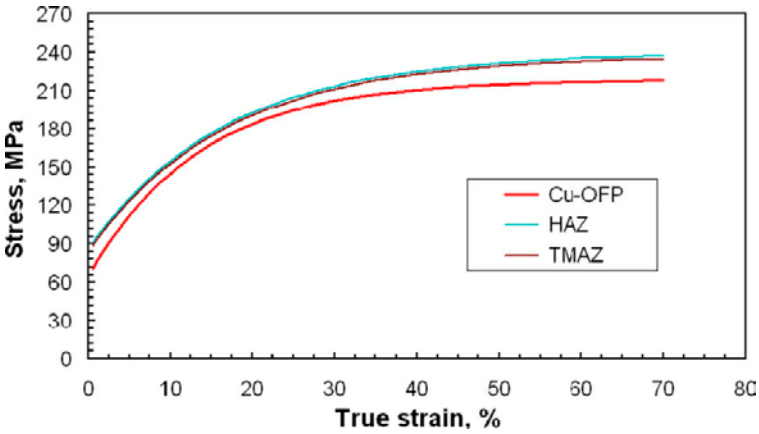

Figure 4-12. *Model of the true stress-strain hardening curves for the parent metal and weld zones at 75 °C at a strain rate of 10^{-8} s^{-1} (Jin and Sandström 2013).*

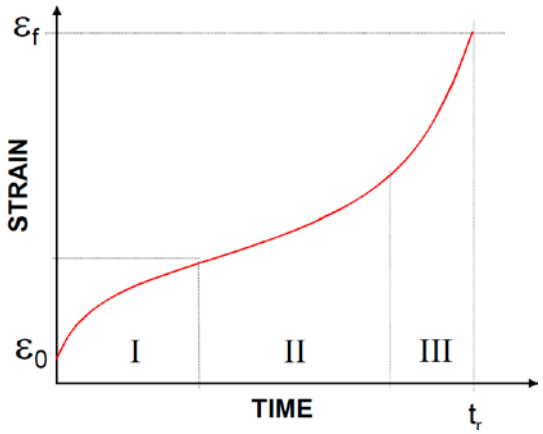

Figure 4-13. *Classical creep curve with a primary (I) creep stage starting at loading with instantaneous strain (ε_0), secondary (II) stage with the minimum creep rate and tertiary (III) stage ending in rupture (at time t_r with a fracture strain ε_f) (Holmström 2010).*

In the first stage, primary or transient creep, the curve has a concave shape starting with an initial strain addition (ε_0) immediately after loading. This stage can be considered to be the hardening stage. In the next stage, secondary creep, the strain evolves roughly linearly as a function of time. In this stage, there is a balance between hardening and thermal softening (where dislocations dissolve). In the third stage, tertiary creep, the curve takes a convex form that ends with rupture (damage accumulation and necking). This stage is associated with dominance of thermal softening as well as significant creep damage development.

The duration and extent of strain accumulated during the different stages naturally depends on the temperature and stress. Stationary creep is defined as deformation, during which the stress distribution in a component remains constant with time and occurs in the secondary stage (*II*). In contrast, non-stationary creep prevails in the primary stage (*I*), when the creep rate is decreasing, and again in the tertiary stage (*III*), when the creep rate is increasing.

Swerea KIMAB and KTH creep model

Theory

This model was developed for oxygen-free P-doped (50 ppm phosphorous) copper. The theory includes rate-dependent inelastic behaviour. For computations of the creep deformation in the canister, models for the stationary and non-stationary creep rate have been used in Sandström and Andersson (2007, 2008). The justification for using this model was the assertion that the model was derived to cover both high-temperature (climb) and low-temperature (glide) conditions. At low temperatures (typically 75 °C), the deformation mechanism judged to be responsible for inelastic deformation is dislocation glide. If the deformation mechanism is glide due to high stresses, a constitutive model should be able to represent the mechanical behaviour of the material, irrespective of whether it is subjected to a prescribed stress, such as during a creep test, or to a prescribed strain rate, such as during a normal tensile test. The Young's modulus is set to 120 GPa, as shown in Figure 4-8, and the Poisson ratio is 0.308 in the Swerea-KIMAB and KTH creep models. Plasticity and creep are defined for the copper, and the FE-code ABAQUS (ABAQUS 2014) calculates the creep strain before entering the plasticity routines; when including creep in the simulation, a user-defined subroutine (CREEP) is used. The subroutine is based on a theory for P-doped copper presented by Andersson-Östling and Sandström (2007). The implementation of the theory, which is similar to that in Raiko et al. (2010), originally followed an internal document received from Sandström with a few changes regarding constants (see Table 4-10). In finite-strain applications, strain variables should be interpreted as logarithmic "true" strains and stresses as "true" stresses. The model was used in the analyses performed by Hernelind (2010, 2014c, 2015a, 2017a).

Table 4-10. Difference constants from the references.

Constant	In Section 4.7.4 below	In Raiko et al. (2010)
m	3	3.06
C	285 (temperature-dependent)	257 (σ_{imax})
ω	Equation (4-11) below	0.45 (ω_c)

In this section, T is the temperature in Kelvin.

The uniaxial case – stationary model

The expression for the stationary creep rate is given by Andersson-Östling and Sandström (2009)

$$\varepsilon_{\mathrm{OFP_{stat}}} = \frac{2bc_L}{m}\frac{D_{s0}b\tau_L}{k_BT}\left(\frac{\sigma}{\alpha mGb}\right)^3 e^{\frac{\sigma b^3}{k_BT}} e^{-\frac{Q}{RT}\left[1-\left(\frac{\sigma}{\sigma_{i\max}}\right)^2\right]} / f_P \qquad (4\text{-}5)$$

The constants in Equation (4-5) can be found in Table 4-11.

Table 4-11. Numerical values of the constants in Equation (4-5).

Parameter description	Parameter	Value
Coefficient for self-diffusion	D_{s0}	1.31×10^{-5} m^2/s
Activation energy for self-diffusion	Q	198 000 J/mol
Burgers vector	b	2.56×10^{-10} m
Strain hardening constant	c_L	57
Taylor factor	m	3
Ideal gas constant	R	8.314 J mol^{-1} K^{-1}
Boltzmann's constant	k_B	1.381×10^{-23} J/K
Constant	α	0.19
Shear modulus	G	$G = 4.75 \times 10^4 - 17 \times T$ MPa, T in K
Max back stress	σ_{imax}	257 MPa
Dislocation line tension	τ_L	7.94×10^{-16} MN
Influence of phosphorus	f_P	3 000 for T < 125 °C (< 75 °C in Sandström and Andersson (2008)

The values of the constants are the same as in Andersson-Östling and Sandström (2009).

The function in Equation (4-5) is the basis of the analysis. A simplified expression for it is introduced as follows:

$$h(\sigma) = \frac{2bc_L}{m}\frac{D_{s0}b\tau_L}{k_BT}\left(\frac{\sigma}{\alpha mGb}\right)^3 e^{\frac{\sigma b^3}{k_BT}} e^{-\frac{Q}{RT}\left[1-\left(\frac{\sigma}{\sigma_{i\max}}\right)^2\right]} / f_P \qquad (4\text{-}6)$$

The stress σ in Equation (4-5) should be taken as

$$\sigma = \sigma_{\mathrm{true}} e^{-\varepsilon} \qquad (4\text{-}7)$$

where σ_{true} is the true stress and ε is the effective creep strain. Thus, the expression to be used in the stationary case is

$$\varepsilon_{\mathrm{OFP_{stat}}} = h(\sigma_{\mathrm{true}} e^{-\varepsilon}) \qquad (4\text{-}8)$$

Non-stationary model

For a non-stationary situation, a back stress is introduced. The back stress increases during the primary creep stage, giving rise to a continuously decreasing creep rate. The creep rate decreases exponentially with the increasing strain until $\sigma_i = C$. In the non-stationary case, an effective stress is introduced:

$$\sigma_{eff} = (\sigma - \sigma_i)e^{-\varepsilon} \quad (4\text{-}9)$$

where σ_i is the back stress, which can be integrated from the following equation:

$$\frac{d\sigma_i}{d\varepsilon} = \omega(C - \sigma_i) \quad (4\text{-}10)$$

where C is the (true) tensile strength and ω is given by

$$\omega = \frac{B\varepsilon^{n_b}}{(T - 273)^{p_b}} \quad (4\text{-}11)$$

The resulting expression for the strain rate is

$$\varepsilon_{\mathrm{OFP_{init}}} = h((\sigma - \sigma_i)e^{-\varepsilon})g_{\mathrm{rate}} \quad (4\text{-}12)$$

Equation (4-12) is the same as Equation (4-5), except that the stress is replaced by the effective stress σ_{eff}, and a factor g_{rate} has been introduced. The expression for g_{rate} in Equation (4-12) takes the following form:

$$g_{\mathrm{rate}} = \left(\frac{t_{\mathrm{min}}}{t_{\mathrm{init}}}\right)^{\phi_2/(1+\phi_2)} \quad (4\text{-}13)$$

where Φ_2 is a temperature-dependent constant, $t$init is the time at the beginning of primary creep, and $t$min is the time when the secondary stage is reached. The constants in Equations (4-9) to (4-12) are summarised in Table 4-12.

Table 4-12. Values of the constants in Equations (4-9) to (4-12).

Parameter description	Parameter	Value
True tensile strength	C	285 MPa at room temperature
Time at the start of primary creep	t_{init}	1 h (converted to seconds in the subroutine)
Time at minimum creep rate	t_{min}	$t_R/3$ where t_R is the rupture time
Parameter in g_{rate}	Φ_2	13.26–0.022T, T in K
Constant	B	4.02 (B1 in the subroutine)
Constant	n_b	0.0481 (exp_nb in the subroutine)
Constant	p_b	0.277

Equation (4-11), which was originally assumed to describe both primary and secondary creep, actually only describes the primary stage. To address this situation, the non-stationary model is considered to be the sum of the stationary model (4-5) and Equation (4-9).

$$\varepsilon_{\mathrm{OFPnon-stat}} = h(\sigma_{true}e^{-\varepsilon}) + h((\sigma - \sigma_i)e^{-\varepsilon})g_{\mathrm{rate}} \quad (4\text{-}14)$$

Figure 4-14 shows the simulated creep curves under uniaxial conditions. The considered case includes a nominal stress of 170 MPa and a temperature of 348 K. The simulated creep curve, as presented in Andersson-Östling and Sandström (2009) and Raiko et al. (2010), is shown in black. The prediction using the creep model implementation described above and provided by 5T Engineering (used in Hernelind 2010) is given by the red curve. As seen in Figure 4-14, the red curve does not agree with the black curve. As a comparison, C and ω were defined in accordance with Raiko et al. (2010) (see Table 4-10). Using these values, the green curve was obtained.

In Danielsson (2015), a creep model corresponding to the study by Raiko et al. (2010) was implemented in ABAQUS using the more general UMAT interface. The response is given by the blue curve in Figure 4-14, which is seen to coincide with the green curve. This suggests that in every respect, except that of C and ω, the implementation of the creep model in Hernelind (2010) follows that of Raiko et al. (2010), with corrections made to the typographic errors identified in Danielsson (2015). It is also interesting to note that despite the implementation of the creep model using two vastly different user interfaces (CREEP and UMAT), the same creep curves are predicted. The minimal differences were likely due to differences in the employed time-integration schemes. It is also worth noting that the CREEP and UMAT implementations were performed completely independently by different individuals.

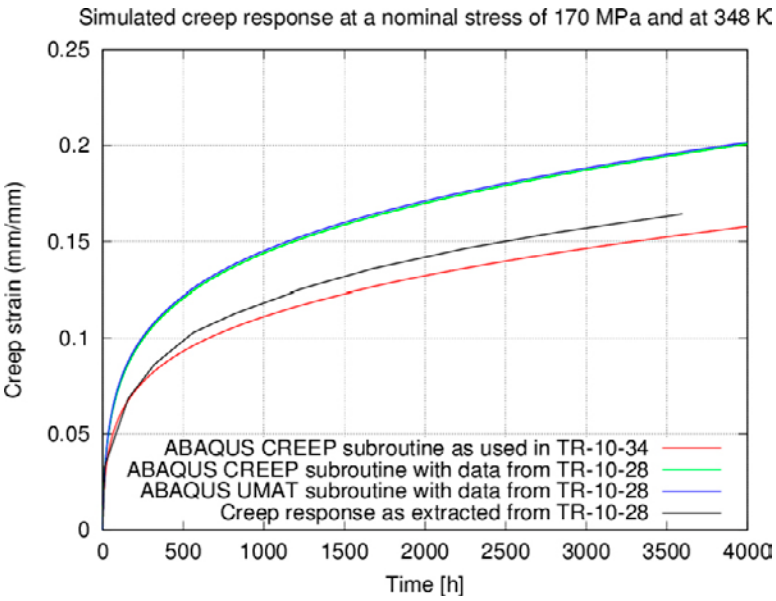

Figure 4-14. *Simulated creep response at a nominal stress of 170 MPa at 348 K (Danielsson 2015).*

The Swerea KIMAB and KTH creep models were made as an attempt to model creep using fundamental principles. However, it was recognised that there are limitations in the fundamental understanding of creep in Cu-OFP. To some extent, this problem can be addressed by applying alternative models. However, a more robust method for handling creep *during displacement-controlled cases* is to apply elastic-plastic modelling with high loads such that the final state is reached and the mechanical properties can then be evaluated. For example, see Section 6.2.4, cases 3 and 4.

VTT creep model

The VTT approach for modelling creep in the copper shell is based on the logistic creep strain prediction (LCSP) model (Holmström 2010) for the post-closure response and the Kohlrausch model in Andersson et al. (2017) for the short-term stress relaxation. The LCSP created at VTT predicts the time to strain as:

$$\log t_\varepsilon = \frac{\log(t_r) + C}{1 + (\log \varepsilon / x_0)^p} - C \qquad (4\text{-}15)$$

where t_ε is the time to strain, t_r is time to rupture and x_0, p and C are fitting parameters. By differentiating Equation (4-15), the strain rate ε is obtained as

$$\dot{\varepsilon} = -\varepsilon k_1 k_2 x_0 \qquad (4\text{-}16)$$

where k_1 and k_2 are functions of the variables t_ε, t_r, and parameters x_0, p and C. The LCSP creep model is calibrated based on the creep strain and time to rupture data produced with single- or multi-specimen constant-load testing machines. The LSCP creep model includes primary, secondary and tertiary creep. The data used for the assessment consist mainly of long-term creep rupture datasets from Swerea KIMAB and VTT. Examples of the parameters for this model calibrated for Cu-OFP, given in Holmström and Auerkari (2009), are given in Table 4-13, and an example of the model performance is shown in Figure 4-15:

Table 4-13. Shape factors of the creep strain model in Equation (4-15) for OFP copper (σ in MPa, T in °C).

Factor	Value
C	3.5
$x0(\sigma/\sigma_{TS}, T)$	$-2.179 + 4.397 \ln(\sigma/\sigma_{TS}) - 0.008T$
$P(\sigma/\sigma_{TS}, T)$	$7.235 + 0.460(\sigma/\sigma_{TS})/\ln(\sigma/\sigma_{TS}) - 0.012T$

However, the above-presented LCSP model was not calibrated with short time-span relaxation deformation data since such information has not previously been available. Therefore, the Kohlrausch model was adopted for its ability to acceptably describe the currently available experimental results. A comparison of the Kolhrausch model fit to the experimental results in Andersson et al. (2017) is presented in Figure 4-16, and the overall correlation is quite adequate with respect to its ability to describe the complex relaxation tests and phenomena.

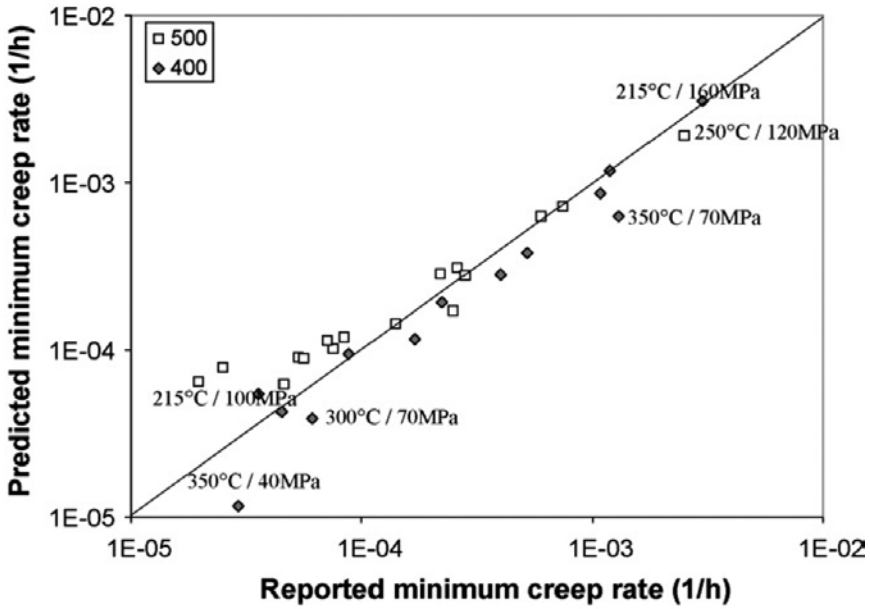

Figure 4-15. *Predicted versus observed minimum creep rates for Cu-OFP (Holmström and Auerkari 2009). The labels 500 and 400 are material batch names.*

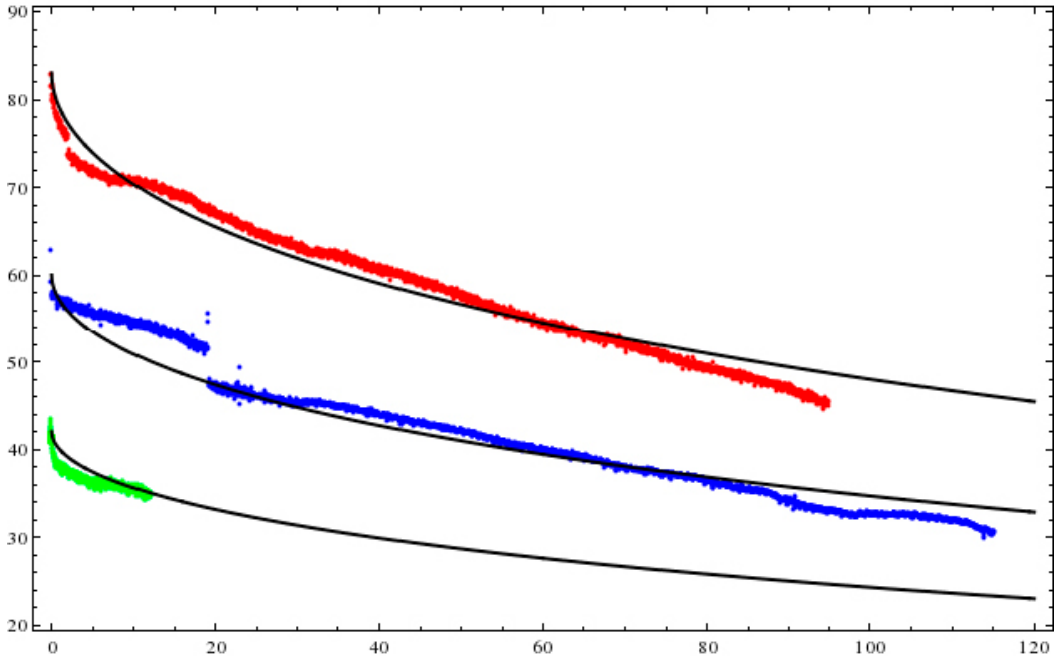

Figure 4-16. *Comparison between the engineering stresses [MPa] and relaxation time [h] according to Andersson et al. (2017). The colours distinguish different creep tests (the coloured curve is for the experimental data and the black line is the model prediction). There are 3 different relaxation tests and corresponding model prediction that begin from different stress levels (red = ~82 MPa, blue ~62 MPa, and green ~42 MPa).*

4.8 Summary – ductility of copper

The purpose of using several constitutive models to determine the inelastic deformation in copper can be ascribed to the complex nature of the phenomenon. It is not trivial to derive an accurate creep model, and one way to increase the credibility of the results is to compare the results achieved with different approaches. The entirety of the outcome is then used in a comprehensive discussion of the problem at hand, where the results of the different approaches serve to illustrate the impacts of the uncertainties in the fundamental understanding of the phenomena during the assessment of the mechanical integrity of the canister.

The mechanical tests of copper at different conditions have also been used to verify the ductility of the FSW material and copper with indentations (Mannesson and Andersson-Östling 2014) and copper that exhibited higher than normal sound attenuation during non-destructive ultrasound testing (Mannesson and Andersson-Östling 2013). The results from the creep tests show that there were sufficient margins with respect to the ductility of the copper and the stated design criteria. Cold work decreases the ductility of copper; cold work can however be accepted as long as the ductility design criterion in Section 6.2.4 is still fulfilled.

Additionally, as mentioned above, a more robust method for handling creep behaviour *for displacement-controlled cases* is to apply elastic-plastic modelling with high loads such that the final state is reached and the mechanical properties can then be evaluated. For example, Section 6.2.4, cases 3 and 4.

4.9 Properties of bentonite

The main safety functions of a KBS-3 repository are to isolate the repository from the surface environment, contain the radionuclides, retain and retard their dispersion into the environment and to protect and preserve the safety functions of the barrier system. According to Posiva SKB (2017), the buffer shall contribute to these main safety functions of a KBS-3 repository by achieving the following:

- ensure diffusive transport,
- limit microbial activity,
- filter colloids,
- mitigate the impact of rock shear on the canister,
- limit pressure on the canister,
- resist transformation,
- keep the canister in position, and
- retain sufficient mass over its life cycle.

The bentonite buffer fulfils two roles; it is a swelling load-generating media, and it is a supporting and flexible substance. All mechanical loads on the canister are transferred through the bentonite buffer, so the material properties of the bentonite define important conditions for the design analysis of the canister. Table 4-14 gives an overview of the dominating bentonite properties in different load cases.

Table 4-14. Overview of the dominating bentonite properties for different load cases.

Loads	Bentonite dominating property
1) Asymmetric loads due to uneven water saturation and imperfections in the deposition hole geometry. No simultaneous hydrostatic pressure. Uneven water saturation effects will decay later and be replaced by permanent loads 2) and 3) acting under saturated conditions.	Dry density, water absorption rate, degree of water saturation, swelling pressure.
2) Permanent asymmetric loads due to uneven bentonite density and imperfections in the deposition hole geometry.	Dry density, swelling pressure, pore water pressure.
3) Isostatic pressure, normal load.	Dry density, swelling pressure, pore water pressure.
4) Glacial pressure (additional isostatic pressure, only during glacial period).	Dry density, swelling pressure, pore water pressure.
5) Rock shear load due to rock displacement. Magnitude less than 5 cm with a shear velocity of 1 m/s.	Stiffness and shear strength.

The documentation of the constitutive model for the bentonite buffer is given in Börgesson et al. (2018). The most important properties of bentonite for the rock shear case are its stiffness and shear strength. These properties vary with the type of bentonite, density, and strain rate. Ca-bentonite generally has a higher shear strength than Na-bentonite despite the similar bentonite composition, and the shear strength increases with the increasing density and strain rates.

The technical design requirements set by Posiva SKB (2017) allow for bentonite forms other than MX-80, if the resulting mechanical properties meet the requirements. For practicality, the properties of Deponit CaN are used for modelling, which has a very similar composition and properties as MX-80Ca. Deponit CaN is used as a reference model because MX-80Ca has not been characterised by a large number of laboratory tests. For the SR-Site, the model reflects the worst-case scenario with the highest allowed density while considering possible ion exchange. Due to Ca-bentonite having higher shear strength than Na-bentonite, the model should correspond to MX-80Ca. This choice is slightly pessimistic and has been used for modelling (see Börgesson et al. 2018).

The material model can be expressed using the von Mises stress (σ_{Mises}), which describes stress in three dimensions according to Equation (4-3). The bentonite is modelled as being linearly elastic with the yield stress defined using von Mises effective stress and isotropic hardening. The plastic hardening relation is modelled as a function of the material strain rate because the shear strength of bentonite is sensitive to the strain rate. The shear strength increases by approximately 10 % for every tenfold increase in the strain rate. Because the rock shear during an earthquake is very fast (1 m/s), the influence is strong. The resulting shear strength differs at different parts of the buffer because the strain rate varies with distance from the shear plane.

The constitutive model in Börgesson et al. (2018) uses the maximum swelling pressure (10 MPa) rather than the pressure used previously in SKB (2009) for a maximum bentonite buffer density at water saturation of 2 050 kg/m^3. This difference will affect the shear strength or the maximum von Mises stress in the material model of the buffer that is used to model the effect of rock shear through a deposition hole.

It is important to note that the material model presented here is based on results from tests on MX-80 and Deponit CaN. An example of uniaxial compression tests using MX-80 is given in Figure 4-17. If another bentonite is going to be used, the material model must be adapted, and the calculations must be re-evaluated or repeated. If the material model is kept the same, the maximum allowed swelling pressure or the choice of the buffer density may be different.

Figure 4-18 from Börgesson et al. (2010) shows the measured deviator stress at failure as a function of the average effective stress (swelling pressure) for a number of triaxial tests using different bentonite samples. This figure shows that the strength of Deponit CaN is higher than the strength of MX-80Ca, which in turn has a higher strength than MX-80.

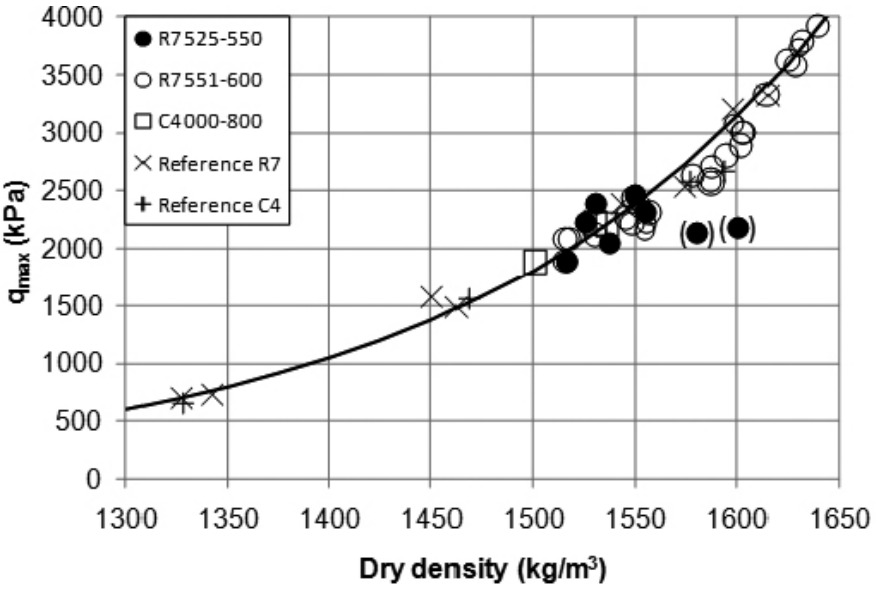

Figure 4-17. *The results from uniaxial compression tests using an MX-80 reference material (solid line) and a material sampled after termination of the Canister Retrieval Test (Börgesson et al. 2018).*

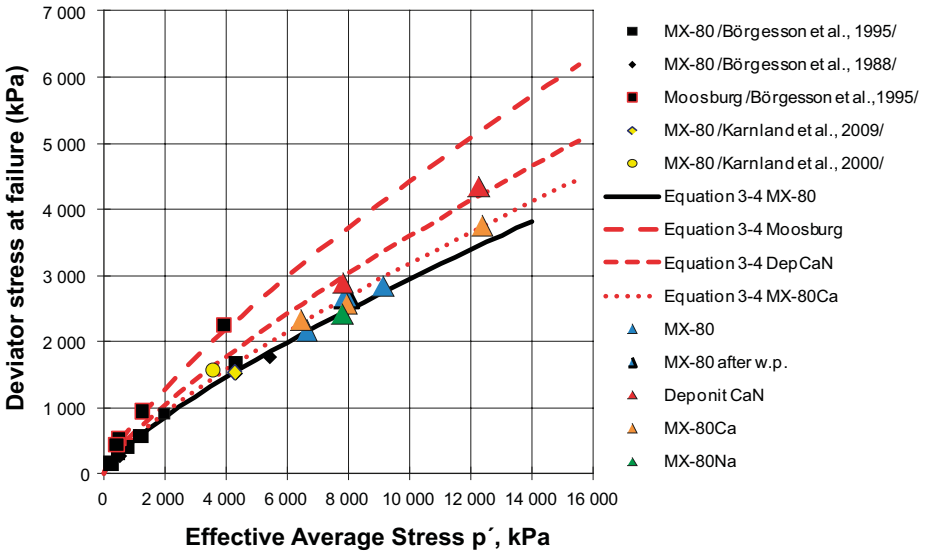

Figure 4-18. *The results from triaxial tests with the deviator stress at failure plotted as a function of the average effective stress. The red triangles refer to Deponit CaN, the orange triangles refer to MX-80Ca, the blue triangles refer to MX-80, and the green triangle represents the test using MX-80Na. The lines represent the evaluation of Equation (3-4) in Börgesson et al. (2010), which corresponds to Equation (4-17) in the present report. See also Table 4-15.*

4.9.1 Theory for von Mises stress for different swelling pressures

Equation (4-17) describes a model of the relation between the deviator stress at failure and effective average stress. This model corresponds to Equation (3-4) in Figure 4-18.

$$q_f = q_{f0}\left(\frac{p}{p_0}\right)^b \tag{4-17}$$

where

q_f = deviator stress at failure at swelling pressure p,

q_{f0} = deviator stress at failure at swelling pressure $p_{0,}$

p_0 = 1 000 kPa, and

b = parameter.

The values of parameters q_{f0} and b are evaluated and shown in Table 4-15 for different bentonite samples. The parameters are based on a shear strain rate of $v_s = 10^{-6}$ s^{-1}.

Table 4-15. Parameters in Equation (4-16) evaluated from the triaxial test results shown in Figure 4-18.

Material (symbol)	b	p_0 (kPa)	q_{f0} (kPa)	Reference
MX-80	0.77	1 000	500	Börgesson et al. (1995)
MX-80Ca	0.77	1 000	540	Börgesson et al. (2010)
Deponit CaN	0.77	1 000	610	Börgesson et al. (2010)
Moosburg Ca	0.77	1 000	750	Börgesson et al. (1995)

Thus, Equation (4-17) can be used to evaluate the maximum deviator stress for a swelling pressure of 10 MPa for Deponit CaN at a strain rate of $v_s = 10^{-6}$ s^{-1}.

$$q_f = 610\left(\frac{10\,000}{1\,000}\right)^{0.77} = 3\,592 \text{ kPa} \tag{4-18}$$

4.9.2 Theory for the rate-dependent deviatoric stresses

Shear strength is rate dependent, and the value in Equation (4-17) corresponds to a shear rate of $v_s = 10^{-6}$ s^{-1}. The rate dependence of the shear strength is described by Equation (2-3) (Equation (3-5) in Börgesson et al. 2010). The model is based on tests with strain rates varying between 10^{-7} and 100 s^{-1} using MX-80 and Deponit Can. The strain rates included in the material model (Table 4-16) vary between 10^{-6} and 1 000 s^{-1}. The strain rate in the rock shear calculation depends on the element size but varies roughly between 0 and 100 s^{-1}.

$$q_{fs} = q_{fs0}\left(\frac{v_s}{v_{s0}}\right)^n \tag{4-19}$$

where

q_{fs} = deviator stress at failure at strain rate v_s (kPa),

q_{fs0} = deviator stress at failure at reference strain rate v_{s0} (kPa),

v_s = strain rate (s^{-1}),

v_{s0} = reference strain rate = 10^{-6} s^{-1}, and

n = rate dependence factor = 0.038.

Because q_{fs0} = 3592 kPa at v_{s0}=10^{-6} s^{-1}, the maximum deviator stress can be calculated for all strain rates.

The stress-strain relation used in the material model has the following behaviour, (Figure 4-19) as described by Börgesson et al. (2010), with a density of 2 050 kg/m^3 at water saturation:

- Linear elasticity between a strain interval of $0 < \varepsilon < 1$ % with an elasticity that yields 58 % of the maximum von Mises stress at a strain of $\varepsilon = 1$ % (blue line in Figure 4-19).
- Plastic hardening at a strain interval of 1 % $< \varepsilon <$ 5.3 % with the maximum von Mises stress determined according to Equations (4-16) and (4-17).
- Almost ideally plastic at $\varepsilon > 5.3$ % (red line in Figure 4-19).

This model is based on the results from many tests and is made of an approximate average of measurements. Thus, the values used are nominal engineering magnitudes.

4.9.3 Theory for converting densities into swelling pressure values

The elastic-plastic stress-strain relations of different densities are derived according to the description in Section 2.2 using a method that is identical to that for the relations used in previous calculations in Börgesson et al. (2010).

The theory for converting densities into swelling pressure values is provided in Equation (4-20) (Equation (3-1) in Börgesson et al. 2010) and Equation (4-21). The void ratio (e) can be derived from Equation (4-20) and Equation (4-21), and ρ_m can be derived from Equation (4-22).

$$p = p_0 \left(\frac{e}{e_0} \right)^{\frac{1}{\beta}} \tag{4-20}$$

$$e = e_0 \left(\frac{p}{p_0} \right)^{\beta} \tag{4-21}$$

where

p = swelling pressure at void ratio e,

p_0 = 1 000 kPa,

e_0 = reference void ratio (= 1.33),

β = −0.254, and

$$\rho_m = (\rho_s + e\rho_w)/(e + 1) \tag{4-22}$$

where

ρ_m = density at saturation,

e = void ratio,

ρ_s = density of solids (= 2 780 kg/m^3), and

ρ_w = density of water = 1 000 kg/m^3).

The parameters derived for Equations (4-20) and (4-21) are valid for Ca-bentonite (MX-80 Ca and Deponit CaN). A swelling pressure of 10 MPa, as evaluated by Equations (4-21) and (4-22), corresponds to the void ratio and density at saturation.

e = 0.741

ρ_m = 2 022 kg/m^3

A swelling pressure of 10 MPa corresponds to the density at a water saturation of approximately ρ_m = 2 022 kg/m^3 for MX-80Ca.

A deviator stress of q_{fs0} = 3 592 kPa at v_{s0} = 10^{-6} s^{-1} and a density at water saturation of ρ_m = 2 022 kg/m^3 correlate well with the model used for different water saturation densities of 1 950 kg/m^3, 2 000 kg/m^3, and 2 050 kg/m^3 at the SR-Site. Figure 4-20 shows a curve of the maximum von Mises stress at a reference strain rate of 10^{-6} s^{-1} as a function of the density at saturation.

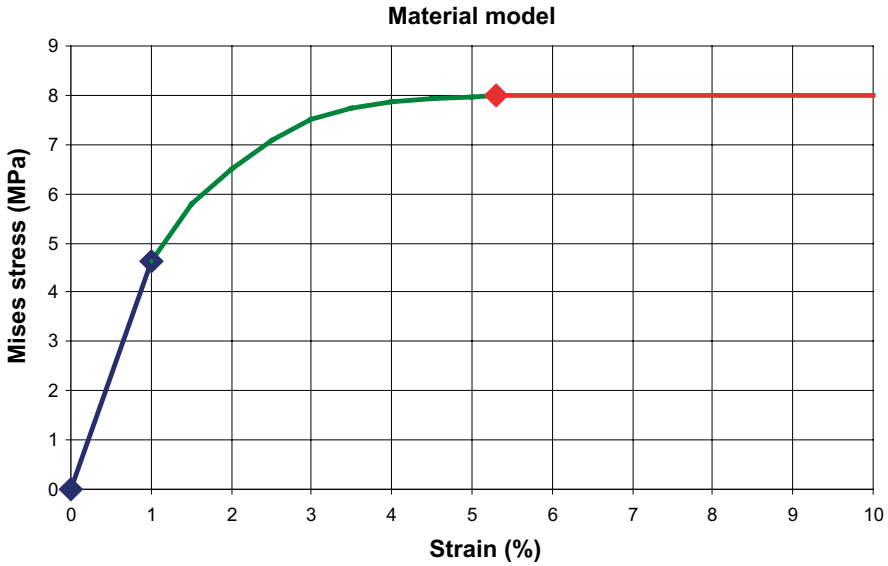

Figure 4-19. *The stress-strain relation used for the buffer material model for the von Mises stress [MPa] versus the engineering strain (nominal strain). The example refers to a density at saturation of 2 050 kg/m^3 at a strain rate of 10 s^{-1}(Börgesson et al. 2018).*

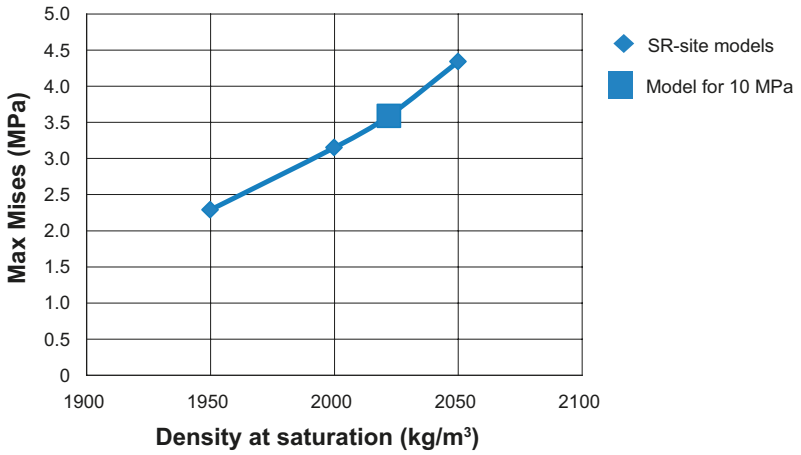

Figure 4-20. *Comparison of the maximum von Mises stress of MX-80 Ca used in the material models for the SR-Site and the model used for a swelling pressure of 10 MPa at a density at saturation of 2 022 kg/m^3 and strain rate of 10^{-6} s^{-1} (Börgesson et al. 2018).*

4.9.4 Rate-dependent elastic-plastic stress-strain relations

The model derived for the maximum swelling pressure (10 MPa) is described in Table 4-16, and the stress-strain relations at different strain rates, which are described in Table 4-16, are shown in Figure 4-21. Because elasticity cannot be strain dependent, the value of E = 381 MPa at a shear rate of 10 s^{-1} is proposed. This is an acceptable approximation because the purely elastic part only occurs for 1 % strain, and the maximum Mises stress is reached after 5.3 % strain. The influence of this approximation is insignificant because the maximum Mises stress and the corresponding strain are not affected.

Table 4-16. A reference bentonite model (MX-80Ca) at a density at water saturation of ρ_m = 2 022 kg/m³. E = 381 MPa should be used.

Material	ρ_m kg/m³	Rate of strain v_s	Elastic part		Plastic part: von Mises true stress σ_{Mises} (MPa) for the following plastic nominal strains ε_p							
			E MPa	v	ε_p = 0	ε_p = 0.004	ε_p = 0.01	ε_p = 0.018	ε_p = 0.026	ε_p = 0.036	ε_p = 0.46	ε_p = 1.0
MX-80Ca	2022	10^{-6}	207	0.49	2.07	2.77	3.19	3.40	3.53	3.59	3.55	3.55
MX-80Ca	2022	10^{-4}	247	0.49	2.47	3.30	3.80	4.05	4.21	4.28	4.23	4.23
MX-80Ca	2022	10^{-3}	269	0.49	2.69	3.61	4.14	4.42	4.60	4.67	4.62	4.62
MX-80Ca	2022	10^{-2}	293	0.49	2.93	3.93	4.52	4.82	5.01	5.09	5.03	5.03
MX-80Ca	2022	10^{-1}	320	0.49	3.20	4.29	4.93	5.27	5.47	5.56	5.50	5.50
MX-80Ca	2022	1.0	350	0.49	3.50	4.69	5.39	5.75	5.97	6.07	6.00	6.00
MX-80Ca	2022	10	381	0.49	3.81	5.11	5.87	6.27	6.51	6.62	6.54	6.54
MX-80Ca	2022	100	417	0.49	4.17	5.58	6.41	6.85	7.11	7.23	7.15	7.15
MX-80Ca	2022	1000	455	0.49	4.55	6.09	7.00	7.47	7.76	7.89	7.80	7.80

The technical design requirement "…*a buffer with an unconfined compressive strength at failure of 4 MPa at a deformation rate of 0.8 %/min.*" is based on the material model at a density at saturation of ρ_m = 2 022 kg/m³. The shear strain rate of 0.8 %/min for the tested bentonite specimens corresponds to a shear strain rate of 1.33×10^{-4} s^{-1}, which agrees well with the material model that uses q_f = 4.28 MPa for a shear strain rate of 1.0×10^{-4} s^{-1}. The shear strain rate of 0.8 %/min is chosen because it is the standard strain rate for uniaxial compression tests.

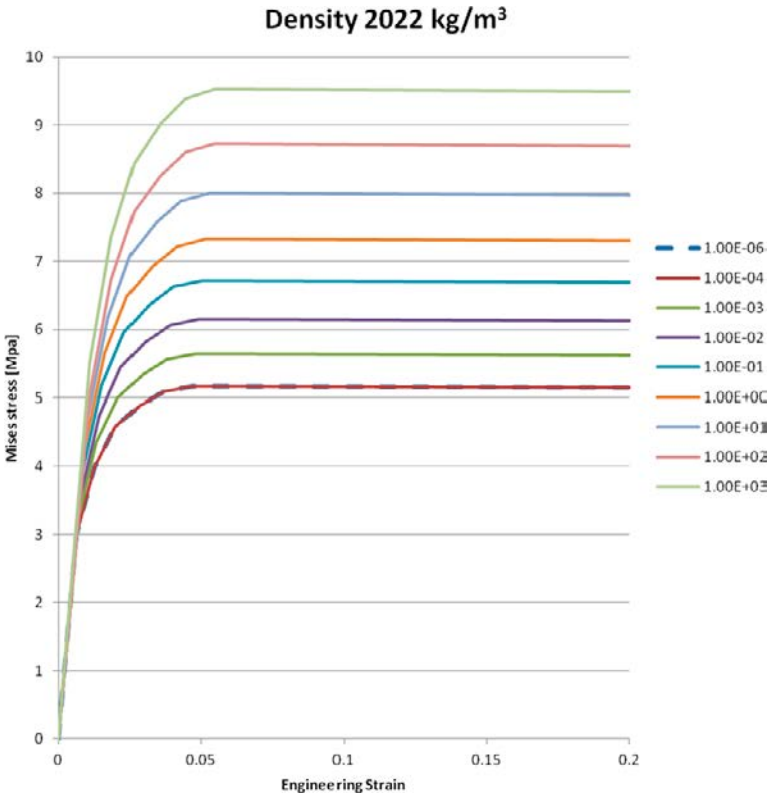

Figure 4-21. *Plot of the material definition of the bentonite buffer at a density of 2 022 kg/m³ and different strain rates [1/s]. The von Mises stress [MPa] versus engineering strain (nominal strain) (Börgesson et al. 2018).*

5 Canister shape and dimensions

The size and shape of the canister were derived based on the space needed for the actual spent fuel assemblies, the mechanical strength, the chemical durability (corrosion resistance), and the subcriticality and radiation protection (max dose rate at the outside surface of approximately 1 Gy/h) referenced in Posiva SKB (2017). The reference geometry of the canister is documented in SKB (2010c).

Other factors influencing the shape and dimensions of the canister are derived from the manufacturability of the canister components, such as the copper shell and the nodular cast iron insert with channels. The shape and dimensions are also different depending on the BWR and PWR spent fuel elements or other miscellaneous fuel elements, such as VVER 440 and EPR.

As stated in Chapter 1, the Finnish nuclear programme for spent nuclear fuel is similar to the Swedish programme; however, a few differences exist. These differences include slightly modified shapes and dimensions while manufacturing the canister components, which are still within the stated reference design of the canister. A compilation of the drawings used for manufacturing the canister components is documented in Hultgren (2014).

All nominal dimensions specified are the final canister dimensions, and they apply at room temperature (+20 °C). See Figure 1-1 for a schematic exploded view of the canister and its components. The shapes and dimensions presented in this section may require several manufacturing steps and are the final shapes and dimensions to fulfil the design requirements and reference design.

5.1 BWR and PWR inserts

The inserts are manufactured from nodular cast iron with steel channel tubes, in which the fuel assemblies are to be positioned. The channel tubes are made of square-profiled steel tubes that are welded together with support plates to form a steel tube cassette that is placed in the casting mould. The detailed design in terms of the support plates between the channel tubes and base plates of the steel cassettes of the inserts may vary slightly; the performance, however, conforms to the reference design. The square tubes used in the welded cassette to form the openings for the fuel elements in the insert are made of standard-type hollow-steel sections made either using cold-formed steel plates (with a longitudinal weld) or hot-formed steel (seamless tubes). The material for the hot-formed VKR (RHS) square hollow sections shall fulfil the requirements in EN 10210-1 S355J2H concerning the chemical composition and mechanical properties (yield stress, tensile strength and elongation). Alternatively, the material for the cold-formed KKR square hollow sections shall fulfil the requirements in EN 10219-1 S355J2H concerning the chemical composition and mechanical properties (yield stress, tensile strength and elongation). The material for the steel plates and flat bars used as support plates in the cassette shall fulfil the requirements in EN 10025 S235JRG2 or similar requirements.

The casting process enables the void space between the fuel channels to be filled, thus avoiding the risk of criticality, even in the case of water filling the canister (Posiva SKB 2017). The cast iron material composition of the insert is specified only for the content of copper, to avoid radiation embrittlement, and is within the limits for the validity of the criticality analyses. The content of copper in the nodular cast iron shall, therefore, not exceed 0.05 % (Posiva SKB 2017). During the development of the casting process for the nodular cast iron inserts, the now expired standard requirements in EN 1563 grade EN-GJS-400-15U have been used. The current material standard for the cast iron is SS-EN 1563:2012. The mechanical requirements for the nodular cast iron are derived and compiled in Chapter 8.

The insert will also be assembled with a steel lid, with or without an integrated valve depending on the design, and a screw with a copper washer under the head of the screw. The Swedish design of the steel lid includes a valve in the lid to permit quick replacement of the atmosphere inside the canister. The milled grooves between the channel tubes in the insert are also present to permit changing the atmosphere inside the canister. The steel lid of the insert is made using a structural steel plate according to EN 10025 S355J2G3 or a similar grade with at least the same tensile strength and ductility under the as-hot-rolled or normalised conditions.

Figures 5-1 to 5-6 and Table 5-1 show the shapes and dimensions of the inserts with a steel lid.

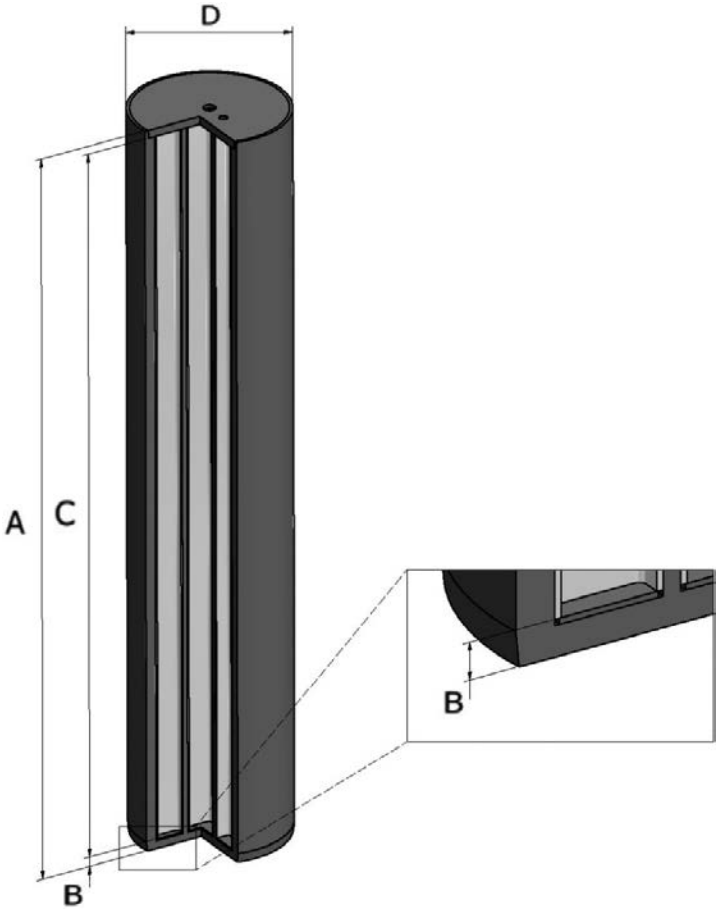

Figure 5-1. *BWR insert with steel lid.*

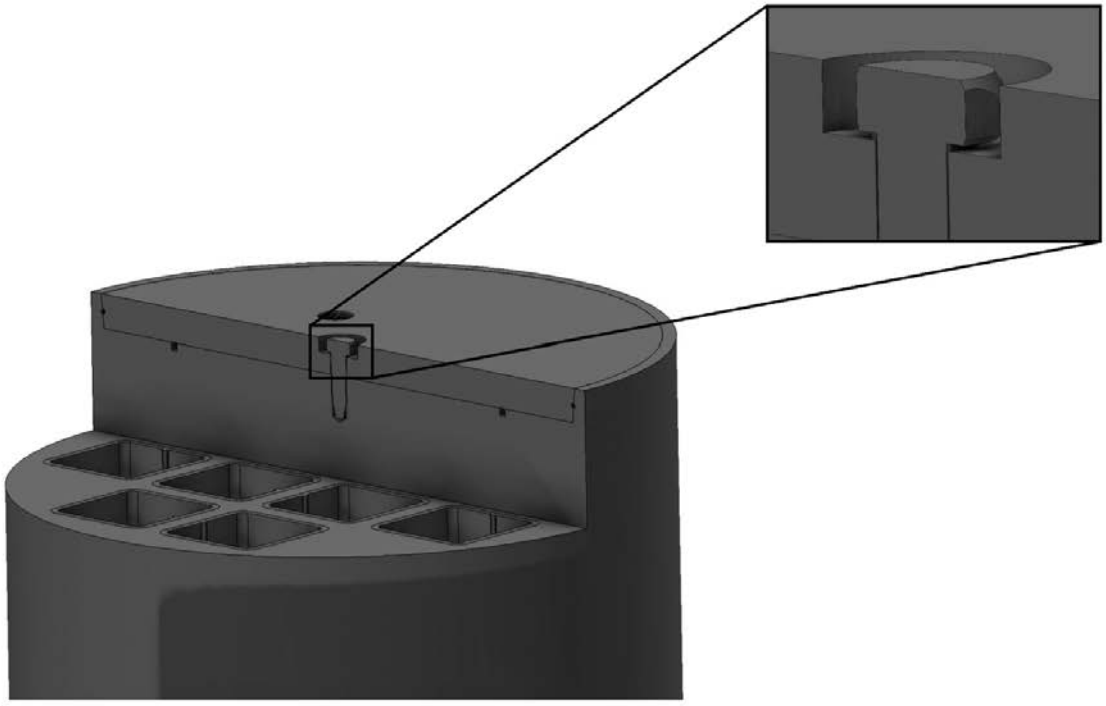

Figure 5-2. *BWR insert with steel lid and screw with copper washer.*

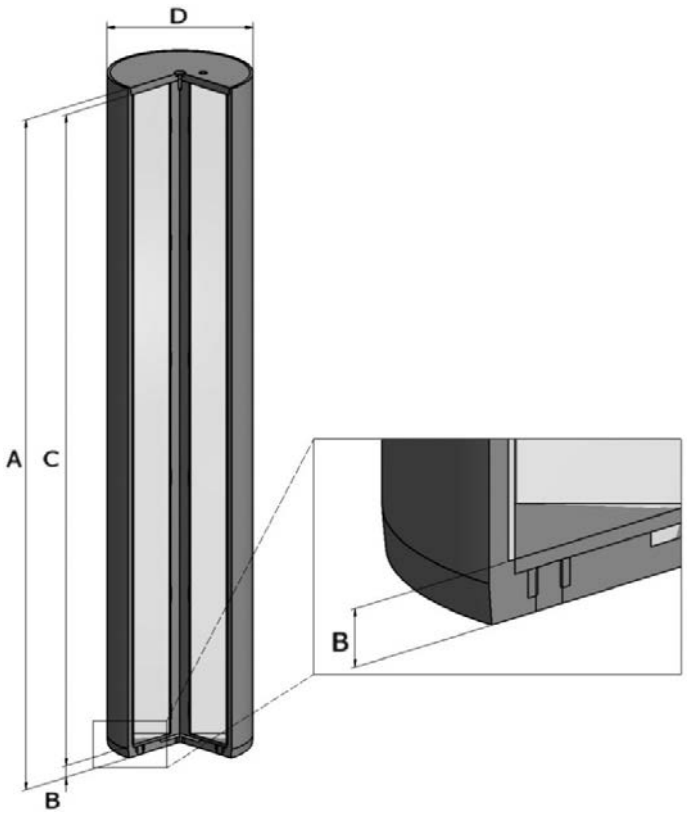

Figure 5-3. *PWR insert with steel lid.*

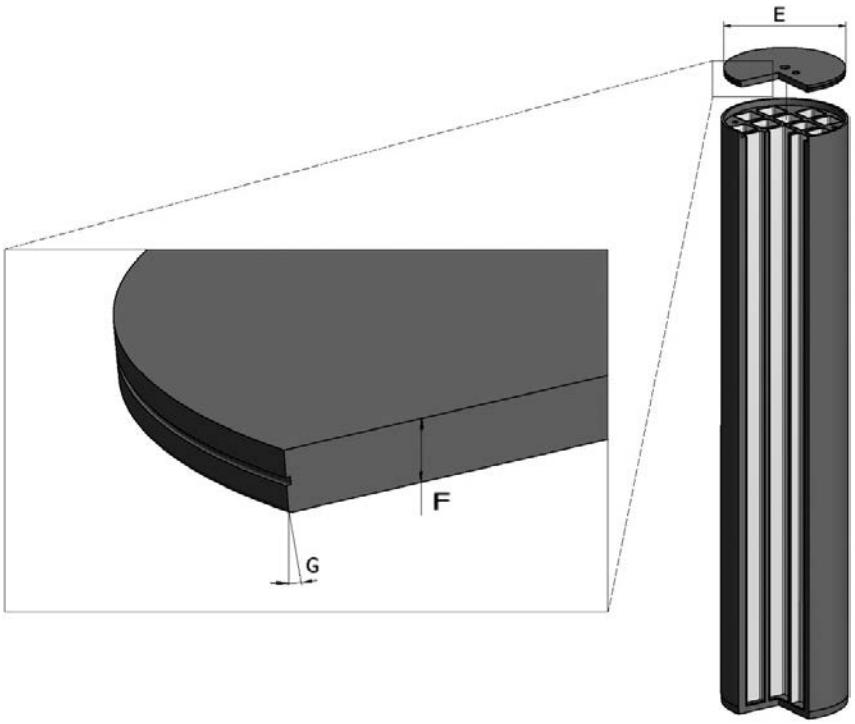

Figure 5-4. *SKB steel lid for the BWR and PWR insert with a hole for the valve (insert in figure is for the BWR).*

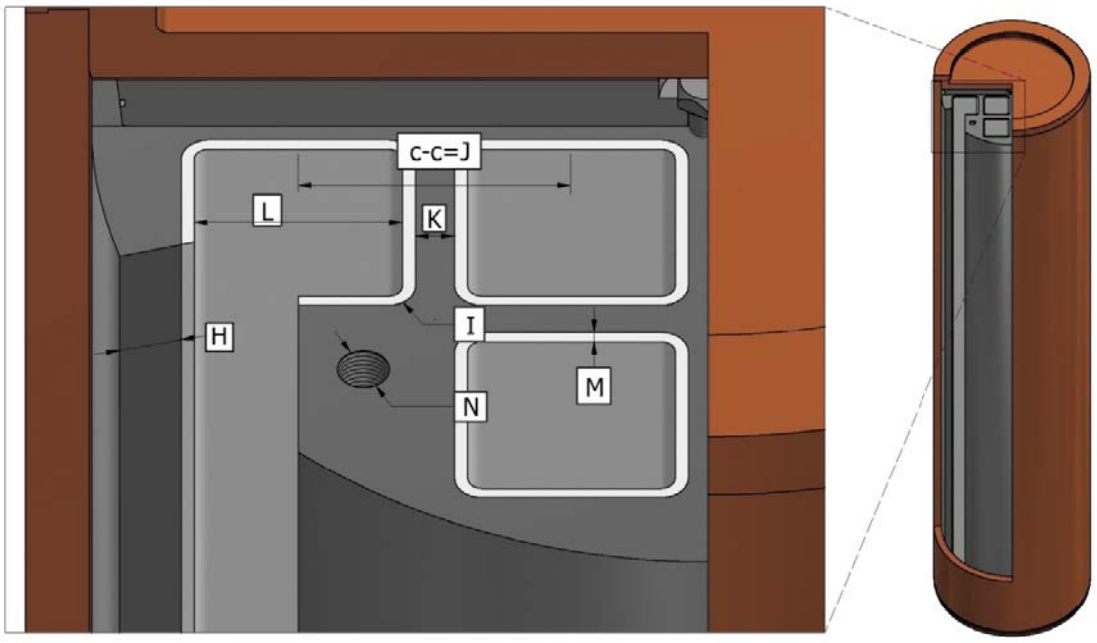

Figure 5-5. *Cross section of the BWR insert with steel channel tubes.*

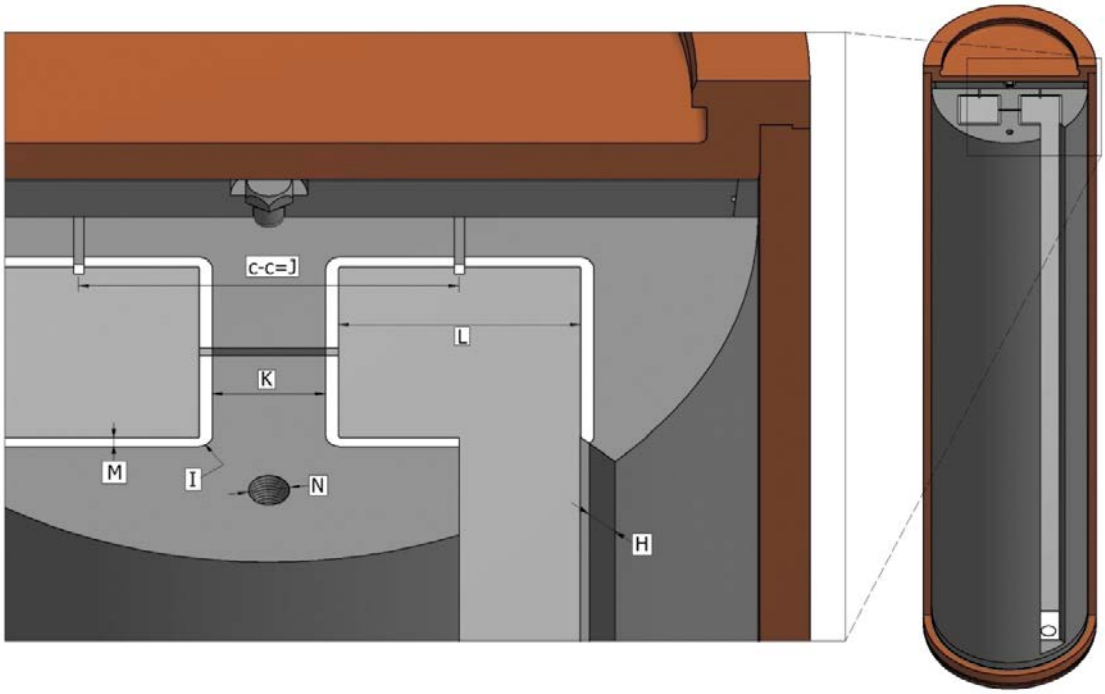

Figure 5-6. *Cross section of the PWR insert with steel channel tubes. The grooves between the channel tubes, used for changing the atmosphere, are visualised.*

Table 5-1. Dimensions specified for the SKB BWR and PWR inserts (Hultgren 2014) used in the analyses.

Figure no, and dimension designation	Description	BWR Nominal value and tolerance (mm)	PWR Nominal value and tolerance (mm)
5-1 A and 5-3 A	Length of insert	$4\,573^{+0}_{-0.5}$	$4\,573^{+0}_{-0.5}$
5-1 B and 5-3 B	Thickness of the insert base including steel and cast iron	$60^{+5.1}_{-5.6}$	$80^{+5.1}_{-5.6}$
5-1 C and 5-3 C	Interior length	$4\,463^{+5}_{-5}$	$4\,443^{+5}_{-5}$
5-1 D and 5-3 D	Insert diameter	$949^{+0.5}_{-0}$	$949^{+0.5}_{-0}$
5-4 E	Steel lid diameter	$910^{+0}_{-0.09}$	$910^{+0}_{-0.09}$
5-4 F	Steel lid Thickness	$50^{+0.1}_{-0.1}$	$50^{+0.1}_{-0.1}$
5-4 G	Steel lid bevel angle	$5^{\circ+0.1^\circ}_{-0.1^\circ}$	$5^{\circ+0.1^\circ}_{-0.1^\circ}$
5-5 H and 5-6 H	Edge distance	33.3^{+10}_{-10}	37.3^{+10}_{-10}
5-5 I and 5-6 I	Channel tube corner radius	20^{+5}_{-5}	20^{+5}_{-5}
5-5 J(=C-C) and 5-6 J(=C-C)	C-C Distance between the channel tubes	210^{+1}_{-4}	$370^{+6.2}_{-6.2}$
5-5 K and 5-6 K	Distance between the channel tubes	$30^{+2.7}_{-4.6}$	$110^{+6.2}_{-6.2}$
5-4 L and 5-5 L	Square hollow channel tube internal dim. before casting	$160 \times 160^{+3.8}_{-3.8}$	$235 \times 235^{+5.1}_{-5.1}$
5-4 L and 5-5 L	Gauge channel tube internal dim. after casting	min 152 × 152	min 222 × 222
5-5 M and 5-6 M	Channel tube thickness	10^{+1}_{-1}	$12.5^{+1.25}_{-1.25}$
5-5 N and 5-6 N	Threaded hole for lifting the insert	*M*	*M*
5-5 and 5-6	Channel tube size, outer	$180^{+1.8}_{-1.8}$	$260^{+2.6}_{-2.6}$

Copper shell

The copper lids and bases are manufactured using hot forging as a reference method. The copper tube can be manufactured in different ways, such as pierce and draw processing or extrusion. These tube manufacturing processes yield different designs for the base of the copper shell. With pierce and draw processing, the copper shells have an integrated base and do not require the copper base to be welded to the extruded copper tube by friction stir welding (FSW). Both the integrated base and the welded base of the copper shell conform to the reference design and are, therefore, presented here.

Figures 5-7 and 5-8 show the shape of the extruded copper shells with FSW for both the copper base and copper lid.

Figure 5-9 shows the shape of the canister with an integrated copper base. This copper shell consists of a copper tube manufactured using the pierce and draw method and a lid welded to the copper tube due to FSW. The shapes and dimensions of the copper lid and copper tube are the same as in Figure 5-8.

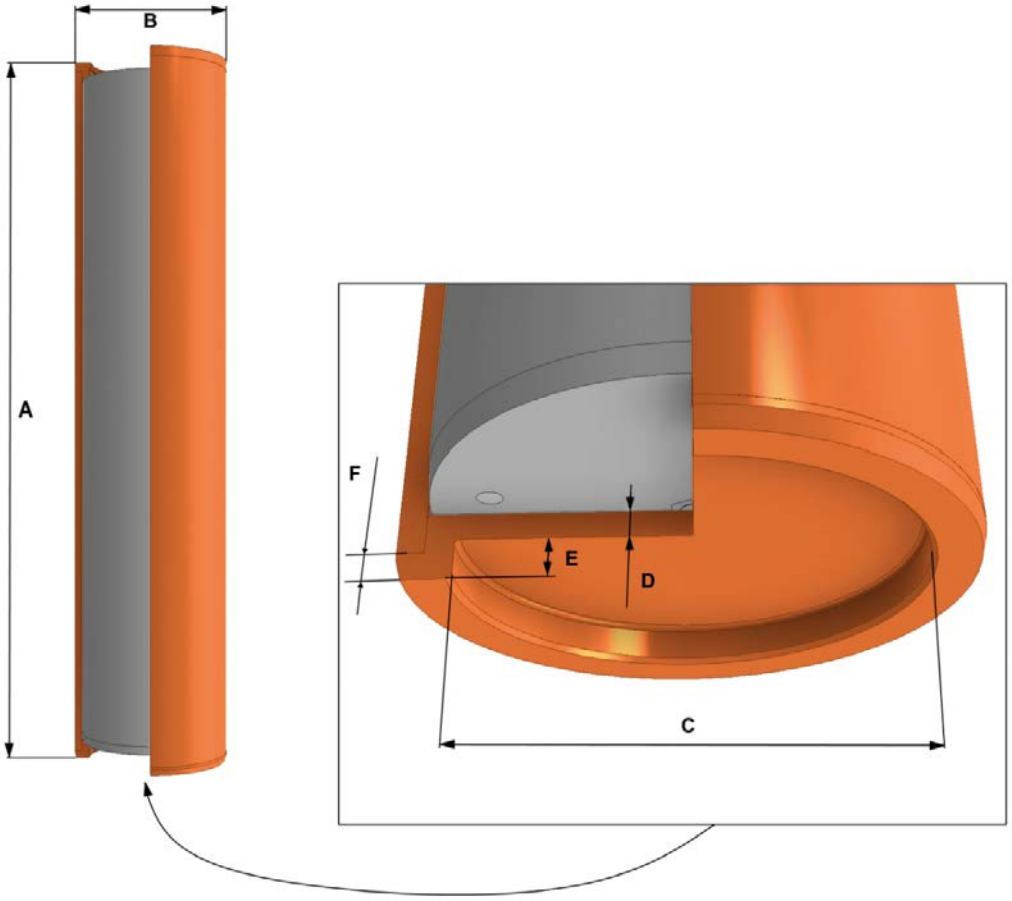

Figure 5-7. *Cross section of the copper shell and welded copper base and the main dimensions.*

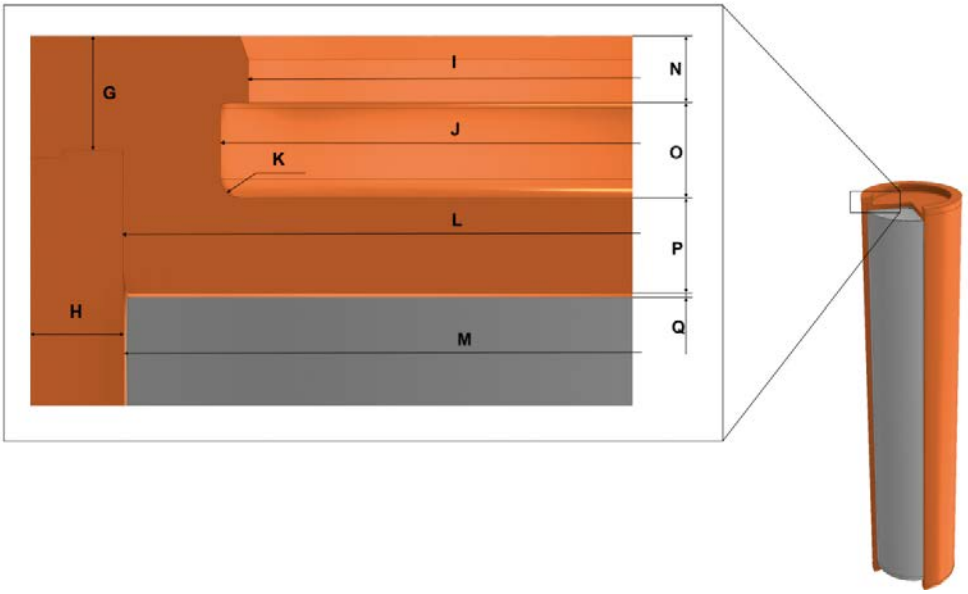

Figure 5-8. *Cross section of the copper shell and shell copper lid and the main dimensions.*

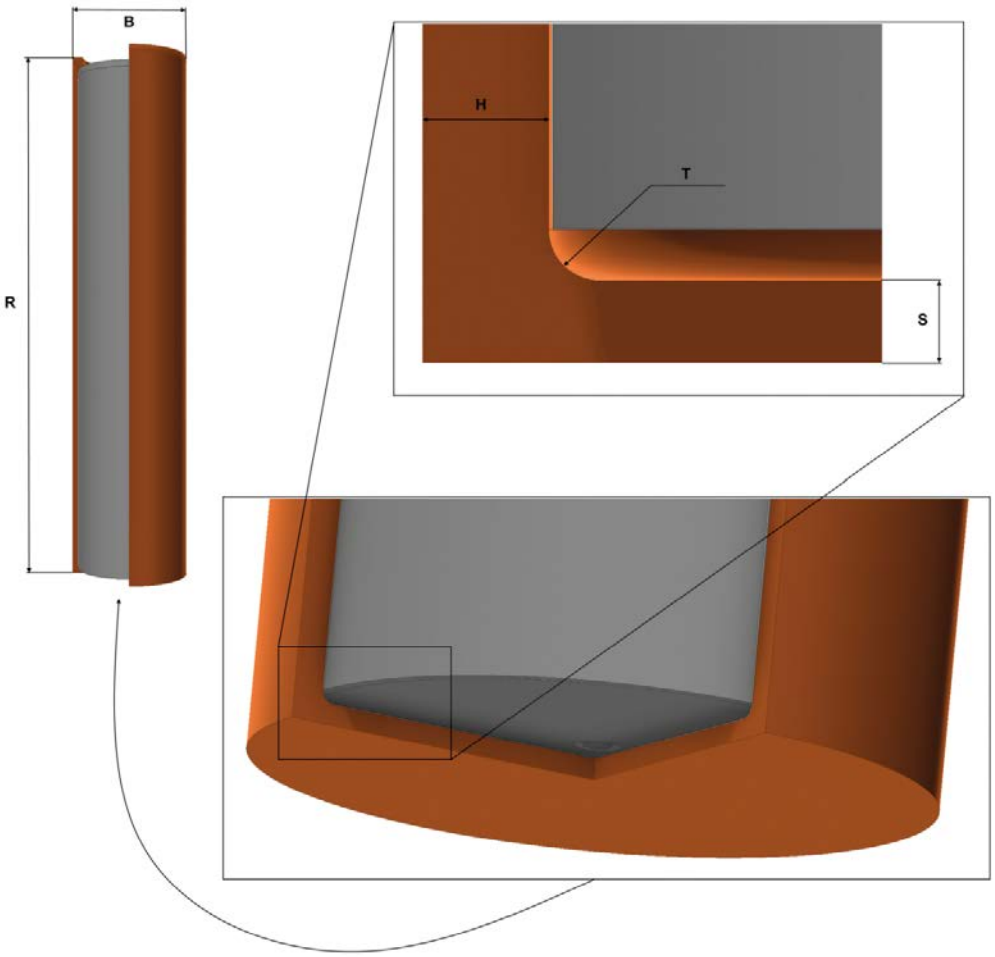

Figure 5-9. *Cross section of the copper shell using the pierce and draw method and the main dimensions.*

5.1.1 Dimensions of the copper shells

Table 5-2 shows the dimensions of the extruded copper shell using FSW for both the copper base and copper lid. The dimensions of the copper shell with an integrated base is following the manufacturing specifications of Posiva.

Table 5-2. Dimensions of the copper shell.

Figure no. and dimension designation	Description	Extruded copper shell with welded base (mm)	Pierce and draw copper shell with integrated base, (mm)
5-7 A and 5-9 R	Total length	$4\,835^{+3.25}_{-2.75}$	$4\,777^{+6.4}_{-1.4}$
5-7 B and 5-9 B	Outer diameter	$1\,050^{+1.2}_{-1.2}$	$1\,050^{+0.5}_{-0.5}$
5-7 C	Inner diameter base	$850^{+0.8}_{-0.8}$	*NA*
5-7 D and 5-9 S	Thickness base	50^{+1}_{-1}	50^{+3}_{-0}
5-7 E	Dimension base, depth	$75^{+0.3}_{-0.3}$	–
5-7 F	FSW position base	50	–
5-8 G	FSW position lid	60	60
5-8 H and 5-9 H	Wall thickness shell	$49^{+1.35}_{-0.85}$	$49^{+0.5}_{-0.85}$
5-8 I	Inner diameter lid, top	$821^{+0}_{-0.5}$	$821^{+0}_{-0.5}$
5-8 J	Inner diameter lid, bottom	$850^{+0.8}_{-0.8}$	$850^{+0.8}_{-0.8}$
5-8 K	Corner radius	10	10
5-8 L	Diameter lid, assembly FSW	$953^{-0.32}_{-0.55}$	$953^{-0.32}_{-0.55}$
5-8 L	Inner diameter shell, assembly FSW	$953^{+0.23}_{-0}$	$953^{+0.23}_{-0}$
5-8 M	Inner diameter shell	$952^{+0.5}_{-0.5}$	$952^{+0.5}_{-0.5}$
5-8 N	Dimension lid	$35^{+0.6}_{-0.6}$	$35^{+0.5}_{-0.5}$
5-8 O	Dimension lid	$50^{+0.3}_{-0.3}$	$50^{+0.3}_{-0.3}$
5-8 P	Thickness lid	50^{+1}_{-1}	$50^{+4.2}_{-0.7}$
5-8 Q	Axial gap between lids, copper and steel	$2^{+1.1}_{-0.3}$	$2^{+1.1}_{-0.3}$
5-9 T	Corner radius	–	20

6 Analysis results

The purpose of this section is to compile the main load analysis results based on the design premises, loads, geometries and constitutive models presented in this report. Chapter 6 is divided into two main parts: results from analyses of the operational loads and results from analyses of the loads in the final repository. In Chapter 7, sensitivity analyses will be presented. Chapter 6 and Chapter 7 should therefore be considered as two parts of the same verification process for the mechanical integrity of the copper canister.

6.1 Operational loads

In the calculations of the handling load cases, the maximum copper surface temperature is 100 °C (Posiva SKB 2017). Therefore, the constitutive model considering elastic-plastic deformation at 125 °C in Section 4.7.2 is used. This is a pessimistic assumption of the strength of the copper shell in this load case as the strength decreases with increasing temperature.

6.1.1 Lifting the canister by the lid flange

In the encapsulation plant, the canisters are lifted, lowered and handled. During the analysis of the components used in the Finnish and Swedish nuclear industries, acceptance criteria are usually adopted from the American ASME code. The geometry of the region of interest is shown in Figure 6-1.

The dynamic load originates from lifting the canister by the lid flange after sealing. Then, unexpected braking while lifting the canister according to Section 2.1 may occur. A damage tolerance analysis via a limit load analysis has been conducted for the copper shell of the PWR canisters in Alverlind (2016c) and further in Unosson (2017). The total PWR canister weight is 28 000 kg according to Posiva SKB (2017), which is the sum of the copper shell and encapsulated components. The justification of using the PWR weight is related to the higher weight of the PWR canister than the BWR canister. For lifting the canister, the criterion for the limit load described in NB-3228.3 is used. The limit load is considered to be the acceptable load. The collapse load $F_{collapse\text{-}ASME}$ in Table 6-1 should be considered to be the load if the grip is lost or the lid weld tears open, and it is derived for a canister with nominal geometry without defects and with defects in Alverlind (2016c) and Unosson (2017), respectively. The acceptable load to lift the canister includes a dimensionless dynamical factor (n), and the formula includes the mass of the canister and gravity constant (g = 9.81 N/kg). Therefore,

$$F_{collapse\text{-}ASME} = S_f \cdot m \cdot g \cdot n \qquad (6\text{-}1)$$

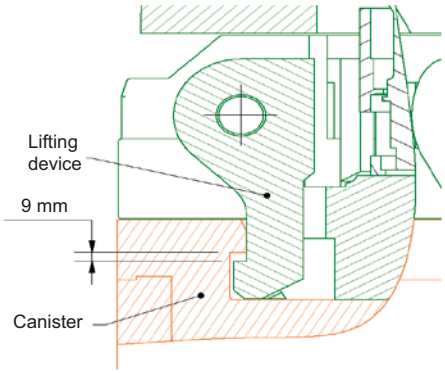

Figure 6-1. *Cross section and details of the lifting device and canister (Unosson 2017).*

The reports conclude that the nominal canister geometry can withstand 2.3 g and fulfil the design criterion in terms of the acceptable normal load according to ASME, and in the emergency and faulty case, n = 2.8. Equation (6-1) can be applied to determine the n-factor for other canister weights as well. An increased canister weight will reduce the n-factor and vice versa.

However, the copper shell may have defects, and the collapse load is dependent on the occurrence of defects. Therefore, limit load analyses have also been conducted for models containing defects. In Alverlind (2016c), a circumferential weld root defect with a width of 18 mm in the radial direction was postulated; the influence of the weld defects was considered to be small. The dynamical factor was n = 2.2 during normal load, and in the emergency and faulty case, n = 2.7. In Unosson (2017), the influence of different defect sizes was investigated along with a forge defect with a width of 10 mm in the radial direction. Using Equation (6-1), the evaluations of the lifting analyses in Unosson (2017) and Alverlind (2016c) are compiled in Table 6-1.

Table 6-1. Results of the ASME limit load analysis for a copper shell with and without defects.

	Copper shell without defects		Copper shell with an 18 mm weld defect		Copper shell with an 10 mm forge defect	
S_f (--)	3/2	5/4	3/2	5/4	3/2	5/4
$F_{collapse\text{-}ASME}$ (kN)	954	954	939	939	945	945
n (--)	2.3	2.8	2.2	2.7	2.3	2.8

It has been shown that the copper shell is resistant to defects. The conclusion is that the dynamic load as a result of lifting the canister by the lid flange has been verified for normal handling and emergency handling, including fully circumferential defects up to at least 10 mm in width. The canister can withstand more than 2 g according to ASME when lifting the lid flange. As long as the collapse loads for the normal load are not exceeded, the canister can be deposited in the final repository, and as long as the collapse loads for the emergency load are not exceeded, the canister should not drop from the lifting device.

6.1.2 Static and dynamic load as a result of handling contact pressure on the copper shell

The transportation and handling of the canister will subject the canister to loads on the copper shell that will result in a contact pressure due to alignment during assembly or the support equipment on-board a vehicle or a vessel. In the report by Unosson (2017), the acceptable global pressure on the outer surface on the copper shell without support from an insert was derived, and the critical handling load is defined here as the highest acceptable uniform pressure on the external surface of the canister that does not result in plastic deformation in the copper shell. In other words, the maximum acceptable uniform pressure applied to the surface of the canister without losing its integrity is 1.8 MPa without applying any safety factors. If a safety factor of 1.5 is applied, a uniform contact pressure of 1.2 MPa can be applied around the copper shell without losing its stability due to buckling.

However, a local higher contact pressure may be accepted. The criterion is that plasticity shall not occur, and if plasticity occurs, the indentation depth shall not exceed the criteria for indentation derived in Section 6.1.3 below. In this approach, the yield stress for copper provides a guideline of the acceptable local pressure that shall not exceed the yield stress of the copper. The yield stress for copper has been found to be in the range of 10 MPa at 125 °C and in the range of 30–50 MPa at room temperature, as shown in Section 4.7. Applying a safety factor of 1.5 is also recommended when designing the manufacturing, transportation and disposal systems.

6.1.3 Accidental surface deformation in the copper shell

When handling the copper canister during manufacturing and preparation for disposal, there may be inadvertent damage to the exterior of the copper canister that could possibly weaken the overall integrity of the canister and cause premature failure of the copper shell. To study the effects of accidental indentations on the structural creep properties of the copper canister, laboratory-scale test specimens made of copper were designed in Unosson (2015) to be used for indentation tests

followed by creep tests. The texture-dependent constitutive model in Unosson (2014) was used, and the maximum true plastic strain in the indentations was approximately 80 %. The creep specimens were tested in both an annealed and indented state (see Mannesson and Andersson-Östling 2014). The indentation marks in the specimens were of conical, spherical and cylindrical shapes with 0.5 mm deep indentations to replicate 5 mm full-scale indentations. The depth of the indentation marks was determined by using a scale replica of the maximum foreseen 5 mm indentation in the copper shell of the finished canister. Creep testing at 75 °C and 125 °C showed normal behaviour for the creep ductility, and there was no difference between the specimens with or without indentations. Therefore, a 5 mm indentation depth can be accepted in the copper shell of a full-scale copper canister, independent of the indentation shape and geometry.

The critical spacing between two indentations with a depth of 5 mm in the copper canister was investigated in Unosson (2017). To avoid interactions between the two indentation marks and to assess whether accidental indentation marks should void a canister, the minimum spacing between two such indentation marks was computed. The basic assumption here is that the plastic strain fields between two indentations with a depth of 5 mm should not interact. The results are given in Table 6-2 as the minimum distance between the edges of two individual, or local, indentations to avoid interactions between the plastic strain fields. The critical indentation spacing is governed by a cylindrical indenter.

Table 6-2 Critical indentation spacing at an indentation depth of 5 mm for three different indenter geometries (Unosson 2017).

Indenter geometry	Minimum distance between indentation edges (mm)
Sphere (radius 10 mm)	115
Cone (angle 45°)	36
Cylinder (radius 10 mm)	180

The critical lateral defect size along the surface of the copper components is shown in Figure 6-2 and was investigated in Unosson (2017). The lateral defect size along the surface of the canister was not a major factor. The critical pressure was reduced by approximately 10 %, and for larger footprints (50 cm), the increased stiffness of the structure due to deformation hardening increased the critical pressure to the same level as that for the unindented structure. In Unosson (2015), it was stated that the indentations in copper can be scaled in size linearly. Therefore, because the minimum edge distance between two defects is 180 mm with a depth of 5 mm in the deepest indentation, the minimum edge distance with a defect depth of 1 mm is 180/5 = 36 mm. An indentation with a depth of 1 mm results in less than 20 % true plastic strain according to Figure 3-2 in Unosson (2015). Therefore, indentations with a depth of less than 1 mm can be accepted, independent of the edge distance between several defects with a maximum depth of 1 mm. This result was also justified in Mannesson et al. (2013), in which creep tests of specimens with three indentation depths of 1, 1.5, and 2 mm were studied with increasing amounts of cold work. The results from the creep testing showed no significant effect on the creep rupture time and creep ductility with the size of the indentation depth.

Therefore, the following conclusions can be drawn:

- The maximum acceptable indentation depth in a single indentation is 5 mm, independent of the shape of the indentation.
- The lateral defect size along the surface of the canister is not a major factor for the post-closure safety of the canister, so no requirement for the maximum acceptable lateral defect size is stated.
- Several defects in the copper shell are acceptable only if the defects can be considered to be local, and the maximum depth is 5 mm among all defects.
- Defects are considered as local if the minimum edge distance between two or several defects is 180 mm, with a depth of 5 mm in the deepest indentation. The minimum edge distance is 36 mm when the indentation depth is 1 mm. Hence, the minimum edge distance between defects can be achieved with interpolation as a function of the depth of the deepest indentation.
- Handling defects with a depth of less than 1 mm are always acceptable, independent of the edge distance between several defects.

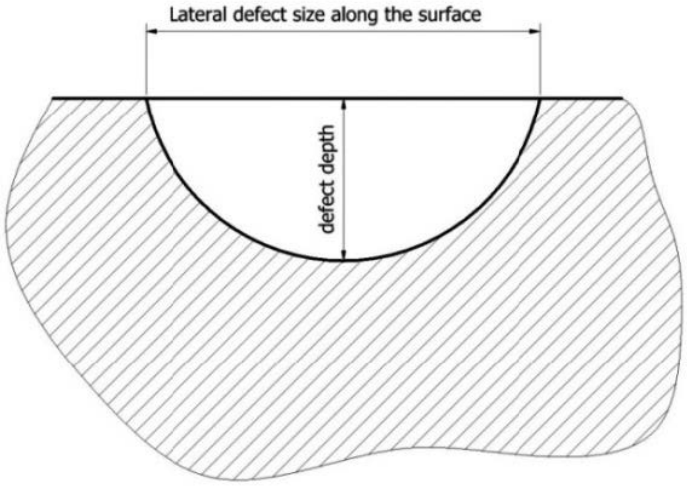

Figure 6-2. *Left: Schematic cut-away view of a surface defect in a component. The definitions of the defect depth and lateral defect size along the surface of the component are shown.*

6.1.4 Lifting the insert in the M45 screw holes

The BWR and PWR inserts are lifting during the manufacture of the inserts and in the canister factory during the assembly step when the insert is installed into the copper shell. The lifting load case of the inserts has been verified by Zeng et al. (2015). The critical lift position at which the worse stress states are caused during the lifting process has been identified, and its consequence has been evaluated through engineering analyses. Thereafter, a defect tolerance analysis in accordance with ASME Sect XI was conducted. The weight of a PWR insert was used; however, the geometry of a BWR insert was postulated. This was motivated by the fact that the PWR insert is heavier, but the BWR insert has "thinner" components in the region near the bolt holes for mounting the lift eyes.

Defect tolerance analyses have been conducted for four postulated defects, and they all show that the structure has a sufficiently large capacity to resist both surface and internal defects postulated near the bolt hole. The reserved safety margin is approximately a factor of 10, which is very high. It was concluded that the stress level is generally low in the ductile iron insert for the lifting load case. No additional integrity requirements are needed with regards to lifting. Inspection with NDT is not required because of the lifting load case. Instead, a pessimistic functional lifting test of the insert is proposed to be conducted before the actual lifting occurs.

6.2 Loads in the repository

All the dimensioning loads act on the canister from the outside. Usually, they are of the isostatic pressure type, but in special cases, unevenly distributed swelling pressure or rock shear may occur. The rock shear load from the deposition hole surfaces is transferred to the canister surface through the bentonite buffer. The resulting presentation will be divided into two main parts: the insert and the copper shell. The numbering of the load cases follows the numbering in Chapter 2. The temperatures in the canister after disposal were investigated in Ikonen (2017).

6.2.1 Loads on the nodular cast iron insert

The insert is the principal load-carrying part of the canister. As long as the insert is supporting the copper shell, the shell cannot collapse inwards. The steel lid is a part of the insert; however, the component is treated as a separate unit in this section. Load cases 1 and 2 are derived from uneven horizontal stresses. The solution approach is to consider the canister as a freely supported beam, as shown in Figure 2-4. This approach causes bending stresses in the insert and results in acceptable defect sizes in terms of radial crack-like defects. An analysis of the temperature evaluation in

the canister was performed in Ikonen (2017). The temperature on the outer radius of the copper canister was pessimistically set to 100 °C. The total power was 1700 W in the BWR and PWR fuel-type canisters, which corresponded to the heat powers during disposal. These analyses indicated 112.7–118.1 °C for the maximum temperature in the cast iron inserts and 147.1–203.0 °C for the fuel pellets using pessimistic assumptions for the copper shell temperature. The conclusion that can be drawn is that the temperatures in the canister do not exceed 125 °C in the insert or 100 °C in the copper shell, provided that the buffer and rock have sufficient thermal conductivity to keep the buffer temperature below 100 °C. This is primarily ensured by the design by setting a sufficient distance between the deposition holes in relation to the thermal conductivity of the rock.

In Appendix A, the defect acceptance criteria for the idealised postulated defects of the inserts are compiled. These can be used as a reference for non-destructive testing requirements.

Cases 1a and 2a – asymmetric loads on the canister before and after full bentonite water saturation

Case 1a – asymmetric loads on the canister before full bentonite water saturation

The first load phase after disposal of the canister is the initiation of bentonite buffer wetting. The buffer is wetted from the water-bearing fractures that intersect the deposition holes. The load case is the result of simplified assumptions during the complicated wetting phase and is likely pessimistic.

Simplified calculations of the stresses in the canister insert yield a maximum axial stress of 105 MPa (Börgesson et al. 2009). Further investigations of this case have been conducted using the finite element method in Hernelind (2014d). From Börgesson and Hernelind (2013), it can be concluded that the maximum axial stress is equal to 79 MPa (see Figure 6-3).

Case 2a – asymmetric loads on the canister after full bentonite water saturation

After the buffer is completely wetted, the pressure will be the sum of the bentonite swelling pressure and water pressure. While the water pressure will be isostatic, the bentonite density variations in combination with imperfections in the deposition hole can impose an asymmetric pressure on the outer surface of the canister, which is considered to be permanent. In the same way as in the water saturation case, the worst situation for the canister in terms of swelling distribution is defined and analysed.

To evaluate the stresses in the case where the banana shape = 8 mm, simplified analytical calculations of the stresses in the canister insert yielded a maximum axial stress equal to 111.5 MPa (Börgesson et al. 2009). Further investigations of the case have been conducted using the finite element method in Börgesson and Hernelind (2013), and it can be concluded that the maximum axial stress is equal to 79 MPa (see Figure 6-3). The resulting stress of 79 MPa in the cast iron insert for cases 1a and 2a is lower than the yield stress of the cast iron (minimum of 240 MPa), so the insert will withstand the stresses elastically, without plastic deformation or risk of damage. The crack sensitivity at the most stressed location of the insert barrel surface was estimated for asymmetric load cases 1 and 2, and the maximum acceptable radial crack size depth is 21.1 mm (Alverlind 2016a).

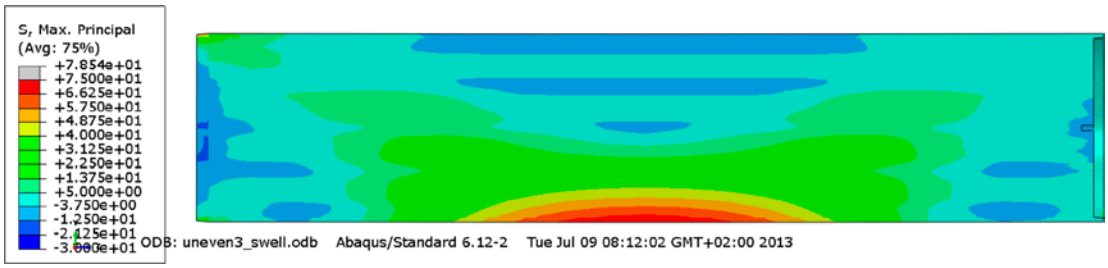

Figure 6-3. *Maximum principal stresses (MPa) in the BWR insert (Börgesson and Hernelind 2013).*

Cases 1b and 1c – radial swelling pressure at the outer surface of the copper lid flange and buffer swelling along the canister

In Hernelind (2014f), load cases 1b and 1c were investigated. Two extreme and pessimistic assumptions are studied here (see Section 2.2.4). The most pessimistic assumption is that the shear stress reaches its maximum value and has a constant magnitude along the surface of the canister of 1.75 MPa. Therefore, the maximum tensile stress in the surface of the insert is also equal to 1.75 MPa. These cases result only in elastic stresses in the nodular cast iron insert and do not lead to requirements of acceptable defect sizes in the insert.

Cases 2b and 2c – stresses caused by homogenisation and density gradients in the buffer

These cases only result in low stresses and strains in the insert. In Hernelind and Börgesson (2018), it is stated that the homogenisation results in a stress of 21.7 MPa stress, and therefore, no plasticity will occur.

Cases 3 and 4 – isostatic pressure load

These cases are related; the load is a uniform outer pressure and is therefore considered to be an isostatic load. As seen in Table 2-1, the design isostatic load case of 50 MPa is the sum of the bentonite swelling pressures, the normal groundwater hydrostatic pressure at the repository depth and, during glacial period, the additional pressure caused by the ice sheet floating on the groundwater. This case is the governing case in terms of the acceptable size of the volumetric defects and axial cracks in the insert, and the operating temperature (in the load condition) during the glacial period will be between 0 and 20 °C. The load case will affect all canisters in the repository. Thus, the reliability of the mechanical integrity of the canister for this load case must be high because the possible risk concerns all canisters in the repository. The failure mechanisms include plastic collapse and initiation of crack growth.

The cast iron insert is analysed using finite element models considering, to varying extents, the variations in the material properties and geometry and the effects of the postulated defects. The stability of the structure and its interaction with the steel tubes and copper shell are analysed. A separate analysis is performed for the insert steel lid. The analyses are performed for both types of inserts: BWR and PWR. The BWR insert has a collapse pressure of 90 MPa with ideal geometry without defects (nominal geometry), as seen in Table 6-3. The collapse pressure of the PWR insert is 109 MPa, and therefore, the BWR insert is the governing case of the two. The verification of the canister insert, insert lid, and insert base against the governing pressure load of 50 MPa is presented in Alverlind (2010, 2016a, b).

Analyses were also performed and presented in Dillström et al. (2010), Hernelind (2015c), Ikonen (2005) and Martin et al. (2009). Table 6-3 shows a comparison of the collapse loads from five different analyses. The difference is explained in terms of the different assumptions regarding the material and geometry. It is clear that the calculated collapse load in Alverlind (2016a) is one of the most pessimistic investigations and that the collapse load can be considered to be verified.

Table 6-3. Calculated collapse loads with a nominal BWR insert geometry.

Ikonen (2005)	Martin et al. (2009)	Dillström et al. (2010)	Alverlind (2016a)	Hernelind (2015c)
90 MPa	117 MPa	99 MPa	90 MPa	97 MPa

The isostatic load case was handled using a probabilistic analysis in Dillström (2009a) for the BWR insert. The analysis shows that the risk of failure of the insert is low up to the design pressure of 50 MPa. For an insert with a nominal geometry and centred steel cassette, the risk of failure was calculated to be $< 1 \times 10^{-50}$, and the corresponding risk of failure with a 10 mm reduction of the edge distance dimension (H) in Figure 5-5 is 1.2×10^{-6}. In (Dillström and Manngård 2017), the case has been further studied. The risk of failure was calculated to be 1×10^{-20}, when the isostatic load is less than 75 MPa. The effectively variable parameters are shown to be the yield stress in compression and the edge distance in the isostatic load case.

Damage tolerance analyses – volumetric defects

Because the isostatic pressure is a significant mechanical load that affects all canisters in the final repositories in Finland and Sweden, the damage tolerance analyses have been pessimistically conducted in terms of mechanical properties of the nodular cast iron. The yield stress was scaled to 240 MPa, instead of using the strength of 270 MPa normally achieved during manufacturing tests (Jonsson 2017). The steel channel tubes in the cassette are assumed to not bond with the cast iron, and the support plates in the cassette are not considered; these are also pessimistic assumptions. In addition, the influence of residual stresses on the nodular cast iron is considered. The radius of the outer corners of the cassette tubes are nominally 20 mm, which is reasonable according to Martin et al. (2009). The copper shell was modelled according to the stress-strain curve in Table 4-9. Three-dimensional analyses were used in both Alverlind (2016a) and Alverlind (2016b). During manufacturing of the insert, the steel tube cassette may be positioned somewhat offset in relation to the centre of the insert. This will cause a decrease in the edge distance of the insert, (dimension *H* in Figure 5-5 and Figure 5-6).

A damage tolerance analysis of components with volumetric defects, either actual or postulated, typically considers the damage mechanism of plastic collapse (ASME III division 2 article 4-136.5, plastic analysis in Alverlind 2016a, b). With a design load of 50 MPa, the minimum collapse load point that satisfies the criteria is 75 MPa. This strategy has been used to verify the largest possible defects, that is, the minimum collapse load shall be fulfilled for the postulated defects.

The results show that the insert including the base is very robust in terms of volumetric postulated defects. All voids that can physically fit in the insert geometry were found to be acceptable with respect to the isostatic design load. A compilation of the acceptable spherical defects is shown in Table 6-4 for the BWR insert and in Table 6-5 for the PWR insert. The threaded M45 holes in the inserts used for lifting are localised; defect no. 4 is located at the top of the BWR insert, and defect no. 1 is located at the top of the PWR insert and is thus smaller than the acceptable hole size (see Figure 6-4 and 6-5).

The combination of a decreased edge distance (dimension *H* in Figure 5-5 and Figure 5-6) and a volumetric defect in this region was also investigated in Alverlind (2016a). Other defects are insignificant in combination with the decreased edge distance. The complete removal of the nodular cast iron material between the steel tubes, which corresponded to the most severe axial location with respect to the collapse loads as shown in Figure 6-5, was found to be acceptable up to lengths of 186 mm and 500 mm for the BWR and PWR canisters, respectively. In the integrated base of the BWR insert, a 20 mm thickness reduction was examined, and the collapse load was greater than 100 MPa for all postulated volumetric defects in the base region of both the BWR and PWR inserts.

Table 6-4. BWR insert collapse loads with volumetric defects from Figure 6-4.

Geometry	Collapse load
Nominal geometry	90 MPa
Defect No 1, Ø75 mm	88 MPa
Defect No 2, Ø50 mm	89 MPa
Defect No 3, Ø30 mm	90 MPa
Defect No 4, Ø160 mm	85 MPa
Defect No 3, Ø20 mm with 10 mm offset steel cassette	82 MPa
BWR, integrated base (for the plate with the chamfered edge containing defects)	> 100 MPa

Table 6-5. PWR insert collapse loads with volumetric defects from Figure 6-4.

Geometry	Collapse load
Nominal geometry	109 MPa
Defect No 1, Ø180 mm	99 MPa
Defect No 2, Ø110 mm	105 MPa
Defect No 3, Ø35 mm	109 MPa
Defect No 3, Ø24 mm with 10 mm offset steel cassette	107 MPa
PWR, integrated base (for the plate with the chamfered edge containing defects)	> 100 MPa

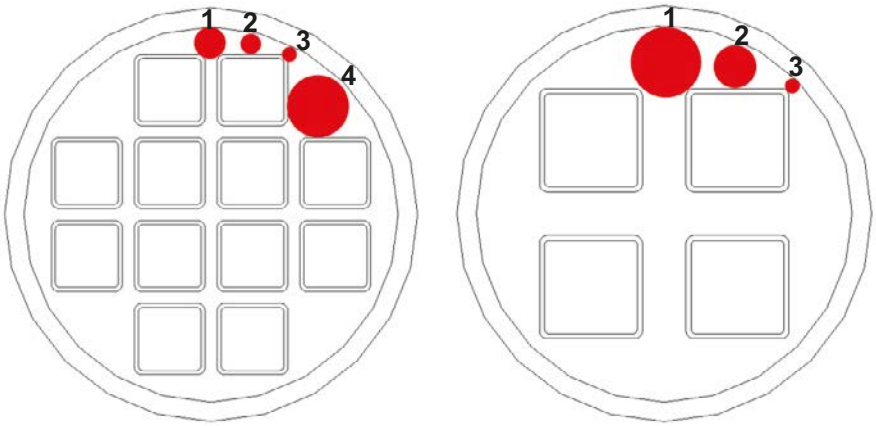

Figure 6-4. *Left: Schematic of the BWR canister cross section with analysed spherical volumetric defects in Table 6-4. Right: Schematic of the PWR canister cross section with analysed spherical volumetric defects in Table 6-5 (Alverlind 2016a).*

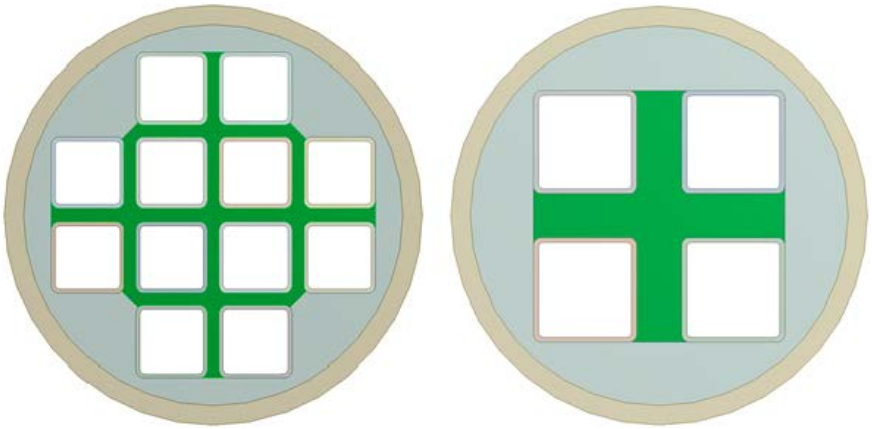

Figure 6-5. *Left: Schematic of the BWR canister cross section, with the green marked area showing the region where all the nodular cast iron material is removed 186 mm from the axial direction. Right: Schematic of the PWR canister cross section, with the green marked area showing the region where all nodular cast iron material is removed 500 mm from the axial direction (Alverlind 2016a).*

Because the magnitude of the stresses was found to only lead to elastic strains in the BWR and PWR inserts at the design load of 50 MPa, the simulated stress state was fully elastic. However, in reality, small plastic strains might exist in sharp corners and other stress concentration points. In Figure 6-6, the maximum principal stress is shown for the BWR, and in Figure 6-7, the maximum principal stress is shown for the PWR.

Damage tolerance analyses – crack-like defects

The acceptable defect size and the effects of other types of crack-like defects in various locations in the insert were examined by conducting a fracture resistance analysis, which is reported in Alverlind (2016a, b). The analysis was performed using the stress intensity factor K_I calculated in various locations for the postulated cracks, and the stress intensity was compared, using a safety factor of $10^{0.5} = 3.16$, with a reference value of the tested material property K_{Ic} at a temperature of 0 °C. In this load case, due to the predominantly elastic insert behaviour, a K_I-based method was instead of a nonlinear J-integral analysis to assess the risk of fracture. The use of the K_{IC} fracture toughness for materials known to exhibit ductile crack growth is a pessimistic assumption.

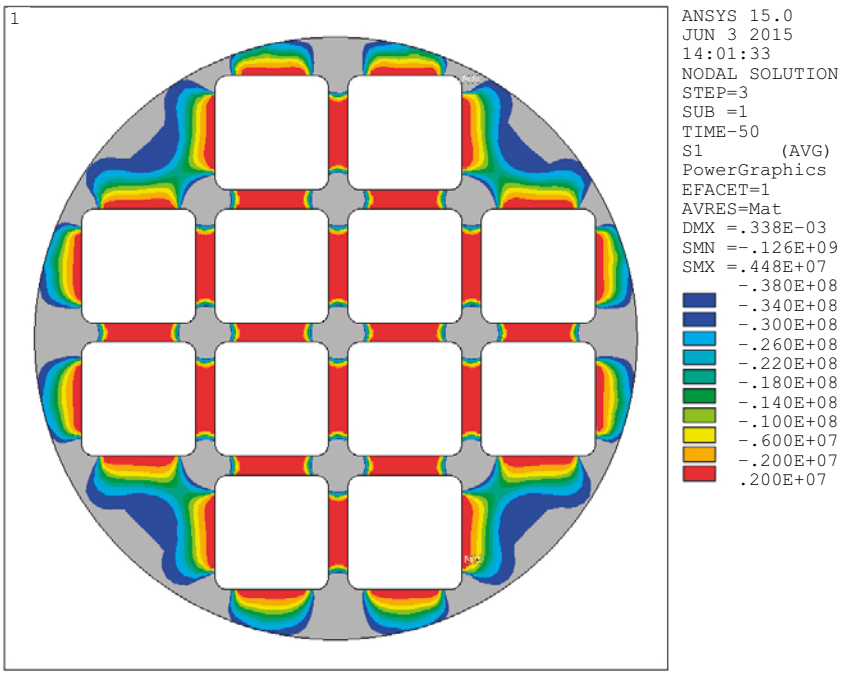

Figure 6-6. *BWR maximum principal stress [Pa] at a 50 MPa pressure load with the steel cassette offset by 10 mm. Red areas indicate the tensile stresses. No significant impact on the stress levels or distribution arises due to the offset of the steel cassette. All tensile and compressive stresses are elastic (Alverlind 2016a).*

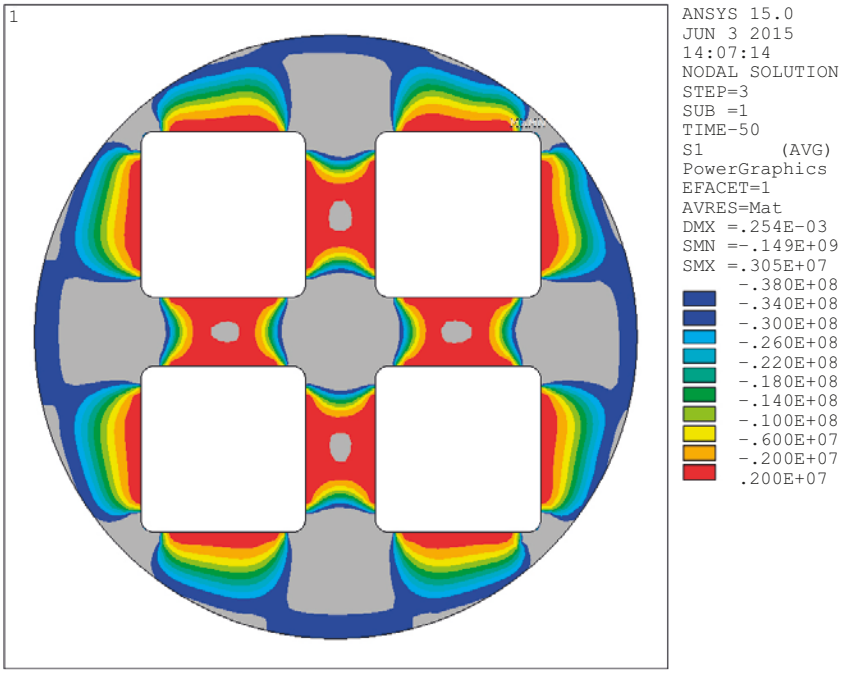

Figure 6-7. *PWR maximum principal stress [Pa] at a 50 MPa pressure load with the steel cassette offset by 10 mm. Red areas indicate the tensile stresses. No significant impact on the stress levels or distribution arises due to the offset of the steel cassette. All tensile and compressive stresses are elastic (Alverlind 2016a).*

In Alverlind (2016a), two routes of crack idealisations were considered: through-wall cracks and semi-elliptical surface cracks oriented with their main axes parallel to the length of the canister, as shown in Figure 6-8. Surface crack-like defects were originally assumed to progress from the inner surfaces of the cast iron and progress towards the outer boundary of the cast iron insert. In this analysis, through-wall cracks were also considered, that is, cracks that extend all the way through the wall thickness of the considered part of the component. The maximum principal stress (contributing to the growth of the postulated cracks) becomes compressive at short distances (~ 1–3 mm) from the steel tubes. At the surface of the iron insert, the stresses from the isostatic pressure load are always compressive.

For the integrated base of the BWR and PWR inserts, the acceptable crack depth was calculated to be > 80 % of the base thickness in the case when semi-elliptical surface cracks are postulated.

As shown in Figure 6-9, cracks are analysed in several positions for both the BWR and PWR versions of the canisters. In Figure 6-9, the cross sections of both types with the studied crack locations are marked with red lines. The locations are chosen such that the results will also be representative of other locations in the insert (for example, PWR crack position 4 is representative of all other locations between two steel tubes in the PWR insert). The postulated positions of the defects are chosen to comprehensively cover the cross sections of the inserts.

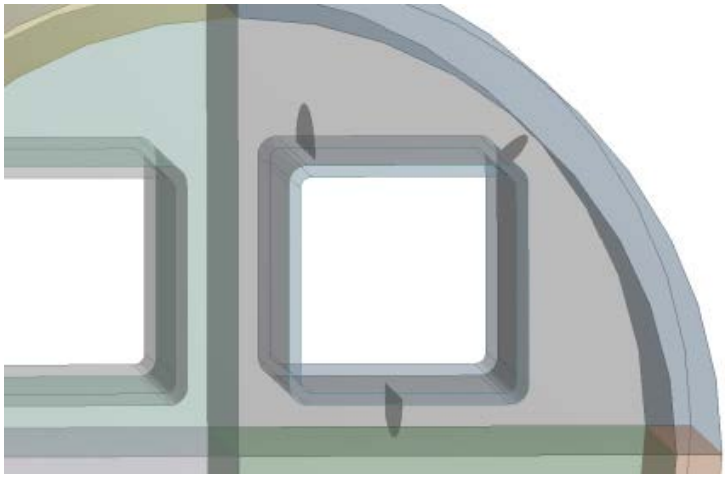

Figure 6-8. *Schematic 3D visualisation of three elliptical surface cracks in the PWR canister. The surface here is considered to be the surface of the cast iron at the interface with the steel channel tube.*

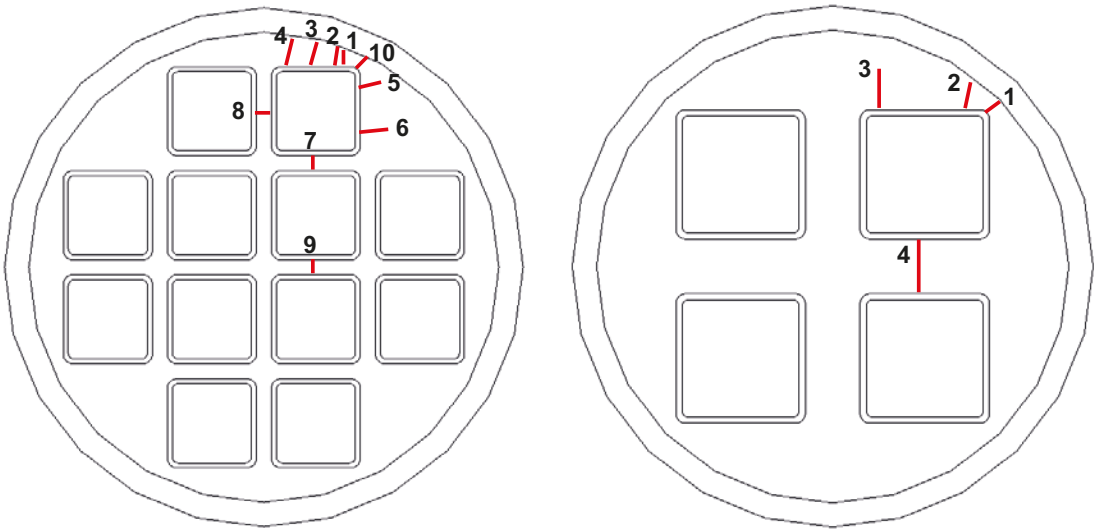

Figure 6-9. *Left: Schematic of the postulated BWR crack positions. Right: Schematic of the postulated PWR crack positions (Alverlind 2016a).*

The acceptable crack sizes in the nodular cast iron considering both a 50 MPa isostatic pressure to act as the primary stress and the residual stresses to act as the secondary stresses are summarised in Tables 6-6 and 6-7. The residual stresses are tabulated in Tables 7-7 and 7-8, and the influence of the residual stresses are further discussed in Section 7.4.2. The maximum length of a through-wall axial crack is 1 000 mm. The shortest axial length of a crack is located between the steel channel tubes in both the BWR and PWR inserts. The acceptable depth and length of the elliptical surface cracks were postulated in order to be consistent with the damage reported previously in Dillström et al. (2010). In Alverlind (2016a), through-wall cracks were also postulated. The acceptable crack length never exceeded 1 000 mm for any crack.

Table 6-6. Acceptable axial crack depths and lengths in the nodular cast iron BWR insert in Figure 6-9 considering the residual stresses.

	Elliptical surface crack		Through wall crack
Position	Crack depth (mm)	Crack length (mm)	Crack length (mm)
1	> 33.9	> 203.9	1 000
2	> 35.4	> 212.5	888.5
3	> 44.9	> 269.6	1 000
4	> 53.0	> 318.1	1 000
5	> 75.5	> 453.1	1 000
6	> 146.6	> 879.7	656.6
7	> 24.0	> 144.0	430.5
8	> 24.0	> 144.0	430.5
9	> 24.0	> 144.0	430.5
10	> 26.4	> 158.5	1 000

Note: Elliptical surface cracks were postulated in order to be consistent with the previous damage tolerance analysis by Dillström et al. (2010). In Alverlind (2016a), through-wall cracks were also postulated, which utilised less pessimistic assumptions. The postulated acceptable depths of the elliptical surface cracks in all cases are larger than 80 % of the wall thickness.

Table 6-7. Acceptable axial crack depths and lengths in the nodular cast iron PWR insert in Figure 6-9 considering the residual stresses.

	Elliptical surface crack		Through wall crack
Position	Crack depth (mm)	Crack length (mm)	Crack length (mm)
1	> 29.8	> 179.1	1 000
2	> 61.3	> 367.9	1 000
3	> 118.2	> 709.4	976.7
4	> 88.0	> 528.0	697.2

Note: Elliptical surface cracks were postulated in order to be consistent with the previous damage tolerance analysis by Dillström et al. (2010). In Alverlind (2016a), through-wall cracks were also postulated, which utilised less pessimistic assumptions. The postulated acceptable depths of the elliptical surface cracks in all cases are larger than 80 % of the wall thickness.

Pressure tests

Two destructive pressure tests were performed using two BWR canisters with insert lengths of 700 mm; the diameter was the actual one according to Chapter 5. The tested inserts were covered by a copper tube and lids with a normal thickness. The first sample was a knowingly poorly cast sample, which contained large defects, and the machining was performed with a 12 mm offset (eccentric) so that the steel cassette was not placed centrally. The second sample was one of the best available samples at that time (2004 –2005). The later developed BWR series (I53 –I57) had better quality (Leskinen and Ronneteg 2013). The first sample was pressurised in a pressure chamber until reaching a large plastic deformation of 20 mm at an external pressure of 130 MPa, and the second sample was pressurised until reaching full plastic collapse and rupture at an external pressure of 139 MPa. The testing was documented and reported in Nilsson et al. (2005).

The pressure tests were simulated with various FE-analyses and were found to match. This showed that the collapse pressure of the canister was remarkably high and that the strength of the canister insert could be predicted and simulated using numerical methods with good accuracy and reliability. The pressure tests and verification strength analyses have been widely reported, and their summaries are given in Dillström (2009a) and Martin et al. (2009).

The pressure test results show that the calculated collapse load results are pessimistic and thus verify the analysis models and reliability of the calculation methods for this type of analysis.

Case 5 – rock shear load

A number of global analyses have been performed over the years with different buffer properties, and different models for the bonds between the nodular cast iron, influence of the edge distance, level of detail in the geometry and density of the mesh, shear planes, and yield stress of the cast iron have also been investigated. A complete description of the analysed variants is presented in Section 7.6. The influence of the decreased edge distance (*H*) is not significant in the shear load case. From the perspective of the insert, the worst shear plane is located perpendicular to the canister axis at ¾ of the height from base.

In the second step, a damage tolerance analysis was performed by applying the following parameters: The shear plane was varied. The temperature of the materials was pessimistically assumed to be constantly 300 K (+27 °C) for the copper and 273 K (0 °C) for the cast iron. The properties of the bentonite were varied, with the values at saturation set to 1950, 2000, 2 022 and 2 050 kg/m^3, which meant that different material model parameters for the bentonite were used.

Rock shear analysis using a global model

The global model rock shear analysis was performed with a 3D-finite-element model using ABAQUS. Symmetric halves of the bentonite buffer, copper canister and cast iron insert were modelled. The model of the deposition hole has a diameter of 1.75 m and a length of 6.9 m. The canister is placed approximately 0.5 m above the bottom and approximately 1.5 m below the top of the deposition hole. Buffer material (bentonite) surrounds the canister, which will fill the deposition hole. The rock shear is then simulated by prescribing boundary conditions at the buffer envelope. The rock shear load was introduced using an applied displacement at the outer boundary of the bentonite buffer. The rock shear analyses are reported in Hernelind (2010, 2017b), which investigated the influence of a 10 MPa swelling pressure as an input for the damage tolerance analysis. The swelling pressure of the bentonite and the hydrostatic pressure of the groundwater (normally 5 MPa or up to 32 MPa under a glacial period) have been added to the actual rock shear load in various analysis cases. The glacial pressure load combined with rock shear load is not the governing load combination, but the combination of the normal hydrostatic pressure + bentonite swelling pressure + rock shear gives the largest impact on the canister. For details of the analysed cases for the damage tolerance analyses of the BWR and PWR inserts, see Hernelind (2010, 2017b).

For each analysis, many results are available; to provide an indication of the results, only a few values are reported here. The reported values all correspond to the case of 5 cm rock shear. However, the results are also available for larger shearing amplitudes in Hernelind (2010, 2017b). For the short-term rock shear analyses, the cross-sectional average and peak values for the von Mises effective stress, effective plastic strain (*PEEQ*) and maximum axial tension stress component S_{33} used for indicating the postulated crack location are summarised in Table 6-8 is as follows. The following is a short description of each model name in Table 6-8: All cases apply for the BWR insert if PWR is not stated. The shear plane location and the density of the buffer are stated. The reference cases “model6 g_newbentonite_quarter_2022” for the BWR and “model6 g_newbentonite_PWR_quarter_2022” for the PWR are highlighted in yellow because these cases form the basis of the damage tolerance analyses of the BWR and PWR inserts. These cases have the highest S_{33}, an entity to which the acceptable defect sizes are sensitive, and they represent the normal rock shear case without glacial pressure.

The square steel tubes are modelled separately in this set of analyses.

Table 6-8. Summary of the results for the insert and channel tubes (Hernelind 2017b). The models highlighted in yellow are used in the damage tolerance analysis of the BWR and PWR inserts for the rock shear case.

Model name	1–nodular cast iron 2–steel channel tubes	PEEQ (%)		Mises (MPa)		S33 (MPa) maximum axial stress
	Shearing (cm)	5		5		5
	Insert material	1	2	1	2	1
model6 g_newbentonite_quarter_2050		0.59	0.99	324	334	334
model6 g_newbentonite_quarter_2022		0.45	0.54	318	329	329
model6 g_newbentonite_quarter_2000		0.34	0.37	311	324	324
model6 g_newbentonite_nintypercent_2050		0.18	0.28	302	308	308
model6 g_newbentonite_nintypercent_2022		0.12	0.12	300	305	305
model6 g_newbentonite_nintypercent_2000		0.08	0.05	298	304	304
model6 g_newbentonite_lid_2050		0	0	143	88	88
model6 g_newbentonite_lid_2022		0	0	128	84	84
model6 g_newbentonite_lid_2000		0	0	117	80	80
model6 g_newbentonite_PWR_quarter_2050		0.52	0.34	320	327	327
model6 g_newbentonite_PWR_quarter_2022		0.39	0.21	314	322	322
model6 g_newbentonite_PWR_quarter_2000		0.24	0.08	307	315	315

Figure 6-10 shows axial stress S_{33} in the insert for a 5 cm rock shear load perpendicular to the canister axis at 75 % of the insert height: BWR insert, buffer density of 2 022 kg/m^3, model name "model6 g_newbentonite_quarter_2022". This is a typical stress plot of the insert.

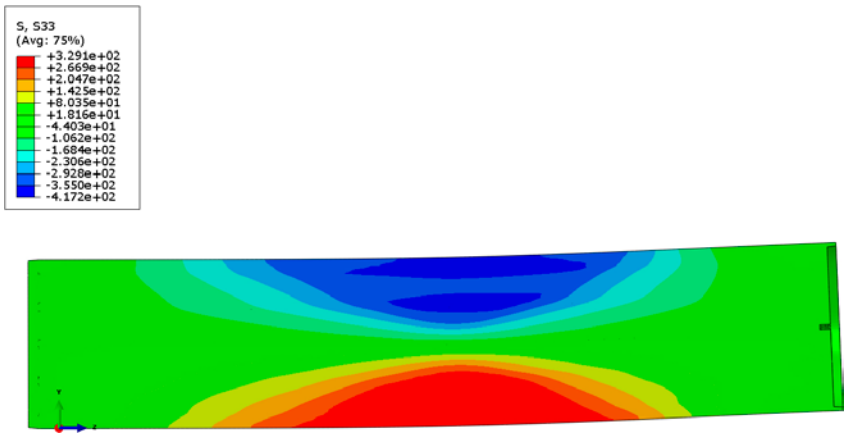

Figure 6-10. *Axial stress S_{33} [MPa] in the BWR insert for a 5 cm rock shear load perpendicular to the canister axis at 75 % of the insert height: buffer density at saturation of 2 022 kg/m^3 and "model6 g_newbentonite_quarter_2022" (Hernelind 2017b).*

It should be noted that the mesh of the finite elements in the model has an impact on the calculated stresses and strains. To evaluate the impact of the mesh and details in the inserts, a comparison was made in Dillström (2015a) between the original global model in Hernelind (2010) for the BWR insert (using a simplified idealisation of the geometry) and the more detailed and advanced model in Hernelind (2014 d) modelled separately from the insert. A similar comparison of the model in Hernelind (2010) and the detailed PWR global model from Hernelind (2015b) was made in Dillström (2015b).

The comparison between the analyses shows that all detailed models have locally higher stresses than the original model in Hernelind (2010). The reason for these high stresses is mainly related to the element meshes, which are not designed to be used in a damage tolerance analysis. For example, many stress concentrations are directly related to the use of wedge elements. In all cases, disregarding the elements that behave poorly significantly reduces the locally higher tensile stresses. There are also regions with slightly elevated stress concentrations, but they are of minor importance because the neighbouring elements have significantly lower stresses. In Figure 6-11 for the BWR insert and Figure 6-12 for the PWR insert, S_{33} is shown; the influence of the elements that behave poorly is omitted in the figures. Additionally, the impact of the manufacturing tolerances is evaluated, where the edge distance is decreased for both the BWR and PWR.

The original global model from Hernelind (2010) and all later global models have axial stresses of the same magnitude in the most important region for the damage tolerance analysis. The maximum strain value in the cast iron insert is less than 1 % in the design rock shear load case of 5 cm. In the square tubes made of steel, the maximum strain is thus approximately 1 % in the rounded corners.

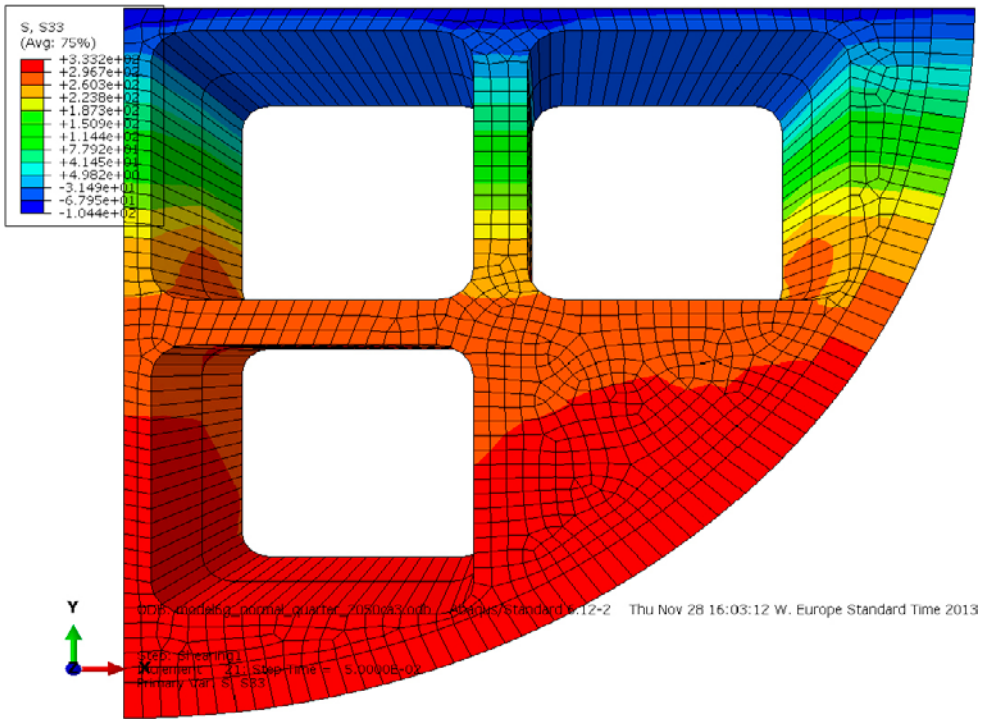

Figure 6-11. *Axial stress S_{33} [MPa] in the BWR insert for a 5 cm rock shear load perpendicular to the canister axis at 75 % of the insert height and a buffer density at saturation of 2 050 kg/m^3. For the detailed BWR model, see Dillström (2015a).*

The rock shear case has also been investigated in terms of the mechanical response at the steel lid (Hernelind 2014e). One shear plane is located at the steel lid at its upper edge, representing the most pessimistic location with respect to the steel lid, and the second shear plane is the reference case in which shearing occurs at 75 % of the insert height. The simulations have different preloadings applied to the screw. The copper gasket under the M30 screw head has been modelled, and the valve in the steel lid has been simply modelled as a hole in the lid. No strength contribution from the valve has thus been considered.

The main difference in the mechanical response of the FE model with the steel lid bonded at the insert, as in Hernelind (2010), compared with a screwed lid occurs in the area around the M30 screw. The copper washer in the screw joint is considerably plastically deformed due to the tension in the screw. The copper washer also affects the mechanical response of the steel lid. The simulations in which the copper washer is omitted exhibit slight slippage between the insert and the steel lid when the prestrain is too low in the screw. This causes the screw to come in contact with the walls of the screw hole in the steel lid. The plastic strain of 6 % is very local in the screw, far less than the elongation of the steel of 23 % under these conditions. In the simulations, only elastic stresses occur in the steel lid. The effect of a broken steel lid was also investigated in Hernelind (2016b). With the very pessimistic postulated defects, the mechanical response does not threaten the mechanical integrity of the canister. A damage tolerance analysis of the steel lid has also been conducted in Barslivo and Jansson (2016). The investigated load cases and design of the screw bond indicated that the steel lid is a very robust part of the canister. The conclusion is that the calculations based on the simplifications used by Hernelind (2010) provide relevant results, and there is no significant difference between these results and the those of the FE-models. It is further concluded that the mechanical response at the steel lid of the insert is such that the mechanical integrity of the canister is not at risk of rock shearing, so the possible defects left from the steel lid manufacturing process can be disregarded.

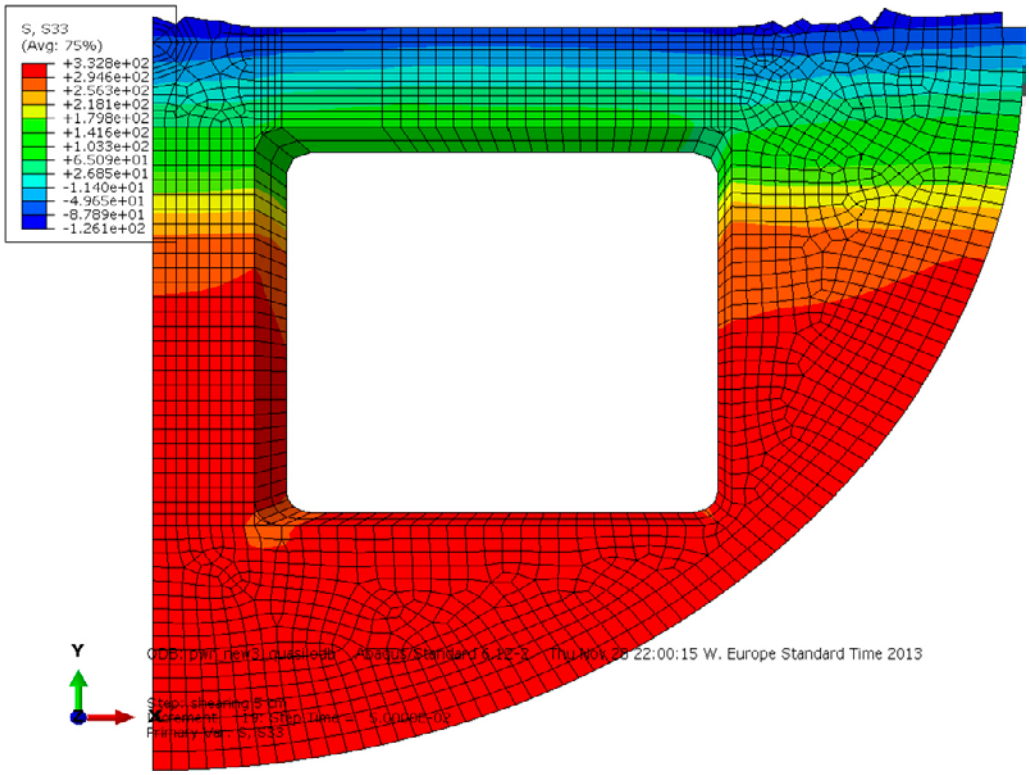

Figure 6-12. *Axial stress S_{33} [MPa] in the PWR insert for a 5 cm rock shear load perpendicular to the canister axis at 75 % of the insert height and a buffer density at saturation of 2 050 kg/m³. For the detailed PWR model, see Dillström (2015b).*

Requirements of ductility in the insert

The cross sections of the BWR and PWR inserts will be loaded with bending stresses, as shown in Figure 6-11 and Figure 6-12. The magnitudes of the stresses show that the nodular cast iron will reach plastic deformation at a distance approximately of 100 mm from the centre point. In Dillström (2017), the requirements of the plastic strain in the nodular cast iron were derived. The magnitude of the plastic strain is moderate, a maximum of 0.5 % and 1.7 % at a 5 cm and 10 cm rock shear magnitude, respectively, for both the BWR and PWR inserts. Considering the safety factor $S_f = 3.16$ derived from ASME XI, a reasonable requirement for the ductility is a minimum of 3 % true plastic strain for the nodular cast iron and steel channel tubes at a distance of 100 mm or more from the centre point of the insert cross section At distances smaller than 100 mm from the centre point, there are no requirements for the ductility.

The assessment of the triaxial stress state in the nodular cast iron material and its effect on the damage tolerance of the canister inserts was conducted in Shipsha (2014). The results demonstrate that the ductile properties of the nodular cast iron under a shear-dominated stress state can be compared with the ductility measured from uniaxial cross-section tensile tests. The effect of triaxiality is of minor importance for most load cases experienced by the nodular cast iron inserts. The deviatoric stress state appears to have an insignificant influence on the effective plastic strains at failure. The presented results also suggested that the nodular cast iron ductility is dependent only on T and is independent of the deviatoric stress state (L). It was concluded in Hernelind (2010) that there is no need to refine the performed analyses of the nodular cast iron inserts where the combination of the isostatic and shear loads is considered.

For the rock shear load case, the stress state was approximately characterised using $T = 0.36$ and Lode parameter $L = –0.88$, which corresponds to the stress state for axisymmetric uniaxial tension ($T = 0.33$ and $L = –1$). The stress state in the tensile test specimen is in agreement with the stress state in the full-scale insert. Therefore, it is justified to evaluate tensile test specimens to characterise the ductility of the nodular cast iron.

Damage tolerance analysis of the canister insert during the rock shear case

The displacement results of the rock shear case from the global model were post-processed in greater detail using higher-order elements in the local submodels. All submodels comprised 20 node brick elements with reduced integration (C3D20R), including defects for the BWR and PWR inserts (see Dillström 2017).

The results, presented below, were obtained using the different submodels with defects. The ABAQUS domain integral method was used to calculate the J-integral. The submodel was placed such that the defect was located where the highest principal stress was identified. The results show that the density of the bentonite clay does have an effect mechanical behaviour. A higher swelling pressure leads to a higher density and higher shear stiffness, which in turn yields higher J-values. As expected, the elliptical surface defects give much higher J-values than the circular surface defects, considering approximate total size of the cracks. The internal defects do not yield J-values as high as the surface defects. These trends between the different types of defects correspond to the handbook solutions for simpler geometries and loading conditions. In Figure 6-13, the placement of a corner submodel relative to the global model is shown.

The dross (slag) defects found on the fracture surfaces of the tensile test specimens from the trial-manufactured BWR inserts I53–I57 and PWR inserts IP23–IP25 were investigated in Dillström and Alverlind (2014). The justification of the postulated aspect ratio for the crack-like defects is derived from the statistics of the slag/dross defects in Bolinder et al. (2017). As a result, the aspect ratio of the defects is approximately (*length l = 2c)/ (depth a)* = 2.5. This fact has been used to determine the acceptable and critical defect sizes for the crack-like defects; a semi-elliptical surface defect with an aspect ratio of $2c = 2.5a$ is used. This was derived from the mean value of 1.81 plus one standard deviation (0.71) from the defect shape data, that is, 1.81 + 0.71 = 2.5.

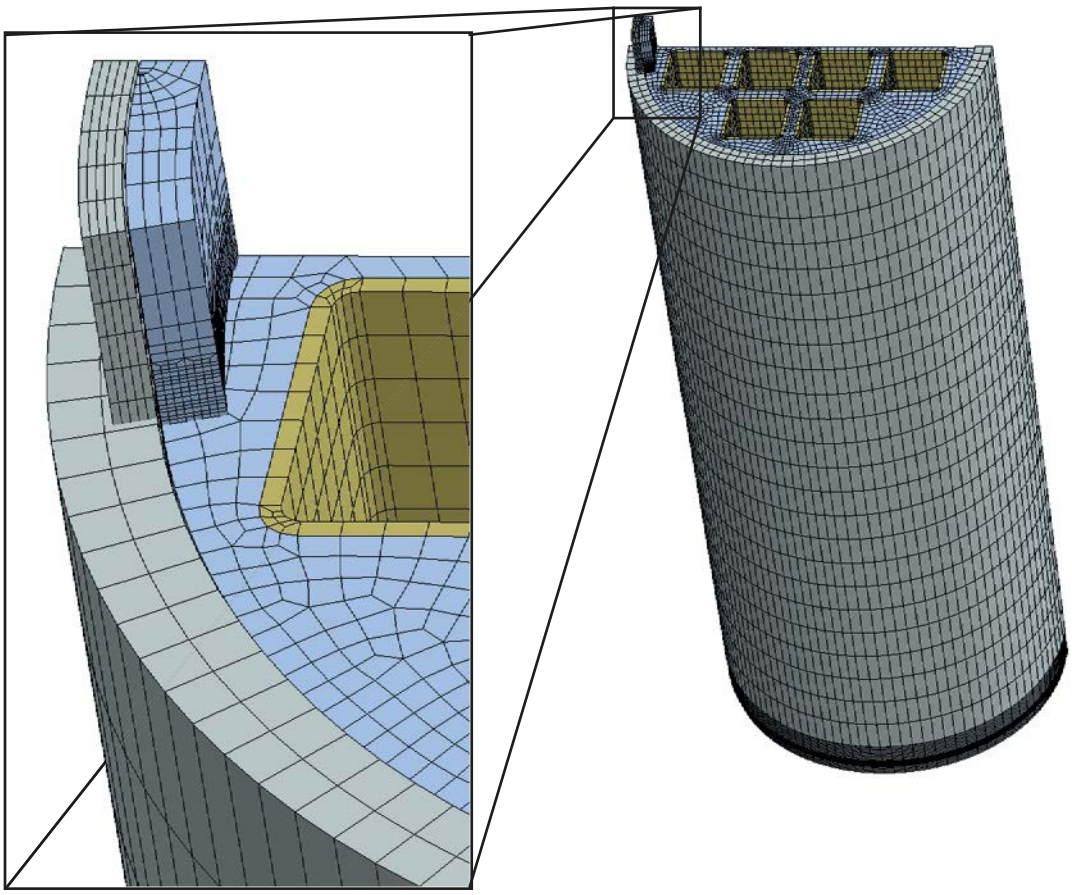

Figure 6-13. *Example of the placement of a submodel relative to the global model (Bolinder et al. 2017).*

Therefore, the assumption regarding the shape of the postulated crack-like defects is to use defect length/depth = 2.5. Below is a summary of the examined cases.

- Semi-elliptical surface crack defects located in the tangential-radial direction.
- Channel tube corner crack located in the tangential-radial direction.
- Acceptable internal crack-like defects located in the tangential-radial direction, near the outer surface of the insert.
- Acceptable internal crack-like defect of the PWR insert located between the steel cassette tubes in the tangential-radial direction.

During the damage tolerance analysis with the postulated defects, the critical defect size is given using the failure criterion $J = J_{mat}$, and the acceptable defect size is given using the criterion $J = J_{mat}/ SF_j$ in (Equation (3-4)). In these equations, J is the applied J-value, as given in Bolinder et al. (2017). The fracture toughness of the cast iron used in the insert (with or without some stable crack growth) is $J_{mat} = J_{2mm} = 88$ kN/m for the BWR and $J_{mat} = J_{2mm} = 78$ kN/m for the PWR. A safety factor (SF_j) of 2 is used when calculating the acceptable defect size, according to the ASME Code for a postulated emergency or faulted condition (level C or D). The assessment guidance for the actual detected indications is given in Bolinder et al. (2017).

As presented in the previous study on the BWR canister (Dillström et al. 2010) and previous studies on the PWR canister in Dillström et al. (2014), the cast iron shows predominantly ductile fracture behaviour. This means that the material does not seem to exhibit a brittle fracture process when J reaches the initiation toughness $J_{mat} = J_{Ic}$. Instead, the material experiences stable crack growth. According to Brickstad (2009), it is reasonable to use a toughness value of 2 mm for stable crack growth in a ductile material, which is especially true in this case because the inserts are subjected to short-term displacement-controlled loading (which is not a force control load and therefore may be considered to be a secondary load). This justifies that J_{mat} should be equal to J_{2mm} in this case.

In Figure 6-14, the acceptable surface crack depth as a function of the axial position for the BWR and PWR inserts with a density at saturation of 2 022 kg/m^3 is shown.

In Table 6-9, the acceptable maximum surface defect sizes in the BWR canister with buffer densities at saturation of 2 022 kg/m^3 and 2 050 kg/m^3 are presented.

Table 6-9. The calculated maximum acceptable defect sizes of semi-elliptical crack-like defects (semi-elliptical, 2c = 2.5a) and the critical defect sizes. The defects are located in the tangential-radial direction. 5 cm rock shear at 75 % of the insert height. BWR insert.

Insert, buffer density		
	Acceptable defect depth a (mm)	**Acceptable defect length 2c (mm)**
BWR – 2 022 kg/m^3	9.0	22.5
BWR – 2 050 kg/m^3	7.4	18.5
	Critical defect depth a (mm)	**Critical defect length 2c (mm)**
BWR – 2 022 kg/m^3	18.0	45.0
BWR – 2 050 kg/m^3	14.8	37.0

In Table 6-10, the acceptable maximum surface defect sizes in the PWR canister with buffer densities 2 022 kg/m^3 and 2 050 kg/m^3 are presented.

Table 6-10. The calculated maximum acceptable defect sizes of semi-elliptical crack-like defects (semi-elliptical, 2c = 2.5a) and the critical defect sizes. The defects are located in the tangential-radial direction. 5 cm rock shear at 75 % of the insert height. PWR insert.

Insert, buffer density		
	Acceptable defect depth a (mm)	**Acceptable defect length 2c (mm)**
PWR – 2 022 kg/m^3	9.0	22.5
PWR – 2 050 kg/m^3	7.0	17.5
	Critical defect depth a (mm)	**Critical defect length 2c (mm)**
PWR – 2 022 kg/m^3	18.0	45.0
PWR – 2 050 kg/m^3	14.0	35.0

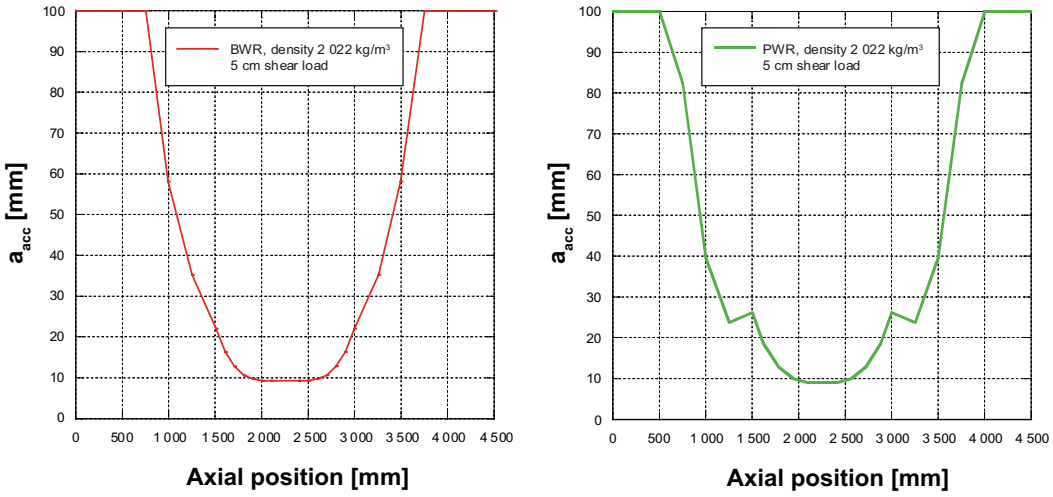

Figure 6-14. *Left: Acceptable surface defect size for the canister with a density of 2 022 kg/m^3 as a function of the axial position ($a_{acc,\ min}$ = 9.0 mm). Left: BWR insert. Right: PWR insert. (Bolinder et al. 2017).*

In Table 6-11, the acceptable crack-like depths for channel tube corner cracks in the BWR and PWR canisters with buffer density of 2 022 kg/m^3 are presented for 5 cm rock shear.

Table 6-11. Acceptable crack-like depths for the channel tube corner cracks located in the tangential-radial direction in the BWR and PWR inserts. 5 cm rock shear at 75 % of the insert height.

Insert, buffer density	Acceptable defect depth (mm)
BWR – 2 022 kg/m^3	12.8
PWR – 2 022 kg/m^3	17.2

The acceptable internal defects are summarised in Tables 6-12 and 6-13.

Table 6-12. Acceptable internal crack-like defects located in the tangential-radial direction near the outer surface of the insert for the BWR and PWR inserts using a defect shape = 2.5.

Insert, buffer density	Acceptable defect depth $2a_{acc}$ (mm)	Acceptable defect length 2c (mm)
BWR – 2 022 kg/m^3	20.7	25.9
PWR – 2 022 kg/m^3	22.7	28.4

Table 6-13. Acceptable internal crack-like defects located between the steel cassette tubes in the tangential-radial direction for the PWR inserts using a defect shape = 2.5.

Insert, buffer density	Acceptable defect depth $2a_{acc}$ (mm)	Acceptable defect length 2c (mm)
PWR – 2 022 kg/m^3	29.6	37.0

Investigations of the largest acceptable defect sizes located between the steel cassette tubes were performed in Andersson et al. (2016). The safety factors were applied according to ASME XI, as described in Section 3.3.2. The geometry of these acceptable defects is given in Figure 6-15. The conclusion was that very large internal crack-like defects can be accepted as shown in Figure 6-15 and by using the applied approach with the ASME code to determine the acceptable defect sizes.

Summary-nodular cast iron insert

The acceptable sizes of the radial and axial cracks in the BWR and PWR nodular cast iron have been determined. Defects located on the channel tube corners in the steel cassette and between the steel tubes have been investigated in detail. The acceptable size of the radial surface crack-like defects is also determined as a function of the axial position. The plastic strain requirements in the nodular cast iron were also determined, and it was justified to evaluate the tensile test specimens to characterise the ductility of the nodular cast iron.

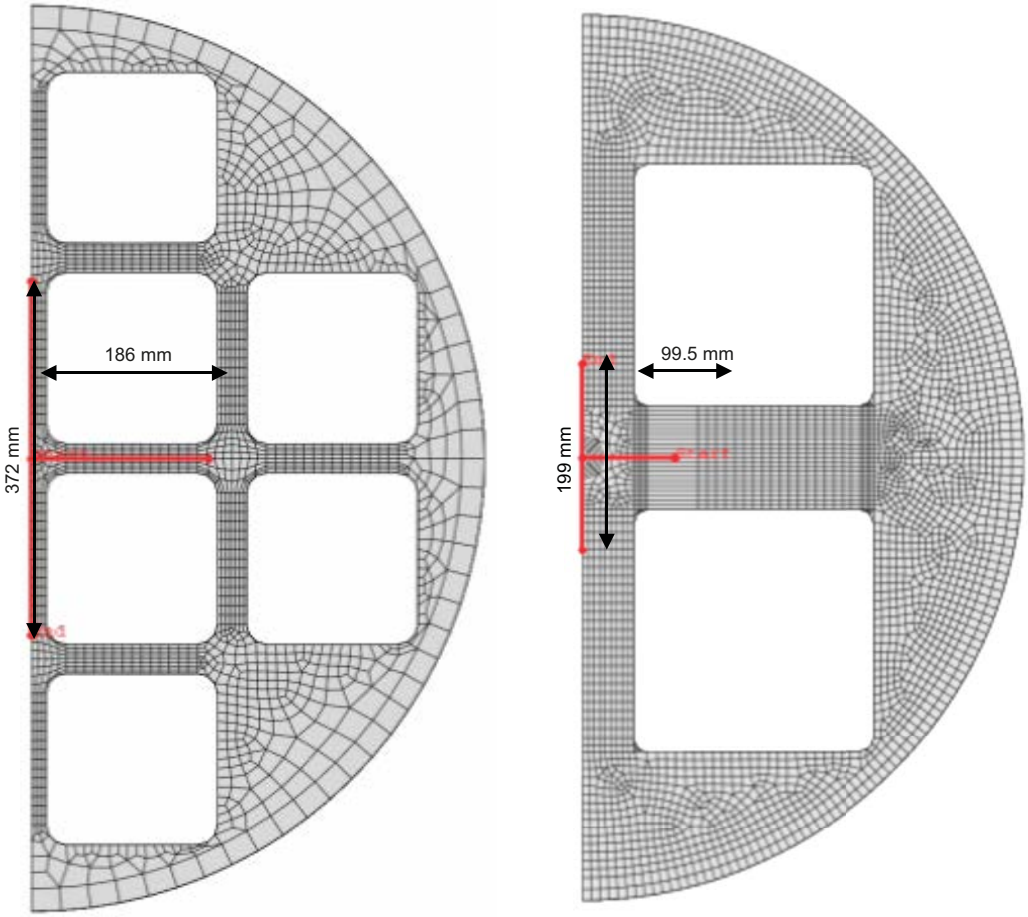

Figure 6-15. *Left: Cross section of the BWR insert. The acceptable defect size is indicated in red, with a defect length parameter equal to 372 mm. Right: Cross section of the PWR insert. The acceptable defect size is indicated in red, with a defect length parameter equal to 199 mm (Andersson et al. 2016).*

The results obtained from the rock shear analyses are summarised as follows:

- The maximum principal stress in the insert mainly originates from bending the canister; the level mainly depends on the shearing magnitude, the properties of the buffer and the location of the shear plane.
- The rock shear plane perpendicular to the canister axis at 75 % of the insert height leads to the highest stresses in the BWR and PWR inserts. The mechanical responses and stress level are approximately the same for both the BWR and PWR.
- Plastic strains in the BWR and PWR inserts occur approximately at the most loaded cross section in the middle of the axial direction. The steel cassette tubes were modelled separately in the global model.
- The support plates constitute a geometrical constraint between the cast iron and steel cassette; the support plates are not crucial for the post-closure integrity of the inserts.
- The variations in the yield stress from manufacturing the nodular cast iron are not significant for the rock shear case.
- The decreased edge distance is not critical for the rock shear case.
- The steel lid design is very robust, and possible defects from manufacturing the steel lid can be disregarded.
- Other loads acting simultaneously with the shear load do not influence the result negatively. The other loads increase the compression stresses of the insert, so the damage analysis would not lead to smaller acceptable defect sizes.

- The rock shear case is a governing load case in terms of the ductility requirements in the nodular cast iron and sizes of the tangential-radial cracks. Very large cracks can be accepted between the steel channel tubes.
- According to Dillström (2014a), it is more likely that the insert will fail due to crack growth than due to global plastic collapse at a 5 cm rock shear load. Dillström (2014a) also studied the probability of failure for 1-10 cm shear movements. The probability for failure of an insert with a rock shear magnitude of 5 cm is in the range of 5.8×10^{-4} to 2.2×10^{-3} in terms of crack growth and, the probability for global plastic collapse is in the range of 5×10^{-14}.

6.2.2 Loads on steel lid

The steel lid is a part of the insert, and its purpose in the final repository is to support the copper shell in terms of the mechanical loads. The isostatic load case has been investigated in Alverlind (2010), and the analyses show that the collapse load of the insert and screw-fastened steel lid is clearly more than 1.5 times the design pressure of 50 MPa. The consequences of the rock shear case with buffer densities at saturation of 2 022 kg/m^3 and 2 050 kg/m^3 were investigated in Hernelind (2014e, 2016b). In Hernelind (2016b), it was stated that only elastic deformation in the steel lid occurs.

According to the design requirements for the canister, the steel lid material S355J2G3 will be manufactured from hot-rolled plates in accordance with standard SS-EN 10025-2:2004. The manufacturing method of the steel lid material entails the risk of defects in the form of laminations in the plate. Conventionally, those types of defects are characterised using non-destructive testing methods, and the acceptable defect margins are determined with the aid of fracture mechanical analyses. As an alternative to this approach, worst-case defects may also be postulated. In Barslivo and Jansson (2016), the consequences of the following defects in the lid were studied:

- The defects are consistent, and the lid is split into two completely separate structures, as investigated in Hernelind (2016b). Regardless of the probability of the manufacturing defects, the split of the lid is assumed to occur in two perpendicular planes – parallel or across the thickness.

Considering the design prerequisites for the canister and required function of the steel lid in the final repository, the steel lid would meet the functional requirements even if considered to be two completely separate segments. This is mainly due to the following, according to Barslivo and Jansson (2016):

- The steel lid is constrained by the insert and copper lid. There is no gap in the radial direction between the steel lid and insert. The axial gap to the copper lid is negligible.
- The steel lid is very stiff in all directions relative to the adjacent structures.

With those conditions, the lid will maintain sufficient support, behaving as one piece, and provide the necessary support to the surrounding substructures.

The impacts of a segmented lid on the existing stress and strength for the canister are expected to be negligible. A redistribution of the stresses in which the lid is aligned against the chamfered surface of the inserts is expected. However, the impact on the stress amplitudes would be negligible. Thus, the impact of the assumed worst-case defects in the lid would be negligible for the integrity of the adjacent substructures. In conclusion, the effects of a very pessimistic postulated broken steel lid on the integrity of the copper shell and insert are negligible, and the steel lid is a very robust part of the canister.

Therefore, possible defects from manufacturing the steel lid can be disregarded.

6.2.3 Loads on the steel cassette

In Manngård and von Feilitzen (2017), the requirements pertaining to the functional or structural behaviour of the steel components, individually or in assemblies and under different load situations, are stated. The requirements cover various loads on the steel components, from those appearing during the manufacturing stages of the inserts and canisters to those during the final deposition of the canisters. It is concluded that the same criterion as for the nodular cast iron of at least 3 % true plastic strain shall be fulfilled in the steel channel tubes after casting.

The damage tolerance analyses of the insert using different modelling assumptions (idealisations) for the insert-to-channel-tube interface yield approximately the same stress magnitudes in the governing regions for the damage tolerance analysis. Interfacial modelling between the nodular cast iron insert and steel channel tubes, including the support plates, is hence assessed to not be critical for the damage tolerance analysis of the inserts. This conclusion is valid for both the isostatic pressure and rock shearing load cases. Hence, the performance of the support plates and other steel parts welded with the steel tubes is not critical with respect to the mechanical load cases in the final repository and, thus, not for the mechanical integrity of the canister.

The overall conclusion is that the existing calculations of acceptable defect sizes for the BWR and PWR inserts are assessed to be unaffected by the steel component requirements defined in Manngård and von Feilitzen (2017).

6.2.4 Loads on the copper shell

The copper shell surrounding the canister insert is not predominantly a load-carrying structure. In the copper shell, slits exist between the cylindrical part and lid and between the cylindrical part and base after welding the canisters without an integrated base. When the copper shell is loaded, these slits may contact each other and close, giving rise to stress concentrations. Moreover, the worst achieved strains and stresses occur in the slit bottom. The geometry of the top and welded base of the copper shell is shown in Figure 6-16, and Figure 6-17 shows the submodel geometries in the FE model for the slit bottom (plane and curved bottom) (Unosson 2017). The width of the slit in the FE-model is 160 µm, which is larger than the 10 µm slit measured in the full-scale welds in Reuterswärd (2015).

Different reports have represented the slit geometries in different ways (see Hernelind 2010, 2014a, f, 2017a, c, Unosson 2017 and Jin and Sandström 2013). In Hernelind (2014a, f), a small 3 mm joint-line hooking root defect in the weld was also modelled. In all of these cases, it is clear that the achieved strains and stresses are influenced by the geometry in the FE model and the mesh density of the finite element discretisation.

Figure 6-16. *The FE model of the slits at the top of the canister (left) and welded base (right) without the root defect. The tips of the arrows indicate the bottoms of the slits where the worst strains and stresses usually occur.*

Figure 6-17. *Submodel geometries for the slit bottom (plane and curved bottom). The width of the slit is 160 µm, and the entire submodel geometry is approximately 2 × 2 mm^2 (Unosson 2017).*

Effects of an uneven swelling pressure

Due to uneven wetting, the rock contours and the bentonite density distribution, uneven swelling pressure on the canister can occur, as identified in Chapter 2 as load cases 1a, 1b, 1c, 2a, 2b and 2c. The asymmetric outer pressures in cases 1a and 2a cause the canister to bend and thereby primarily affect the bending stresses of the insert. Because of the external outer pressure, the copper shell collapses against the insert. Thereafter, the insert supports the mechanical strength of the copper shell, and the deformation of the copper shell can be derived as the sum of the strain caused by the external pressure and the small bending of the copper shell. However, cases 1b, 1c, 2b and 2c affect the copper shell, causing uneven loading in the axial direction and thus giving rise to significant deformation in the copper.

Cases 1a and 2a – asymmetric loads on the canister before and after full bentonite water saturation

Uneven horizontal swelling pressure on the canister caused by a banana-shaped deposition hole in combination with the most unfavourable stress situation in the buffer will bend the canister. This case has been conducted using the finite element method in Börgesson and Hernelind (2013), considering a hole with curvature δ_1 = 8 mm, as shown in Figure 2-4.

The plastic strain *PEEQ* in the copper shell is judged to be moderate in this case. In the simulation in Börgesson and Hernelind (2013), the plastic strain *PEEQ* in the copper shell was found to be in the range of 4 %, which is a moderate strain compared to strains that the rock shear load may result in, as shown below.

Cases 1b and 1c – radial swelling pressure at the outer surface of the copper lid flange and buffer swelling along the canister

Cases 1b and 1c were studied in Hernelind (2014f). The buffer swelling along the canister also creates shear forces on the outer surface of the copper shell. The distribution of the axial shear stresses must be in equilibrium (if the gravity load is neglected, half the length of the copper shell surface has shear stresses pointing upwards and the other half has shear stresses pointing downwards). The most pessimistic assumption is that the shear stress reaches its maximum value and has a constant magnitude along the surface of the canister of 1.75 MPa (Börgesson et al. 2010), which corresponds to the shearing capacity of the buffer.

The load case was further investigated in Hernelind (2017a). One of the targets was to investigate if the loading is controlled by forces or displacements. Another issue of concern was whether a creep material model is needed for the copper shell or if elastic-plastic modelling of the copper material could be used. This was determined by analysing the case with the Swerea-KIMAB and KTH creep model during 1 000 000 years and comparing the achieved inelastic strain *CEEQ* values with the *PEEQ* values that were results from the elastic-plastic analyses in Hernelind (2014f).

The highest value of the plastic strain *PEEQ* in the copper shell of 6.2 % occurs in case 1c, as shown in Figure 6-18. The *CEEQ* was found to be 5.2 % in Hernelind (2017a). Case 1b results in very similar plastic strains, 5 % for *PEEQ* and *CEEQ*, regardless if creep is included in the analysis or not. The maximum *PEEQ* occurs in the base weld of the copper shell, but the top of the copper shell also has a higher magnitude for this case because the support from the insert is lost. Figure 6-18 shows the plastic strain for the top of the copper shell. In case 1b, the swelling pressure is only applied at the top, and in case 1c, swelling pressure is applied at the top, and swelling pressure and shear stress are applied on the outer copper shell surface. Figure 6-19 shows the plastic strain for the base of the copper shell of cases 1b and 1c.

The small differences between the results, considering creep during 1 000 000 years and the elastic-plastic analyses, lead to the conclusion that it is reasonable to consider these cases as displacement-controlled with respect to the copper shell. The deformation developed in the copper shell is small and does not threaten the integrity of the canister.

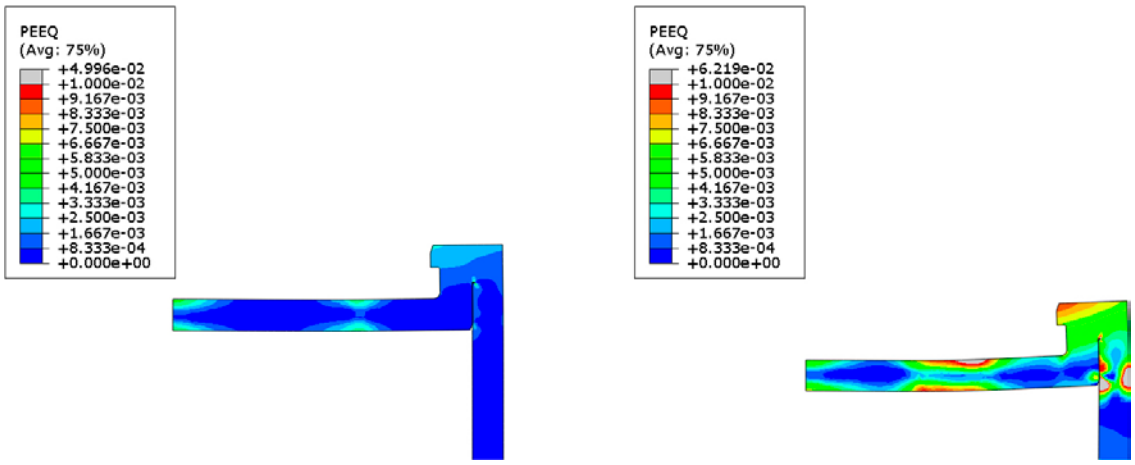

Figure 6-18. *PEEQ in the copper shell top. In case 1b, swelling pressure is only applied at the top (left), and in case 1c, swelling pressure is applied at the top, and swelling pressure and shear stress are applied on the outer copper shell surface (right) (Hernelind 2014f).*

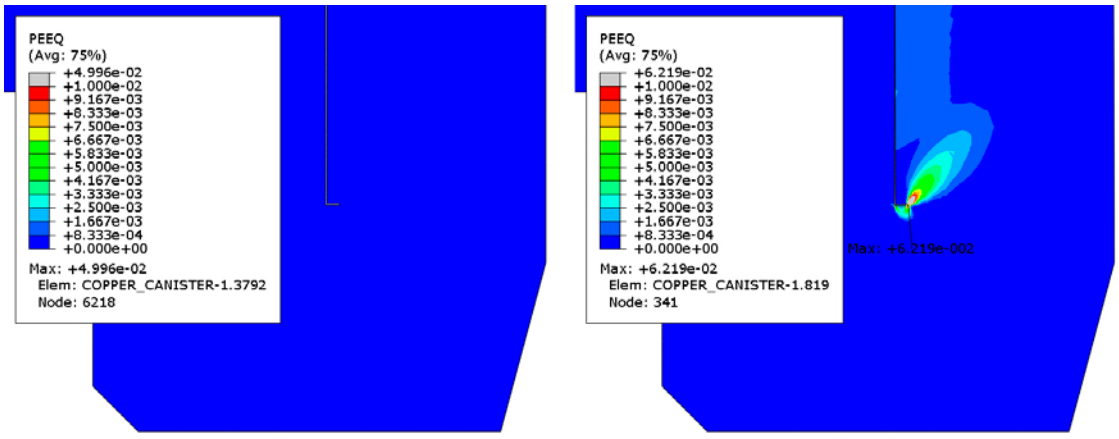

Figure 6-19. *Effective plastic strain (PEEQ) in the welded copper-shell base. In case 1b, swelling pressure is only applied at the top (left), and in case 1c, swelling pressure is applied at the top, and swelling pressure and shear stress are applied on the outer copper shell surface (right).*

Cases 2b and 2c – uneven vertical stresses caused by vertical density gradients in the buffer

Cases 2b and 2c for a permanent inhomogeneous buffer after full water saturation were investigated in Hernelind and Börgesson (2018).

The maximum true plastic strain in the copper is 1.6 % for case 2b. Case 2c features an uneven vertical density distribution for a simplified geometry without any welds with a shear stress of $\tau = 0.77$ MPa, and thus, no plastic strain occurs. The conclusion is that the integrity of the copper shell is not threatened.

Cases 3 and 4 – isostatic pressure load

The canister is exposed to an external pressure of approximately 15 MPa at a temperature of approximately 75 °C after its disposal. When the glacial load occurs after 50 000 years or later, the magnitude of the isostatic pressure increases to 50 MPa, and the temperature is in the range of 0–20 °C. The isostatic cases are dominated by primary loads; that is, the cases are forced controlled with respect to the insert but not to the copper shell.

Radial and axial gaps exist between the cast iron insert and copper shell. When an external pressure is applied, inward deflection occurs. For the cylindrical part of the copper shell, an inward deformation will also occur, except at the lid and base. Then, the shell becomes slightly hourglass shaped.

Because of the complex nature of the creep phenomenon, the isostatic load cases have also been analysed with elastic-plastic approaches. The purpose here is to determine the maximum deformation of the copper that can occur during isostatic loads that are relevant in the repository environment, having first demonstrated that these cases are deformation controlled. The elastoplastic analyses were conducted by increasing the outer pressure far beyond the expected load, such that the final deformation state is reached but in a much shorter time than the same final state would be reached with a creep model and a realistic load. This final state is then evaluated against the failure criteria of the copper shell.

When sufficient plastic deformation has occurred, the copper shell establishes contact with the insert at the lid and base and along the cylindrical part of the copper shell. The inelastic deformation of the copper consists of both elastic-plastic and creep strain; the regimes occur simultaneously and cannot be separated. This process will continue until the deformation of the copper shell reaches a steady state, that is, the deformation will remain constant as long as the load is constant. After the copper shell has reached this "final state", the strains cannot increase, and a stress relaxation state may occur. This is a consequence of the design of the KBS-3 canister and the compressive nature of the external pressure load. When the stress-state in the copper shell reaches equilibrium, there is no longer a driving force for further deformation since this is prevented by the presence of the insert. Therefore, it is sufficient to determine the magnitude of the inelastic deformation in the copper shell and evaluate the strain and stress states in terms of triaxiality using the failure criteria stated in Section 3.3.1.

The determinations of the inelastic deformation have been made using different approaches. In principal, the first approach is to consider creep and accurately analyse the evaluation in the final repository in terms of deformation, temperature and load as a function of time. The achieved plastic deformation after 100 000 years will be used to assess the fulfilment of failure criteria. This approach has been used in Hernelind (2015a) using the "Swerea KIMAB and KTH creep model" and in Andersson et al. (2017) using the "VTT creep model", both of which are described in Section 4.7.4. Because of the complex nature of the creep phenomenon, the isostatic load cases have also been analysed with elastic-plastic approaches, with the purpose of determining the deformation of the copper shell that can occur under an isostatic load. This is done using a significantly increased outer pressure on the copper shell. Hence, the magnitude of the load is increased, and the final deformation state is reached in the final repository, depending on the conditions of the isostatic load due to the creep deformation.

Swerea KIMAB and KTH creep model

An investigation of the isostatic load over 100 000 years was performed in Hernelind (2015a). The analysis considered the thermal evolution and internal and external pressures. In the FE-model, the mesh of the slit area was shown to have a great impact on the result. The 3 mm root defect in the lid weld shown in Figure 6-20 achieved a local inelastic strain (*CEEQ*) in the range of 40–60 %; this range mainly depends on the presence of distorted elements. The justification to neglect results from highly distorted elements is derived from the fact that unrealistic results may be achieved for values extrapolated from the integration points to the element nodes, especially given that the element sizes are very small.

In Figure 6-21, the inelastic strain is shown without removing any distorted elements; the magnitude of the strain is approximately 60 %. Furthermore, in the slit of the welded base, the peak of the inelastic strain is also very local, but the magnitude of the inelastic strain is approximately 20 %. The copper shell and the cast iron insert have different coefficients of thermal expansion, which means that the copper shell will expand more when the temperature is increasing. The external pressure will compress the copper shell until it makes contact with the insert. Due to the similar thermal expansion values for copper = 1.7×10^{-5} and cast iron = 1.18×10^{-5}, a temperature change of 50 °C will result in an insignificant increase in the strain of approximately $50 \times (1.7–1.18) \times 10^{-5} = 2.6 \times 10^{-4}$, which is a negligibly small strain.

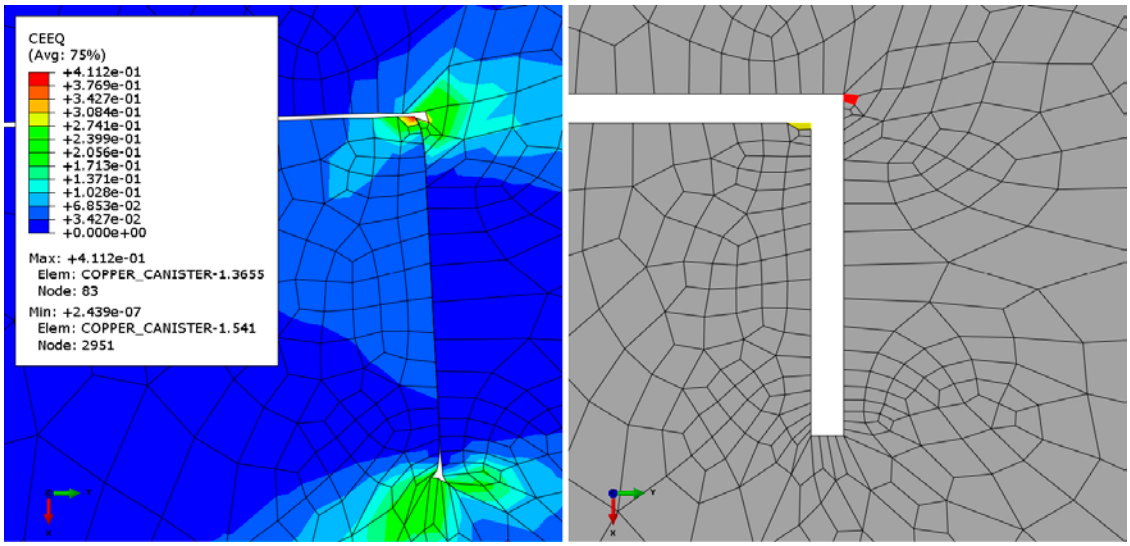

Figure 6-20. *Inelastic strain (CEEQ) at the top of the copper shell after 100 000 years. This represents the situation after glaciations. Element 946 (red in the right plot showing undeformed geometry) was removed before generating the contour plot (Hernelind 2015a).*

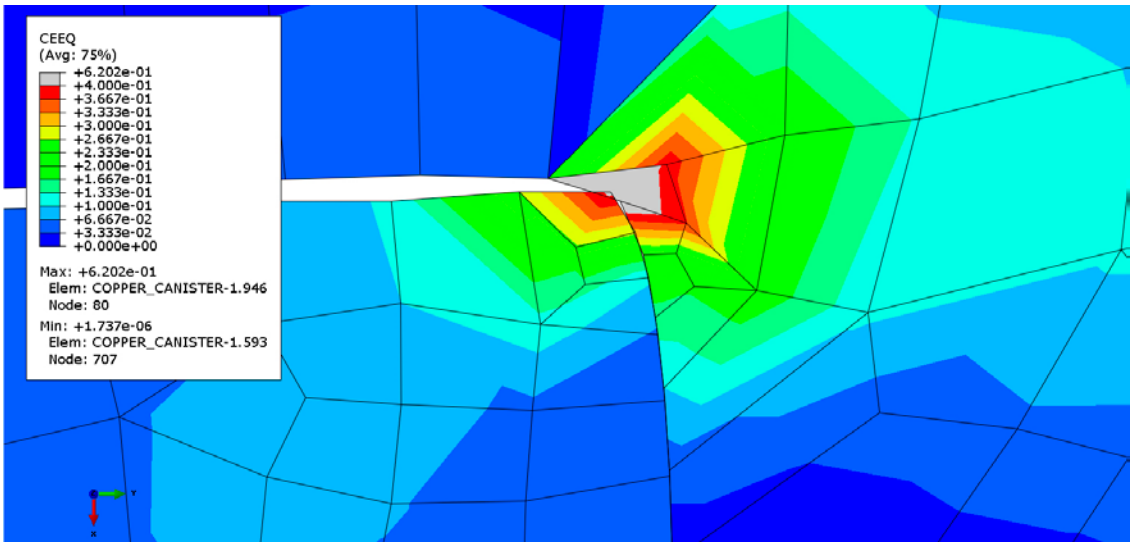

Figure 6-21. *Inelastic strain (CEEQ) at the top of the copper shell after 100 000 years (axi-symmetric analysis). This represents the situation after glaciations. The peak value is very local and occurs in a highly distorted element. No elements were removed (Hernelind 2015a).*

The stresses and strains in the copper shell are compressive. In Figure 6-22, T is shown. The maximum T is approximately 0.55, and according to Figure 4-11, the plastic strain at failure is 130 % at $T = 0.55$.

The overall inelastic strains in the copper shell in Hernelind (2015a) fall in the range of 3 %. The highest inelastic strains occur at the top of the copper shell, see Figure 6-23, where the strain is approximately 30 % and the triaxiality is approximately 0.3. Other areas with high triaxiality have only small inelastic strains.

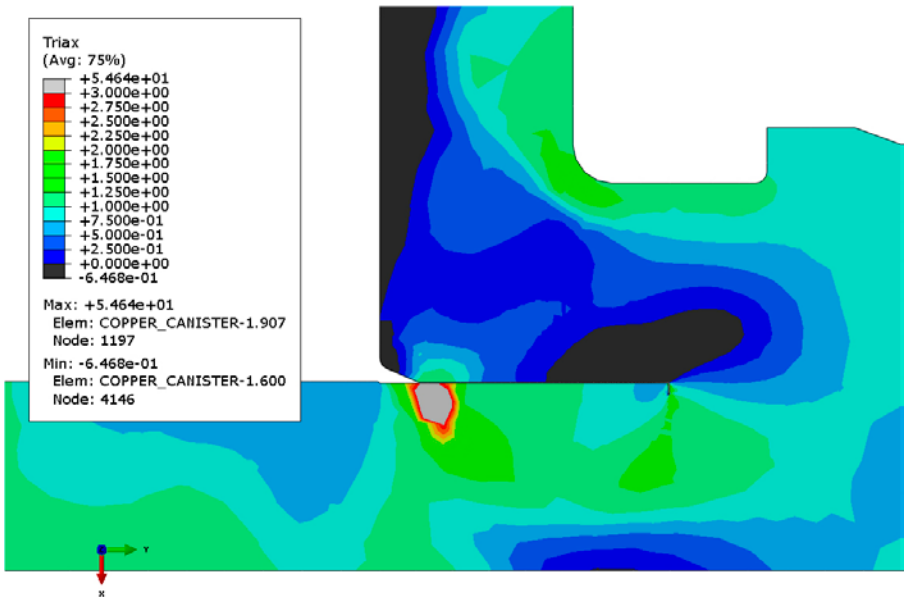

Figure 6-22. *Plot of triaxiality and the ratio of p/q (pressure divided by von Mises stress) at the top of the copper shell (axi-symmetric case).*

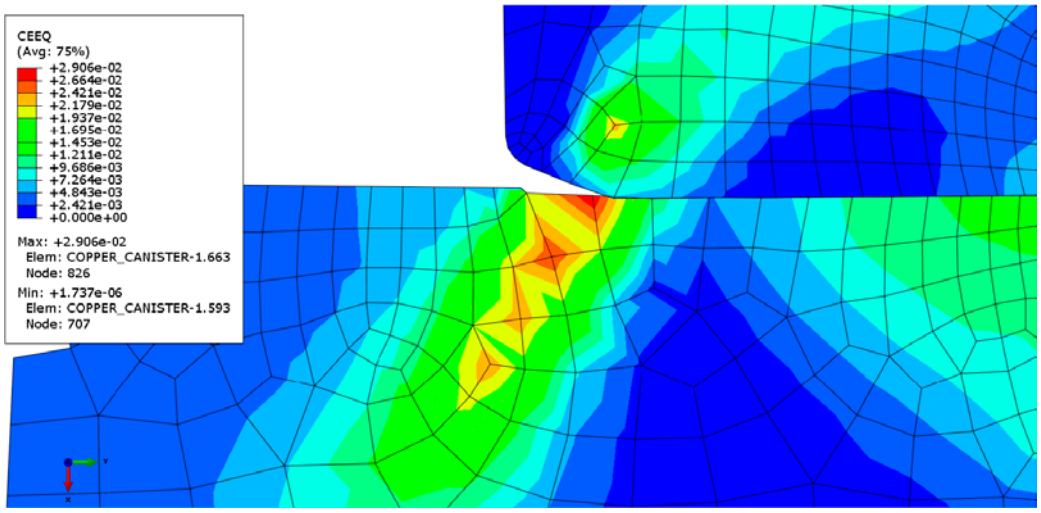

Figure 6-23. *Inelastic strain (CEEQ) at the top of the copper shell after 100 000 years (axi-symmetric analysis). This represents the situation after glaciations (Hernelind 2015a).*

The principal strains in the top weld area are illustrated in Figures 6-24 and 6-25.

The in-plane strains are represented by arrows. Arrows denoted “< >” indicate tension, and arrows denoted “> < “ indicate compression.

The magnitudes of the strains are indicated according to the colour palette but are also indicated by the length of the arrows.

The out-of-plane principal strains are indicated by the symbol “+” but are too small to be noticed. The magnitudes of the strains are indicated according to the colour palette but are also indicated by the sizes of the symbols.

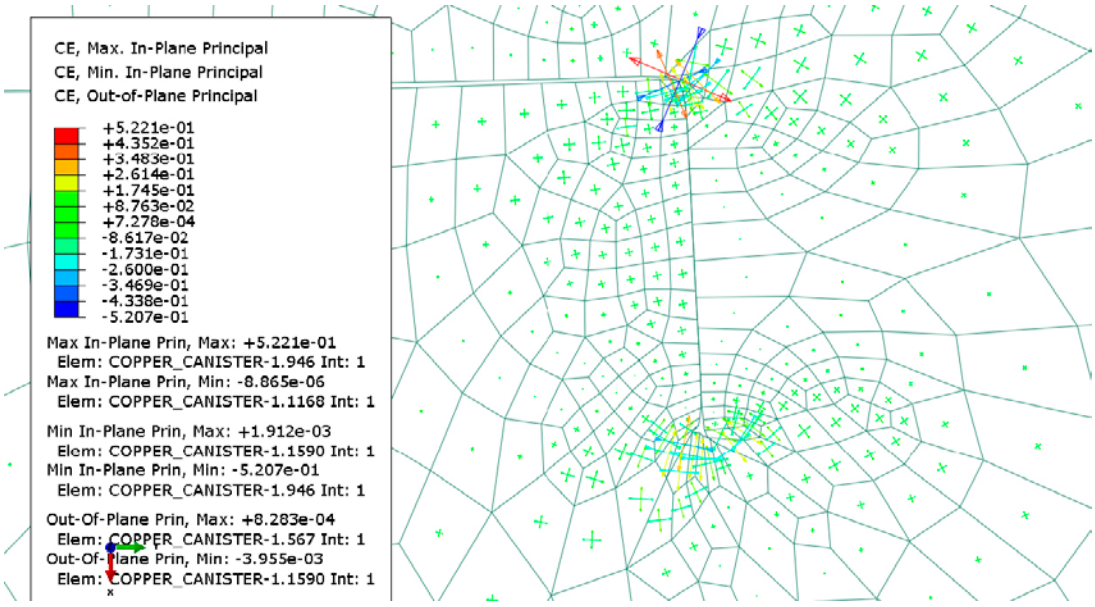

Figure 6-24. *Principal creep strains at the top of the copper shell after 100 000 years (axi-symmetric analysis). This represents the situation after glaciations.*

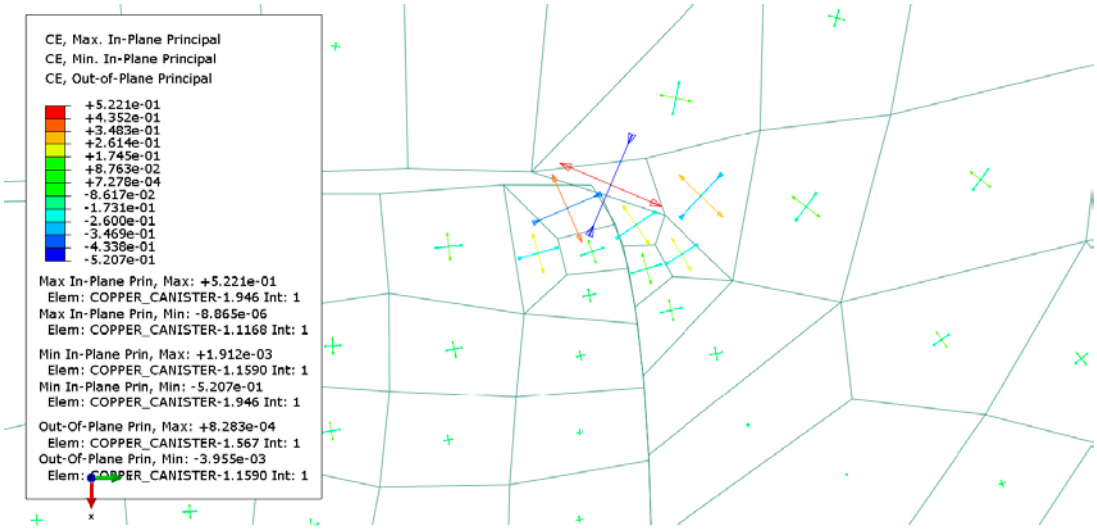

Figure 6-25. *Principal creep strains at the root area of the weld in the copper lid after 100 000 years (axi-symmetric analysis). This represents the situation after glaciations.*

Jin and Sandström (2013), elastic-plastic analysis

In Jin and Sandström (2013), an external pressure of 15 MPa was analysed using the flow curves in Figure 4-12. The local plasticity was in the range of 23 % true plastic strain for a 15 MPa isostatic outer pressure in load case 3. The plastic strain of the inner wall of the copper tube along the insert was found to be less than 1 %.

VTT creep analysis

The LSCP long-term creep model combined with the short-term Kohlrausch relaxation model was applied for simulating the copper shell creep strain accumulation for isostatic buffer swelling pressure and glaciation pressure load cases in Anderson et al. (2017). In the study, the copper shell with a welded base was found to be more critical than the integrated base alternative. Therefore, only the simulation model with a welded-base copper shell was subjected to the same canister temperature evolution, buffer swelling and glaciation loads as in Hernelind (2015a).

The most stressed regions in the copper shell were found to be the inner rounded corners of the copper lid and the joint-line hooking-type initial defects. For the canister base, the slit between the outer shell and the bottom was found to exhibit the highest stresses. Regarding creep strain and deformation, at the top region, the joint-line hooking-type defect along with the internal corners of the lid were found to be the regions that accumulated deformation. At the copper-shell base, the greatest inelastic strains were located near the insert corner. Overall, the largest inelastic strains were on the order of 2 % during the full 100 000 year simulation time period. It seems that the model used in the VTT assessments was far less refined in the slit region compared to the simulations performed by Hernelind, and the 2 % inelastic strain is a global value. The magnitude of the inelastic strain (60 %) that was determined by Hernelind is a local value.

Investigation of the limit analysis of the maximum achievable strains in the copper shell

In Unosson (2017), the magnitude of the achievable inelastic deformation in the copper shell was determined. The analysis approach was to employ the elastic-plastic constitutive model from Unosson (2014) described in Section 4.7.3 and increase the outer pressure to determine the maximum plastic strains at the slits.

The postulated outer pressure on the canister exceeded 50 MPa and reached steady-state deformation, thus determining the magnitude of the inelastic deformation that may occur in the copper shell during the post-closure isostatic load cases. The geometries of the slit bottom shown in Figure 6-17 affected the results. However, the true plastic strain is in the range of 30–60 %, with the lower strain for the curved slit end and the higher strain for the plane bottom. The high plastic strains are very local, as demonstrated in Figure 6-26.

The local stress state in the curved and plane slit bottom at a hydrostatic pressure of 1 000 MPa is shown in Figure 6-27. As seen, the triaxiality is low, less than +0.05. The mechanical integrity of the copper shell is thus found to be sufficient.

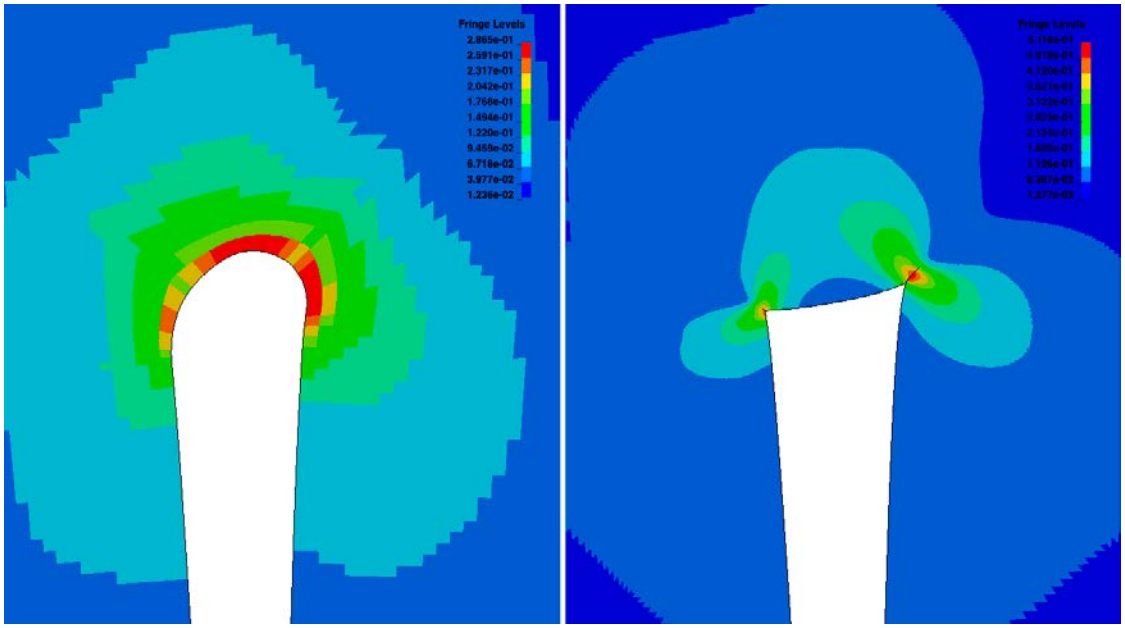

Figure 6-26. *Details showing the deformed geometries and effective plastic strains (–) at the slit bottom for the curved and plane (non-local characteristic length 10 µm) slit bottom at a hydrostatic pressure of 1 000 MPa (Unosson 2017).*

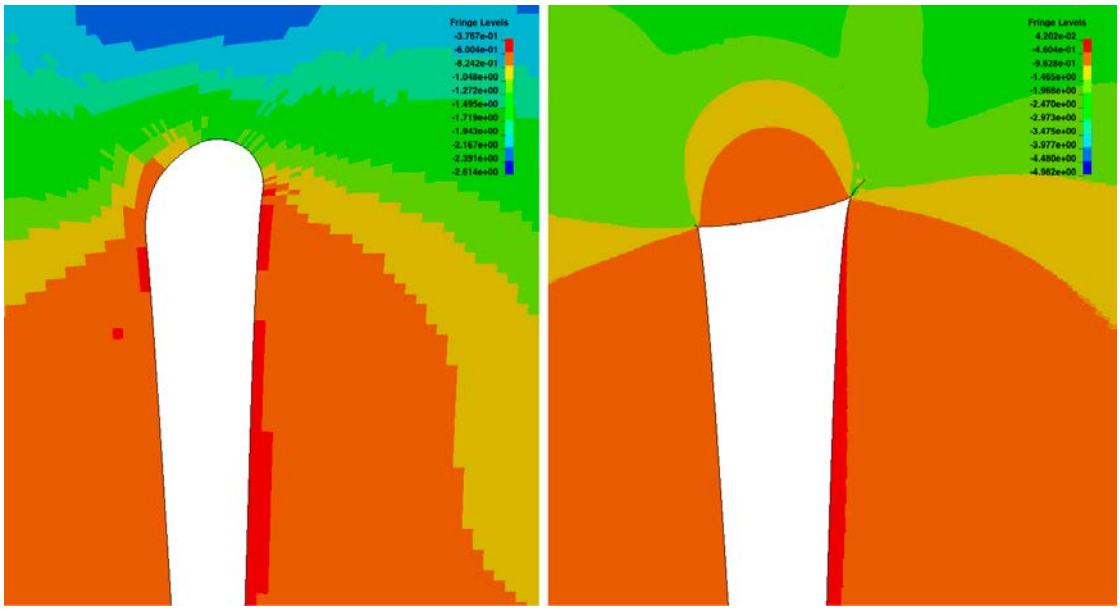

Figure 6-27. *Details showing the deformed geometry and stress triaxiality (-) at the slit bottom for the curved and plane (non-local characteristic length of 10 µm) slit bottom at a hydrostatic pressure of 1 000 MPa (Unosson 2017).*

Case 5 – rock shear load

The rock shear case may hit the canister at any location and direction according to the design premises. Therefore, the impact of different shear planes has been investigated. The rock shear was analysed in Hernelind (2010) with different external pressures on the copper shell. The influence of the shear strength of the buffer was further studied in Hernelind (2014a, 2017b). The impact of a shear plane located above the steel lid was also investigated in Hernelind (2014b). Shearing at the welded or integrated base of the copper shell was investigated in Hernelind (2017c).

All results below are given for a rock shear magnitude of 5 cm; the shear plane is perpendicular to the canister axis unless otherwise not stated. The BWR insert is usually used in the analyses. The influence of the type of insert is negligible in terms of the strains in the copper shell because the rock shear case is a displacement-controlled case. Because the rock shear case lasts only for a fraction of a second, the case can be solved with elastic-plastic constitutive models; creep in the copper can be neglected.

Case 5a – symmetric loads in combination with the rock shear load case

The effects of hydrostatic groundwater pressure and symmetric swelling pressure are combined with the rock shear load case in Hernelind (2010). The results from Hernelind (2010) show that the magnitude of the outer pressure is insignificant in combination with the rock shear case in terms of the copper shell. The rock shear perpendicular to the axis of the canister at 50 % of the height from the base and with a bentonite density at saturation of 2 050 kg/m^3 resulted in plastic strains concentrated in the geometric discontinuities of the copper lid, and the maximum plastic strain of copper was approximately 21 %. However, Hernelind (2014a) showed that the influence of the shear plane location significantly affects the strains in the copper shell; a shear plane perpendicular to the canister axis at 90 % of the insert height was more harmful to the copper shell; *PEEQ* was found to be 33 %.

In Hernelind (2014b), the impact of shearing the canister above the steel lid or below the insert in the base of the canister was found to result in 33 % plastic strain (*PEEQ*) for the bentonite density at a saturation of 2 050 kg/m^3. This shear plane was further investigated in Hernelind (2016b). An improved mesh and decreased stiffness in the buffer with a density of 2 022 kg/m^3 resulted in 26 % true plastic strain in the top weld; the shear plane perpendicular to the canister axis at 90 % of the insert height yielded 27 % true plastic strain. In the canister with the welded base, 13 % true plastic strain occurred at the base weld (Hernelind 2017c). The integrated base design is stiffer; shearing at

the insert base or perpendicular to the canister axis at 10 % of the insert height results in effective plastic strain in the range of 4–6 % in the copper shell. Displacements of the buffer and canister are shown in Figure 6-28. The displacements in the figure are magnified by a factor of 2 to increase their visibility.

Case 5b – asymmetric loads in combination with the rock shear load case

The rock shear case is not combined with the asymmetric loads described in Section 2.2.2 because these loads are extreme values that are considered to have a low probability of occurrence. Their combination would thus be a combination of two events with low probability. However, the combined impact of an asymmetric outer pressure and the rock shear case has been investigated.

SKB and Posiva have previously estimated that the combined load case of shear and bending stresses does not have to be considered (Raiko et al. 2010). The analyses of the rock shear loads on the canister reported in Hernelind (2010) were conducted as FEM-based global simulations.

Considering the variations in the postulated bentonite density and resulting initial stresses, global shear simulations were conducted with the rock shear plane perpendicular to the main axis of the canister in two positions and with the two different rock shear magnitudes of 5 and 10 cm. The two axial positions of the shear planes were 75 % and 50 % of the insert height.

In Börgesson and Hernelind (2013), the true plastic strain in the copper shell was approximately 10 % and local for case 5b. Since these strains are lower than those in case 5a, this load case is not considered to be harmful to the mechanical integrity of the copper shell.

Requirements for the ductility in the copper shell

The plastic strain and triaxiality in the copper shell have been investigated using different approaches, and the conclusion is that the peak strains are very local in the slit in the range of 20–60 % true plastic strain. Therefore, it is reasonable to specify the design criterion of acceptable true inelastic strain (ε) in the copper shell in the final repository as

$$\varepsilon \leq 80\ \% \qquad (6\text{-}2)$$

It was demonstrated in Danielsson (2016) that the parent copper metal is insensitive even to severe defects, such as notches. Because the creep ductility of different parts of the friction stir welds is approximately the same as that of the parent metal, the weld will not be sensitive to defects. The absence of creep crack growth derived in Section 3.2.1 and the large amount of plastic deformation in the CT-specimens verified in Danielsson (2016) demonstrates that the slow propagation of the notch occurs due to blunting of the notch and plastic deformation of the specimen. Hence, the tests demonstrated that creep in copper is not notch sensitive. Then, applying Equation (3-2), it can be stated that the copper test specimens will show that

$$\varepsilon_f \geq 160\ \% \qquad (6\text{-}3)$$

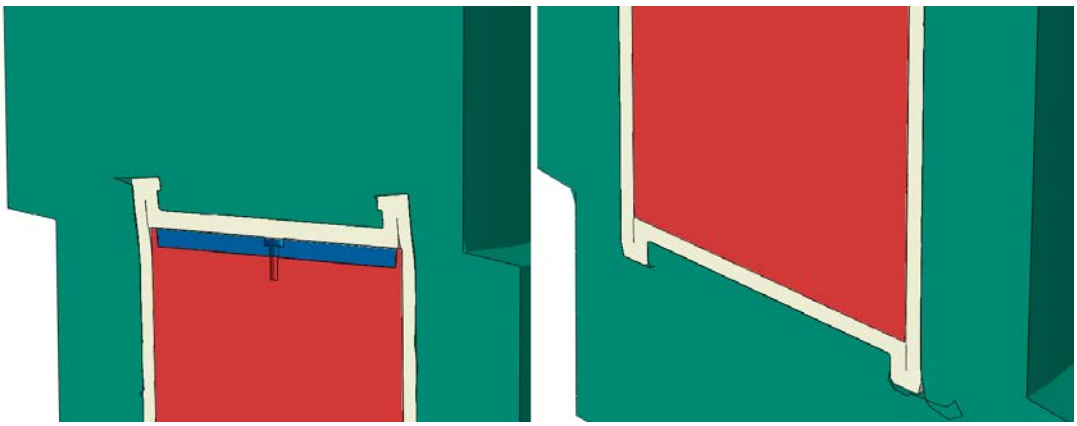

Figure 6-28. *Displaced geometry with a scale factor of 2 and shearing magnitude of 10 cm at the insert lid (left) and at the insert base with a welded base on the copper shell (right). (Hernelind 2014b).*

Hence, the reduction in the fracture area in a tensile test specimen is at least 80 % according to Equation (3-1). Thus, the true plastic strain (ε) should not exceed 80 % in the copper shell in the final repository. The true plastic strain at failure (ε_f) should be 160 % at minimum in the creep or elastic-plastic material test specimens at the uniaxial state, where $T = 0.33$ or higher. The required true plastic strain of copper at failure, $\varepsilon_f \geq 160$ %, was derived from the load cases in the final repository.

As seen in Figure 6-27, the triaxiality is low, less than +0.05, so the design criterion maximum of 80 % true plastic strain can be used for the verification of the copper shell. These results lead to the conclusion that the plastic strains in the copper shell are local, below the design criterion maximum of 80 % true plastic strain, and the stress state does not create a triaxiality that is harmful to the ductility of the copper and post-closure mechanical integrity of the copper shell. The mechanical integrity of the copper shell is thus found to be acceptable.

In Figure 6-29, the failure strain as a function of the triaxiality derived from the elastic-plastic evaluation tests is shown. From this curve, the failure strain of Cu-OFP is 210 % for pure tension, 400 % for pure shear/torsion and 760 % for pure compression. The relatively high compression value is a consequence of the failure model used, which is mainly focused on ensuring the prediction of shear/tensile material failure while reflecting the magnitude differences between the tensile and compressive states.

It was judged from the FE simulation in Danielsson (2016) using creep test specimens that Cu-OFP can withstand significant creep deformation at very low strain rates as well as higher strain rates achieved during conventional mechanical testing.

Furthermore, in Tables 14-8 and 14-9 in Sandström and Andersson (2008), the reduced areas of the uniaxial cross sections in the creep test specimens from FSWs and the lid and tube material are stated. The area reductions are in the range of 80–90 % corresponding to 160–230 % true plastic strain according to Equation (3-1) at a stress state similar to that in Figure 4-2. The copper material satisfies the design criteria for elastic-plasticity and creep ductility for the post-closure mechanical integrity in the final repository.

Summary-copper shell

A material model that is used to simulate creep in a structure for more than 100 000 years will always be questioned. Therefore, under such conditions, the main focus should be on the robustness of the application of the model. In the isostatic load case, creep deformation must be considered to determine the required ductility of the copper shell. This can be done using a conventional elastic-plastic model or a model including creep. The post-closure mechanical integrity of the copper shell will be fulfilled as long as the ductility requirements are fulfilled. The required ductility is therefore independent of the strain rate that occurs in the final repository.

Different constitutive models have been used to increase the credibility of determining the requirements of plastic strain in the copper shell. The conclusions are that the peak strains are very local in the slit, in the range of 20–60 % true plastic strain, and the stress state does not create a triaxiality that is harmful to the ductility of the copper. These results lead to the conclusion that the local plastic strains in the copper shell are local, below the design criterion maximum of 80 % true plastic strain, and are not harmful to the post-closure mechanical integrity of the copper shell.

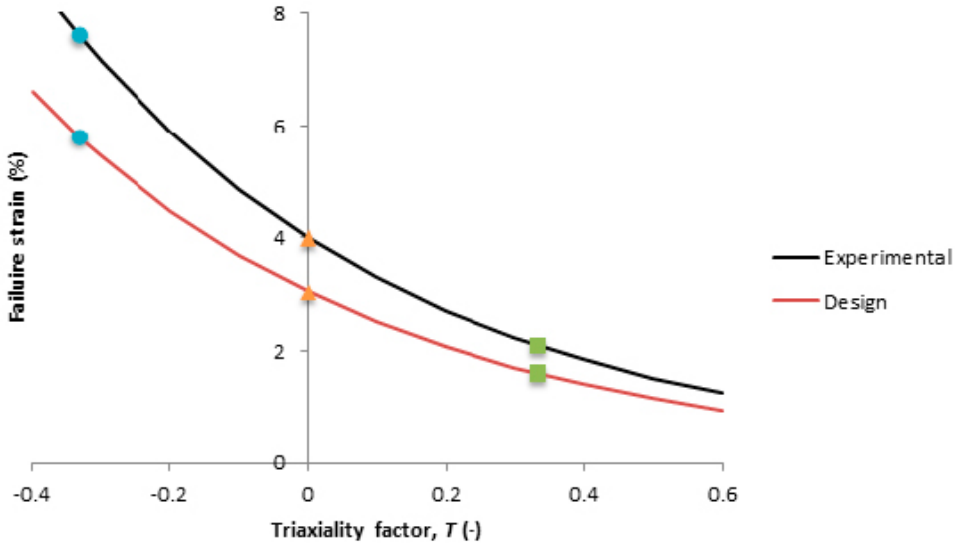

Figure 6-29. *Elastic-plastic (time-independent/static/non-creep) failure strain function for the copper alloy (Cu-OFP) used by SKB and Posiva. The black curve is fitted to tensile and torsion test data from Brosius (2008) and Unosson (2014). The red curve represents the design value approach based on the SKB-Posiva design criteria for160 % true failure strain in tension. The circles denote uniaxial compression; triangles indicate simple shear, and squares represent uniaxial tension (Unosson 2017).*

7 Assessment of the effects of input data and conceptual uncertainties

The performed analyses in Chapter 6 are based on the design premises, loads, geometries and constitutive models presented in this report. To make the verification of the mechanical strength of the canister more comprehensive, structured assessments of the uncertainties are also required. This chapter compiles results of various types of uncertainty analyses. They assess the impacts on the calculation results *i*) when varying uncertain input parameters and *ii*) for conceptual uncertainties associated with the models used.

Table 7-1 gives an overview of the uncertainty analyses of the results presented in this report, including references to sections for results and the corresponding uncertainty analysis.

7.1 Uncertainty analysis and handling loads

The present report does not claim that all possible and realistic handling loads have been investigated. The chosen handling loads were analysed with the purpose and scope to determine the magnitude of the handling loads that the canister can withstand without affecting the post-closure safety of the canister so that the canister can still be deposited.

7.1.1 Insert

In Zeng et al. (2015), the weight of a PWR insert and geometry of a BWR insert were used. These are pessimistic assumptions. The results were computed using a large dynamic amplification factor of 2, compared with a factor of approximately 1.2 for common situations according to Swedish norms for lifting (SIS 1986). A safety factor of 10 was set in accordance with ASME Sect XI (ASME 2008b). The computed results indicate that the stresses are relatively low and that no plasticity will be involved, even in the region near the sharp edge between the bolt hole surface and the top surface. Altogether, it is concluded that the verification in Section 6.1.4 was performed pessimistically and that there are sufficient margins.

7.1.2 Copper shell

The PWR weight was used since the weight of the PWR canister is higher than that of the BWR canister, and therefore, this is a pessimistic assumption.

For the analyses of lifting the canister by the lid flange, the results have been verified in terms of the American ASME code. In Bolinder (2011), the constitutive model for the copper in Table 4-6 derived at room temperature was used, and the collapse load for the copper shell without defects was found to be 5 000 kN. During the handling load cases, the maximum copper surface temperature is 100 °C. Therefore, the properties derived from tensile testing of annealed copper at 125 °C in Section 4.7.2 were used in the lifting case of the canister in Alverlind (2016c) because the case is force-controlled and mainly depends on the yield stress of the copper. The collapse load for the copper shell without defects was found to be 953 kN in Alverlind (2016c), which is lower than that in Bolinder (2011) by more than a factor of 5. The reason is that different constitutive models and temperatures for the copper were applied during the calculations. However, lifting the canister by the lid flange was also analysed in Unosson (2017) considering 125 °C, and the ASME collapse load used for comparison with numerical simulations was 763 kN without defects. The difference compared with Alverlind (2016c) was ascribed to a slight difference in the constitutive model in different FE-software.

In addition to the ASME failure criterion, in Unosson (2017), the critical dynamic loads during lift were also verified in terms of a physical failure criterion based on the risk of material failure for an initial velocity of 2 m/s. A damage parameter (D) was computed based on the model in Unosson (2014) for selected critical positions in the canister. Material failure corresponds to $D = 1$, and the maximum obtained damage is $D = 0.14$; hence, there is no risk of material failure.

In total, the handling loads were determined using pessimistic parameters in terms of handling the copper shell.

7.2 Uncertainty analysis, uneven swelling loads, insert

These load cases are aimed at reflecting worst-case scenarios. If the analysis results are found to be critical, a more elaborate analysis will be needed. The load analysis results are given in Section 6.2.1, considering water saturation effects and permanent asymmetric loads.

The full details of the analysis approach are presented in Börgesson and Hernelind (2013), Hernelind (2014f) and in Börgesson et al. (2009). The resulting stresses in the insert were determined using a simplified calculation method with beam theory as well as with FE solutions of the load cases. The assumptions made in the calculations are based on a worst-case scenario and hence reflect a very low-probability event.

An evaluation of the uneven swelling loads based on the FE simulation in Börgesson and Hernelind (2013) was also performed in Alverlind (2016a) with respect to the damage tolerance of the insert. The crack sensitivity at the most stressed location on the insert barrel surface was estimated for asymmetric load cases 1 and 2, and the maximum acceptable radial crack size depth was equal to 21.1 mm compared with a 9.0 mm acceptable radial crack size depth in the rock shear case.

In Hernelind and Börgesson (2018), further analytical calculations with a banana shape = 85 mm were performed. The result showed that the stresses in the canister insert yielded a maximum axial stress equal to 330 MPa, compared to 79 MPa obtained in Börgesson and Hernelind (2013) with an 8 mm banana-shaped deposition hole. The results from Hernelind and Börgesson (2018) are most likely pessimistic.

7.2.1 Uncertainties in input

Assumptions regarding the load distribution

The uncertainty of the assumptions can be considered to be low because the worst scenario philosophy is applied. The bentonite density distribution, deposition hole deviation and temporary swelling distribution are combined in the most unfavourable way.

7.2.2 Uncertainties in the analysis methodology

Calculation method for the load distribution

The pressure build up is both simplified and pessimistic; the approach is determined for the worst case.

Calculation method for the stresses

Possible errors in determining the section modulus (W) (BWR insert) are not given in Börgesson et al. (2009). The calculation of W is based on the nominal geometry of the insert cross section. The acceptable deviations of the geometry are insignificant when calculating W. Possible errors in the calculations of the bending moment and bending stress are not given, but the maximum error can be estimated to be ± 2 % (Raiko et al. 2010). The same error will also be transferred to the stress results. Possible axial pressure components, which will reduce the main tensile stress component, are not considered in Section 6.2.1.

The numerical FE solution used in Börgesson and Hernelind (2013) and Hernelind (2014f) implies improved accuracy in terms of the numerical errors in the complex cases compared with those of the simplified and empirical solutions in Börgesson et al. (2009). The uncertainty in the damage tolerance analysis (acceptable defects) is discussed in Section 7.3.

7.2.3 Estimation of uncertainties in the results

The consequences of the simplifications in the analysis method are not given in Börgesson et al. (2009). However, the pessimistic approach for the assumptions will yield pessimistic results that consequently have a low probability of occurrence.

The FE solutions in Börgesson and Hernelind (2013) and Hernelind (2014f) verify that the results in Börgesson et al. (2009) are pessimistic in the range of 30–50 %.

7.3 Uncertainty analysis, uneven swelling loads, copper shell

In the analyses of the buffer before saturation, the swelling pressure of 12.3 MPa has pessimistically been considered, which corresponds to a bentonite density at saturation of 2 050 kg/m^3 (Hernelind 2014f). The buffer swelling along the canister also creates shear forces on the outer surface of the copper shell. However, the shear stress is limited to 1.75 MPa (Börgesson et al. 2010), which corresponds to the shearing capacity of the buffer. The most pessimistic assumption is that the shear stress reaches its maximum value and has a constant magnitude along the surface of the canister.

The highest values occur when the shear stress caused by buffer swelling is 6.2 %, which is considered to be well below the failure criterion for the ductility of the copper shell. The maximum *PEEQ* values in the base weld of the copper shell and also at the top of the copper shell have higher magnitudes for this case since the support from the insert is lost. The hydrostatic pressure is positive for regions with high equivalent plastic strain.

The previous calculations shown in Andersson-Östling and Sandström (2009) were recalculated and presented in Jin and Sandström (2013). The new estimates include three load cases: 0, 1 and 2. Load case 0 is a reference case with only an isostatic load acting on the canister. Load cases 1 and 2 are taken from Figure 4-1 and Figure 4-3, respectively, in Börgesson et al. (2009). For the calculations of the axial shear stresses in the copper shell, the bentonite and copper were joined, but the shear stresses were limited by the bentonite shear strength according to the Mohr-Coulomb failure criterion. This implied that the friction angle must not exceed a certain value (see Börgesson et al. 1995, Chapter 2). While modelling the loads on the canister, the contact between the cast iron insert and copper shell is determined via the "penalty-barrier" method. When contact is reached, no relative vertical movement is allowed between the copper shell and insert. It is indirectly assumed that the friction is very high. The calculations performed show that the largest strains in the copper shell appear in the gaps in the lid and base welded zones. In these areas, however, the radial compressive principal stress causes the material to compress and deform. The maximum value of strain in the copper shell is obtained at the end of the slit towards the base of the copper shell, which occurs in load case 2 (maximum shear stress). The deformed area is small, and the maximum true plastic strain is very local at 74 %, lower than the allowed 80 % true plastic strain in the canister; thus, the integrity of the canister is not threatened.

7.3.1 Uncertainties in the inputs

The uncertainties in the assumptions in Hernelind and Börgesson (2018), Hernelind (2014f) and Jin and Sandström (2013) can be set to zero because the worst-case scenario philosophy is applied. The bentonite density distribution and, hence, the swelling distribution are combined in the most unfavourable way, so the postulated maximum density at saturation of 2 050 kg/m^3 is well above the maximum density at saturation of 2 022 kg/m^3 according to the design premises for the canister. The increased stiffness and density lead to increased deformation in the canister, so the postulated properties of the buffer can be considered to be pessimistic.

7.3.2 Uncertainties in the analysis methodology

The load cases are solved with elastic-plastic constitutive models, justified by the premises of the cases. The magnitude of the buffer swelling depends on the range of the swelling pressure, which in turn depends on the density of the bentonite. Therefore, the cases with uneven swelling can be considered to be displacement-controlled cases, specifying an upper limit of the possible deformation that may occur. Therefore, the elastic-plastic and creep approaches can be used; the critical result is the magnitude of the plastic strain in the copper shell, and the time to reach the final state is of subordinate importance. The extrapolation of testing data to the final disposal conditions is also discussed in Section 7.5.3.

The influence of the mesh in the FE-models has a direct impact on the achieved results. Because the cases have been solved with different commercial FE-software programmes and meshes, the uncertainties are considered.

7.3.3 Estimation of uncertainties in the results

The uncertainties have not been explored in detail because the worst-case scenario philosophy has been applied, as explained above. The influence of the used elastic-plastic models on the final result has been shown to be small, and the results show that the strains in the copper shell are below the acceptable 80 % true strain in the copper shell.

7.4 Uncertainty analysis, glacial load, insert

The results regarding the glacial load are given in Section 6.2.1 and can be summarised as follows. It has been confirmed during pressure tests (Nilsson et al. 2005) that there is a margin well above 2 in terms of the technical design requirements of a 50 MPa isostatic load, full plastic collapse and rupture at an isostatic pressure over 100 MPa. The basic design verification analyses also show that the limit load of the insert, including the integrated base and screw-fixed steel lid, is higher than 1.5 times the design pressure of 50 MPa, which is the ASME III- code requirement for the safety factor.

It was also concluded in Section 6.2.1 that the inserts have been analysed against the design pressure with large volumetric defects and other types of material losses in various zones. The analyses are based on the limit load method using a safety factor of 1.5 according to ASME III rules. The acceptable volumetric defect sizes are given in Tables 6-4 and 6-5. Additionally, the combination of a scaled stress-strain curve of the nodular cast iron with a yield stress of 240 MPa, a decreased edge distance and a volumetric defect in the edge with decreased nodular cast iron has also been considered. The influence of residual stresses on axial crack-like defects has also been taken into account. The results show that the insert structure is insensitive to different types of material imperfections.

In Posiva SKB (2017), it is stated that recent models of climate and ice sheet development are primarily interpreted by SKB such that a maximum ice sheet thickness of 4 000 m, corresponding to an isostatic pressure contribution of 36 MPa, may have to be considered at the Forsmark site. As stated in Chapter 2, it is expected that this load case begins after 50 000 years; however, in the analyses, it is assumed that the case begins after 20 000 years and remains up to 100 000 years as a result of uncertainties in the ice age scenario (see Table 7-1).

7.4.1 Overview of the uncertainties in the analysis methodology and results

An overview of the extensive analysis presented in Alverlind (2016a, b) is given in Table 7-2, in which each uncertainty is justified. In Table 7-3, a summary of different sensitivity analyses for input parameters different from those of Alverlind (2016a, b) is given. Tables 7-4 and 7-5 provide an overview of the uncertainty analyses for the insert base and the steel lid, respectively.

In Dillström and Manngård (2017), the influence of the steel tube stress-strain properties was investigated for the isostatic load case. The insert casting process affected the mechanical properties of the steel channel tubes. An overview is shown in Figure 7-1. The outer collapse load was found to be 91 MPa for the canister considering "as-manufactured" stress-strain properties for the steel in the channel tubes and nodular cast iron. This is well above the required collapse load of 75 MPa derived in Section 6.2.1 and close to the deterministic collapse load of 90 MPa used for the damage tolerance analyses in Alverlind (2016a, b).

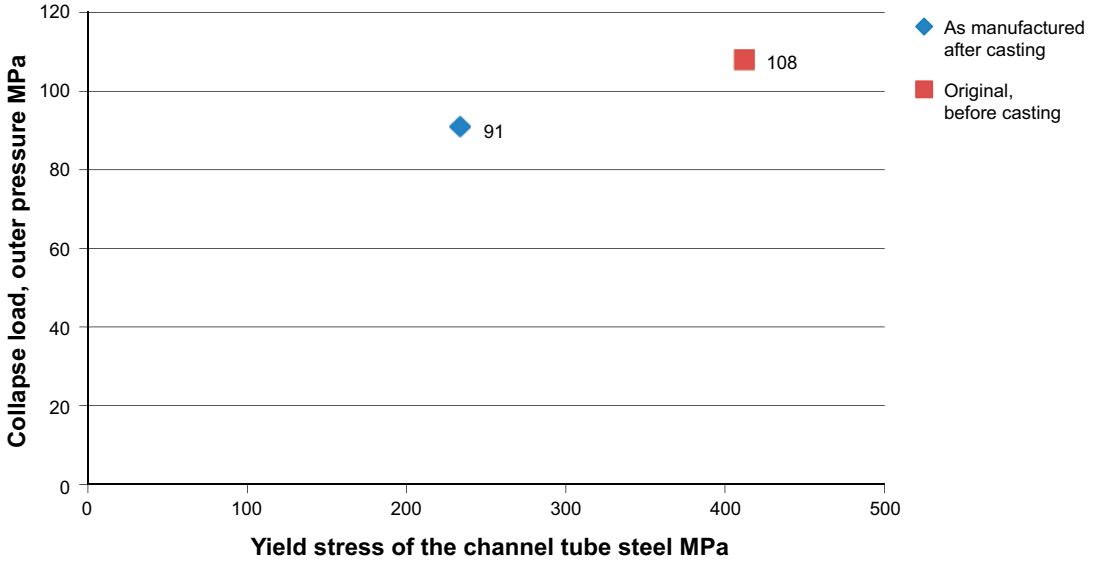

Figure 7-1. *Schematic of the influence of the yield stress of the steel channel tubes on the collapse load on a BWR insert. The influence of using two different stress-strain curves for samples that are "original before casting", as in Table 4-4, or "as manufactured after casting", are shown. In practice, the lower yield stress of the steel in the channel tubes after casting the insert reduces the outer pressure collapse load from 108 MPa to 91 MPa, using the "as-manufactured" stress-strain properties for the nodular cast iron material. (From Dillström and Manngård 2017).*

Table 7-1. Overview of uncertainty analyses of the results regarding the final repository, including references to results and the corresponding uncertainty analysis. The coloured boxes correspond to the possible periods for the load case (1…5).

Uncertainty analysis **Repository evolution phase**		**Water saturation**	**Temperate**	**Glacial**	**Subsequent permafrost and glacial periods**
Years after closure of the repository		**0 years → 10 000 years**	**10 000 year → 50 000 years.**	**50 000 years→ 60 000 years**	**60 000 years → 1 000 000 years.**
Canister temperature T (°C)		***T* < 125/100 (Fe/Cu)**	**20 < *T* < 125/100**	**0 < *T* < 20**	**0 < *T* < 20**
Load case #)	**Deformation rate**				
1) Asymmetric loads due to uneven water saturation and imperfections in the deposition hole geometry. No simultaneous hydrostatic pressure. Uneven water saturation effects will decay later and be replaced by permanent loads 2) and 3) acting in the saturated condition.	**Insert** Static	Results in 6.2.1 and 6.2.3 Uncertainty in 7.2			
	Copper shell Creep or static	Results in 6.2.4 Uncertainty in 7.3			
2) Permanent asymmetric loads due to uneven bentonite density and imperfections in deposition hole geometry. 3) Groundwater hydrostatic pressure + isostatic swelling pressure of the bentonite.	**Insert** Static		Results in 6.2.1 Uncertainty in 7.2	Results in 6.2.1 Uncertainty in 7.2	
	Copper shell Creep or static		Results in 6.2.4 Uncertainty in 7.5	Results in 6.2.4 Uncertainty in 7.5	
4) Glacial isostatic pressure (additional isostatic pressure, only during glacial period).	**Insert** Static				Results in 6.2.1, 6.2.2 and 6.2.3 Uncertainty in 7.4
	Copper shell Creep or static				Results in 6.2.4. Uncertainty in 7.5
5) Shear load due to rock displacement. Amplitude is 5 cm and shear velocity is 1 m/s.	**Insert** Short-time forced displacement			Results in 6.2.1, 6.2.2 and 6.2.3 Uncertainty in 7.6	
	Copper shell Short-time forced displacement			Results in 6.2.4 Uncertainty in 7.7	

Table 7-2. Uncertainty analyses, glacial load on the insert, cylindrical part.

#	Purpose	Task	Subtask	Analysis methodology	Safety factors	Input Data (BWR, PWR)	Comment
1	Analyse dimensioning of insert.	Determine limit load.		Elastic-plastic stress analysis, 2D and 3D.	**Design pressure** S_F = 1.5 –> 50 × 1.5 = 75 MPa.	$R_{p0.2}$ = 240 MPa	Result judged to be pessimistic. Used $R_{p0.2}$ value lower than “as manufactured”.
2	Define acceptance criteria.	Find acceptable defect sizes.	Postulate volumetric defects, spherical holes and slits.	Elastic-plastic stress analysis 3D.	**Design pressure** S_F = 1.5 –> 50 × 1.5 = 75 MPa.	$R_{p0.2}$ = 240 MPa	Result judged to be pessimistic. Used $R_{p0.2}$ value lower than “as manufactured”.
3	Define acceptance criteria.	Find acceptable defect sizes.	Postulate crack-like defects, semi-elliptical.	Linear damage tolerance analysis.	Safety factor for crack initiation S_{FK} = 3.16. Safety factor for plastic collapse S_{FL} = 2.7.	BWR: K_{IC} = 78.0 MPa(m)$^{1/2}$, PWR: K_{IC} = 70.6 MPa(m)$^{1/2}$ $R_{p0.2}$ = 240 MPa Dataset at room temperature. Comparison to data at 0 °C shows no differences in the results. Use of fracture toughness data on 2 mm crack growth not allowed for the isostatic load case.	Results judged to be pessimistic in total.
4	Define acceptance criteria.	Handle limitations in inspectability with NDT.	Remove material in central area and determine acceptable size on fictive slits.	Elastic-plastic stress analysis 3D.	**Design pressure** S_F = 1.5 –> 50 × 1.5 = 75 MPa.	$R_{p0.2}$ = 240 MPa	Result judged to be very pessimistic in terms of the postulated defects.
5	Determine effect of asymmetric loads.	Find acceptable defects sizes.	Postulate crack-like defects, semi-elliptical.	Linear damage tolerance analysis.	Safety factor for crack initiation SF_K = 3.16. Safety factor for plastic collapse SF_L = 2.7.	BWR: K_{IC} = 78.0 MPa(m)$^{1/2}$ $R_{p0.2}$ = 293 MPa Dataset at room temperature. Comparison to data at 0 °C shows no difference in the results. The use of data on 2 mm crack growth is not allowed for force-controlled load cases.	The insert will withstand the stresses elastically, without plastic deformation or risk of damage. The results judged to be pessimistic.

Table 7-3. Sensitivity analyses to estimate possible errors due to simplifications and idealisations in the analysis of the insert, cylindrical part.

#	Purpose	Task	Subtask	Comments
1	Sensitivity analyses: geometry and canister components.	Sensitivity analysis, structural components.	Analyse: A) Only insert. B) Insert + Cu shell. C) Insert + Cu shell + insert tubes.	Additional structural components give only marginal increase on load capacity.
2	Sensitivity analyses: geometry and canister components.	Sensitivity analysis of the cross-section size.	Analyse nominal geometry and maximum offset steel cassette in combination with defects.	The worst-case combination is considered in the damage tolerance analysis.
3	Influence from assumption regarding friction coefficient between components.	Sensitivity analysis on the friction between the copper shell and insert.	See Dillström et al. (2010).	At interesting stress levels, the possible errors are small.
4	Uncertainty analysis methodology.	Validate approach.	Compare analyses between different works, see Table 6-3.	The magnitude of the collapse load shows that a pessimistic analysis was used for the damage tolerance analysis of the isostatic load case.
5	Uncertainty analysis methodology.	Validate simplified tension model.	Compare to generalised tension model; see Dillström et al. (2010).	No effect can be traced.
6	Material model of channel tubes does not consider the possible softening during casting.	Validate the influence of the global insert strength.	Analyse the “as-manufactured” properties of the insert, including the steel channel tubes.	Performed during the probabilistic analysis of the isostatic load case in Dillström and Manngård (2017). The collapse load for the inserts is still higher than 75 MPa.

Table 7-4. Uncertainty analyses of insert base. The analysis follows the same methodology as that for the cylindrical part of the insert.

#	Purpose	Task	Subtask	Analysis strategy and methodology	Safety factors	Input Data	Comment
1	Analyse dimensioning of the base.	Determine limit load.		Elastic-plastic stress analysis, 2D.	**Design pressure** S_F = 1.5.	σ_s = 240 MPa	Result judged to be reliable. Set margin > 2 to limit load. Base of BWR 20 mm thinner than nominal can be accepted.
2	Define acceptance criteria.	Find acceptable defect sizes.	Postulate crack-like defects, semi-elliptical	Linear analysis.	Safety factor for brittle fracture S_{FK} = 3.16. Safety factor for plastic collapse S_{FL} = 2.4.		Analysed in 6.2.1. Acceptable crack size > 80 % of the base thickness.
3	Determine geometry and insert geometries.	Choose least favourable tolerances.					Analysed in 6.2.1. Acceptable crack size > 80 % of the base thickness.
4	Material model of channel tubes does not consider the possible softening during casting.						Judged to have minimal influence on the results.

Table 7-5 Uncertainty analyses insert lid (steel lid).

#	Purpose	Task	Subtask	Analysis strategy and methodology	Safety factors	Input Data	Comment
1	Analyse dimensioning of the insert.	Determine limit load.		Elastic-plastic stress analysis, 2D.	Design pressure SF 1.5 according to ASME III.	According to SS-EN10025 minimum values.	Result judged to be reliable. Set margin >2 to limit load.
2	Determine geometry and insert geometries.	Choose least favourable tolerances.	Investigate the mechanical response.	Elastic-plastic stress analysis, 3D.			The manufacturing tolerances of the steel lid are narrow. It has been shown that macroscopic defects can be accepted.
3	Material model for the channel tubes does not consider possible softening of the material during casting						Judged to have minimal influence on the results for the steel lid.
4	Set prestrain in the M30 screw.	Analyse different prestrains in the screw.	Include or exclude the copper gasket also.	Elastic-plastic stress analysis, 3D.		Different prestrains and shear planes.	The prestrain and the influence of the copper gasket have a small influence on the results.
5	Establish mechanical components in the lid, valve, spring, and organic gaskets.	Determine the function of the components in the final repository.	Determine whether the deformation in the steel lid is plastic.	Elastic-plastic stress analysis, 3D.		Different shear planes.	Only elastic strains occur in the steel lid; result judged to have minimal influence on the results.

7.4.2 Residual stresses in inserts

Residual stresses induced in the material during manufacturing processes such as welding, hot-deformation, casting or machining are secondary stresses. The origin of these types of residual stresses is the casting process. The cylindrical surface is solidified first, and the shrinking of the melt iron inside the thicker sections later causes tension, which in turn causes compression in the surface areas as a balancing reaction. The residual stresses do not have any external driving force that would continue their existence after yielding or thermal stress relief treatment of the material.

Residual stress measurements in the BWR and PWR inserts were performed via two different techniques: deep-hole drilling (DHD) and incremental centre-hole drilling (ICHD). All residual stress measurements are summarised in Table 7-6 (see Shipsha 2015). The ICHD method provides near-surface measurements up to depths of approximately 1 mm, and the DHD technique is generally suitable and capable of residual stress measurement through the entire cross-section of a component, except for 1 mm near-surface regions. The two methods are thus complementary.

Table 7-6. Summary of the residual stress measurements in the BWR and PWR inserts (Shipsha 2015).

Measurement method	BWR inserts			PWR inserts	
	I63	I54	I56	IP25	IP8
ICHD	–	27 pos.	9 pos.	2 pos.	26 pos.
DHD	5 pos.	–	–	3 pos.	–

In Shipsha (2015), a very pessimistic assumption and a local extreme stress value of 90 MPa of hoop stress developed in the support plates are used as data during the calculations of surface defects in the PWR inserts. These local peaks in the residual stresses are likely due to the different material properties between iron and steel. If the approach to use extreme values is applied when analysing the through-thickness cracks in the nodular cast iron, unrealistic results are obtained. Therefore, the tensile residual stresses affecting the PWR regions are based on the general stress level from the residual stress test specimen from the region. The residual stresses have a significant impact on the acceptable sizes of the through-thickness cracks but do not affect the results for the surface defects. Table 7-7 shows the postulated residual stresses used during the analysis of the axial crack-like defects in the PWR inserts (Alverlind 2016a).

Table 7-7. Residual stresses used for the analysis of axial crack-like defects in the PWR insert (Alverlind 2016a).

PWR defect position in Figure 6-9	Residual hoop stress (MPa)	Residual radial stress (MPa)
1, 2	0	–
3	20	–
4	–	20

The residual stresses in the BWR insert were likewise pessimistically estimated in Shipsha (2015), using extreme values from locations deep within the insert. Table 7-8 shows the residual stresses for the axial crack positions evaluated for the BWR insert in Alverlind (2016a). The analysed residual stresses were measured through the support plate.

Table 7-8. Residual stresses used for the analysis of the axial crack-like defects in the BWR-inserts (Alverlind 2016a).

BWR defect position in Figure 6-9	Residual hoop stress (MPa)	Residual radial stress (MPa)
1, 2, 5 and 10	0–60 MPa	–
3, 4	10 MPa	–
6	30 MPa	–
8, 9 (7)	–	30 MPa

7.4.3 Summary of the analysis of the canister and insert under the glacial load

BWR and PWR insert, cylindrical part

The calculations are based on statistically well-documented data and well-established analysis procedures; the uncertainties are judged to be small compared to using the design load of 50 MPa. This is further supported by a probabilistic analysis in Dillström (2009a) and two pressure tests in Nilsson et al. (2005). The residual stresses are judged to be secondary and are considered during the investigation of acceptable axial cracks.

BWR and PWR insert integrated base

The calculations are based on statistically well-documented data and well-established analysis procedures; the uncertainties are judged to be small compared with the design load of 50 MPa. The collapse load is greater than 100 MPa for the BWR when the base is 20 mm thinner than the nominal thickness, in Table 5-1. The integrated base is a robust part of the insert in terms of mechanical strength.

Steel lid for the BWR and PWR inserts

The results for the steel lid are given in Section 6.2.2. The calculations are based on minimum standard requirements and well-established analysis procedures; the uncertainties are judged to be small compared with the design load of 50 MPa. The steel lid is a very robust part of the canister in terms of mechanical strength.

7.5 Uncertainty analysis, glacial load, copper shell

The results for the copper shell are given in Section 6.2.4 and can be summarised as follows:

The isostatic load case has been investigated in different studies with different constitutive models, and the maximum plastic strain is in the range of 20–60 % in the copper shell. This includes both the initial plastic strain and the successive creep strain that occurs after 100 000 years at the geometrically singular point at the root of the weld. Generally, at the global level, the strains are much lower. The singular point peak creep strain value cannot cause any global damage because the loading is displacement controlled.

The copper shell will deform when the glacial load is applied, and the initial gaps between the copper shell and iron insert will be closed. The insert will have small deformations less than 1 mm.

7.5.1 Uncertainties in the input data

The following assumptions for the input data that can influence the final results have been identified:

The influence of the temperature on the ductility of copper has been investigated using creep tests and very low strain-rate tests. The ductility is at least 160 % plastic true strain in the copper shell at 125 °C. The temperature in the repository during this condition will be in the range of 0–100 °C. Therefore, the ductility is satisfactory in the temperature range of the repository conditions.

The influence of the simulation time for the creep analysis was investigated in Hernelind (2017a) from 100 000 years to 1 000 000 years as a sensitivity analysis. The creep rate was very low. The maximum inelastic deformation increased by 3 % during the prolonged analysis time of 900 000 years, which confirms that the maximum deformation is controlled by constraints due to the isostatic pressure and design of the KBS-3 canister to withstand pressure load. Figure 7-2 shows the evolution of the inelastic strain (*CEEQ*) as a function of time after disposal.

The initial nominal geometry of the canister was used in the analysis. In practice, bentonite swelling and water pressure will initiate creep at an earlier stage and thus reduce the creep strain under glaciation. A special condition included an eccentric insert positioned relative to the copper shell and an uneven pressure load acting on the copper base and lid of the canister, as studied in Hernelind (2017a). The eccentric-positioned insert did not seem to influence the maximum strain level, and the magnitude was approximately 60 % plastic strain close to the welded region of the lid for both the centric and eccentric insert.

The influence of the geometry at the bottom of the slit (the root of the weld) has been investigated. A sharp geometry for the slit bottom in combination with a high outer pressure has been investigated.

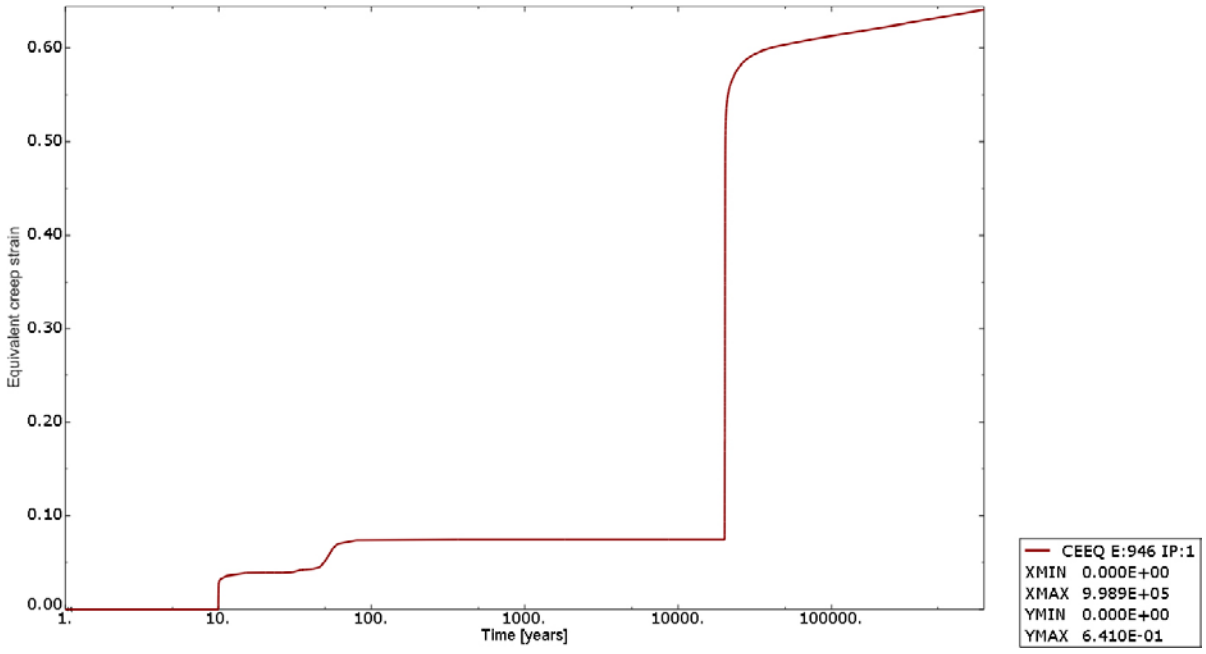

Figure 7-2. *Maximum inelastic strain (CEEQ) versus time for the "red_dim"case, that is, the isostatic case with assumptions of a dry deposition hole and a postulated 60 MPa outer pressure after 20 000 years (Hernelind 2017a). As seen, the inelastic strain converges in the range of 60 % after 100 000 years, and the prolonged analysis time of 900 000 years increases the inelastic strain by approximately 3 %.*

7.5.2 Uncertainties in the calculations

The uncertainty in the creep model used in Hernelind (2015a) was reported in Hernelind (2010), regarding a creep strain rate that was magnified by a factor of five. Therefore, in Hernelind (2010), the creep model was used with a factor of five regarding the creep rate, when used in conjunction with the rock shear global model. The result of this model is also valid for other results using the same copper creep model.

To reduce the uncertainties, different strategies have been used for calculating deformation in the copper shell. The elastic-plastic approach and a very high isostatic load were used to determine the upper magnitude of the possible plastic deformation that can occur during the design of the KBS-3 canister and isostatic load. The VTT creep model was also used to complete the sensitivity study.

The mesh density and shape of the finite elements impact the final results. However, in order to consider these uncertainties in the performed analyses, different mesh densities, FE-software programmes and copper shell geometries have been used.

7.5.3 Uncertainties in the results

The creep ductility in OFP copper has been shown to be sufficient as an "as-manufactured" material for the tubes, lids and FSWs. However, the amount of cold work in the copper components after manufacturing must not be excessively high; the requirement of a minimum of 160 % true plastic strain must be fulfilled for the copper shell, with the exception of local acceptable indentations due to incorrect handling of the copper. Therefore, the requirements of the copper shell components have been derived from the loads and conditions in the final repository.

The most uncertain part of characterizing the creep-related deformation in copper is to extrapolate the creep ductility achieved from the creep tests performed for thousands of hours to represent the ductility properties from a post-closure safety perspective for hundreds of thousands of years. However, the deformation of the global copper shell is small, and the highest plastic strains are very local, so the margins in the final repository are judged to be sufficient.

7.5.4 Residual stresses in the copper shell

In Raiko et al. (2010), it was stated that the residual stresses in the copper shell are primarily related to the possibility that stress corrosion cracking may appear for some situations or that elastic deformation may occur. However, the measurements presented in Raiko et al. (2010) show that the residual stresses in the copper shell and the FSW were modest and rather evenly distributed; all values obtained had an absolute value less than 60 MPa. The crucial parameter is the ductility of the copper in terms of the mechanical integrity.

Nevertheless, it should be noted in this report that the true plastic strain (ε) should not exceed 80 % in the copper shell in the final repository, as stated in Section 6.2.4. A consequence of this range for inelastic strain is that the stress in the copper shell may reach a magnitude of 300 MPa, according to Figures 4-8 and 4-9, which is a much higher magnitude than the measured residual stress levels. Hence, it is justified to exclude the residual stresses from the mechanical analyses of the copper shell.

7.5.5 Summary of the analysis of the canister under glacial load for the copper shell

Overall, the isostatic load case is judged to be well analysed, and the different studies present reasonable results; the true plastic strain does not exceed the failure criterion of 80 % in the copper, and there is no result that threatens the mechanical integrity of the copper shell. As long as the ductility of the copper is sustained from a post-closure safety perspective, the failure criterion is fulfilled, and the canister will remain leak tight from a mechanical point of view.

7.6 Uncertainty analysis, rock shear load, insert

The rock shear analyses consist of a series of subsequent analyses in which the damage tolerance analyses from Dillström (2017a) and Bolinder et al. (2017) are set as the inputs for this design analysis report. This section consider the uncertainties given in Hernelind (2010, 2016b) as input uncertainties and addresses the uncertainty in the results given by ASM (1990).

7.6.1 Uncertainties in the inputs

In Hernelind (2010), a number of uncertainties are given that generated uncertainties in the inputs used in Dillström and Bolinder (2010). These uncertainties are as follows:

The stress-strain relationship of the bentonite has a great effect on the outcome from the study by Hernelind (2010).

All canister materials, and the bentonite, experience strain-rate effects; the stress-strain relationships change when the strain rate changes. This was not fully implemented for the copper shell in all analyses in Hernelind (2010).

Initial conditions in terms of homogenisation of the buffer may have an influence. Therefore, rock shearing analyses have been performed in which the shearing is assumed to start as an initial condition for the swelling pressure based on the results from the homogenisation analysis of the buffer and with an initial geometry corresponding to the final geometry from the homogenisation analysis.

The position for the worst case shear plane of the insert is assumed to be a 5 cm rock shearing load perpendicular to the canister axis at 75 % of the insert height. In Hernelind and Börgesson (2018), the locations at 70 % and 80 % of the insert height were investigated.

The coefficients of friction to define the interactions between the different components used in Hernelind (2010) may influence the results and have therefore been subjected to a sensitivity analysis.

The natural scattering in the material data for the nodular cast iron shown in Figures 4-4, 4-5 and 4-7 has been investigated in Hernelind (2014a) and further investigated in the probabilistic analysis of the rock shear load case in Dillström (2014a). The influence of the yield stress on the global response is small, which in turn leads to a small influence on the stresses and strains that occur in the insert. This is the justification for neglecting the yield stress of the nodular cast iron as a design parameter in terms of the rock shear case. In the damage tolerance analysis, statistically averaged values for the stress-strain relationship and fracture toughness are used.

The analyses of the rock shear case are based on material data from the BWR inserts. However, the difference between the BWR and PWR stress-strain curves is small and well within the investigations in Hernelind (2014a). The used fracture toughness is lower for the PWR inserts than the BWR inserts to achieve margins in terms of the manufacturing requirements for the PWR inserts.

The influence of the steel tube cassette positioned offset in relation to the centre of the insert and the resulting decreased edge distance of the insert, dimension *H* in Figure 5-5 and Figure 5-6, was studied in Hernelind (2014d, e, 2015b). The results in Dillström (2015a and 2015b) and Hernelind (2015c) show that the decreased edge distance does not influence the mechanical response in the rock shear case or the acceptable defect sizes derived from rock shearing.

The influence of the steel channel tubes was also investigated in Hernelind (2014a, d, e, 2015b). Basically, the steel channel tubes have been modelled related to the insert and without support plates, and they have been compared with models with contact between the nodular cast iron-steel channel tubes, including the support plates and other steel components in the base of the inserts. The conclusion in Hernelind (2010, 2017b) was that the simplified geometry of the steel channel tubes tied to the nodular cast iron without support plates is a satisfactory numerical idealisation of the geometry and mechanical response of the insert and canister.

In Hernelind and Börgesson (2018), the influence of the steel tube stress-strain properties was investigated. The insert casting process affects the mechanical properties of the steel channel tubes. The compilation is shown in Table 7-8.

Table 7-8. Summary of the results for the insert and channel tubes of the BWR and PWR inserts for the rock shear case after a 5 cm shear load (Hernelind and Börgesson 2018).

Model name, comment	1–nodular cast iron 2–steel channel tubes	PEEQ (%)		Mises (MPa)		S33 (MPa) maximum axial stress
	Insert material	1	2	1	2	1
PWR_quarter_2022, PWR insert, original steel data from Table 4-4 before casting of insert		0.35	0.20	312	415	319
PWR_quarter_channels_2022, PWR insert, steel data from after casting of insert		0.39	0.36	314	241	320
quarter_2022, BWR insert, reference model, original steel data before casting of insert		0.45	0.54	318	419	329
quarter_channels_2022, BWR insert using new material model for the channel tubes		0.54	1.13	324	255	332
quarter_new_2022_E381, BWR insert, reference model – improved mesh		0.45	0.54	316	419	328
quarter_new_channels_2022, BWR insert using new material model for the channel tubes – improved mesh		0.44	0.80	317	249	332

The findings are summarised as the following:

- For the nodular cast iron in the insert, *PEEQ* increases slightly (3–15 %) when using the material definitions based on measurements after casting. The largest increase is achieved for the BWR insert using the original mesh – the improved mesh only implies an increase of 3 %.
- For the channel tubes, the use of material definitions based on measurements after casting implies a substantial decrease in the maximum von Mises stress (40–50 %). The decrease is as expected due to the decrease in the strain hardening. The *PEEQ* also increases substantially (35–65 %) due to less strain hardening, using material definitions based on measurements after casting.
- For the copper shell maximum, the *PEEQ* is 8 % regardless of the material definition used for the channel tubes.
- The ductility requirement of a minimum of 3 % elongation at failure is judged to be sufficient for the steel channel tubes, which is the same for the nodular cast iron.
- In total, the influence of the steel channel tube stress-strain properties can be considered as negligible in the rock shear case.

The influence of a volumetric defect in the insert during the rock shear case was investigated in Hernelind (2014g). The effect of the global response of the insert with spherical void defects in the rock shear case was investigated. The defects were not considered to be crack-like. For this case, the rock shear was assumed to occur perpendicular to the canister axis at 75 % of the insert height. The shear calculations have conducted up to a total shear of 10 cm. Based on the results, the mechanical integrity of the canister is not considered to be threatened. Therefore, volumetric defects are not considered to be critical for the rock shear case.

7.6.2 Uncertainties in the analysis methodology

The analysis methods used are well established, but some uncertainties can be identified:

Overall, displacements from the Hernelind global analyses were transferred to Inspecta, where a quality check was conducted before the damage analyses occurred. The uncertainty in the data transfer was analysed in Dillström and Bolinder (2010), in which the principal stresses generated in Hernelind (2010) and in Dillström and Bolinder (2010) were compared. The differences are considered to be sufficiently small to not significantly influence the results.

The mesh has been shown to influence the results in terms of the strains and stresses (see Section 6.2.1). The reason for the high stresses is mainly dependent on the element meshes, which are not designed to be used in a damage tolerance analysis. For example, many stress concentrations are directly related to the use of wedge elements. In all cases, disregarding the elements that behave poorly significantly reduces the locally higher tensile stresses. The global analyses of the rock shear case have also been modelled by other authors using other FE-software programmes (see Andersson et al. 2016 and Unosson 2016). The consistency between the different works shows that uncertainties in the analysis methodology can be considered to be low.

7.6.3 Estimation of the uncertainties in the results

A range of uncertain factors influence the results of the shear load case and, hence, also the derived acceptable defect sizes.

In Dillström and Bolinder (2010), a sensitivity analysis showed that the density of the bentonite has a major influence on the acceptable defect size. In Hernelind (2010), it is stated that the used stress-strain relationship was likely slightly pessimistic in that the used values corresponded to somewhat higher densities than the actual ones when including the strain-rate effects. Thus, the presented values for the acceptable defect sizes are, in this respect, judged to be slightly pessimistic in Hernelind (2010). This is also valid for other reports by Hernelind.

The influence of the *initial* conditions for the buffer was investigated in Hernelind and Börgesson (2018). The initial mean stress (pressure) has previously been assumed to build up due to the swelling pressure (dependent on the density and type of bentonite) and external water pressure, which is dependent on the vertical position of the deposition hole. The initial conditions of the buffer have been based on average values corresponding to a completely homogeneous buffer, and therefore, the initial condition stress has been defined using approximate values of the average dry density of the bentonite in the deposition hole, which should result in an approximately correct mean stress in the buffer at the start of rock shearing.

The worst location of the rock shear plane was shown to be at approximately 75 % of the insert height. Both 70 % and 80 % of the insert height resulted in less stresses and strains for the insert in Hernelind and Börgesson (2018). The PEEQ shows maximum values when rock shearing is positioned at an 80 % distance from the insert height both for the insert and the channel tubes. However, the difference is judged to be small, in the range of 0.3 % in terms of plastic strain in the nodular cast iron at a 5 cm rock shear load.

The *strain-rate effect for the rock shear case* also influenced the results in Dillström and Bolinder et al. (2010) and in Bolinder et al. (2017). However, it is concluded in Dillström (2014c) that the influence from strain rate on the final result is small and can be negligible.

The influence of the *coefficient of friction* defining the interactions between different canister parts was shown in Hernelind (2010) to have a negligible influence on the detrimental axial stress (S_{33}) level in the insert.

The influence of the *rock shear velocity* was investigated in Hernelind (2014a). Two different rock shear velocities, 5 cm/s and 1 m/s, were used (different by a factor of 20), and the influence on the stresses and strains was in the range of only a few percent.

Scatter in the experimental stress-strain data for the canister materials will always be present. The used values are judged to be representative of the materials at the present conditions.

The scatter in the fracture toughness in terms of the *J*-integral is handled by using a confidence interval, as recommended in the well-known R6 method (R6 uses 95 % as a confidence level). The same approach is used in SSM report 2009:26 (Dillström 2009b), in which a confidence level of 90 % is recommended for the deterministic analysis by implementing safety factors into the analysis; small local variations are considered to be negligible in the analysis. It should also be noted that fracture toughness tests of the nodular cast iron have been performed using large-scale test specimens from

the BWR and PWR inserts (see Jonsson 2017). The nodular cast iron material is capable of stable crack growth in the range of 30–40 mm or even longer. This proves that the toughness of the inserts is very high, and the use of J_{2mm} derived from 2 mm stable crack growth from the fracture toughness tests as a failure criterion for the full-scale inserts is pessimistic and applicable.

The influence of the deformation rate on the fracture toughness was investigated in Rydén (2012). Because the approaches for the displacement rate of the rock were sinusoidal or constant, the obtained maximum strain rates in the insert at 5 cm shear were 0.33 s^{-1} and 0.21 s^{-1}. Therefore, a pessimistic approach is to use 0.5 s^{-1} as an upper limit of the elastic-plastic strain rate for the insert. However, the relevant parameter for estimating the deformation rate near a sharp crack-like defect is the change in the *J*-value per unit time, that is, $\partial J/\partial t$. In Faleskog (2012b), $\partial J/\partial t$ was estimated to be 2 000 kN/(ms) in the insert during the rock shear case. In Jonsson (2017) and Öberg and Faleskog (2012), the high rate of $\partial J/\partial t$ during the fracture toughness tests of the BWR material was found to be in the range of 2 000–7 000 kN/(ms). The high strain rate in the fracture toughness tests was also shown to result in a higher fracture toughness compared with the quasi-static testing following the standard ASTM E 1820:2009 (see Jonsson 2017). The conclusion is that the fracture toughness tests were performed within the strain rate margin in the postulated rock shear case and that the used fracture toughness derived from the quasi-static tests is pessimistic in terms of the strain rate.

The influence of the shear plane at the canister with a minimal edge distance was investigated in Hernelind (2014d). The influence was shown to be small, and the acceptable defect sizes were unaffected.

The compressive residual stresses on the component surfaces are beneficial for surface cracks due to their crack-closing tendency as well as for global bending loads due to the larger applied tensile stress required to cause yielding. The residual stresses have no practical influence on the limit load or other higher loads that cause yielding because the manufacturing-based residual stresses are expected to vanish when the material yields. For the postulated cracks, residual stresses might increase the load assumption in the case of brittle fracturing, but in the case of plastic tearing or stable crack growth, the loading effect of the residual stresses is low due to the secondary character of the load. Canister inserts including postulated acceptable cracks, do not behave in a brittle manner in any load case or condition assessed in this report (Raiko et al. 2010).

One extreme case of for an uneven density distribution of the buffer in a deposition hole was analysed regarding the effect of rock shear on the canister. The combination of load case 2 and load case 5, bending stresses in the canister in combination with a rock shear, was analysed in Börgesson and Hernelind (2013). The results show that the modelled case yields lower stresses in both the copper shell and cast iron insert than the corresponding base case with a 2 050 kg/m^3 density of the buffer for both the PWR and BWR canisters and for both cases of shear plane locations. The maximum principal stresses in the insert before shear were approximately 70 MPa, which is lower than the analytical result of 111.5 MPa in Börgesson et al. (2009). This mainly depended on the smoother stress distribution in the FE-simulation cases than that applied in the simplified analytical calculation in Börgesson et al. (2009) and on the copper shell that reduced and redistributed the stresses from the bentonite.

Axial cracks in combination with the rock shear case were investigated in Bolinder et al. (2014) using a bentonite density at a saturation of 2 050 kg/m^3. A very large postulated axial defect (length ~ 2 m) between the BWR channel tubes was almost acceptable for the design case (safety factor = 1.74). This means that the acceptable axial crack length (length ~ ½ –1 m) derived from the isostatic load case is smaller and dimensioning for these defects.

One important question pertains to the consequence of unstable crack growth due to an initial crack-like defect size larger than the acceptable defect size. This question has been investigated in Andersson et al. (2016), Unosson (2016), and Hernelind (2016a).

In Unosson (2016), a study was carried out to investigate the propagation and consequences of a large crack in the insert for the case of earthquake-induced rock shear, both through the deposition hole and acting on the canister after emplacement in the deposition hole. A finite element simulation study is presented for the BWR version of the canister. Six loading cases are considered with two types of initial crack planes present in the insert, including the largest conceivable circumferential crack between the channel tubes and cases with surface cracks; see examples in Figure 7-3.

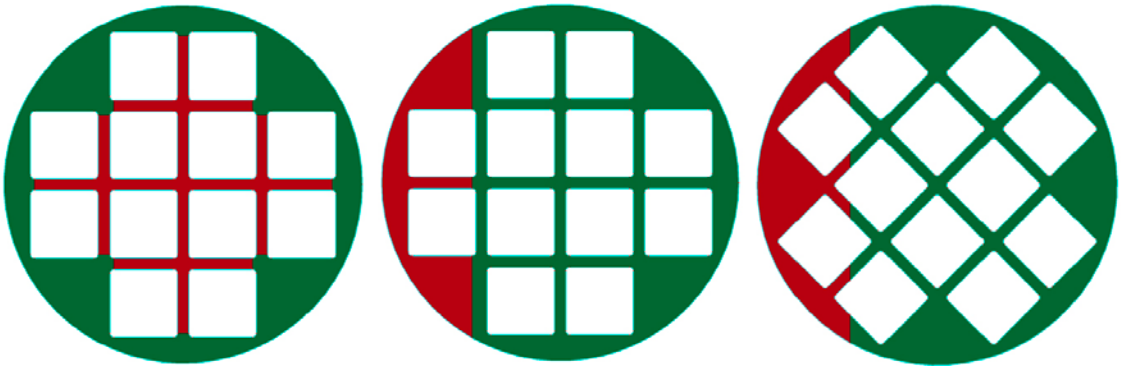

Figure 7-3. *Cross section of the insert showing the extent of the crack planes (red area) between the steel channel tubes (Unosson 2016).*

The analysis shows that the postulated internal crack will propagate for all except two load cases. The results show that there is no risk of material failure in the copper shell and that the global dynamic stability of the canister is preserved for shearing magnitudes of at least 10 cm. Because the investigation shows that very large circumferential cracks between the channel tubes and surface cracks in the BWR inserts do not threaten the integrity of the copper shell of the canister for the loading range in this study, it can be concluded that these cracks can be accepted and that inspection is not required. Thus, the analysis in Unosson (2016) was not aimed to follow the ASME code and should be considered to provide important information in terms of the mechanical response of the insert in the case of a rock shear and the presence of unacceptable defects. The steel channel tubes behave like reinforcing composite bars in the cast iron and prevent the cracks from cutting the insert into separate pieces; the mechanics are judged to be extrapolated to the PWR as well. The justification is due to the similar nominal mechanical responses of the BWR and PWR inserts during the rock shear case (Hernelind 2010). The steel channel tubes enable the compressive state in the cast iron, as shown in Figure 7-4.

In Andersson et al. (2016) and in Hernelind (2016a), the influences of large initial crack defects between the channel tubes of the BWR and PWR inserts were also investigated, but with the conventional ASME Section XI approach. The main conclusions from the damage tolerance analysis are the following: With regards to the BWR insert, the resulting acceptable defect length is 372 mm from a damage tolerance perspective using ASME safety factors. With regards to the PWR insert, the defect length parameter equal to 140 mm is acceptable from a damage tolerance perspective using ASME safety factors; see Figure 7-5 for an illustration of the acceptable defects between the channel tubes of the BWR and PWR inserts.

A purely hypothetical rock shear case, in which the insert is postulated to be broken into two separate pieces, was also investigated in Hernelind (2014c). The rock shearing was assumed to occur perpendicular to the canister at a distance 2/3 from the base of the insert when the insert and channel tubes were assumed to have an entire crack through them inclined 5 ° to the normal direction of the centre axis in tension. The shear calculations were carried out to a total shear of 10 cm. In addition to rock shear, the model has been used to analyse the effects of increasing the glaciation pressure to 15 or 45 MPa combined with rock shear when considering creep in the copper shell, using the "Swerea KIMAB and KTH creep model" in Section 4.7.4. The conclusion is that the copper shell will remain tight even for these very pessimistic assumptions.

Altogether, the uncertainties given here imply that the acceptable defect sizes given in Section 6.2.1 are pessimistic.

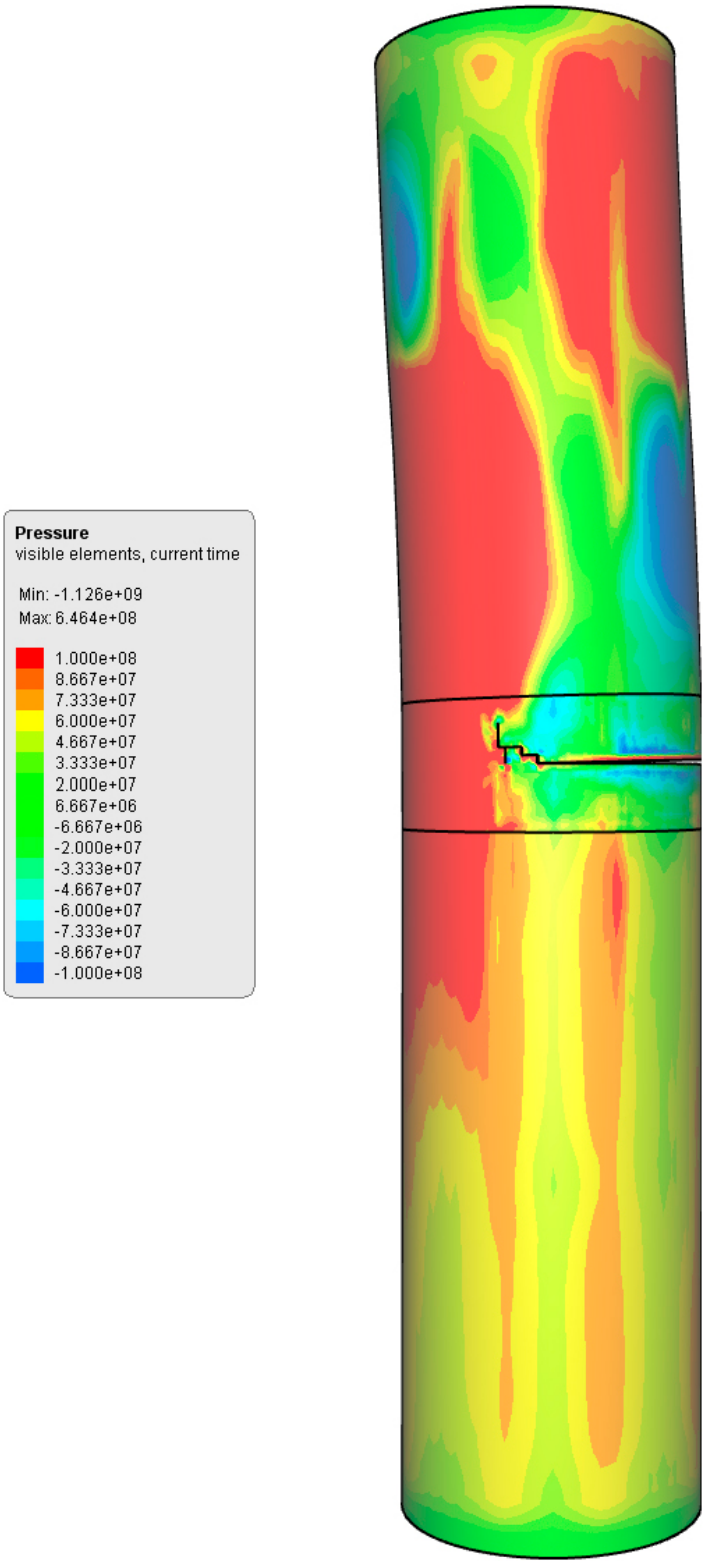

Figure 7-4. *Compressive (positive values, green to red) and tensile (negative values, green to blue) zones at a stage during the shear loading of the insert with a large initial crack (Unosson 2016).*

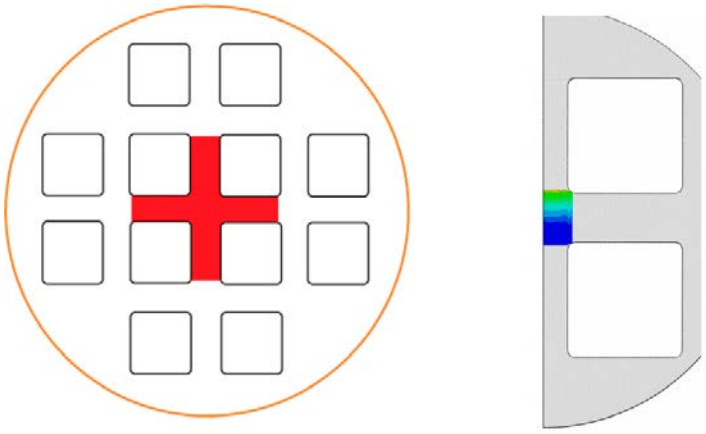

Figure 7-5. *Schematic of the initial acceptable crack-like defects in the BWR (left) and PWR (right) derived in Andersson et al. (2016). The initial crack sizes are shown with the coloured areas in the cross sections.*

7.7 Uncertainty analysis, rock shear load, copper shell

7.7.1 Uncertainties in the input parameters

Most uncertainties in the results for the copper shell depend on the accuracy of the used constitutive model. Therefore, rock shearing was modelled with two different elastic-plastic constitutive models described in Section 4.7.3. These models are valid at room temperature. The justification to use these models in the rock shear case is derived from the estimated temperature in the range of 0–20 °C when the rock shear occurs and the fact that the rock shear occurs during a short time (a fraction of a second so that creep in the copper shell is excluded). The strain rate is not an explicit parameter in the constitutive models. However, in Unosson (2014), the influence of the strain rate was discussed and the tensile tests were modelled. After necking, the material in the bar was subjected to a range of strain rates between approximately 1 s^{-1} and 10^2 s^{-1} for a displacement-controlled constant loading rate, and the simulations and measurements were in agreement. The strain rate in the copper shell in the final repository was near zero for all load cases except the rock shear case, in which the strain rate was locally in the range of approximately 10^2 s^{-1} when the shear plane was located at the copper lid. This is approximately the same strain rate as in the test specimens after necking. Therefore, it can be concluded that the influence of uncertainties in the strain rate in the rock shear case can be neglected.

The assumption made for the coefficient of friction between the copper and surrounding materials may influence the deformation of the copper shell.

Different rock shear planes have been used. The most pessimistic shear plane with respect to the deformation in the copper shell is located at the top of the canister, or possibly the base if a welded base is used. The integrated copper base is stiffer than the welded base.

The rock shear case may appear after thousands of years. The dimensions of the copper shell may change due to corrosion. Therefore, an investigation of the rock shear case was performed with decreased thickness in the copper shell; half of the wall thickness of the copper shell was postulated in Hernelind (2015d). In accordance with current design criteria for the canister, plastic strain in the copper shell was used as a failure mechanism and criterion when evaluating the results. A comparison between the constitutive models for the copper shell was also included, and the conclusion was that the canister will maintain its mechanical integrity for the shear load case, even with half of the copper shell thickness (2.5 cm).

Analyses in which the creep strain rate was increased by a factor of 5 are presented in Hernelind (2010). The change in the results was very small for both the short-term and long-term rock shear load analyses because the rock shear case is a displacement-controlled case In addition, the copper shell sooner or later reaches its “final state” due to outer overpressure when the deformations and strains can no longer increase, and a stress relaxation state may occur, as described in Section 6.2.4.

A sensitivity analysis on the influence of the coefficient of friction in Hernelind (2010) showed that the influence is negligible for both the stress and strain levels in the copper shell after rock shear.

The combination of the isostatic load case of 30 MPa and the rock shear case was considered in Hernelind (2010). The combination of load cases was concluded to not threaten the mechanical integrity of the copper shell.

7.7.2 Uncertainties in the analysis methodology

The same uncertainties are valid for the copper shell as for the insert in Section 7.5.2. Specifically, the influence of the mesh has been shown to have an influence on the results in terms of the strains and stresses. Global analyses of the rock shear case have also been modelled by other authors using other FE-software programmes (see Andersson et al. 2016, Hernelind 2017b and Unosson 2016). Moreover, in terms of the plastic deformation in the copper shell, the consistency between the different reports lends support to the conclusion that the results are reliable.

8 Assessment of analysis results against the failure criteria

The failure criteria defined in Section 3.2 have been used to evaluate the acceptability of the calculated results in Chapter 6 and 7. All set criteria are assessed separately in the following subsections. The design verification of the canister as a load-carrying component has been conducted according to mechanical design codes where applicable. As an example, the ASME Boiler and Pressure Vessel Code (ASME 2008a, b) provide methods and application rules for design verification of the reactor pressure vessels. The code provides practical guidance to perform the integrity assessment. However, the canister components are manufactured from atypical materials compared to customary vessels and shells. Thus, examinations on the properties of the construction materials (cast iron and OFP-copper) have been emphasised. The material tests and test data analyses that have been carried out are comprehensive and extensive, and the experimentally determined properties used in the design verification analyses are considered to be reliable.

Moreover, the justification for using the ASME codes was given in Smedstad (2016). The main findings were as follows: *The use of the nodular ductile cast iron in conjunction with ASME III, Division 3 2008 for a Class SC application is possible, but some measurements should be considered. The scope includes defined load cases and references of methodologies, analyses and tests (ASME III division 3 subsection WC).*

8.1 Plastic collapse criteria

As stated in Section 3.2, plastic collapses are not relevant for the copper shell. Since the insert supports the copper shell, the shell cannot collapse inwards.

The basic design verification of the insert against the design pressure **isostatic load** of 50 MPa was conducted according to the ASME Code guidance utilising the limit load method. The canister was modelled using both 2- and 3-dimensional finite elements, in which all components, gaps, tolerances and materials were modelled pessimistically or as realistically as possible, and the limit load was estimated. The acceptance criterion was that the design load shall not exceed 2/3 of the limit load. Separate analyses were performed for the insert cylinder, insert base and steel lid. All of these analyses fulfilled the design criteria. The safety margins used were those recommended by ASME III NB-3213.25 for assessing nuclear pressure vessels under normal operation, as shown in Section 6.2.1 and further in Section 7.4.

In addition to the basic design verification analyses, the strength was also investigated with modelled deviations in the nominal geometry, tolerances, lack of material or inclusions in the cast, and eccentric installation of steel cassettes and axial cracks. The canister was shown to be robust and insensitive to these types of imperfections with respect to its mechanical integrity, based on the failure criteria in Section 3.3.2, the results in Section 6.2.1 and Section 7.4.

The pressure load capacity of the canister was demonstrated previously using two model tests, in which 700 mm long sections of actual canisters were pressure tested up to the limit load. The pressure tests showed that the collapse pressure was between 130 and 140 MPa in both cases, that is, more than twice the design pressure. The pressure tests have also been used for validating the calculation method described in Section 6.2.1.

8.2 Strain criteria – copper shell

The **operational loads** for the copper shell have been analysed; the governing case involves lifting the canister by the lid flange. The strength is sufficient for quasi-static lifting of the canister by the lid flange considering very pessimistic postulated defects according to an analysis performed using ASME XI safety factors. However, the yield stress of the copper is lower than at room temperature

because the canister is heated from the spent fuel inside the sealed canister. For a copper shell with or without defects, the canister lid flange can withstand more than 2 g; the influence of the acceptable defects is small. The canister can withstand an instantaneous stop from a maximum free fall velocity of 2 m/s. The acceptable defect depth due to handling the canister is 5 mm. These conclusions are based on the failure criteria in Section 3.3.1 and the results in Sections 6.1 and 7.1.2.

For cases involving an **isostatic pressure load** or **asymmetric pressure load**, the inelastic strain in the copper shell is moderate. The cases have been investigated in several reports, and the maximum plastic strain is found to arise in the slits of the copper shell. The magnitude of the true inelastic strain is found to be in the range of 20–60 % at a triaxiality of approximately 0. Sensitivity analyses have shown that plastic strain at a magnitude of 74 % occurs very locally. However, it is below the allowed 80 % plastic strain at the triaxiality of 0.33. These conclusions are based on the failure criteria in Section 3.3.1 and the results in Sections 6.2.4, 7.3 and 7.5.

For the **rock shear case,** the plastic strain in the copper shell is significantly affected by the shear planes located near the ends of the canister. The worst shear plane is located approximately 0.5 m from the top of the canister at the 90 % position, and the plastic strain in the copper shell reaches 33 %, albeit locally; this strain is well below the allowed 80 % plastic strain limit. These conclusions are based on the failure criteria in Section 3.3.1 and the results in Sections 6.2.4 and 7.7.

8.3 Strain criteria – insert

For cases involving an **isostatic pressure load** or **asymmetric pressure load**, a plastic strain requirement can be neglected because elastic strains only occur in the BWR and PWR inserts for these cases, based the failure criteria in Section 3.3.2 and the results in Sections 6.2.1 to 6.2.3, 7.2 and 7.4.

For the **rock shear case**, the insert will be subjected to bending. This is the only case that may lead to significant deformation and plastic strain in the insert. Rock shear is, however, a "displacement-controlled load" that causes only secondary stresses according to ASME nomenclature. If the load is secondary, the possible local yielding or cracking leads to decreasing stiffness and increasing deformation in the structure, and consequently, the load would decrease. The analysis results for the rock shear case show that in the case of 5 cm shear, the required plastic strain (ε_{req}) of the nodular cast iron is 3 %. All tensile specimens from BWR inserts I53–I57 and PWR inserts IP23–IP25 in Jonsson (2017) fulfil the elongation at failure criterion. The mechanical tensile properties of BWR inserts were also investigated in Holst and Sarnet (2017) using a statistical approach, showing that the mechanical properties of these inserts mainly meet the requirements of elongation at failure. Table 8-1 and Figure 4-7 indicate that future measurements of the elongations at failure will be above the required 3 %. In the square steel channel tubes, the same criterion of 3 % true plastic strain was judged to be fulfilled. Moreover, in the steel lid, the stresses and strains are low, so plasticity may occur in the solitary contact areas; on the global level, there are only elastic strains in the steel lid. These conclusions are based on the failure criteria in Section 3.3.2 and the results in Sections 6.2.1 to 6.2.3 and 7.6.

Table 8-1. BWR insert elongation measurements for the top slice at 4.6 m.

Insert \ Sample	1	6	2	5	3	4	Average
I53	14.3	13.1	18.1	17.6	14.7	8.9	14.45
I54	7.6	11.7	17.3	9.1	9.9	9.0	10.77
I55	13.4	20.0	14.7	16.3	18.0	17.7	16.68
I56	13.1	16.1	17.7	17.9	12.0	7.6	14.07
I57	12.1	16.4	7.3	16.6	12.3	11.0	12.62
I63	19.4	18.1	14.4	16.1	11.3	7.6	14.48
I72	21.8	15.3	10.1	12.9	9.6	7.5	12.87
I76	16.6	12.2	17.5	14.5	10.4	8.8	13.33
Average	**15.1**		**14.9**		**11.0**		**13.7**

8.4 Fracture resistance criteria and acceptable defect sizes

The material testing has shown that the copper cracks bluntly under tension load and that crack growth does not occur at the applicable temperatures. Therefore, in Section 3.2, brittle failure and crack growth were excluded as failure processes of the copper shell for all load cases.

For the **isostatic load case**, very large cracks with extension in the axial direction can be accepted in the insert. As stated in Dillström (2014b), this is because the tensile stresses are very low in the isostatic load case. Radial/circumferential cracks are not harmful with respect to this load case. With the combination of residual stresses and an isostatic pressure of 50 MPa, it was shown that the acceptable axial length of a through-wall defect is at least 430 mm for the BWR insert and 697 mm for the PWR insert. The safety margins used are those recommended by ASME for assessing nuclear pressure vessels under normal operation. These give a margin of 3.16 against initiation of fracturing for the nodular cast iron based on the failure criteria in Section 3.3.2 and the results in Sections 6.2.1 to 6.2.3 and 7.4

For the **asymmetric pressure loads**, the canister will be subjected to bending, in which case defects of interest include circumferentially oriented cracks propagating from the surface of the insert. The maximum acceptable size is a crack-like surface defect with a depth of 21.1 mm and length of 126 mm on the insert cylinder surface lying in a circumferential orientation for the BWR insert. In this case, the margin is 3.16 against the initiation of fracturing for the nodular cast iron based the failure criteria in Section 3.3.2 and the results in Sections 6.2.1to 6.2.3 and 7.2.

The dimensioning load case with respect to the acceptable circumferentially oriented crack sizes for the BWR and PWR inserts proved to be the **rock shear case**. The design rock shear case is rare and will occur only for very few canisters or none at all. The load will be very short-lived, and there is a low probability that the shear movement will occur more than once for a given canister. The rock shear is classified as a level D load case (emergency condition), according to the ASME Code (ASME 2008b), and the safety factor is likewise determined. A safety factor of 2 is used when defining the acceptable *J*-parameter value from the fracture toughness test results at a stable crack growth of 2 mm. The maximum acceptable surface crack-like defect size on the BWR cylinder surface is a 9.0 mm deep and 22.5 mm long defect lying in a circumferential orientation; the corresponding defect for the PWR is 9.0 mm in depth and 22.5 mm in length. This damage tolerance analysis is the governing case of the canister insert for near-surface volumes. However, the acceptable sizes of the internal defects were found to be larger than the near-surface defects. Between the steel channel tubes, there is no need to require an acceptable circumferentially oriented crack size for the BWR and PWR inserts, and there is no need for NDT inspection requirements. These criteria are based the failure criteria in Section 3.3.2 and the results in Sections 6.2.1 to 6.2.3 and 7.6.

The canister withstands the specified loads with an applicable safety factor even if the material has acceptable-sized defects.

8.5 Essential design parameters

Essential design parameters that have an influence on the canister integrity have either an effect on the static strength or damage tolerance of the canister. The essential design parameters are collected in Table 8-2. The processes on which the parameter has an effect, an estimate of the qualitative sensitivity and a reference to possible manufacturing specification values are also included in Table 8-2.

The performed damage tolerance analyses for the BWR insert are valid also for the VVER insert in terms of the requirements in Table 8-2 and acceptable defect sizes. This approximation is justified in Raiko (2013).

Table 8-2. Essential design parameters.

Parameter	Effects on	Sensitivity	Value derived from the design analysis
Yield stress of the cast iron in compression at room temperature.	Isostatic load case, plastic collapse.	Important but with significant margins.	Minimum 240 MPa true stress.
Ultimate stress of the cast iron in compression at room temperature.	Isostatic load case, plastic collapse.	Less important, plasticity is not achieved in the isostatic load case.	Minimum 323 MPa true stress.
Displacement of the steel cassette in the BWR and PWR insert.	Isostatic load case, plastic collapse.	Important because the collapse load is directly ruled by the weakest load-carrying part of the insert.	Maximum 10 mm deviation from the nominal value.
Fracture toughness of the cast iron at initiation at room temperature or a lower temperature.	Isostatic load case, crack initiation.	Important	K_{IC} > 78.0 MPam$^{0.5}$ BWR, K_{IC} > 70.6 MPam$^{0.5}$ PWR, with 90 % confidence according to Dillström (2009b).
Plastic strain of the cast iron and steel channel tubes at room temperature.	Rock shear case, exceeds plastic strain.	Important but with significant margins.	Minimum 3 % true strain at a distance over 100 mm from the centre point of the insert.
Yield stress of the cast iron in tension at room temperature.	Rock shear case, exceeds plastic strain.	Less important for any load case as long as the plastic strain is fulfilled.	Minimum 240 MPa true stress.
Fracture toughness of the cast iron, including 2 mm stable crack growth (J_{2mm}) at room temperature.	Rock shear case, stable crack growth.	Important	J_{2mm} > 88.1 kNm BWR, J_{2mm} > 78.0 kNm PWR, with 90 % confidence according to Dillström (2009b).
Elastic-plastic strain of the copper shell.	Rock shear case, rupture due to excessive plastic deformation.	Important for the integrity of the canister.	Maximum 80 % true plastic strain in the copper shell. Minimum 160 % true plastic strain at a triaxiality of T = 0.33 in the test specimens.
Creep strain of the copper shell.	Isostatic load case, rupture due to creep deformation.	Important for the integrity of the canister.	Maximum 80 % true plastic strain in the copper shell. Minimum 160 % true plastic strain at a triaxiality of T = 0.33 in the test specimens.
Gap dimensions between the insert and copper shell.	Limits the plastic or creep deformation of the copper shell.	Sensitive and important but strictly set tolerances keep the effect within acceptable limits.	Axial gap 1.7–3.1 mm, radial gap 1.25–2.0 mm.
Wall thickness of the copper shell.	Corrosion resistance.	Non-dimensioning in the design analysis.	Nominal 5 cm.
Radius of the deposition hole.	Uneven swelling.	Low	Smallest verified radius in the bottom part = 0.873 meter largest verified radius in the top part = 0.905 meter.

9 Summary

The mechanical strength of the canister (BWR and PWR types) was studied. The handling load analyses were conducted to determine the magnitude of the handling loads that the canister can withstand without affecting the post-closure safety of the canister so that the canister can still be deposited. The analysed loads in the repository after closure were derived in Posiva SKB (2017). In addition, some derived load cases, especially the uneven bentonite swelling cases, are further developed in this study and its references. The canister geometry is described in detail, including the manufacturing tolerances of the dimensions. The material properties that have been used are summarised. The data is based on a widely used materials testing programme to which there are references. Test specimens from the nodular cast iron show that the material is ductile, and the use of 2 mm stable crack growth is motivated using a large fracture toughness specimen with a 30–40 mm stable crack depth. Failure mechanisms for the canister components are described along with derived failure criteria with numerical values.

The combinations of various load cases are rationalised, and pessimistic combinations are defined. Moreover, the probabilities of various load cases and combinations are used for setting reasonable safety margins. The safety margins according to ASME Code principles for safety class 1 components are applied. A justification for using the ASME codes for nodular cast iron is made.

The governing load cases, which are the isostatic and rock shear cases, are analysed with 2D or global 3D finite element models, including large deformation and nonlinear material modelling and, in some cases, creep. The acceptable defect sizes are determined using the measured fracture resistance curves of the iron insert as a reference with relevant safety factors according to the ASME Pressure Vessel Code requirements. Both the BWR and the PWR inserts are analysed. The conclusions are described in the following.

The canister is shown to be robust for the 50 MPa isostatic pressure load case, and this result has been obtained in different deterministic studies, based on the condition that there are no unacceptable fractures in the insert. The analysis of plastic collapse is performed as a global collapse analysis, which is more realistic than considering local collapse, which is mainly a measure of the amount of the local plasticity in a section of the insert. Pressure tests confirm that the collapse of the insert will occur at a much higher external pressure than the isostatic pressure in the repository. Furthermore, the copper shell will remain intact as long as the insert withstands the outer pressure load. In general, the design of the PWR insert is more robust than that of the BWR insert; however, lower fracture toughness values are used for the PWR insert than the BWR insert, which have an impact on the critical and acceptable defect sizes of the crack-like defects.

The isostatic load case is also investigated using a probabilistic analysis for the BWR insert for isostatic loads. The risk of failure was calculated to be 1×10^{-20}, when the isostatic load is less than 75 MPa.

In regard to copper creep deformation, this report demonstrates that all relevant load cases are in principle displacement controlled, although the full displacement may not occur until long after the load is applied. This means that the final mechanical state in the copper shell can be derived with elastic-plastic models. Both this approach and time-dependent creep modelling are used in the report. The fact that elastic-plastic models can be used for all relevant load cases is significant in terms of the robustness of the conclusions since, as also described in the report, unresolved conceptual uncertainties exist regarding creep in copper. By using elastic-plastic constitutive models, creep modelling can be circumvented for displacement-controlled cases for the copper shell, which is possible because of the load-bearing insert.

For the rock shear load case, the stresses and strains in the canister are high and, depending on the shear amplitude, so are the shear angle and intersection point. The governing case for the insert is a shear impact perpendicular to the canister main axis at approximately 75 % of its length, whereas the governing case for the copper shell is perpendicular to the canister main axis at 90 % of the insert height. The integrity assessments were carried out using stress and strain results from global models

and fracture resistance analyses using the submodelling technique. The submodel analyses utilise the deformations from the global analyses as constraints on the submodel boundaries, and more detailed finite-element meshes are defined with defects included in the models along with elastic-plastic material models. The *J*-integral is used as the fracture parameter for the postulated defects. Rock shear is the governing case with respect to radial crack-like defects because the rock shear will bend the canister more than the worst uneven swelling case. The consequences from unacceptably large initial defects on the integrity of the copper shell in the BWR and PWR inserts are investigated in addition to an insert completely braking into two pieces. The conclusion is that the copper shell will remain leak tight after a rock shear with these very pessimistic insert defects.

Moreover, the rock shear load case is investigated using a probabilistic analysis for the BWR insert. The result shows that the probability for failure of an insert with a rock shear magnitude of 5 cm is in the range of 5.8×10^{-4} to 2.2×10^{-3}.

The corrosion protection layer, the copper shell, is made of soft (hot-worked) copper, so its ability to withstand plastic deformation is particularly high. The design case of the 5 cm rock shear leads to effective plastic strains typically between 5 and 33 %, predominantly in locations of geometrical discontinuities (or even at geometric singularities). This observation applies directly to the short-term analysis, and approximately the same results apply to the creep analysis. In this analysis, the creep does not play an important role in the rock shear case and the inelastic deformation in the copper is sufficiently high for the copper shell to withstand the mechanical loads. The insert also experiences plastic deformation due to rock shear load, but the ductility of the nodular cast iron insert and steel components in the insert are shown to be sufficiently high to withstand the rock shear case.

The combined load of isostatic pressure and rock shear is also analysed in two alternative sequences: either the glacial load exists prior to and during the rock shear or it is applied after the rock shear. The results show that in both cases, the maximum von Mises stress in the insert increases, and the maximum plastic strain in the copper shell also increases compared with the rock shear case without additional glacial pressure load. However, in both analysed cases, the maximum principal stress (in tension) decreases. These results indicate that the damage tolerance of the insert increases if the pressure loads are combined with the rock shear case. This can be explained by the fact that an external pressure load adds compressive stresses in all orientations in the insert, which reduces the maximum tension stress level caused by bending during the rock shear case. Thus, the acceptable faults become larger if the isostatic pressure load acts when the rock shear occurs. The insert also maintains its pressure-bearing properties to all postulated isostatic loads acting during or after a rock shear case.

The requirements for handling the insert and entire canister via the copper shell are investigated. The damage tolerance analysis for the different load cases leads to a number of requirements for inspecting the insert, among which the most rigorous are derived from the rock shear load case. The inspection requirements from the 50 MPa case are more modest; very large volumetric defects in the BWR and PWR inserts can be accepted. The isostatic load case also considers the combination of defects in the cast iron with the lowest acceptable yield stress and minimum acceptable edge distance. The defect requirements in the steel lid and other steel components in the inserts are investigated. For the copper shell, it is important to avoid impact damage or other cold work to prevent the copper ductility from deteriorating; this most likely should be confirmed by appropriate inspections.

The asymmetric loads that may exist owing to the uneven wetting process during the first decades and the loads due to density or geometry variations in the bentonite buffer later in the saturated condition are both shown not to be the governing load cases.

It can thus be concluded that the BWR and PWR canister can withstand all given load cases within the design premises with moderate safety factors. The canisters also have a tolerance against material defects. The reference requirements for the components in terms of their mechanical properties and acceptable idealised defects are stated in this report.

References

SKB's (Svensk Kärnbränslehantering AB) publications can be found at www.skb.com/publications.
SKBdoc-documents will be submitted upon request to document@skb.se.
Posiva's publications can be found at http://posiva.fi/en/databank.

ABAQUS, 2014. Version 6.13.1. Dassault Systèmes Simulia Corp.

Alverlind L, 2010. Designanalys av stållock till kapsel för använt kärnbränsle – geometriuppdatering. Rapport 50008640-1, Revision , Inspecta Technology AB. SKBdoc 1177857 ver 1.0, Svensk Kärnbränslehantering AB. (In Swedish.)

Alverlind L, 2016a. Isostatic pressure load of canister with scaled iron material model. Report 5000484-1, Revision 4, Inspecta Technology AB. SKBdoc 1089758 ver 3.0, Svensk Kärnbränslehantering AB.

Alverlind L, 2016b. Canister bottom structural integrity. Report 50008630-1, Revision 13, Inspecta Technology AB. SKBdoc 1207429 ver 3.0, Svensk Kärnbränslehantering AB.

Alverlind L, 2016c. Damage tolerance analysis of the copper shell in PWR and BWR canisters during handling of the entire canister with revised material data. Report 50010850-1, Revision 4, Inspecta Technology AB. SKBdoc 1278273 ver 1.0, Svensk Kärnbränslehantering AB.

Andersson D, Sollander R, Bolinder T, 2016. BWR and PWR canister inserts subjected to shear loads, analysis with large postulated cracks. Report 5000486-1, Revision 4, Inspecta Technology AB. SKBdoc 1512763 ver 1.0, Svensk Kärnbränslehantering AB.

Andersson T, Laukkanen A, Fortino S, Sippola M, 2017. Creep modeling and life assessment of FSW welded copper canister. VTT Technical Research Centre of Finland, Posiva LP-00005985, Posiva Oy.

Andersson-Östling H C M, Sandström R, 2007. Creep during power-law breakdown in phosphorus alloyed copper. In Proceedings of CREEP8 Eighth International Conference on Creep and Fatigue at Elevated Temperatures, San Antonio, Texas, 22–26 July 2007, PVP2007-26518.

Andersson-Östling H C M, Sandström R, 2009. Survey of creep properties of copper intended for nuclear waste disposal. SKB TR-09-32, Svensk Kärnbränslehantering AB.

ANSYS 2007. Version 11.0, Swanson Analysis Systems Inc.

ASM, 1990. ASM handbook. Vol. 2, Properties and selection: nonferrous alloys and special-purpose materials. 10th ed. Materials Park, OH: ASM International.

ASME, 2008a. ASME boiler and pressure vessel code. Section III – Rules for construction of nuclear power plant components – Divisions 1 and 2. New York: American Society of Mechanical Engineers.

ASME, 2008b. ASME boiler and pressure vessel code. Section XI – Rules for inservice inspection of nuclear power plant components. New York: American Society of Mechanical Engineers.

ASTM E1820:2009. Standard test method for measurement of fracture toughness. West Conshohocken, PA: ASTM International.

Barslivo G, Jansson C, 2016. SKB – Impact of the earthquake induced displacements on the canister steel lid. QP.50124.007-105261606, Version 2.0, Vattenfall AB. SKBdoc 1522977 ver 1.0, Svensk Kärnbränslehantering AB.

Barsoum I, Faleskog J, 2007. Rupture mechanisms in combined tension and shear – Experiments. International Journal of Structures 44, 1768–1786.

Björkblad A, Faleskog J, 2016. Evaluation of Cu-OFP creep crack growth and theoretical fracture models for Cu-OFP. Swerea KIMAB. SKBdoc 1519789 ver 1.0, Svensk Kärnbränslehantering AB.

Bolinder T, 2011. Damage tolerance analysis of the copper shell in PWR and BWR canisters during handling of the entire canister. Report 50008120-1, Revision 4, Inspecta Technology AB. SKBdoc 1206868 ver 1.0, Svensk Kärnbränslehantering AB.

Bolinder T, Dillström P, Alverlind L, 2014. Additional analysis of BWR canister inserts subjected to shear loads. Report 50010530-1, Revision 3, Inspecta Technology AB. SKBdoc 1285768 ver 2.0, Svensk Kärnbränslehantering AB.

Bolinder T, Alverlind L, Sollander R, 2017. BWR and PWR canister inserts with postulated defects at different positions in the axial direction and defects positioned at the channel tube corner subjected to shear loads. Report 5000486-2, Revision 5, Inspecta Technology AB. SKBdoc 1526006 ver 1.0, Svensk Kärnbränslehantering AB.

Brickstad B, 2009. Analys av driftinducerade skador i svenska kärntekniska anläggningar. Utredningsrapport 2008/232, Swedish Radiation Safety Authority. (In Swedish.)

Brissonneau l, Barbu A, Bocquet J-L, 2004. Radiation effects of the long-term ageing of spent fuel storage containers. RAMTRANS 15, 12–130.

Brorsson A, 2017. Examination of fractures in tensile test specimens. Exova Materials Technology AB. SKBdoc 1571067 ver 1.0, Svensk Kärnbränslehantering AB.

Brosius, C, 2008. Hållfasthetsprovning och kornstorleksbedömning av koppar. LR200819-01, Bodycote Materials Testing AB. SKBdoc 1177795 ver 1.0, Svensk Kärnbränslehantering AB. (In Swedish.)

Brosius, C, 2009. Dragprovning och Kornstorleksbedömning av kopparprov T53. LR200724-02, Bodycote Materials Testing AB. SKBdoc 1092882 ver 1.0. Svensk Kärnbränslehantering AB. (In Swedish.)

Burman G, 2005. Dragprovning av EBW- och FSW-svets. PRO05-0331, CSM Materialteknik. SKBdoc 1037633 ver 1.0, Svensk Kärnbränslehantering AB. (In Swedish.)

Börgesson L, Hernelind J, 2013. Earthquake induced rock shear through a deposition hole – Part 2. Additional calculations of the influence of inhomogeneous buffer on the stresses in the canister. SKBdoc 1407337, ver 1.0, Svensk Kärnbränslehantering AB.

Börgesson L, Johannesson L-E, Sandén T, Hernelind J, 1995. Modelling of the physical behaviour of water saturated clay barriers. Laboratory tests, material models and finite element application. SKB TR 95-20, Svensk Kärnbränslehantering AB.

Börgesson L, Johannesson L-E, Raiko H, 2009. Uneven swelling pressure on the canister simplified load cases derived from uneven wetting, rock contours and buffer density distribution. SKBdoc 1206894 ver 1.0, Svensk Kärnbränslehantering AB.

Börgesson L, Dueck A, Johannesson L-E, 2010. Material model for shear of the buffer – evaluation of laboratory test results. SKB TR-10-31, Svenska Kärnbränslehantering AB.

Börgesson L, Hernelind J, Jonsson M, 2018. PM regarding a new material model of bentonite buffer for shear calculations. SKBdoc 1485821 ver 1.0, Svensk Kärnbränslehantering AB.

Dahlberg C F O, Öberg M, Faleskog J, 2014. Continuum modeling of nodular cast iron using a porous plastic model with pressure-sensitive matrix – Experiments, model calibration & verification. KTH Hållfasthetslära. SKBdoc 1414719 ver 1.0, Svensk Kärnbränslehantering AB.

Dahlberg C F O, Faleskog J, Larsson P-L, 2017. Continuum modelling of ductile fracture in a nodular cast iron based on micromechanics and small scale experiments. KTH Hållfasthetslära. SKBdoc 1512736 ver 1.0, Svensk Kärnbränslehantering AB.

Danielsson M, 2015. Simulation of creep testing of specimens with local indentations. SKBdoc 1442132 ver 1.0, Svensk Kärnbränslehantering AB.

Danielsson M, 2016. Characterisation of the stress state during mechanical testing of phosphorous alloyed copper. SKBdoc 1494364 ver 1.0, Svensk Kärnbränslehantering AB.

Dillström P, 2009a. Updated probabilistic analysis of canister inserts for spent nuclear fuel. 50006980-2, Rev. 1, Inspecta Technology AB. SKBdoc 1207426 ver 1.0, Svensk Kärnbränslehantering AB.

Dillström P, 2009b. Tillämpning av stabil spricktillväxt vid brottmekanisk bedömning av defekter i sega material. Rappor 2009:26, Swedish Radiation Safety Authority. (In Swedish.)

Dillström P, 2014a. Probabilistic analysis of BWR canister inserts for spent nuclear fuel in the case of an earthquake induced rock shear load. Report 50014130-1, Revision 5, Inspecta Technology AB. SKBdoc 1412158 ver 1.0, Svensk Kärnbränslehantering AB.

Dillström P, 2014b. Summary of important characteristic parameters for the BWR- and PWR-insert, based on performed strength and damage tolerance analyses. Report 50017500-1, Revision 4, Inspecta Technology AB. SKBdoc 1288292 ver 1.0, Svensk Kärnbränslehantering AB.

Dillström P, 2014c. PM Probabilistisk analys av skjuvlastfallet. PM 50011100-1, Revision 3, Inspecta Technology AB. SKBdoc 1336557 ver 2.0, Svensk Kärnbränslehantering AB. (In Swedish.)

Dillström P, 2015a. Damage tolerance analysis of BWR-canister inserts for spent nuclear fuel in the case of an earthquake induced rock shear load – Influence of using more detailed models. Report 5000264-1, Revision 2, Inspecta Technology AB. SKBdoc 1450913 ver 1.0, Svensk Kärnbränslehantering AB.

Dillström P, 2015b. Damage tolerance analysis of PWR-canister inserts for spent nuclear fuel in the case of an earthquake induced rock shear load – Influence of using more detailed models. Report 5000264-2, Revision 1, Inspecta Technology AB. SKBdoc 1459222 ver 1.0, Svensk Kärnbränslehantering AB.

Dillström P, 2017. Evaluation of the defect assumptions made in the damage tolerance analysis of the iron insert and requirements regarding the elongation at failure of nodular cast iron. Report 5000483-1, Revision 7, Inspecta Technology AB. SKBdoc 1525318 ver 1.0, Svensk Kärnbränslehantering AB.

Dillström P, Alverlind L, 2014. Defect distributions for BWR- and PWR-insert material. Report 50017480-1, Revision 2, Inspecta Technology AB. SKBdoc 1417759 ver 1.0, Svensk Kärnbränslehantering AB.

Dillström P, Bolinder T, 2010. Damage tolerance analysis of canister inserts for spent nuclear fuel in the case of an earthquake induced rock shear load. SKB TR-10-29, Svensk Kärnbränslehantering AB.

Dillström P, Manngård T, 2017. Probabilistic analysis of BWR canister inserts for spent nuclear fuel in the case of an isostatic pressure load. Report 5001090-1, Revision 4, Inspecta Technology AB. SKBdoc 1585534 ver 1.0, Svensk Kärnbränslehantering AB.

Dillström P, Bergman M, Brickstad B, Zang W, Sattari-Far I, Andersson P, Sund G, Dahlberg L, Nilsson F, 2008. A combined deterministic and probabilistic procedure for safety assessment of components with cracks – Handbook. Report 2008:01, Swedish Radiation Safety Authority.

Dillström P, Alverlind L, Andersson M, 2010. Framtagning av acceptanskriterier samt skadetålighetsanalyser av segjärninsatsen. SKB R-10-11, Svensk Kärnbränslehantering AB. (In Swedish.)

Dillström P, Bolinder T, Bonnaud E, 2014. Analysis of PWR canister inserts using data acquired from PWR material. Report 50010510-1, Revision 8, Inspecta Technology AB. SKBdoc 1288288 ver 2.0, Svensk Kärnbränslehantering AB.

Faleskog, 2012a. Inverkan av spänningstillståndet på duktilitet i segjärnsinsats — En summering av experimentella data. SKBdoc 1392347 ver 1.0, Svensk Kärnbränslehantering AB. (In Swedish.)

Faleskog, 2012b. Kommentar – Belastningshastighetens inverkan på brottseghet. SKBdoc 1355310 ver 1.0, Svensk Kärnbränslehantering AB. (In Swedish.)

Fourlakidis V, 2013. Bedömning av brottmekanism i provstavar från insats I53. Swerea SWECAST AB. SKBdoc 1415249 ver 1.0, Svensk Kärnbränslehantering AB. (In Swedish.)

Hernelind J, 2010. Modelling and analysis of canister and buffer for earthquake induced rock shear and glacial load. SKB TR-10-34, Svensk Kärnbränslehantering AB.

Hernelind J, 2014a. Global simulation of copper canister-final deposition. SKBdoc 1339902 ver 1.0, Svensk Kärnbränslehantering AB.

Hernelind J, 2014b. Shearing of copper canister at top and base. SKBdoc 1403930 ver 1.0, Svensk Kärnbränslehantering AB.

Hernelind J, 2014c. Modelling of a canister with broken insert subjected to earthquake induced shear and subsequent glacial load. SKBdoc 1404369 ver 2.0, Svensk Kärnbränslehantering AB.

Hernelind J, 2014d. Detailed models for BWR-canisters for earthquake induced rock shearing. SKBdoc 1439722 ver 1.0, Svensk Kärnbränslehantering AB.

Hernelind J, 2014e. Detailed models for PWR- and BWR-canisters for earthquake induced rock shearing. SKBdoc 1415152 ver 2.0, Svensk Kärnbränslehantering AB.

Hernelind J, 2014f. Analysis of canister with unfavourable pressure load. SKBdoc 1419643 ver 1.0, Svensk Kärnbränslehantering AB.

Hernelind J, 2014g. Modelling and analysis of canister with insert void defects for earthquake induced rock shear. SKBdoc 1427299 ver 1.0, Svensk Kärnbränslehantering AB.

Hernelind J, 2015a. Analysis of creep in the KBS-3 copper canister due to internal and external loads. SKBdoc 1399768 ver 2.0, Svensk Kärnbränslehantering AB.

Hernelind J, 2015b. Detailed models for PWR-canisters for earthquake induced rock shearing. SKBdoc 1439730 ver 1.0, Svensk Kärnbränslehantering AB.

Hernelind J, 2015c. Hydrostatic pressure for detailed BWR/PWR-canisters. SKBdoc 1454226 ver 1.0, Svensk Kärnbränslehantering AB.

Hernelind J, 2015d. Modelling and analysis of BWR-canister and buffer for earthquake induced rock shear with copper corrosion. SKBdoc 1469524 ver 1.0, Svensk Kärnbränslehantering AB.

Hernelind J, 2016a. Modelling and analysis of BWR-canister with large crack. SKBdoc 1487674 ver 1.0, Svensk Kärnbränslehantering AB.

Hernelind J, 2016b. Broken steel lid for PWR-canisters for earthquake induced rock shearing. SKBdoc 1519809 ver 1.0, Svensk Kärnbränslehantering AB.

Hernelind J, 2017a. Additional analyses of eccentric insert inside the copper shell and sensitivity analyses of creep. SKBdoc 1551711 ver 1.0, Svensk Kärnbränslehantering AB.

Hernelind J, 2017b. Effect of changing design criterion for buffer to swelling pressure 10 MPa. SKBdoc 1516736 ver 1.0, Svensk Kärnbränslehantering AB.

Hernelind J, 2017c. Comparison of integrated and welded base of the copper shell. SKBdoc 1519489 ver 1.0, Svensk Kärnbränslehantering AB.

Hernelind J, Börgesson L, 2018. Global analyses to validate buffer properties corresponding to swelling pressures of 3–10 MPa and sensitivity analyses of buffer and steel tube properties. SKBdoc 1550977 ver 1.0, Svensk Kärnbränslehantering AB.

Holmström S, 2010. Engineering tools for robust creep modeling. PhD thesis. Aalto University, Finland.

Holmström S, Auerkari P, 2009. Predicting creep rupture from early strain data. Materials Science and Engineering: A 510–511, 25–28.

Holst L, Sarnet J, 2017. Sammanställning och analys av dragprovningsmätningar från kopparkapslars segjärnsinsatser för använt kärnbränsles slutförvaring. SKB R-17-14, Svensk Kärnbränslehantering AB. (In Swedish.)

Hultgren J, 2014. Ritningsförteckning för kapselkomponenter. SKBdoc 1203875, ver 2.0, Svensk Kärnbränslehantering AB. (In Swedish.)

Hökmark, H, Lönnqvist, M, Fälth, B, 2010. THM-issues in repository rock. Thermal, mechanical, thermomechanical and hydro-mechanical evolution of the rock at the Forsmark and Laxemar sites. SKB TR-10-23, Svensk Kärnbränslehantering AB.

Ikonen K, 2005. Mechanical analysis of cylindrical part of canisters for spent nuclear fuel. Posiva Working Report 2005-12, Posiva Oy.

Ikonen K, 2017. Temperatures inside SKB and POSIVA type disposal canisters for spent fuel. VTT Technical Research Centre of Finland, Posiva LP-00005994, Posiva Oy.

Jin L-Z, Sandström R, 2008. Creep of copper canisters in power-law breakdown. Computational Materials Science 43, 403–416.

Jin L-Z, Sandström R, 2013. Influences of load variations on the plastic deformation in friction stir welds and contour slits in copper shells. SKB TR-13-25, Svensk Kärnbränslehantering AB.

Johnson G R, Cook W H, 1985. Fracture characteristics of three metals subjected to various strains, strain rates, temperatures and pressures. Engineering Fracture Mechanics 21, 31–48.

Jonsson M, 2017. Mechanical properties on cast iron inserts for encapsulation of spent nuclear fuel, summary report. SKBdoc 1207576 ver 3.0, Svensk Kärnbränslehantering AB.

Jonsson M, Ronneteg U, 2014. Manufacturing and testing of copper components. SKBdoc 1432038 ver 1.0, Svensk Kärnbränslehantering AB.

Kallio H, 2016. Mechanical testing of steel channel tubes from BWR and PWR inserts after casting. Research Report VTT-S-03815-16, VTT. SKBdoc 1549023 ver 1.0, Svensk Kärnbränslehantering AB.

Kallio, H, 2017. Mechanical testing of steel channel tubes from PWR insert after casting. Research Report VTT-S-04912-16, VTT. SKBdoc 1571085 ver 1.0, Svensk Kärnbränslehantering AB.

Leskinen N, Ronneteg U, 2013. Tillverkning av kapselkomponenter. SKBdoc 1175208 ver 8.0, Svensk Kärnbränslehantering AB. (In Swedish.)

Lilja C, 2012. Inre övertryck i kapseln. SKBdoc 1333208 ver 2.0, Svensk Kärnbränslehantering AB. (In Swedish.)

Mannesson K, Andersson-Östling H C M, 2013. Creep of copper with different NDT sound attenuation. KIMAB-2013-124, Swerea KIMAB. SKBdoc 1411196 ver 1.0, Svensk Kärnbränslehantering AB.

Mannesson K, Andersson-Östling H C M, 2014. Creep of indented copper – cone, sphere and cylinder. KIMAB-2014-114, Swerea KIMAB. SKBdoc 1442561 ver 1.0, Svensk Kärnbränslehantering AB.

Mannesson K, Andersson-Östling H C M, Sandström R, 2013. Influence of local cold work in creep failure of phosphorus doped oxygen free copper. SKB R-13-32, Svensk Kärnbränslehantering AB.

Manngård T, von Feilitzen C, 2017. Setting of requirements for the steel components. BWR and PWR cast iron inserts. Report 5000763-1, Revision 4, Inspecta Technology AB. SKBdoc 1527986 ver 1.0, Svensk Kärnbränslehantering AB.

Martin O, Nilsson K-F, Jakšić N, 2009. Numerical simulation of plastic collapse of copper castiron iron canister for spent nuclear fuel. Engineering Failure Analysis 16, 225–241.

Martinsson Å, Andersson-Östling H C M, Seitisleam F, Wu R, Sandström R, 2010. Creep testing of nodular iron at ambient and elevated temperatures. SKB R-10-64, Svensk Kärnbränslehantering AB.

Müller K, Baer W, Wossidlo P, 2002. Fracture toughness behaviour of thick-walled nodular cast iron at elevated loading rates. Department of Materials Engineering, Federal Institute for Materials Research and Testing (BAM), Berlin, Germany.

Nilsson K-F, Lofaj F, Burström M, Andersson C-G, 2005. Pressure tests of two KBS-3 canister mock-ups. SKB TR-05-18, Svensk Kärnbränslehantering AB.

Nilsson S, 2014. Dragprovning av koppar från locksvets FSWL 77 vid förhöjd temperatur. Provningsrapport PRO11-1010, utgåva 2, Exova AB. SKBdoc 1293032 ver 1.0, Svensk Kärnbränslehantering AB. (In Swedish.)

Olsson M, 2015. Materialstudie – Tillverkning och dragprovning av kopparprovstavar. SKBdoc 1464901 ver 1.0, Svensk Kärnbränslehantering AB. (In Swedish.)

Persson G, 2005. Provningsintyg EN10204-3.1B, Test number 626217, SSAB Tunnplåt, Borlänge. Kils Verkstad AB. SKBdoc 1213477 ver 1.0, Svensk Kärnbränslehantering AB. (In Swedish.)

Platdepan, 2003. Inspection certificate according to EN 10 204-31B, Spec. No. 31080003, U.S. Steel Košice, s.r.o., Košice, Slovak Republic. SKBdoc 1213475 ver. 1.0, Svensk Kärnbränslehantering AB.

Posiva, 2012a. Safety case for the disposal of spent nuclear fuel at Olkiluoto – Performance Assessment 2012. Posiva 2012-04, Posiva Oy.

Posiva, 2012b. Safety case for the disposal of spent nuclear fuel at Olkiluoto – Synhesis 2012. Posiva 2012-12, Posiva Oy.

Raiko H, 2013. Canister design 2012. Posiva 2012-13, Posiva Oy.

Raiko H, Sandström R, Rydén H, Johansson M, 2010. Design analysis report for the canister. SKB TR-10-28, Svensk Kärnbränslehantering AB.

Reuterswärd H, 2015. Macro sample of FSW110. Test report PRO15-1040, Exova Materials Technology AB. SKBdoc 1494040 ver 2.0, Svensk Kärnbränslehantering AB.

Rydén H, 2012. Förtydligande information angående belastningshastighetens inverkan på brottsegheten för insatsen. SKBdoc 1355363 ver 2.0, Svensk Kärnbränslehantering AB. (In Swedish.)

Sandström R, Andersson H C M, 2007. Creep during power-law breakdown in phosphorus alloyed copper. In Hasegawa K, Scarth D A (eds). Proceedings of the ASME Pressure Vessels and Piping/ Creep8 Conference. San Antonio, Texas, 22–26 July 2007. New York, NY: American Society of Mechanical Engineers.

Sandström R, Andersson H C M, 2008. Creep in phosphorus alloyed copper during power-law breakdown. Journal of Nuclear Materials 372, 76–88.

Sandström R, Hallgren J, Burman G, 2009. Stress strain flow curves for Cu-OFP. SKB R-09-14, Svensk Kärnbränslehantering AB.

Shipsha A, 2013. Statistical data analysis of cast iron properties for PWR-inserts from tension, compression and fracture toughness testing. Report 50017490-1, Revision 2, Inspecta Technology AB. SKBdoc 1414800 ver 1.0, Svensk Kärnbränslehantering AB.

Shipsha A, 2014. Evaluation of the effect of triaxial stress state on damage tolerance of nodular cast iron inserts. Report 50017510-1, Revision 1, Inspecta Technology AB. SKBdoc 1418263 ver 1.0, Svensk Kärnbränslehantering AB.

Shipsha A, 2015. Evaluation of residual stress measurements. Effect of measured residual stresses on damage tolerance of cast iron PWR- and BWR-inserts. Report 50018390-1, Revision 3, Inspecta Technology AB. SKBdoc 1416697 ver 2.0, Svensk Kärnbränslehantering AB.

SIS, 1986. IKH Lyftdonsnormer. 2nd ed. Stockholm: Standardiseringskommissionen i Sverige. (SIS handbok 154). (In Swedish.)

SKB, 2009. Design premises for a KBS-3V repository based on results from the safety assessment SR-Can and some subsequent analyses. SKB TR-09-22, Svensk Kärnbränslehantering AB.

SKB, 2010a. Design and production of the KBS-3 repository. SKB TR-10-12, Svensk Kärnbränslehantering AB.

SKB, 2010b. Spent nuclear fuel for disposal in the KBS-3 repository. SKB TR-10-13, Svensk Kärnbränslehantering AB.

SKB, 2010c. Design, production and initial state of the canister. SKB TR-10-14, Svensk Kärnbränslehantering AB.

SKB, 2010d. Design, production and initial state of the buffer. SKB TR-10-15, Svensk Kärnbränslehantering AB.

SKB, 2011. Long-term safety for the final repository for spent nuclear fuel at Forsmark. Main report of the SR-Site project. SKB TR-11-01, Svensk Kärnbränslehantering AB.

SKB, 2013. Svar till SSM på begäran om komplettering rörande lång återmättnadsfas. SKBdoc 1385067 ver 3.0, Svensk Kärnbränslehantering AB. (In Swedish.)

Posiva SKB, 2017. Safety functions, performance targets and technical design requirements for a KBS-3V repository. Conclusions and recommendations from a joint SKB and Posiva working group Posiva SKB Report 01, Posiva Oy, Svensk Kärnbränslehantering AB.

Smedstad M, 2016. The use of nodular ductile cast iron in storage canisters for spent nuclear fuel in conjunction with ASME Section III. FSD1021312-01, Rev 07, FS Dynamics Sweden AB. SKBdoc 1527035 ver 1.0, Svensk Kärnbränslehantering AB.

SS-EN 10002-1:2001. Metallic materials – Tensile testing – Part 1: Method of test at ambient temperature. Stockholm: Swedish Standards Institute.

SS-EN 10025-2:2004. Hot rolled products of structural steels – Part 2: Technical delivery conditions for non-alloy structural steels. Stockholm: Swedish Standards Institute.

SS-EN 1563:2012. Founding – Spheroidal graphite cast irons. Stockholm: Swedish Standards Institute.

SS-EN ISO 6892:2009. Metallic materials – Tensile testing – Part 1: Method of test at room temperature. Stockholm: Swedish Standards Institute.

Unosson, M, 2014. A constitutive model for texture dependent deformation hardening and pressure dependent initiation of ductile failure in metallic materials. SKBdoc 1393179 ver 2.0, Svensk Kärnbränslehantering AB.

Unosson, M, 2015. Design of test specimens for indentation and creep testing of copper. SKBdoc 1287236 ver 2.0, Svensk Kärnbränslehantering AB.

Unosson, M, 2016. Numerical simulation of earthquake induced rock shear through a deposition hole – Crack initiation and propagation in an insert with pre-existing intertubular and edge crack planes. SKBdoc 1474363 ver 1.0, Svensk Kärnbränslehantering AB.

Unosson, M, 2017. Investigation of criteria for handling and the principal of mechanical requirements of the copper shell. SKBdoc 1492223 ver 1.0, Svensk Kärnbränslehantering AB.

Wells S, 2008. Fracture toughness testing of copper cylinder T31 and lid weld FSWL27. D7475, Bodycote Engineering and Technology. SKBdoc 1187725 ver 1.0, Svensk Kärnbränslehantering AB.

Wu R, Sandström R, 2015. Influence of cold work and notches on creep failure of Cu-OFP. SKB R-15-04, Svensk Kärnbränslehantering AB.

Zeng L, Adriansson S, Luo C, 2015. Structural integrity requirements for the canister insert with regard to lifting. Report 6075302-001 Ed.3, ÅF-Industry AB. SKBdoc 1526681 ver 1.0, Svensk Kärnbränslehantering AB.

Öberg H, 2009. Brottmekanisk provning av gjutjärn. PM SKB0903, KTH Hållfasthetslära. SKBdoc 1203550 ver 2.0, Svensk Kärnbränslehantering AB. (In Swedish.)

Öberg M, Faleskog J, 2012. Uppskattning av dJ/dt för brottseghetsprover. Rapport SKB120807-2, KTH Hållfasthetslära. SKBdoc 1353649 ver 2.0, Svensk Kärnbränslehantering AB. (In Swedish.)

Appendix A

Compilation of defect acceptance criteria for idealised postulated defects of the inserts

The acceptance criteria are based on the acceptable sizes calculated for the idealised postulated defects. It is beyond the scope of this report to determine whether the real defects, such as dross/slag and blowholes, shall be considered as crack-like or volumetric defects. Locally, the stresses in the insert are low, and thereby, the occurrence of defects in these volumes do not affect the tightness of the copper shell, which determines the integrity of the canister. Based on this, no specific defect requirements are necessary in some volumes, as developed below. The purpose of this appendix is to compile the defect acceptance criteria for the idealised postulated defects of the inserts that in turn can be used as reference data for non-destructive testing requirements.

Two main types of idealised defects have been postulated: volumetric and crack-like defects. The crack-like defects have been postulated both with their main propagation along the axial and circumferential directions. Based on these postulations, the following three specific defect cases are described below:

- Spherical volumetric defects.
- Axial crack-like defects, that is, defects with a normal perpendicular to the canister axis.
- Circumferential crack-like defects, that is, defects with a normal parallel to the canister axis.

Zones in the inserts

The cross sections of the BWR and PWR inserts are divided into zones for in Figure A-1 and in Figure A-2, respectively.

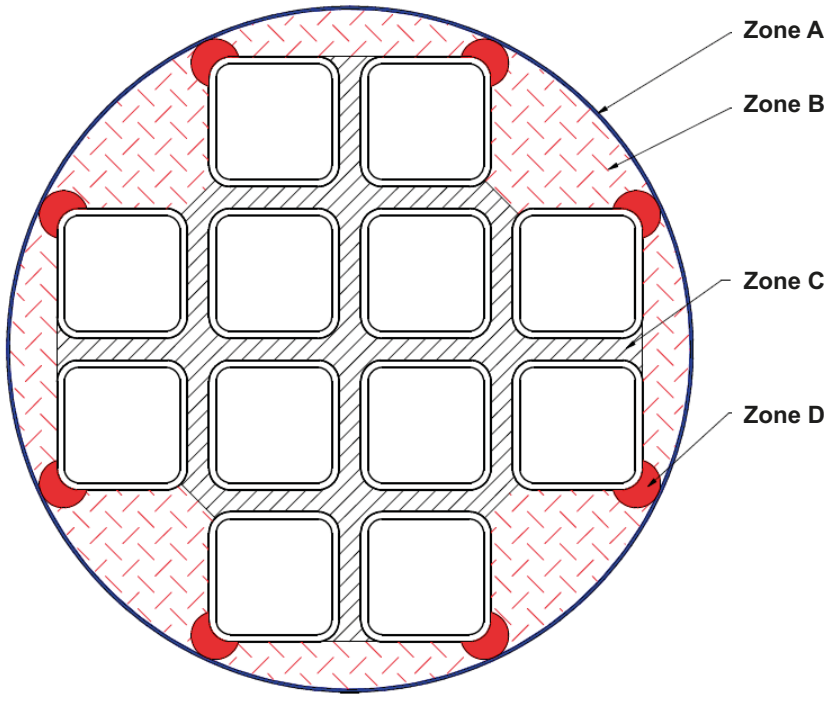

Zone A (blue)	Zone B	Zone C	Zone D (red)
0–5 mm from the surface.	From zone A down to the channel tubes.	Between the channel tubes.	A radius from the outer channel tube corner corresponding to the edge distance *H* in Table 5-1 (nominal 33.3 mm) (BWR).

Figure A-1. *Schematic definition of the zones in the BWR insert cross section.*

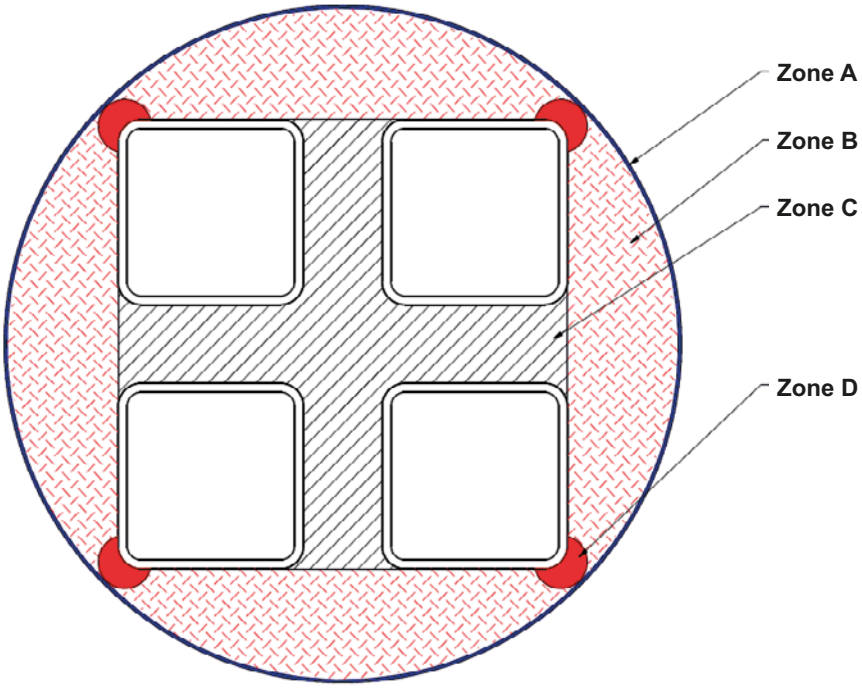

Zone A (blue)	Zone B	Zone C	Zone D (red)
0–5 mm from the surface.	From zone A down to the channel tubes.	Between the channel tubes.	A radius from the outer channel tube corner corresponding to the edge distance *H* in Table 5-1 (nominal 37.3 mm) (PWR).

Figure A-2. *Schematic definitions of the zones in the PWR insert cross section.*

The BWR and PWR inserts are divided into axial zones according to Figure A-3. The axial zones are the same for both the BWR and PWR inserts.

Volumetric defects

The volumetric defects can be considered as a localised lack of material and can be analysed with elastic-plastic methods for the isostatic load case, see Table A-1 and Table A-2. These defects are defined for the nodular cast iron material in the insert, except for the integrated base.

The rock shear case was also investigated with postulated volumetric defects in zone $A–B$ = 40 mm diameter and in zone D = 20 mm diameter (see Hernelind 2014 g). The conclusion is that the volumetric defects are insignificant in the rock shear case.

Table A-1. Maximum acceptable three-dimensional sizes for the volumetric defects in the BWR insert. The zones are defined according to Figure A-1.

Defect	Zone A	Zone B	Zone C	Zone D
Volumetric, spherical	A defect with a depth of 9.0 mm and a propagation along the surface of 22.5 mm.	As large a diameter that can be contained between zone A and zone C or the steel channel tubes is allowed as long as it is not physically surface breaking. Ø36–160 mm is acceptable depending on the location in zone B, and Ø less than 35 mm is always acceptable.	No requirements for the volumetric defects.	A Ø30 mm (Ø20 mm*) defect is allowed as long as it is not physically surface breaking.

* In combination with the minimum edge distance (reduced by 10 mm).

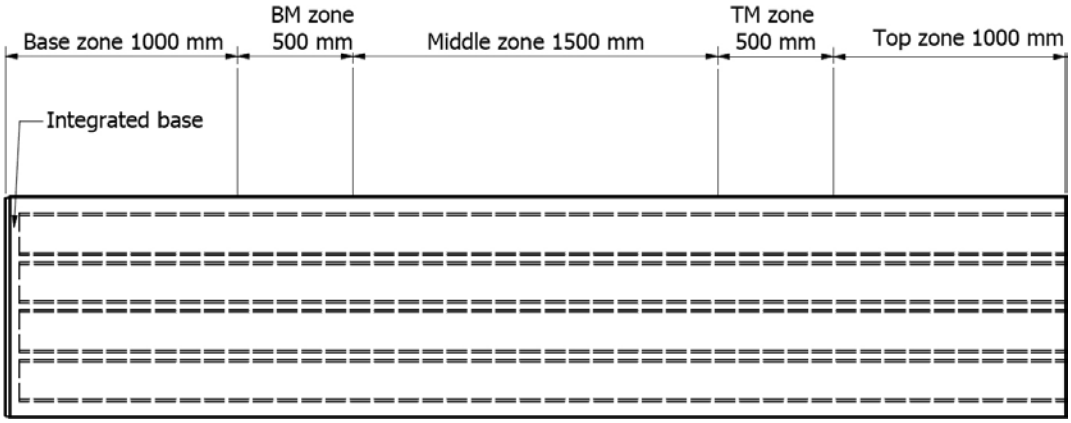

Figure A-3. *Schematic definition of the axial zones in the BWR and PWR inserts.*

Table A-2. Maximum acceptable three-dimensional sizes for volumetric defects in the PWR insert. The zones are defined according to Figure A-2.

Defect	zone A	zone B	zone C	zone D
Volumetric, spherical	A defect with a depth of 9.0 mm and a propagation along the surface of 22.5 mm.	As large a diameter that can be contained between zone A and zone C or the steel channel tubes. Ø75–180 mm is acceptable depending on the location in zone B, and Ø less than 75 mm is always acceptable.	No requirements for the volumetric defects are needed in this zone.	A Ø35 mm (Ø24 mm*) defect is allowed as long as it is not physically surface breaking.

* In combination with the minimum edge distance (reduced by 10 mm).

Locally, the stresses in the insert are low and thereby the occurrence of defects in these volumes does not affect the tightness of the copper shell, which determines the integrity of the canister. Based on this, no specific defect requirement is necessary for some specific volumes. The justification to remove volumetric defect requirements in zone *C* is derived from the results in Alverlind (2016a); all material in zone *C* can be removed 186 mm along the axial direction of the BWR insert and 500 mm for the PWR insert. This shows that the inserts are very robust in terms of the volumetric defects in zone *C*. The integrated base is excluded since the base was determined in Alverlind (2016b) to be very robust in terms of the volumetric defects. Therefore, there is no requirement for NDT inspection of the volumetric defects in zone *C* and in the integrated base of the inserts.

In Figures A-4 and A-5, examples of volumetric defects are shown for the BWR and PWR inserts.

Crack-like defects

The crack-like defects are defined as defects with their main extension along the axial or circumferential direction. In contrast to the volumetric defects, crack-like defects have a semi-circular or semi-elliptical shape and require fracture mechanical analysis methods. The acceptable axial crack-like defects are governed for the isostatic load case, and the acceptable sizes for the circumferential direction are governed for the rock shear case.

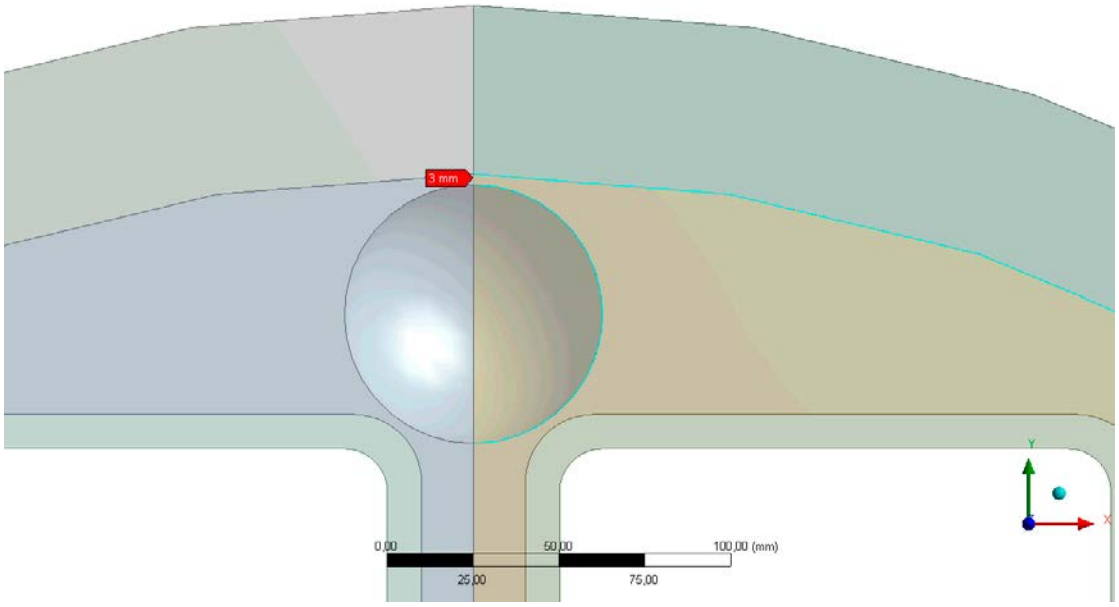

Figure A-4. *Example of the ligament with a thickness of 3.0 mm; a hole in zone B with a diameter of 75 mm in the BWR insert is shown.*

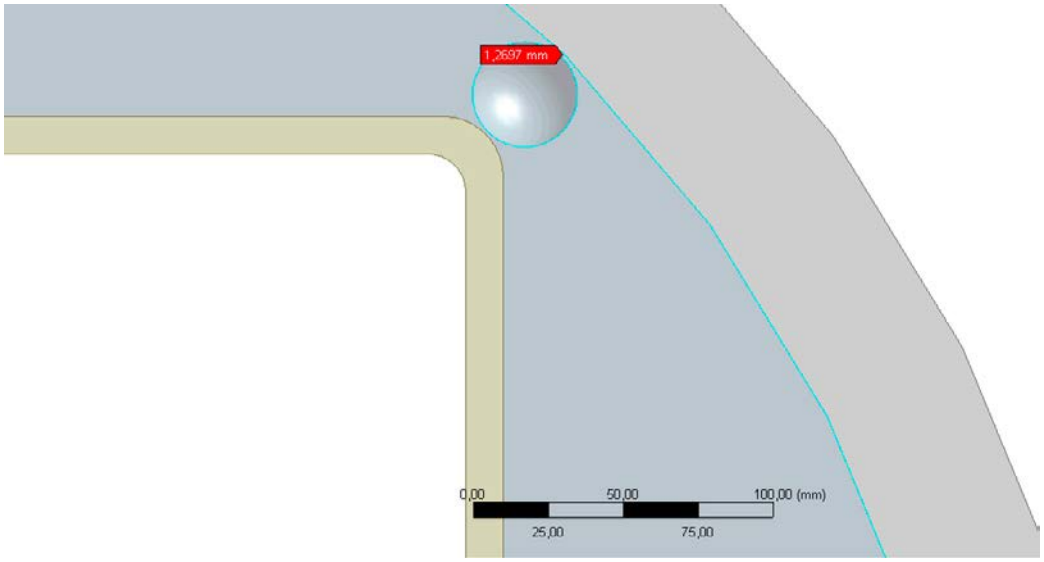

Figure A-5. *Example of the ligament with a thickness of 1.26 mm; a hole with a diameter of 35 mm in zone D in the PWR insert is shown.*

Axial crack-like defects

The maximum acceptable sizes for the axial crack-like defects of the BWR insert are shown in Table A-3 and are shown in Table A-4 for the PWR-insert, see Figure A-6 for the schematic positions. The through-wall crack-like defects are assumed to propagate through zones *A*, *B*, *C* or *D*. The maximum acceptable crack lengths are restricted to 1 000 mm, and at some positions, even shorter lengths are required (Alverlind 2016a). In Tables A-3 and A-4, the presence of residual stresses has been considered. The tables should be interpreted as guidelines for further determining the acceptable sizes of real defects. Longer acceptable lengths for crack-like defects that do not pass through the wall may be acceptable but need to be further investigated.

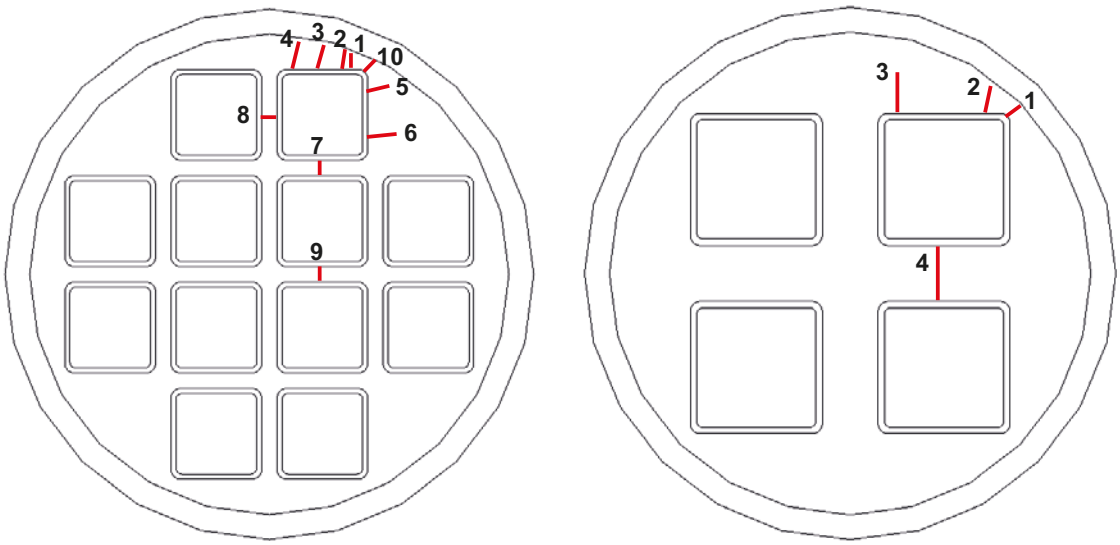

Figure A-6. *Schematic position of the axial crack-like defects in the BWR and PWR insert cross sections.*

Table A-3. Maximum acceptable sizes for the axial crack-like defects in the BWR insert. The positions are from Figure A-6.

Position	Zones	Through wall crack, acceptable length (mm)
1	A and B	1 000
2	A and B	888
3	A and B	1 000
4	A and B	1 000
5	A and B	1 000
6	A and B	656
7	C	430
8	C	430
9	C	430
10	A and D	1 000

Table A-4. Maximum acceptable sizes for axial crack-like defects in the PWR insert. The positions are from Figure A-6.

Position	Zones	Through wall crack, acceptable length (mm)
1	A and D	1 000
2	A and B	1 000
3	A and B	976
4	C	697

Circumferential crack-like defects

Surface defects are characterised as semi-elliptical cracks (see Figure A-7). Internal defects are characterised as elliptical cracks (see Figure A-8). The characterising parameters of the crack are defined as follows:

a) The depth of surface crack a corresponds to half of the minor axis of the ellipse.

b) The depth of an embedded crack of $2a$ corresponds to the minor axis of the ellipse.

c) The length of crack l corresponds to the major axis of the ellipse for the surface and internal cracks.

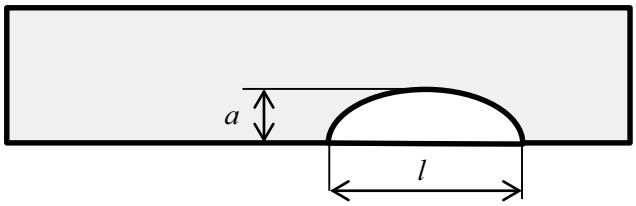

Figure A-7. *Schematic of a crack-like surface defect. This defect has length l and defect depth a (defect shape = l/a).*

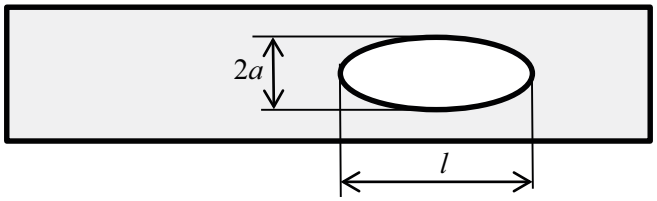

Figure A-8. *Schematic of a crack-like internal defect. This defect has length l and defect depth 2a (defect shape = l/2a).*

In case the plane of the defect does not coincide with a plane normal to a principal stress direction, the defect shall be projected onto normal planes of each principal stress direction. Then, according to this procedure, one of these projections is chosen for the assessment that gives the most pessimistic result.

Schematics of the surface and internal defects in the inserts are shown in Figures A-9 and A-10.

When a defect is situated near a free surface or is close to other defects, the interaction shall be taken into account according to the present rules in Dillström et al. (2008). The compound defect size is determined using the length and depth of the geometry described above, which circumscribes the defects.

Defects in the cast iron located close to the steel channel tube corners are shown in Figure A-11.

The maximum acceptable circumferential defect sizes are specified for the BWR insert in Table A-5 and for the PWR insert in Table A-6. In zone *C*, there are no requirements for the crack-like circumferential defects. The justification is from the result in Andersson et al. (2016), in which a very large defect in zone *C* can be accepted according to ASME. Further studies in Unosson (2016) have shown that the integrity of the copper shell is not threatened if the most pessimistic rock shear occurs on the canister. Thus, inspection with NDT can be excluded in zone *C*, and therefore, no requirements are needed.

The distance from the surface for which an internal defect should be considered to be a surface defect is 4.1 mm for the BWR insert and 4.4 mm for the PWR insert (Dillström 2017). Since zone *A* has a radial extension of 5 mm, a defect is pessimistically considered to be internal if it is not located in zone *A*.

The acceptance criterion in zone *D* is considered with the inclusion of the minimum acceptable edge distance. Furthermore, the defect in zone *D* is considered with respect to originating in the nodular cast iron at the corner of the steel tube and extending in the direction against the barrel surface of the insert.

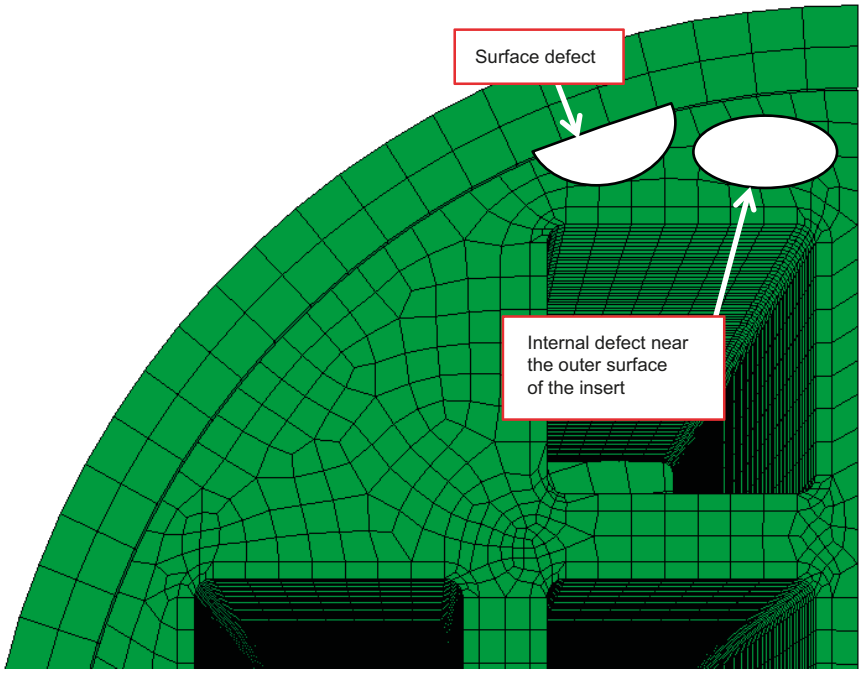

Figure A-9. *Surface and internal crack-like defects in the BWR insert.*

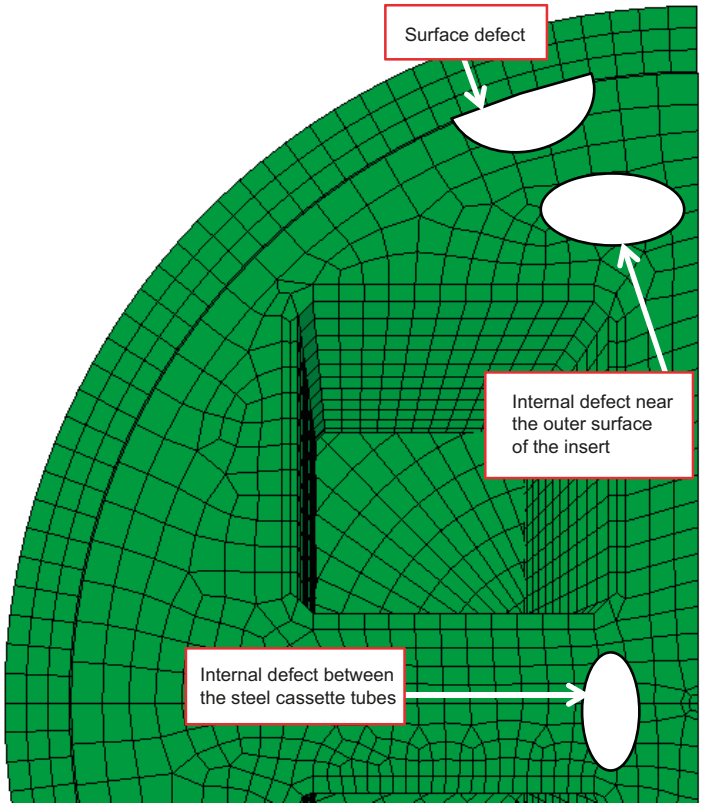

Figure A-10. *Surface and internal crack-like defects in the PWR insert.*

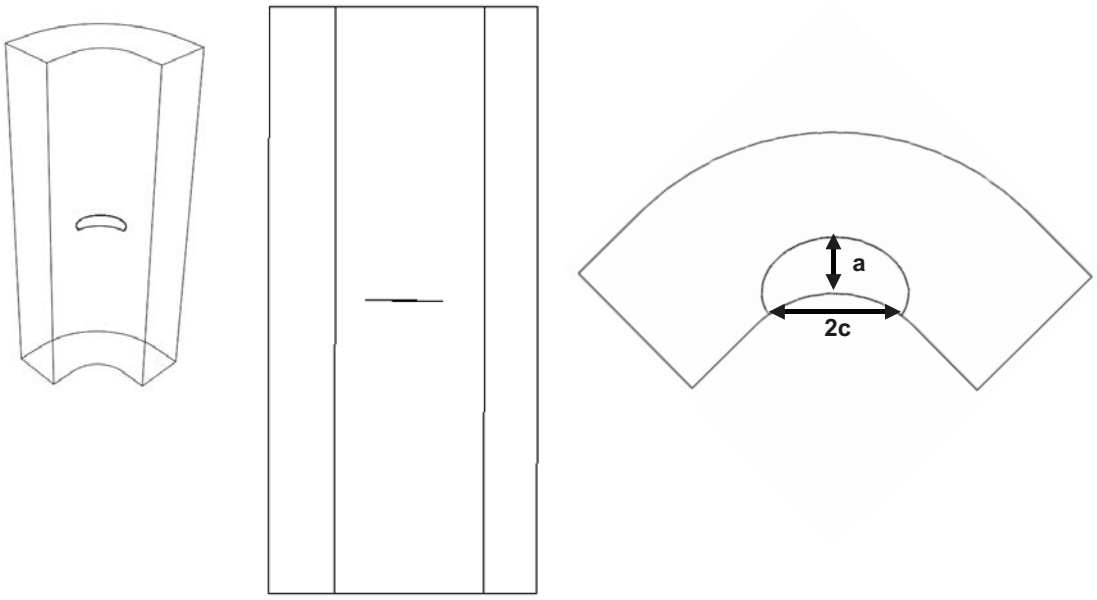

Figure A-11. *Schematic of the geometry of the channel-tube corner crack.*

Table A-5. Maximum acceptable sizes for the circumferential crack-like defects for the BWR insert.

		Radial depth (circumferential length l in parenthesis), (mm)			
Defect	**Axial zone**	**Zone A**	**Zone B**	**Zone C**	**Zone D**
Circumferential crack-like defect.	Base zone and top zone.	50 (125)	20.7 (51.8)	No requirements	12.8 (32)
Circumferential crack-like defect.	BM zone and TM zone.	20 (50)	20.7 (51.8)	No requirements	12.8 (32)
Circumferential crack-like defect.	Middle zone.	9.0 (22.5)	20.7 (51.8)	No requirements	12.8 (32)

Table A-6. Maximum acceptable sizes for circumferential crack-like defects for the PWR insert.

		Radial depth (circumferential length l in parenthesis), (mm)			
Defect	**Axial zone**	**Zone A**	**Zone B**	**Zone C**	**Zone D**
Circumferential crack-like defect.	Base zone and top zone.	40 (100)	22.7 (56.8)	No requirements	17.2 (43)
Circumferential crack-like defect	BM zone and TM zone.	20 (50)	22.7 (56.8)	No requirements	17.2 (43)
Circumferential crack-like defect	Middle zone.	9.0 (22.5)	22.7 (56.8)	No requirements	17.2 (43)

Arkitektkopia AB, Bromma, 2018

A CO-OPERATION REPORT BETWEEN SVENSK KÄRNBRÄNSLEHANTERING AB AND POSIVA OY

SKB's and Posiva's programmes both aim at the disposal of spent nuclear fuel based on the KBS-3 concept. Formal cooperation between the companies has been in effect since 2001. In 2014 the companies agreed on extended cooperation where SKB and Posiva share the vision "Operating optimised facilities in 2030". To further enhance the cooperation, Posiva and SKB started a series of joint reports in 2016, which includes this report.